REPUBLIC OF CAMEROON
UNIVERSITY OF YAOUNDE I
FACULTY OF SCIENCE

REPUBLIQUE DU CAMEROUN
UNIVERSITE DE YAOUNDE I
FACULTE DES SCIENCES

POSTGRADUATE SCHOOL OF SCIENCE, TECHNOLOGY AND GEOSCIENCES
CENTRE DE RECHERCHE ET DE FORMATION DOCTORALE EN SCIENCES, TECHNOLOGIE ET GEOSCIENCES

RESEARCH AND DOCTORAL TRAINING UNIT FOR CHEMISTRY AND ITS APPLICATIONS
UNITE DE RECHERCHE ET DE FORMATION DOCTORALE EN CHIMIE ET APPLICATIONS

DEPARTMENT OF INORGANIC CHEMISTRY
DEPARTEMENT DE CHIMIE INORGANIQUE

APPLIED INORGANIC CHEMISTRY LABORATORY
LABORATOIRE DE CHIMIE INORGANIQUE APPLIQUEE

Thermal stability of cements resulting from alkaline activation of kaolin, metakaolin and volcanic scoria with partial replacement of aluminium hydroxide

"Thesis"

Submitted and defended publicly in total fulfilment of the requirements for the degree of

Doctor of Philosophy in **Chemistry**

Speciality: Inorganic Chemistry

Option: Physico-Chemistry of Mineral Materials

By
TIFFO Emmanuel
Registration number: **07T526**
Master in Sc. Chemistry (UYI)

Supervised by:
ELIMBI Antoine
Professor

Year 2021

REPUBLIQUE DU CAMEROUN
Paix – Travail – Patrie
UNIVERSITE DE YAOUNDE I
FACULTE DES SCIENCES
B.P. 812 Yaoundé
Département de Chimie Inorganique
Tel: (237) 22 10 81 29

REPUBLIC OF CAMEROON
Peace – Work - Fatherland
UNIVERSITY OF YAOUNDE I
FACULTY OF SCIENCE
P.O. Box 812 Yaoundé
Department of Inorganic Chemistry
Phone: (237) 22 10 81 29

ATTESTATION DE CORRECTION DE THESE DE DOCTORAT / Ph.D DE

Monsieur TIFFO Emmanuel

Nous soussignés, les membres du jury, attestons que **M. TIFFO Emmanuel**, Matricule **07T526**, a pris en compte toutes les observations relevées lors de la soutenance publique de sa thèse de Doctorat / Ph.D du Département de Chimie Inorganique, **le lundi 13 décembre 2021 à 13 heures, dans la salle S01 / S02** du nouveau bloc pédagogique de la Faculté des Sciences de l'Université de Yaoundé 1 sur le thème intitulé: «***Thermal stability of cements resulting from alkaline activation of kaolin, metakaolin and volcanic scoria with partial replacement of aluminium hydroxide***».

En foi de quoi la présente Attestation lui est délivrée pour servir et valoir ce que de droit.

Fait à Yaoundé, le 26 janvier 2022

Président

Justin Nenwa
Professeur

Rapporteur

Antoine Elimbi
Professeur

Dedication

This work is dedicated to my late father Mr. TALIE Maurice for his tireless support along my educational career.

Acknowledgements

This work was done by the research team of Physico-Chemistry of Mineral Materials, Applied Inorganic Chemistry Laboratory, Department of Inorganic Chemistry, Faculty of Science at the University of Yaoundé I. This work is a contribution for the valorisation of local Cameroonian aluminosilicate resources toward the elaboration of cements. However, many persons have contributed to its achievement through moral, material and financial support of which I want to express my gratitude.

My acknowledgements are directed to:

- firstly, to my supervisor Professor ELIMBI Antoine for his availability, criticisms, understanding, valuable suggestions, discussions, corrections and advices;
- secondly, all the members of jury who have accepted to assess this research work;
- Professor AGWARA Moïse ONDOH, the Head of the Department of Inorganic Chemistry for all the administrative facilities;
- all the team of lecturers of both Inorganic and Organic Chemistry Departments for all the knowledge acquired in Chemistry since the undergraduate level;
- Professor DEDAVID Berenice Anina, Professor NJOYA Dayirou and Professor TCHAKOUTE KOUAMO Hervé, Dr POUNTOUENCHI Amadou, Dr DJON LI NDJOCK Benjamin Igor, Dr BOYOM TATCHEMO Franck William, Dr MOUAFON Mohamed and Mrs. SIGNE GOUMWE Stella for the characterisation of samples as well as their constant motivations and supports along this thesis;
- Mrs. WOJUNWO LONTSI Mireille and Mrs. NGONLUNG EBONTAB Sainte Orliane for the proofreading of the manuscript;
- my elders and juniors in the laboratory for the lively and amazing working environment;
- my mother Mrs. SIGNOU Anne, my brothers Mr. TAMBOLA Jean Claude and Mr. SATIDOK Rigobert and my sisters Mrs. MAKUETE Marceline, Mrs. MANDEH Honorine, Mrs. TSAPIT Jeannette and Mrs. NDAPANG Justine for their love, care, moral, advice and financial support as well as Mr. TABUFOR Samson FONGOH and Mrs. MANJIH Delphine for the accommodation and unconditional support;
- my heartfelt thanks to my wife NGANNO Sylviane Delima and my son TAMBOLA TIFFO Ethan Borel for their unconditional love and encouragements;

Finally, I express my gratitude to all those that I have forgotten to mention here but who have contributed in one way or the other towards the achievement of this work.

Table of Contents

List of Abbreviations

Acronym	Definition
OPC	Ordinary Portland Cement
ICP / OES	Inductively Coupled Plasma and Optical Emission Spectrometry
CCD	Charge Coupled Device
SEM	Scanning Electron Microscope
ESEM	Environmental Scanning Electron Microscope
FEG / FEI	Field Electron Gun and Field Electron and Ion
EDS	Energy Dispersive Spectrometry
WDS	Wavelength Dispersive Spectrometry
INSA	Institut National des Sciences Appliquées
DTA	Differential Thermal Analysis
DSC	Differential Scanning Calorimetry
TGA	Thermogravimetric Analysis
DTG	Differential Thermogravimetric Analysis
TMA	Thermo-Mechanical Analysis
Tg	Glass Transition temperature
FTIR	Fourier Transform Infrared spectroscopy
ATR	Attenuated Total Reflection
EPMA	Electron Probe Micro Analysis
CRT	Cathode Ray Tube
ASTM	American Society for Testing and Materials
ICDD	International Centre for Diffraction Data
PDF	Powder Diffraction File
BET	Brunauer, Emmett and Teller
EN	European Norm
XRD	X-Ray Diffraction
A	amorphous aluminium hydroxide
B	aluminium oxy-hydroxide
K	kaolin
MK	metakaolin
Z	volcanic scoria
G	geopolymer or alkali-activated binder

TS	Thermal Shrinkage
BD	Bulk Density
OP	Open Porosity
WA	Water Absorption
CS	Compressive Strength
GGBFS	Ground Granulated Blast Furnace Slag
SF	Silica Fume
CSH	Calcium Silicate Hydrate
CASH	Calcium Aluminosilicate hydrate
NASH	Sodium Aluminosilicate hydrate
T	Temperature
L / S	liquid to solid mass ratio
LOI	Loss on ignition
D	Dimension
Sc.	Science

List of Symbols

Symbol	Definition
%	percentage
°C	degree celsius
MPa	Mega Pascal
pH	hydrogen potential
°	degree
Å	angstron
μ	micron
μm	micrometer
mm	millimeter
mg	milligramme
Min	minute
m	meter
m^2	meter square
m^3	meter cube
m^2 / g	meter square per gramme
mol^{-1}	per mole
eV	electron volt
KeV	kilo electron volt
KV	kilo volt
KN	kilo Newton
mW/ mg	milliwatt per milligramme
ρ	Rho
α	alpha
β	beta
θ	theta
δ	delta
γ	gamma
σ	sigma
Ø	empty set
Kg / m^3	kilogramme per meter cube
cm	centimeter
cm^{-1}	per centimeter

NOx	nitrogen oxide
N_2	nitrogen
SOx	sulphur oxide
CO_2	carbon dioxide
NaOH	sodium hydroxide
$Ca(OH)_2$	calcium hydroxide
SiO_4	silicon in IV-fold coordination
AlO_4	aluminium in IV-fold coordination
AlO_6	aluminium in VI-fold coordination
Na_2O	sodium oxide
K_2O	potassium oxide
CaO	calcium oxide
SiO_2	silicon oxide
Al_2O_3	aluminium oxide
MgO	magnesium oxide
H_2O	water
$Al(OH)_3$	aluminium hydroxide
AlO.OH	aluminium oxy-hydroxide
FeO.OH	iron oxy-hydroxide
Fe_2O_3	iron oxide
TiO_2	titanium oxide
SO_3	sulphur trioxide
P_2O_5	phosphorus pentoxide
Cr_2O_3	chromium (III) oxide
Mn_2O_3	manganese (III) oxide
OH	hydroxyl
H_2SO_4	sulphuric acid
NH_4OH	ammonium hydroxide
$NH_4Al(SO_4)_2$, 12 H_2O	alum
$AlCl_3$, 6 H_2O	aluminium chloride hexa-hydrates
$Si(OH)_4$	orthosilicic acid
Si^{4+}	silicon ion
Al^{3+}	aluminium ion
Na^{+}	sodium ion

K^+	potassium ion
Li^+	lithium ion
Ca^{2+}	calcium ion
H_3O^+	hydronium ion
Al	aluminium
Fe	iron
Ti^{4+}	titanium (IV) ion
Fe^{2+}	iron (II) ion
Cr^{3+}	chromium (III) ion
N	Avogadro number

List of Tables

List of Figures

Abstract

This work concerns the study of the thermal stability of cements resulting from alkaline activation of kaolin (K), metakaolin (MK) and volcanic scoria (Z) with partial replacement of aluminium hydroxide. To that end, two replacements (amorphous aluminium hydroxide (A) and aluminium oxy-hydroxide (B)) were used to substitute the aluminosilicate precursors (0, 10, 20 and 30 % by mass) and the resulting mixtures were activated in alkaline medium. Depending on the starting materials and the synthesised products, the thermal behaviour, the physical and mechanical properties as well as the products obtained by thermal treatment (300-1200 °C) were studied. The synthesised products with replacement showed low compressive strength as compared to those without aluminium hydroxide. This is due to the fact that the replacements behave as fillers. Contrarily, the synthesised products initially containing the replacement and heated at elevated temperatures exhibited improved compressive strength and volume stability. In fact, without replacement, the synthesised products from K or MK showed weak volume retention (weak swelling) and cracks whereas those from Z showed swellings at 1100 °C. Also, without replacement, the synthesised products from K or MK were morphologically damaged whereas those from Z melted completely at 1150 °C. Inversely, the synthesised products obtained by partial replacement of 10 % of A or 30 % of B exhibited good volume stability up to 1200 °C, with the absence of cracks and swellings. In addition, the synthesised products from K with 30 % of B and heated at 1100 °C showed compressive strength of 29.1 MPa whereas those replaced with 10 % of A showed compressive strength of 60.2 MPa at 1150 °C. Heated at 1150 °C, the synthesised products from MK and from Z replaced with 30 % of B presented compressive strength of 76.7 and 35.0 MPa respectively. This is due to their densification and the formation of new crystalline phases (mullite, corundum, nepheline and carnegieite). Unfortunately, heated at 1200 °C, these products lead to partial dissolution of nepheline and carnegieite, which generates closed pores, thereby lessening their compressive strength. Hence, during their alkaline activation, the partial replacement of aluminosilicates (K, MK or Z) with 10 % of A or 30 % of B improves compressive strength and thermal stability of heated products.

Keywords: Aluminosilicates; Aluminium hydroxide; Alkaline activation; Compressive strength; Thermal stability.

Résumé

Ce travail porte sur l'étude de la stabilité thermique de ciments résultant de l'activation alcaline de kaolin (K), métakaolin (MK) et scories volcaniques (Z) avec substitution partielle d'aluminium hydroxyde. A cet effet, deux adjuvants (aluminium hydroxyde amorphe (A) et aluminium oxy-hydroxyde (B)) ont été utilisés pour substituer les précurseurs aluminosilicates (0, 10, 20 et 30 % en masse) et les mélanges résultant ont été activés en milieu alcalin. Outre les matières premières et les produits de synthèse, le comportement thermique, les propriétés physiques et mécaniques ainsi que les produits obtenus par traitement thermique (300-1200 °C) ont été étudiés. Les produits de synthèse avec adjuvant ont des résistances à la compression moins élevées que ceux n'ayant pas d'hydroxyde d'aluminium. Ceci tient de ce que les adjuvants se comportent comme des fillers. Au contraire, les produits de synthèse contenant initialement l'adjuvant et traités aux hautes températures ont leur résistance à la compression et leur stabilité en volume améliorées. En effet, sans substitution, les produits de synthèse à base de K ou MK ont une faible rétention en volume (léger gonflement) et des craquelures alors que ceux à base de Z ont des boursouflures à 1100 °C. Par ailleurs, sans adjuvant, les produits de synthèse à base de K ou de MK sont morphologiquement détériorés alors que ceux à base de Z fondent totalement à 1150 °C. Inversement, les produits de synthèse obtenus par substitution de 10 % en A ou 30 % en B étalent une bonne stabilité en volume jusqu'à 1200 °C, une absence de craquelures et de boursouflures. En plus, les produits de synthèse à base de K avec 30 % de B et traités à 1100 °C ont une résistance à la compression de 29,1 MPa alors que ceux substitués avec 10 % de A ont une résistance à la compression de 60,2 MPa à 1150 °C. Traités à 1150 °C, les produits de synthèse à base de MK et à base de Z substitués avec 30 % de B accusent respectivement les résistances à la compression de 76,7 et 35,0 MPa. Ceci tient de leur densification et de la formation de nouvelles phases cristallines (mullite, corindon, néphéline et carnegieite). Malheureusement, traités à 1200 °C, ces produits conduisent à la dissolution partielle de la néphéline et la carnegieite, ce qui génère les pores fermés, d'où une diminution de leur résistance à la compression. Ainsi, au cours de leur activation alcaline, la substitution partielle des aluminosilicates (K, MK ou Z) avec 10 % de A ou 30 % de B améliore la résistance à la compression et la stabilité thermique des produits de cuisson.

Mots clés: Aluminosilicates; Aluminium hydroxyde; Activation alcaline; Résistance à la compression; Stabilité thermique.

General introduction

Ever since, concrete remains one of the most widely used construction materials known all over the world. Each year, the cement industries produce approximately 12 billion tons of concrete and this requires about 1.6 billion tons of Ordinary Portland Cement (OPC) [1]. However, in OPC producing industries, the production of 1 ton of OPC releases approximately 0.94 ton of carbon dioxide (CO_2) along with other anthropogenic gases such as nitrogen oxides (NOx) and sulphur oxides (SOx) into the atmosphere, which form part of greenhouse gases responsible for global warming and acid rain [1-4]. Additionally, the cement industry accounts for 5–8 % of worldwide CO_2 emission [1] and this really causes serious environmental impact. Yet, seeking for alternative construction binders with low environmental impact appears to be a major concern for researchers.

Over the past decades or more, several studies focusing on the synthesis of eco-friendly building material binders were undertaken. Among the promising ones viewed as good alternative to OPC, alkali-activated binders and geopolymers attracted much interest in both academic and commercial fields [5-6]. Actually, these binders are obtained by alkaline activation of both reactive silica and alumina rich materials known as aluminosilicates, under ambient temperature curing or slightly elevated temperature (90 °C) [7-8]. Known as sustainable binders endowed with good physical properties, durability and eco-friendliness, geopolymers and alkali-activated binders can be potentially fire-resistant thanks to their ceramic-like amorphous structure [9-12].

However, the concern on thermal resistance or thermal stability of building material binders remains one of the research interests [11-16]. Indeed, thermal stability can be defined as the ability of building material binders to resist the action of heat and to maintain its properties such as strength, toughness or elasticity at a given temperature ranges. Determination of thermal stability of building material binders is important among others for insurance of safe usage and durability [17]. Additionally, thermal stability is also important to ensure that building material binders are safe for usage at certain temperature ranges [17]. Though, to make use of geopolymers and alkali-activated binders as fire-resistant building materials, thermal performance needs to be examined at micro, meso, and macro-scales [18]. Micro-scale refers to microstructural or chemical stability of building material binders subjected to elevated temperature. The ability of building material binder to resist volumetric change and thermally induced-cracking and to maintain good mechanical strength at elevated temperature refers to meso and macro-scale thermal stability. For instance, when a building material binder is to be used for high temperature applications, its volumetric stability, phase stability and resistance to strength deterioration play significant roles [19]. From the past

decades, several studies based on thermal resistance of geopolymers and alkali-activated binders obtained from wide range of aluminosilicate precursors have been reported. Globally, it was found that heating metakaolin-based geopolymers and alkali-activated volcanic scoria obtained via alkaline activation at elevated temperatures led to products with low compressive strength and low volume stability [20-21]. Therefore, improvement of both volume stability and compressive strength of these building material binders is required. Actually, this can be done thanks to the use of mineral additives. It is worth pointing out that, thermal stability of calcined-clay based-geopolymers was extensively reported but there is a lack of data regarding the thermal resistance of kaolin-based geopolymers. It is important to indicate that the use of kaolin in alkaline activation is limited as result of its low reactivity. Hence, prior to be used for fire-resistance applications, characteristics such as thermal stability and compressive strength of alkali-activated aluminosilicate sources need to be tested. The present research aims at studying the thermal stability of cements resulting from alkaline activation of kaolin, metakaolin and volcanic scoria respectively with partial replacement of amorphous aluminium hydroxide and aluminium oxy-hydroxide. Actually, aluminium hydroxide compounds are usually used industrially to prepare transitional aluminas having metastable structures and mostly refractory materials [22-26]. Also, they appear as suitable alumina sources that can be used to improve fired properties of aluminosilicate precursors.

This thesis layout is presented as follows:

- the first chapter gives details information on alkaline activation technology of aluminosilicates, factors affecting engineering properties and thermal stability of resulting products (pastes, mortars and concretes) and applications, an overview on aluminas; characterisation methods of starting materials and synthesised products along with the motivations of the thesis;
- the second chapter describes the starting materials involved and reports in details the experimental procedures as well as the analytical techniques employed;
- The third chapter reports the results and discussion obtained from the aforementioned experiments. It is subdivided into five (05) subparts:
    - the first subpart presents the characterisation of starting materials involved;
    - the second subpart presents the influence of amorphous aluminium hydroxide and aluminium oxy-hydroxide on the thermal stability of kaolin-based geopolymers;

- the third subpart presents the influence of amorphous aluminium hydroxide and aluminium oxy-hydroxide on the thermal stability of metakaolin-based geopolymers;
- the fourth subpart presents the influence of amorphous aluminium hydroxide and aluminium oxy-hydroxide on the thermal stability of alkali-activated volcanic scoria;
- the fifth subpart compares the thermal stability of the resulting alkali-aluminosilicate products based on their thermal behaviours and residual compressive strengths.

This thesis ends with a general conclusion and some perspectives for further research.

Chapter I: Literature review

This first chapter gives detail informations on alkaline activation technology of aluminosilicates, factors affecting engineering properties of resulting products, thermal stability of resulting products (pastes, mortars and concretes) and applications, an overview on aluminas; characterisation methods of starting materials and synthesised products along with the motivations of the thesis.

I.1 Alkaline activation of aluminosilicates

I.1.1 Definition and historical background

Alkaline activation of aluminosilicates is a globally growing technology used in forming solid materials, with properties similar to those of hardened OPC products thanks to the reaction between a powder of a reactive silica and alumina rich material and an alkaline activator to yield alkaline cement [27-28].

Formerly, the scientific basis of alkaline activation of aluminosilicates was established by Purdon since 1940 [27]. Indeed, he activated more than 30 types of blast furnace slags with sodium hydroxide (NaOH) solutions or by combining calcium hydroxide ($Ca(OH)_2$) with different sodium salts. He observed that the rate of strength development and final strength achieved were similar with those of OPC products. Moreover, the enhancement of tensile and flexural strength of slag-alkali cements compared to OPC products of similar compressive strength was also observed as well as the low solubility of hardened binder phases and low heat evolution. Also, he commented that this method of producing concrete is ideal for use in ready-mixed and precast applications where activator dosage can be accurately controlled. However, the sensitivity of activation conditions and the amount of water added along with the difficulties inherent in handling concentrated caustic solutions were recorded as major drawbacks. In spite of that, the studies of alkaline cements have gone a long history as from the former Soviet Union, Scandinavia and Eastern Europe. They had an exponential increment after the research results of J. Davidovits which developed and patented binders obtained from alkaline activation of metakaolin known as geopolymers [29-30]. Indeed, geopolymers can be considered as a subset of alkali-activated binders (Figure 1) in which the aluminosilicate used (metakaolin) contains very low calcium content. This new type of binder as initially described by J. Davidovits is generated by an adjustment of the process formerly used in ancient Roman and Egyptian constructions [30]. Also, it was hypothesised that the superior durability of this ancient concretes over OPC products was attributed to the coexistence of cements containing calcium silicate hydrate (C-S-H) with some form of alkaline aluminosilicate hydrate phases [31].

Hence, alkaline activation of aluminosilicates appears therefore as a complex chemical process involving dissolution of raw materials, transportation or orientation and poly-condensation of reaction products [30]. Nowadays, investigations focused on alkaline cements have attracted much interest by the research community as result of their environmental performance, eco-friendliness and superior durability over OPC products [30].

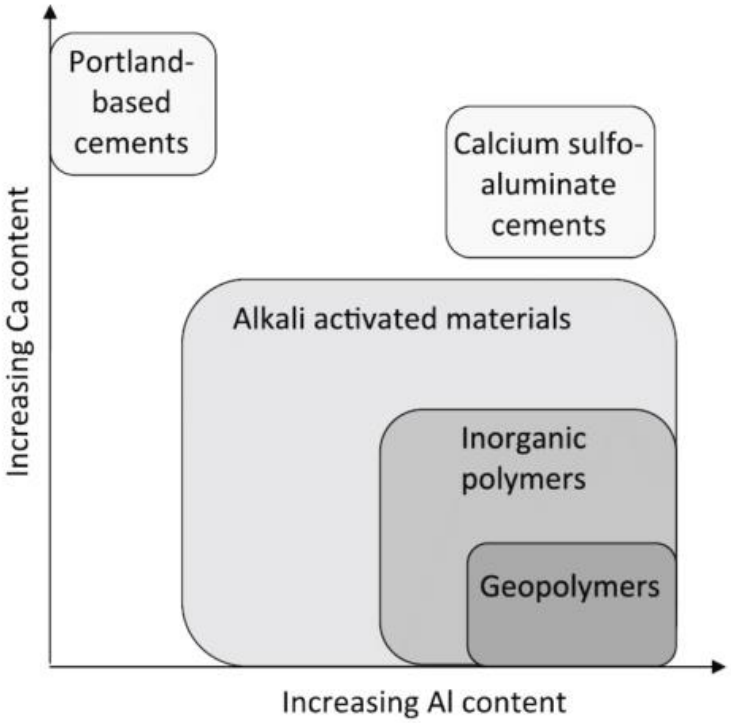

Figure 1: Classification of different subsets of alkali-activated binders with comparisons to OPC and calcium sulfo-aluminate cements [32].

I.1.2 Terminology and chemical structure of resulting products

It is well established that alkaline activation of a reactive aluminosilicate precursor leads to the production of alkaline cement. The latter can be classified as alkali-activated binder or geopolymer depending on the chemical composition of raw materials and activators employed [5, 30, 32-33].

However, within an alkali-activated binder obtained from a raw material having high calcium content, the binding phase is composed of gels such as calcium silicate hydrate (C-S-H) and some form of alkaline aluminosilicate hydrate phases as usually encountered in hardened OPC products [32, 34]. Conversely, geopolymers, obtained from a raw material having low calcium content, are aluminosilicates or inorganic polymers designated under the term poly(sialate) [34-35]. Basically, the term inorganic is the reciprocal of organic polymers in which the carbon atom is replaced by the silicon atom [6]. Also, the term sialate (Figure 2) is an abbreviation of silicon-oxo-aluminate [35]. Therefore, poly(sialates) are chain and ring

polymers with Si^{4+} and Al^{3+} in IV-fold coordination with oxygen and ranges from amorphous to semi-crystalline [6]. Additionally, the geopolymeric network is of three-dimensional silico-aluminate structures composed of SiO_4 and AlO_4 tetrahedra units linked alternatively by sharing all the oxygen atoms (Figure 2) [36]. Moreover, the negative charge in AlO_4 unit generated by the substitution of Si^{4+} by Al^{3+} in IV-fold coordinated sites is balanced by compensating ions such as Na^+, K^+, Li^+, Ca^{2+}, H_3O^+, etc. present in the framework cavities [35, 37].

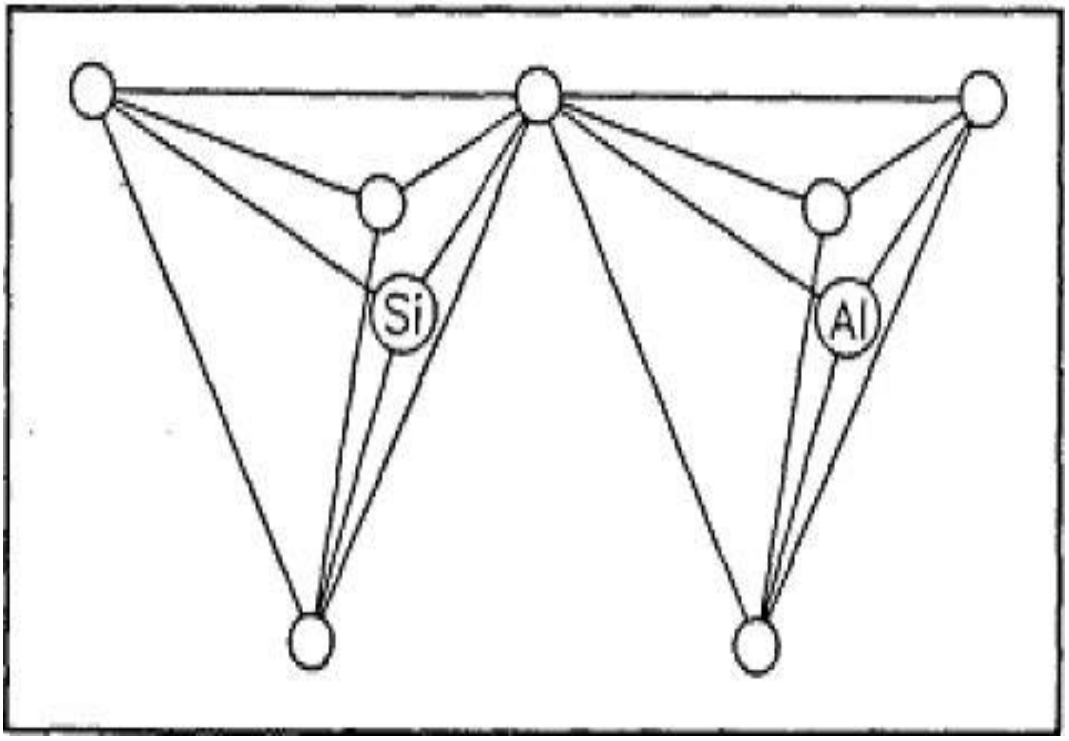

Figure 2: SiO_4 and AlO_4 tetrahedra units in the basic sialate network [6].

According to J. Davidovits, the empirical chemical formula of geopolymers also known as poly(sialates) is as follows: $M_n [(SiO_2)_z AlO_2]_n.wH_2O$ where M is a cation, n is the degree of poly-condensation, z is the Si / Al molar ratio and could take values of 1, 2, 3 or higher up to 32 and w represents the quantity of water present in the geopolymer material [3, 6, 35].

So far, J. Davidovits introduced the “sialate” nomenclature to describe aluminosilicate structures. The type of linkage Si-O-Al was named sialate bond whereas Si-O-Si one was called siloxo bond [3]. This provided a means of describing the composition of geopolymers thanks to their Si / Al molar ratios. The different structures of poly(sialate) oligomers with respect to their Si / Al molar ratios as formerly defined by J. Davidovits are shown in Figure 3.

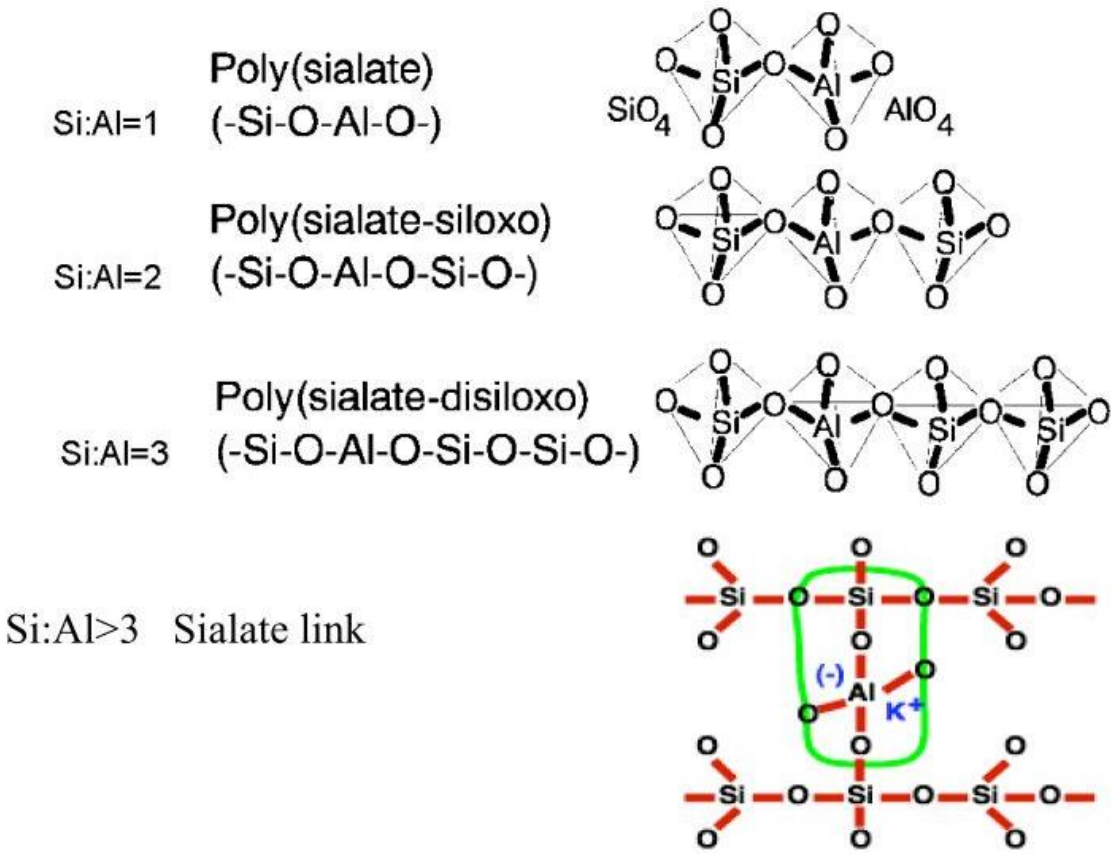

Figure 3: Types of poly(sialate) according to their Si / Al molar ratio and the three-dimensional macromolecular structures of geopolymers [36].

However, each type of structure is formed as followed [37-38]:

- poly(sialate) results from the poly-condensation of the monomers ortho-sialate $(OH)_3$-Si-O-Al-(OH);
- poly(sialate-siloxo) results from the condensation of ortho-sialate with ortho silicic acid $Si(OH)_4$;
- poly(sialate-disiloxo) results from the condensation of ortho-sialate with two molecules of ortho-silicic acid $Si(OH)_4$;
- poly(sialate-multisiloxo) results from the cross-linking of poly-silicate chains or sheet with a sialate link (-Si-O-Al-O-) (2D or 3D cross-link).

Concerning geopolymer compound composed of ferro-silico-aluminate units (-Fe-O-Si-O-Al-O-), they correspond to poly(sialate) binders' type in which some of the Al atoms are substituted with Fe atoms. Their empirical formula is based on [Ca, Na, K]-$[-Fe-O-]_x$ -$[Si-O-Al-O-]_{1-x}$-$[-Si-O-]_y$ wherein "x" is less than or equal to 0.5, "y" is a value between 0 and 25 [37, 39].

Elsewhere, the various studies performed on zeolite and aluminosilicate materials as from 1980 have helped to adopt a new notation to describe the skeleton of alkali-

aluminosilicates. This notation is given as $Q^n(mAl)$ with $0 \leq m \leq n \leq 4$ where Q represents a tetrahedral site with Si atom at the centre, n = 4 the coordination number of the Si centre while m and (n – m) are numbers of neighbouring Al and Si respectively [40]. This notation as established by Engelhardt et *al.* [40] was successfully used to describe the aluminosilicate systems. Indeed, for n equal to 4, the value observed in the geopolymer matrix is as shown in Figure 4.

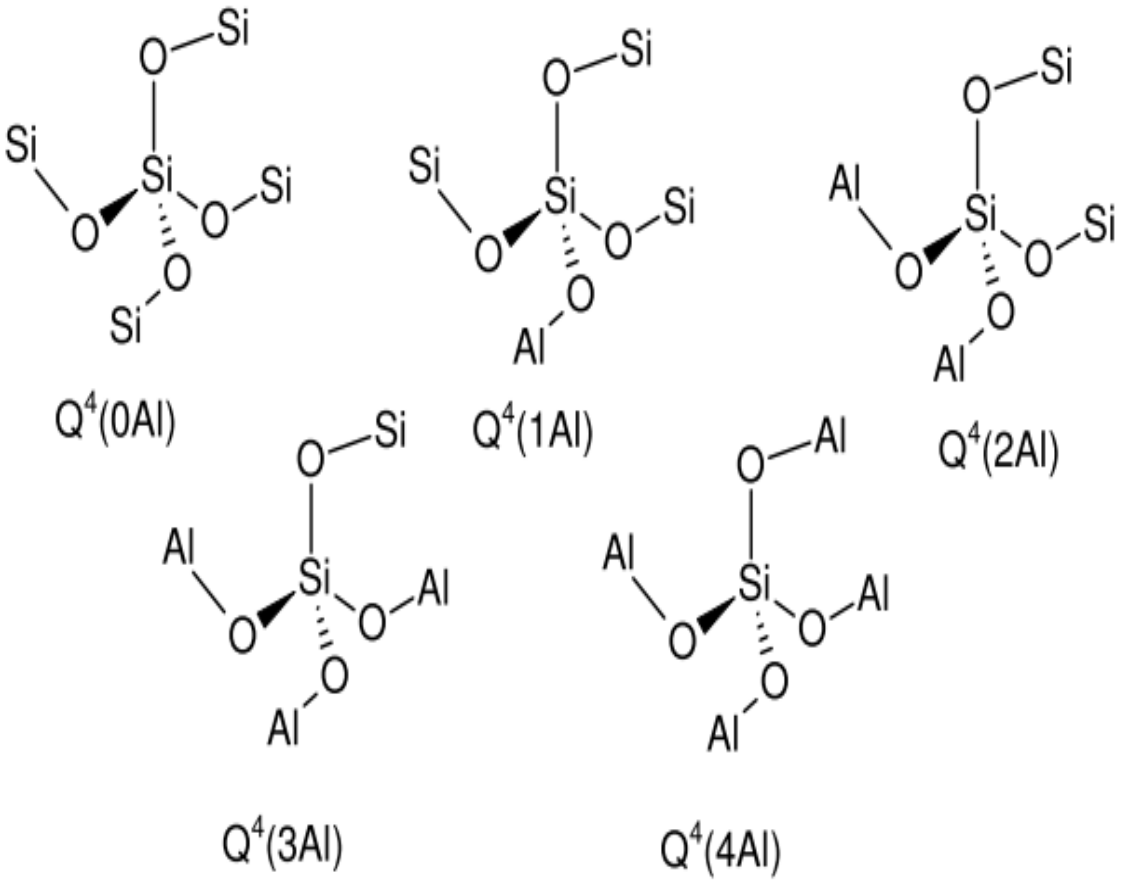

Figure 4: Coordination of silicon centres as described by Engelhardt et *al.* [40-41].

Regarding the structure, geopolymers could have amorphous or crystalline structures depending on the condensation temperature. Most often, amorphous geopolymers are obtained at temperature ranging between 20 and 90 ˚C whereas crystalline ones are obtained at temperature ranging between 150 and 200 ˚C [42]. It is worth recalling that the structures of crystalline polymers are similar to those of zeolites. A structural model of geopolymer material as proposed by Barbosa et *al*. [43] is presented in Figure 5.

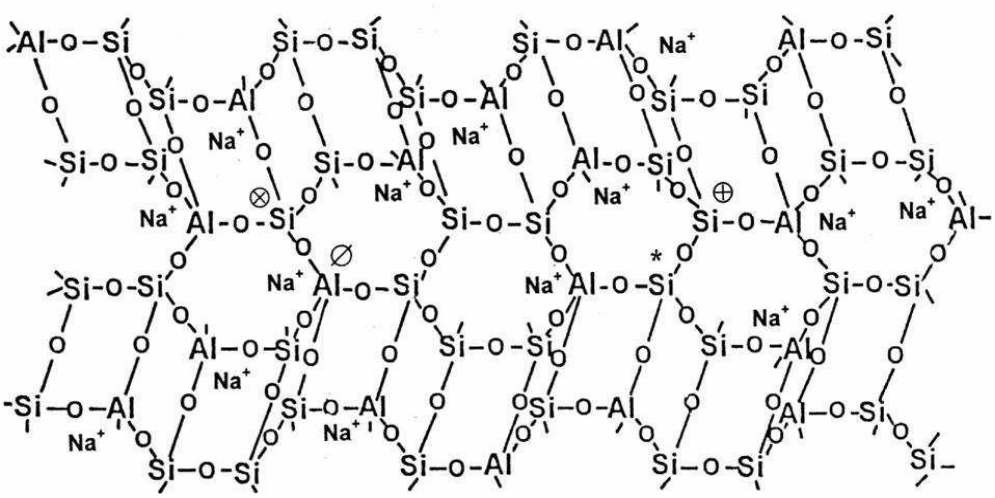

Figure 5: Structural model of geopolymer as proposed by Barbosa et *al.*[43].

After all, the main differences between an alkali-activated binder and geopolymer are summerised in Figure 6. As indicated earlier, alkali-activated binders are calcium-rich raw materials activated with high alkaline solutions. After the dissolution of precursors, a binder paste with hydraulic potential is build leading to simultaneous formation of C-S-H gels and aluminosilicate polymers. Conversely, geopolymers are structured around tetrahedral coordinated Si^{4+} and Al^{3+}, forming a polymer chain or ring, 2D or 3D network. There is chemical bonding of geopolymer precursors into oligomers leading to the formation of aluminosilicate inorganic polymers.

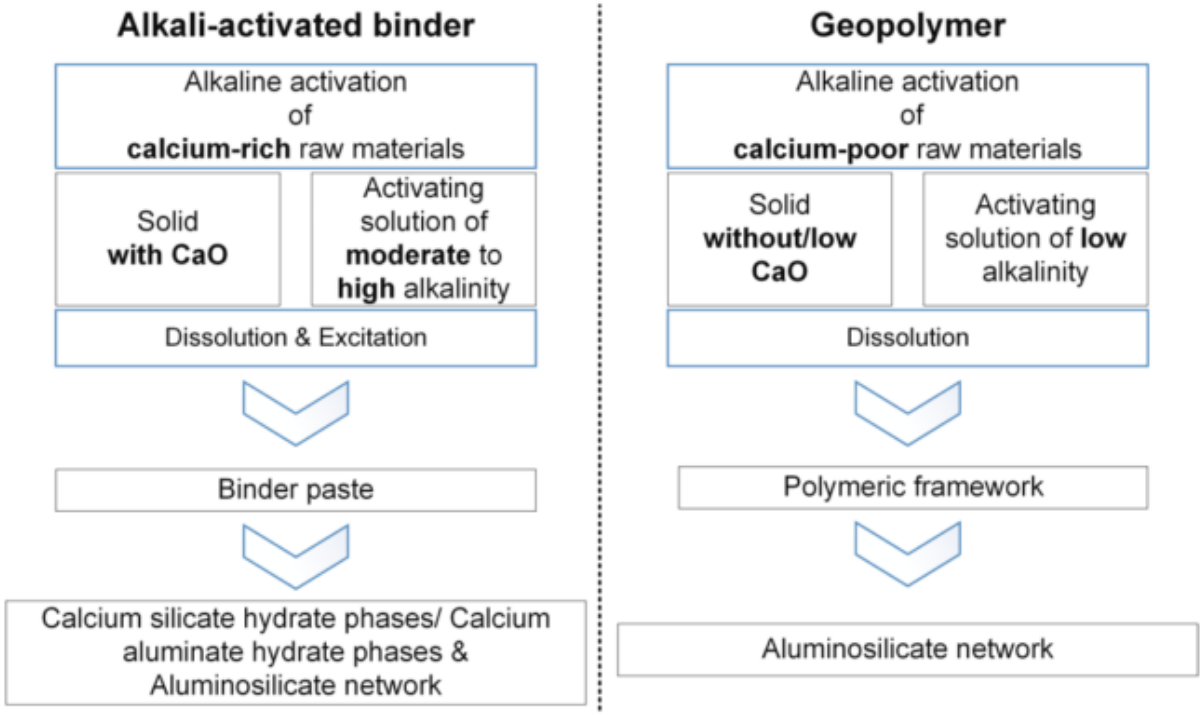

Figure 6: Differences between an alkali-activated binder and geopolymer [32].

I.1.3 Chemistry of resulting products

A general reaction mechanism for alkaline activation of aluminosilicates containing reactive silica and alumina was established since. This model proposed by Glukhovsky is composed of conjoined reactions of destruction–coagulation–condensation–crystallisation [27, 44]. The first step consists of a breakdown of the covalent bonds Si–O–Si and Al–O–Si which happens when the pH of the alkaline solution rises, followed by their transformations into a colloid phase [29]. Then, the accumulation of the destroyed products occurs, which interacts among them to form a coagulated structure, leading in a third phase to the generation of a condensed and crystallised structure [45]. Recently, alkali-activated binders and geopolymers have been widely studied [29-30, 46]. Figure 7 presents a highly simplified reaction mechanism for alkaline activation. This mechanism outlines the key processes occurring in the transformation of a solid aluminosilicate source into a synthetic alkali-aluminosilicate material [44].

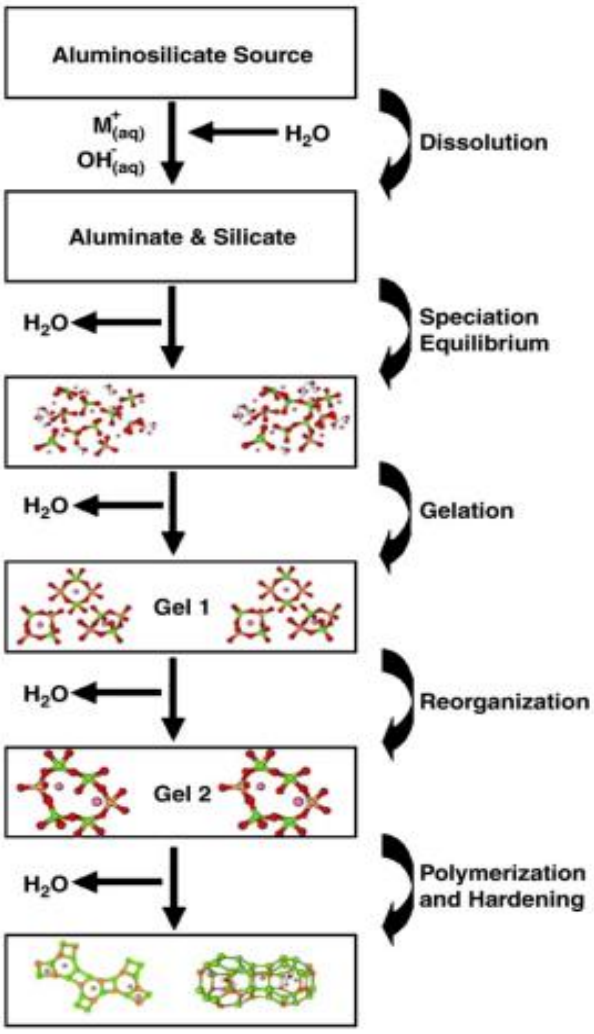

Figure 7: Conceptual model for alkaline activation of aluminosilicate [44].

At the first stage, the dissolution of aluminosilicates in alkaline medium through the severing of covalent Si–O–Si and Al–O–Al bonds leads to the formation of silicate and aluminate species. This process is initiated by the hydroxyl OH^- groups which after bonding to the silicon atom make the Si–O–Si bond more susceptible to breaking. Dissolution of reactive aluminosilicates is rapid at high pH. With metakaolin precisely, this dissolution leads to the formation of ortho-sialiate molecule ($(OH)_3Si–O–Al(OH)_3^-Na^+$) which is the primary unit in geopolymerisation [47]. At the second stage, the condensation of silicate and aluminate monomers leads to form a gel, until the solution reaches saturation with liberation of NaOH which reacts again. Actually, Duxson et *al*. [44] claimed that there is coexistence of two types of gel consisting of an aluminium-rich gel yielding to the geopolymer matrix and another gel yielding to crystallised zeolite phases. Also, this process releases the water that was nominally consumed during the first step. Finally, poly-condensation and structural reorganisation of the gel yield the three-dimensional aluminosilicate network of geopolymers known as N–A–S–H gel [47-49].

Regarding ground granulated blast furnace slag (GGBFS) which contains reasonable amount of calcium and low aluminium content inside the glassy phase, its reaction mechanism during alkaline activation is quite different from that of metakaolin [45]. Alkaline hydration of GGBFS corresponds to a complex process that is composed of several steps, including the initial destruction of GGBFS followed by later poly-condensation of reaction products. Considering that the glassy phase contains high calcium and low aluminium content, Figure 8 provides an illustration of the dissolution mechanism of a glass containing both monovalent and divalent network-modifying cations. The primary distinction between Na^+ and Ca^{2+} sites shown is much greater extent of damage caused to the glass structure by the removal of a divalent cation than a monovalent one. By analysing the heat released in the alkali-activated GGBFS, it was observed that the higher Na_2O and silica modulus (Ms) were related to high hydration levels. Meanwhile, the process begins with a destruction of slag bonds Ca–O, Mg–O, Si– O–Si, Al–O–Al and Al–O–Si, and then a Si–Al layer formed all over the surface of slag grains and, finally, the formation of hydration products [45]. Therefore, the main reaction product resulting from alkaline activation of GGBFS is calcium aluminosilicate hydrate gel (C-A-S-H) which is similar to the gel generated in hardened OPC hydrated product (C-S-H gel) in which aluminium is incorporated [48-49].

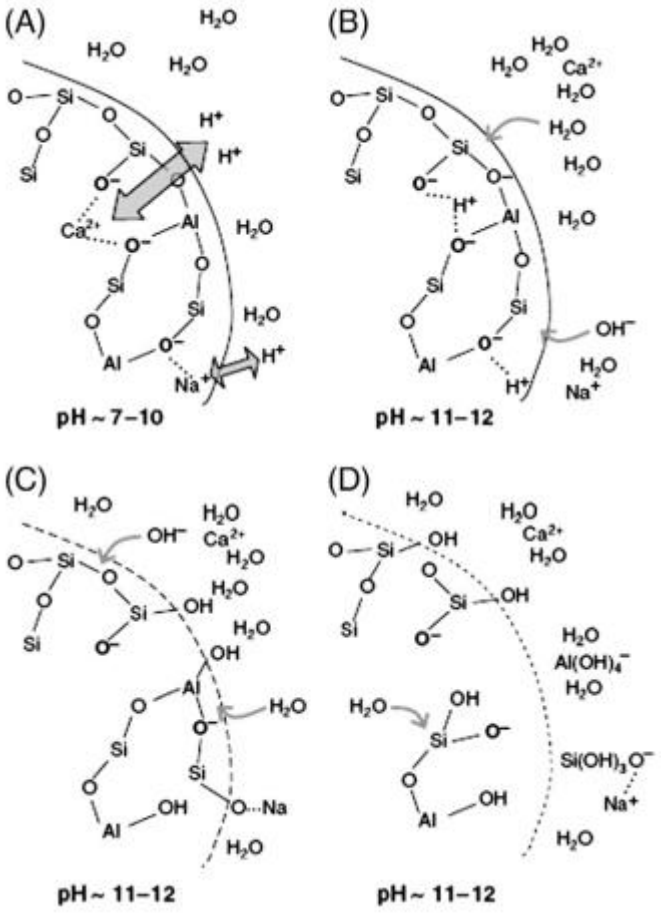

Figure 8: Dissolution mechanism of an aluminosilicate glass during the early stage of reaction: (A) exchange of H^+ for Ca^{2+} and Na^+, (B) hydrolysis of Al–O–Si bonds, (C) breakdown of the depolymerised glass network, and (D) release of Si and Al [45].

I.1.4 Precursors used in alkaline activation of aluminosilicates

I.1.4.1 Aluminosilicates

Basically, any type of aluminosilicate material composed of considerable amount of reactive silica and alumina can be potentially used for alkaline activation [50]. So far, several investigations performed have used the following starting materials: kaolinitic clays; metakaolin resulting from thermal treatment of kaolin; un-calcined and calcined laterites (iron rich component), volcanic scoria resulting from volcanic activities; fly ashes resulting from coal combustion (calcium poor components); coal bottom ash, rice husk ash, palm oil fuel ash, blast furnace vitreous slag (calcium rich components); mine tailing resulting from extractive industries, granite waste, bauxite, silica fume as well as mixtures of some or several of these precursors [9, 30, 34, 37, 51-53]. Globally, the basic ingredient in all these precursors is the high silica and alumina contents. Figure 9 shows an overview of the composition of some aluminosilicate precursors reported in the ternary diagram for $CaO\text{-}SiO_2\text{-}Al_2O_3$ system.

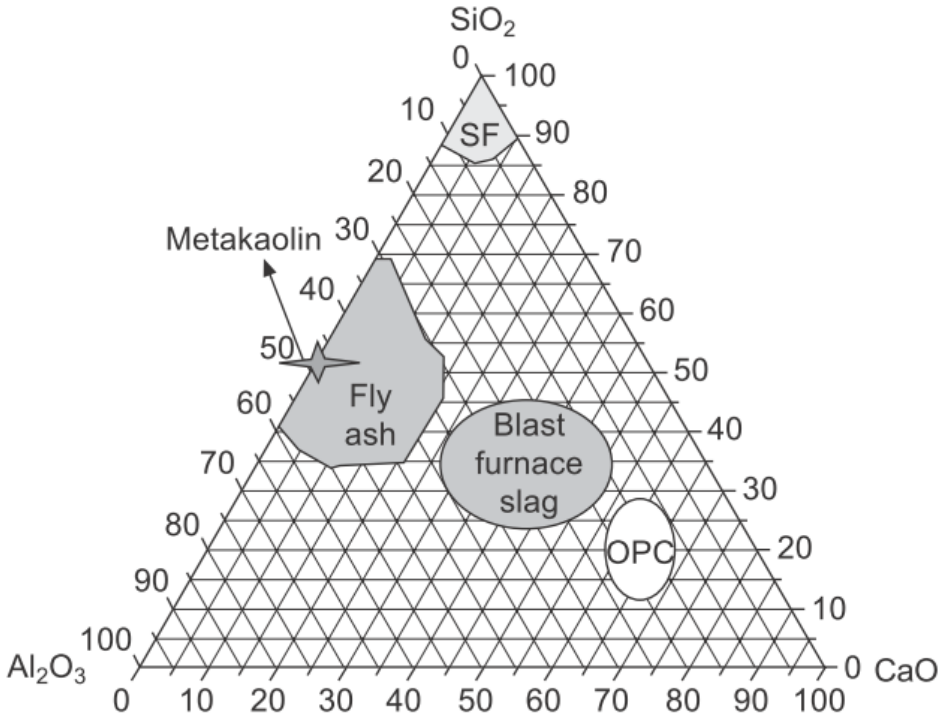

Figure 9: Ternary diagram for CaO-SiO_2 -Al_2O_3 system [34, 49].

I.1.4.2 Alkaline activators

These are the second essential component used for the development of alkaline cements [49]. The preparation of an activator solution used to initiate a chemical reaction during alkaline activation can be done by mixing at least two of the following reagents [29, 34, 37]:

- alkalis, MOH;
- weak acid salts, M_2CO_3, M_2SO_3, M_3PO_4, MF;
- silicates, M_2O. $nSiO_3$;
- aluminates, $M_2O.nAl_2O_3$;
- aluminosilicates, M_2O $Al_2O_3.(2–6)SiO_2$;
- strong acid salts, M_2SO_4

in which M is an alkali metal, generally Na^+ or K^+.

I.1.5 Engineering properties of alkali-aluminosilicate products

Alkaline activation of aluminosilicates yields products with different physical and / or chemical properties, due to both aluminosilicate material and synthesis conditions employed [37]. As result of that, alkali-aluminosilicate products exhibit some attractive engineering properties of interest, including [47, 54]:

- high flexural and compressive strength, such as 28 days compressive strength of paste > 90 MPa;
- fast hardening with some types of alkaline cement achieving 70 % of their final compressive strength within 4 h;
- high thermal stability with mass loss < 5 % and compressive strength loss < 60 % at 1000 °C;
- effective passivation of reinforcing steel;
- strong adhesion to metallic and non-metallic surfaces;
- low permeability;
- dimensional stability in service with shrinkage as low as 0.2–0.4 %;
- long-term durability properties;
- low CO_2 footprint linked to its production, etc.

I.1.6 Factors affecting engineering properties of alkali-aluminosilicate products

As indicated earlier, the resulting engineering properties of alkali-aluminosilicates are strongly related to the nature of aluminosilicate (chemical and mineralogical compositions, particle size and glass content) and synthesis conditions [47]. The latter includes the type and concentration of activator solution, curing conditions (hydrothermal, oven dry or autoclave) along with curing temperature [55]. Regarding to the nature of precursors used, the release rate of silica and alumina in alkaline medium plays significant role in the development of alkali-aluminosilicate network and its final engineering properties [47]. Indeed, high silica availability leads to more contribution of aluminium in the matrix and this promotes more homogenous binder gel. Though, a more homogeneous gel is observed with slow alumina released. Additionally, it was observed that dissolution rates of silica-rich materials are much higher than those of aluminosilicates. Yet, among the aluminosilicates studied, metakaolin showed a distinctively higher release of silicon species from the very early hours of dissolution while the release rate of silicon and aluminium species was almost similar in fly ash and slag [47]. These observations can be attributed to the reactivity of solid aluminosilicate precursors involved in the synthesis. Nevertheless, this reactivity can be enhanced by several methods such as mechanical, thermal, physical separation and chemical activation. Moreover, combination of some of these treatment methods can also be performed (Figure 10), in order to obtain a reactive precursor endowed with fine particle size along with great content of reactive silica and alumina.

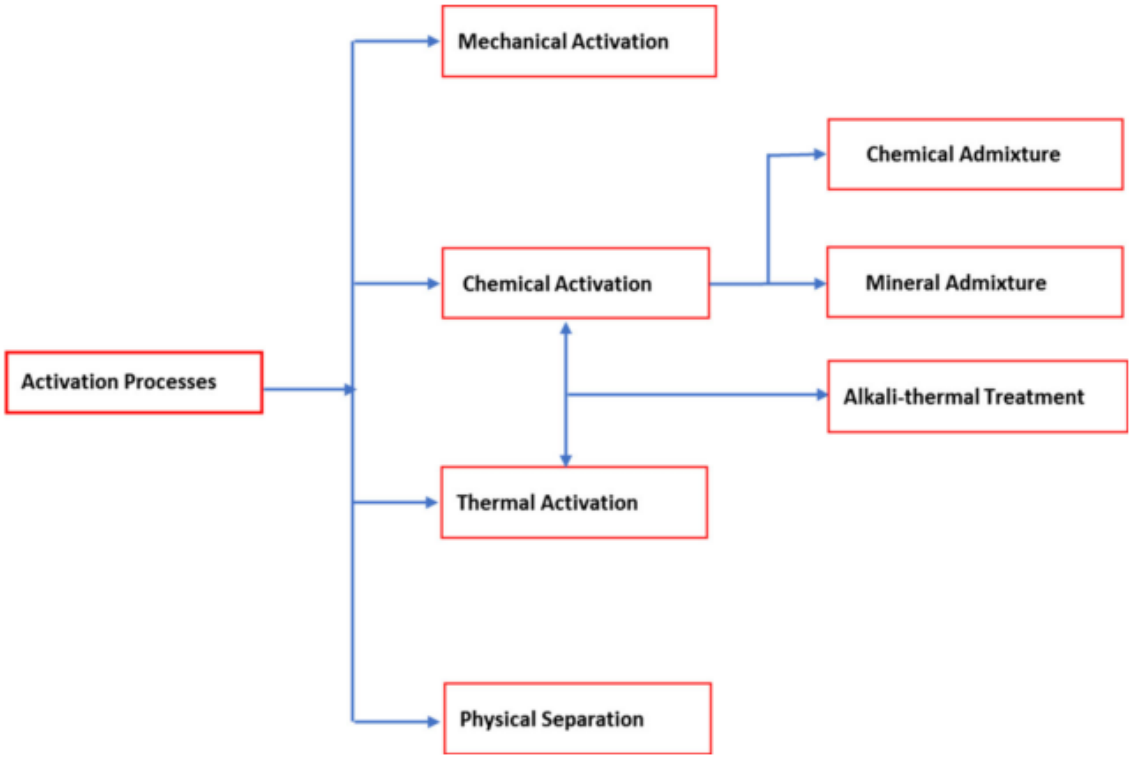

Figure 10: Summary of activation methods [47].

I.1.7 Influence of mineral additives on engineering properties of alkali-aluminosilicates

Precursors such as volcanic ashes are known to be less reactive aluminosilicate sources during alkaline activation [56] compared to its counterpart such as metakaolin, fly ash, etc. So, the incorporation of some reactive materials rich in SiO_2, Al_2O_3 and CaO known as mineral additives can compensate its deficiency in these elements and significantly enhance the final engineering properties [55]. For instance, Tchakouté et *al.* [57] studied the effect of adding alumina on the characteristic of geopolymers made from metakaolin and volcanic ashes respectively. They observed that the addition of alumina to volcanic ash favours the dissolution of alumina and silicate species, subsequently promoting the formation of $[SiO(OH)_3]^-$ and $[Al(OH)_4]^-$ intermediates. The poly-condensation and formation of polymeric binders are promoted which result in an increase of compressive strength of geopolymers. Djobo et *al.* [58] investigated the effect of using metakaolin as mineral additive to substitute two volcanic scoriae with different reactivities. They reported that even for less reactive volcanic scoria, the addition up to 25 % by mass of metakaolin considerably increased the physical and mechanical properties of resulting geopolymer pastes. Elsewhere, Djobo et *al.* [59] also studied the use of bauxite and calcined oyster shell respectively as source of aluminium and calcium to volcanic ash during the synthesis of volcanic ash-based geopolymers. They observed a decrease of linear shrinkage for any percentage of addition.

The addition of calcined oyster shell up to 20 % by mass lessened the initial setting time while trivial increase of 28-day compressive strength was recorded. This behaviour was due to the higher crystallinity of mineral additives, which, for a certain amount, became detrimental to the reaction. Globally, precaution should be taken since the mineral additive itself must be more reactive than the aluminosilicate precursor used, otherwise, it will be inert in the system and play as aggregate or filler, with little improvements of mechanical properties after curing under ambient conditions [55].

I.1.8 Thermal stability of alkali-aluminosilicate pastes

Ever since, the concern on thermal resistance or thermal stability of building material binders remains one of research interest [11, 13-16]. Determination of thermal stability of building material binders is important among others for insurance safe usage and durability [17]. Additionally, thermal stability is also important to ensure that building material binders are safe for usage at certain temperature ranges [17]. However, to make use of alkali-aluminosilicates as fire-resistant building materials, thermal performance needs to be examined at micro, meso, and macro-scales [18]. Micro-scale refers to microstructural or chemical stability of alkali-aluminosilicates subjected to elevated temperature. The ability of an alkali-aluminosilicate to resist volumetric change and thermally induced-cracking and to maintain good mechanical strength at elevated temperature refers to meso and macro-scale thermal stability. For instance, when an alkali-aluminosilicate is to be used for high temperature applications, its volumetric stability, phase stability and resistance to strength deterioration play significant roles [19]. From the past decades, many studies based on thermal resistance of alkali-aluminosilicates obtained from wide range of aluminosilicates have been reported. Elimbi et *al*. [20] studied the thermal behaviour of metakaolin based-geopolymers obtained by alkaline activation. They observed that the thermal behaviour was characterised by removal of bound water up to 750 °C followed by sintering and crystallisation of new phases along with significant decrease of compressive strength. Lahoti et *al.* [18] studied the effects of Si / Al molar ratio on the strength endurance and the volume stability of metakaolin based-geopolymers subjected to elevated temperature. They observed that thermal shrinkage induced the formation of cracks which dominate the residual strength for geopolymer mixes with Si / Al molar ratio ≤ 1.50. Inversely, densification of matrix was the governing factor of the residual strength for geopolymer mixes with Si / Al molar ratio > 1.50. Tchakouté et *al.* [60] investigated the possibility of using alternative alkaline activators such as sodium waterglass from rice husk ash and waste glass to prepare metakaolin-based

geopolymers with high compressive strength and good high-temperature performance. They found that the thermal properties of geopolymers prepared from alternative sodium waterglass were similar to those produced with typical commercial sodium waterglass. Additionally, they found that sodium waterglass produced from rice husk ash and waste glass could be suitable alkaline activators to prepare metakaolin-based geopolymers with high-temperature performance. Sun et *al*. [16] investigated on the synthesis and thermal behaviour of geopolymer-type material from waste ceramic. They noticed that the waste ceramic-based geopolymer exhibits favourable thermal stability in terms of compressive strength evolution after thermal exposures. Moreover, higher compressive strength was acquired after 2 h calcination at 1000 °C, which may be due to the viscous sintering and the completion of further geopolymerisation. Jiao et *al*. [9] studied the thermal stability of silica-rich vanadium tailing-based geopolymer. They found that the superior thermal stability of the as-prepared geopolymer sample can be confirmed by its thermal behaviour at 900 °C along with the increase of compressive strength, suggesting its potential use for elevated temperature applications. Lemougna et *al*. [21] investigated the thermal properties of alkali-activated volcanic ash and obtained specimens relatively stable to heat so that 60 % of initial compressive strength and low shrinkage were recorded up to 900 °C. Also, it is worth pointing out that there are not enough data in regard with thermal stability of alkali-activated volcanic scoria. Globally, physical and mechanical properties of as-obtained specimens along with their heated products are guided by the precursor characteristics and synthesis conditions employed. Hence, prior to be used for fire-resistance applications, characteristics such as thermal stability and residual compressive strength of alkali-activated aluminosilicate sources need to be tested.

I.1.9 Comparison of thermal stability of Ordinary Portland Cement and geopolymers

Figure 11 presents compressive strength (CS) of geopolymer and OPC pastes versus heating temperature. On one hand, it was observed that CS of geopolymers increased as temperature increases, attaining a maximum CS of 77 MPa at 300 °C. Subsequently, this CS was gradually deteriorated for the remainder of heating regime. However, a final CS of 58 MPa was recorded at 800 °C, which was still a 5.4 % improvement compared to reference specimen. On the other hand, CS of OPC specimens dropped considerably between 300 and 400 °C. This CS deterioration was attributed to calcium hydroxide ($Ca(OH)_2$) decomposition (Equation (E1)) that occurs around 400 °C [14, 17].

$$Ca(OH)_2 \longrightarrow CaO + H_2O \quad \text{(E1)}$$

From the above, it can be observed that geopolymer paste exhibits enhanced thermal stability thanks to its geopolymeric structure (Figure 5) as compared to hardened OPC paste. Additionally, the geopolymeric structure can also be reinforced through the use of reinforcements such as mineral additives in order to obtain a binder material endowed with improved fired characteristics, which can be applied for elevated temperature applications.

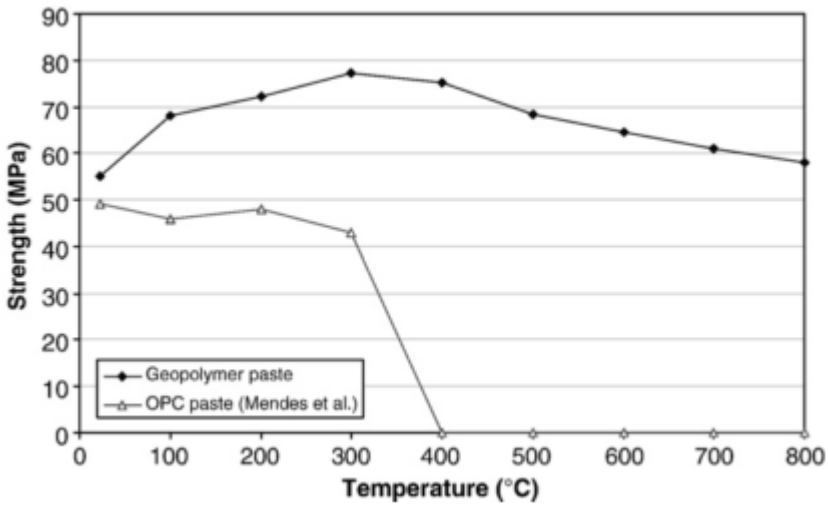

Figure 11: Compressive strength of geopolymer and OPC pastes at various temperatures [14].

I.1.10 Influence of mineral additives on thermal stability of alkali-aluminosilicate products

Presence of mineral additive can influence physical and mechanical properties of resulting alkali-aluminosilicate material obtained under ambient curing conditions and / or after heating. In the past, Kamseu et *al*. [61] studied the effect of added phases (silica and alumina fillers) on sintering behaviour of geopolymer matrices for applications at high temperature. They found that the addition of silica or alumina fillers helped to shift the densification temperature as compared to conventional geopolymer compositions. Moreover, the presence of fillers acted as additional effect to crystalline phases (kalsilite and leucite) for the inhibition of the development of liquid phase. It was therefore suggested that alumina or silica sand can be used to control the shrinkage due to dehydration and dehydroxylation in order to control the properties of heated products. Kuenzel et *al*. [15] investigated the mechanical properties and microstructure of metakaolin derived geopolymer mortars containing 50 % by weight of silica sand, after thermal exposure up to 1200 °C. They observed that the addition of fine silica sand enhances mechanical properties of both as-obtained geopolymers and heated products (1000 °C). Conversely, above 1000 °C, the

crystalline phases such as nepheline and carnegieite soften and partially melt and coarse closed pores are formed within the microstructure that significantly reduces mechanical properties. Ye et *al*. [19] studied the effect of elevated temperature on the properties of geopolymer synthesised from calcined ore-dressing tailing of bauxite and ground-granulated blast furnace slag. They found that after exposure at 1200 °C, a compressive strength gain was observed due to densification and self-healing caused by viscous sintering and formation of ceramic phases (anorthite). Rovnanik et *al*. [42] investigated the behaviour of geopolymer materials based on the combination of metakaolin and fly ash with chamotte aggregate subjected to elevated temperatures (200-1200 °C). They observed that chamotte aggregate improves the performance of metakaolin geopolymer because it considerably reduces shrinkage of geopolymer binder during heating. Unfortunately, it had a slightly negative effect on compressive strength of fly ash geopolymer. However, above 800 °C chamotte was attacked by alkalis, which causes partial sintering in the contact zone between aggregate and geopolymer matrix. This effect plays a substantial role in the improvement of residual mechanical properties at 1000 °C and helps metakaolin mortar to resist higher temperatures without damage. Globally, chamotte aggregate improves the performance of geopolymer material by increasing the thermal stability of geopolymers via sintering of aggregate particles with geopolymer matrix in the contact zone. Rovnanikova et *al.* [62] reported the properties of alkali-aluminosilicate materials with fire-resistant aggregate after high temperature loading. They observed that substantial increase of compressive strength after exposure at 1200 °C can be attributed to sintering of alkali-activated slag matrix with electrical porcelain. Furthermore, the sintering of matrix with electrical porcelain had considerable positive effect on the improvement of flexural strength of about 450 %. From the above findings, it appears that alumina sources are the potential mineral additives that can be used to improve fired characteristics of aluminosilicate precursors for their potential applications at elevated temperatures.

I.1.11 Uses of alkali-aluminosilicate products

The different applications of resulting products obtained from alkaline activation of aluminosilicate precursors depend mainly on their inherent properties which are closely related to the type of alkali-aluminosilicate chain or network formed after reaction [37]. As result of that, J. Davidovits has summarised the various uses (Figure 12) of these materials based on their Si / Al molar ratios [36].

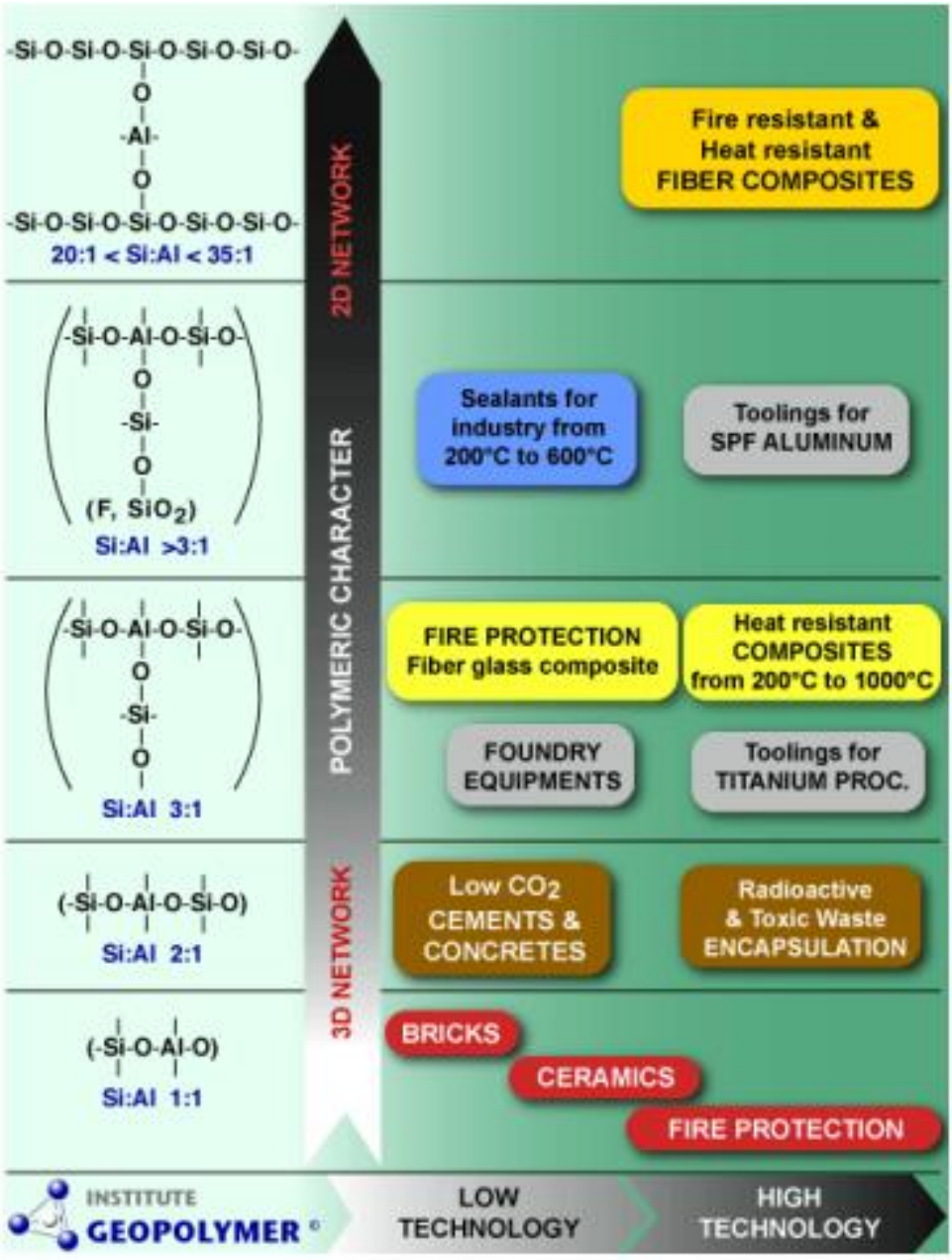

Figure 12: Applications of alkali-aluminosilicate products [36].

I.2 Overview on aluminas

I.2.1 Introduction

Aluminium oxide (Al_2O_3) or alumina is an oxide of aluminium naturally occurring in hydrated form in bauxite rocks, clays and most often associated among other with various impurities such as ruby, sapphire, emery, etc. [63-64]. It is industrially used to produce aluminium, abrasives, refractories, ceramics and electrical insulators [64]. Approximately 30 million tons of aluminas are produced annually around the world from bauxite rocks thanks to Bayer process [63]. However, 3 million tons are required for other specific uses in many

domains of applications [63]. Indeed, technical aluminas are the most commonly used such as aluminium hydroxides and oxy-hydroxides, alumina gels, transition aluminas, calcined aluminas, sintered or tabular aluminas, molten aluminas or corundums and ultrapure aluminas [63].

I.2.2 Aluminium hydroxides and oxy-hydroxides

I.2.2.1 Structure and description of aluminium hydroxide polymorphs

A number of crystalline aluminium hydroxides are found in nature or synthesised in laboratory. Among these, four principal polymorphic forms of $Al(OH)_3$ known as gibbsite, bayerite, nordstrandite and doyleite are observed [64-65].

a) Gibbsite

It usually occurs widely in soils and in concentrated manner in bauxite deposits. It is the principal component of tropical bauxites formed in areas characterised by a hot rainy climate with alternating dry periods [66]. Its crystal structure is monoclinic [66] with mostly a tabular pseudo-hexagonal crystalline form (Figure 13) [65]. In that structure, both crystallographically independent aluminium atoms are located at the general positions (0.1679, 0.5295, -0.0023) and (0.3344, 0.0236, - 0.0024) respectively. It is described as close-packed sheets of hydroxyl (OH) groups with Al^{3+} ions occupying two-thirds of the octahedral holes in alternate layers [65].

However, gibbsite is an important by-product of Bayer process in industrial extraction of alumina from bauxite ores. During Bayer process, gibbsite is extracted along with boehmite and diaspore. Though, Bayer process is known to be the most applied industrial way to produce gibbsite as an intermediate. Additionally, many commercially synthesised gibbsites are manufactured with different properties and designated with more than 120 different names [65]. Hence, gibbsite is the most important alumina chemical used as precursor in the manufacture of advanced ceramics, catalysts, adsorbents and aluminium [64].

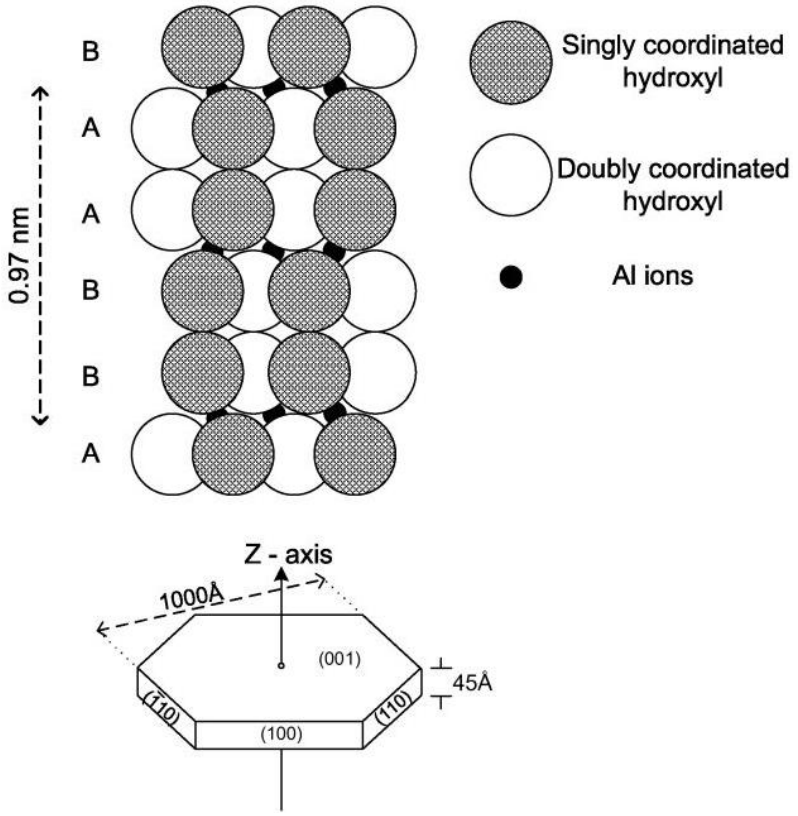

Figure 13: Crystal structure of gibbsite [65].

b) Bayerite

It is closely related in structure to gibbsite and is formed under similar conditions. It can be formed in various stages of Bayer process despite the fact that it is an undesirable by-product since the process is principally used for refining bauxite to produce alumina. Like gibbsite, bayerite is also formed upon the aging of aluminium hydroxide gels precipitated from aluminium salt solutions in water. Its abundance depends on the concentrations of aluminium and electrolyte in water. This polymorphic form is stable only in the absence of the alkali ions (Na^+ and K^+). In their presence, bayerite converts irreversibly into gibbsite. Bayerite crystal structure is monoclinic (Figure 14) [65]. The aluminium atoms are located at the general positions (0.5114, 0.1642, 0.0004) and (0.0326, 0.3315, -0.0015) respectively. The aluminium atoms also form hexagonal close-packed layers resulting in higher density of bayerite compared to that of gibbsite. The aluminium atoms deviate a maximum of 0.015 Å from the (002) plane, so that they are closer to the structure of graphite layers. The most commonly observed forms of bayerite are spindle or hourglass shapes formed by stacking of $Al(OH)_3$ layers in a direction perpendicular to the basal plane. The bayerite lattice is also composed of double layers of hydroxyl (OH), but hydroxyl groups of one layer lie in the depressions between the hydroxyl positions of the second [65].

Hence, bayerite is industrially used to prepare aluminium oxide used as supports for catalysts [64].

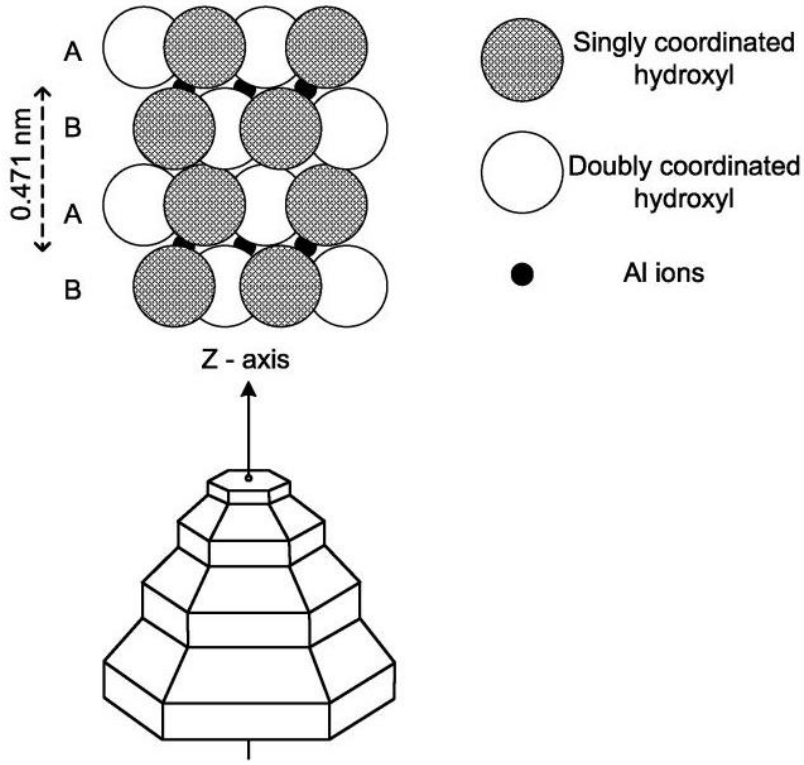

Figure 14: Crystal structure of bayerite [65].

c) Nordstrandite

Van Nordstrand was the first to identify this crystalline form of $Al(OH)_3$ as a synthetic product mixed with gibbsite and bayerite [65]. Nordstrandite has been synthesised in a pure state by reacting slightly hydrolysed aluminium foil or non-crystalline precipitated aluminium hydroxide gel in an ethylene-diamine solution or by aging hydrolytic precipitation products of aluminium with aqueous ethylene glycol [65]. Organic chelating anions and clay mineral surfaces, particularly at pH > 8, have been shown to help induce the crystallisation of pure nordstrandite. However, natural occurring crystals of nordstrandite have been found in some places such as Guam, Borneo, Montenegro, Croatia, Hungary, Jamaica, Sydney, Australia and North-western Colorado [65]. It has a triclinic crystal structure (Figure 15). The aluminium atoms are located at the general position (0.337, 0.333, 0.010). Yet, nordstrandite crystal structure is intermediate to those of gibbsite and bayerite. Indeed, double layers of hydroxyl groups of gibbsite structure alternate with those of bayerite structure. Also, in the structure of nordstrandite, the aluminium atoms form hexagonal layers that are somewhat more regular and stacked in the . . . ABBAAB . . . sequence (Figure 15), though slightly displaced with respect to each other.

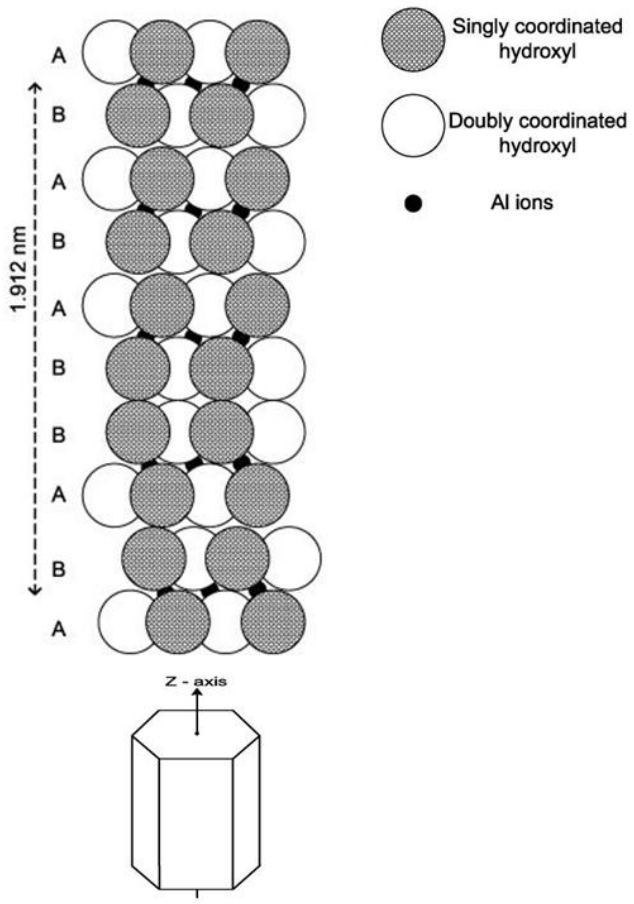

Figure 15: Nordstrandite crystal structure [65].

d) Doyleite

It appears to be rare in nature with only few reports mentioning its occurrence in Quebec, Canada and China [65]. It is unstable at ambient temperature and pressure, which might be attributed to the absence of intra-layer hydrogen bonds. Doyleite has a similar bi-layer structure to the other forms of $Al(OH)_3$, comprising double layers of hexagonal close-packed oxygen atoms with aluminium atoms occupying two-thirds of the octahedral interstices. Nonetheless, it is distinct from the other forms in its lateral displacement of adjacent layers and in aspects of the hydrogen bonding pattern. Crystal structure of doyleite has been characterised as a triclinic (Figure 15). Intra-layer interactions between hydroxyl groups appear to involve limited, if any, bonding between a hydrogen and the next-nearest-neighbour oxygen, contrarily to other $Al(OH)_3$ polymorphs [65].

Hence, the four polymorphic forms (gibbsite, bayerite, nordstrandite and doyleite) differ in the relative disposition of the double layers of hydroxyl groups and in the hydrogen bonding between and within the layers [65]. The stacking of the double layers of hydroxyl groups can be summarised as follows [65]:

- in bayerite, each layer is stacked directly above the layer below in an -AB-AB-AB- sequence, in which A represents the close-packed oxygen layer above the aluminium atoms, B represents the close-packed oxygen layer below the aluminium atoms and the combination AB represents one oxygen double layer;
- in gibbsite, each alternate layer inverted in an –AB–BA–AB– sequence;
- in nordstrandite, the stacking is –AB–AB–AB– as in bayerite, but with an accompanying shift of 1.82 Å along a direction inclined approximately at an angle of 35° to the bayerite a-axis;
- in doyleite, the stacking is again –AB–AB–AB– but the lateral displacement is approximately at right angles to that of nordstrandite, being at 25° to the b-axis of bayerite.

I.2.2.2 Structure and description of aluminium oxy-hydroxide polymorphs

The polymorphic forms of crystalline aluminium oxy-hydroxides are boehmite and diaspore.

a) Boehmite

It is a mineral with the composition AlO.OH and it appears as major constituent in many bauxite rocks. However, bauxite deposits with mainly boehmite seem to be more restricted to the subtropical areas known as Mediterranean type bauxite [66]. The processes by which it is formed in bauxite deposits in preference to gibbsite are not well understood. Its crystal structure is orthorhombic and has been described as composed of double layers of oxygen and hydroxyl in cubic packing [65-66]. As in gibbsite, the double layers are joined by hydrogen bonds and crystals exhibit preferential cleavage in the direction perpendicular to the general direction of the hydrogen bonding.

However, aluminium oxy-hydroxide structures have some similarities with those of iron oxy-hydroxides and a considerable amount of Fe^{3+} can replace Al^{3+} in the boehmite crystal lattice. Though, boehmite is an important precursor used for the production of aluminium oxide. Additionally, fine crystalline synthetic boehmite is produced as precursor for activated aluminas used in the manufacture of catalysts and absorbents [64-65].

b) Diaspore

It is a naturally occurring mineral. It appears as major constituent of some bauxite ores, aluminium-rich clays and metamorphic rocks [65]. However, thermal action or low-grade metamorphism mostly favours its formation [66]. Also, it is found as minor constituent

in many types of bauxite rocks combined with gibbsite and boehmite. Studies of the crystal structure of diaspore indicate that the Al^{3+} are somewhat distorted in octahedral coordination with the O^{2-} and OH^- ions in the crystal. Diaspore (α-AlO.OH) has similar structure with goethite (α-FeO.OH) which is orthorhombic [66]. Its oxygen sheets are in hexagonal close packing with two-thirds of the octahedral sites filled with aluminium ions [66]. Diaspore differs from boehmite in the coordination of the oxygen atoms, all of which are hydrogen bonded to another oxygen. The hydrogen atoms are closest to the oxygen farthest from the aluminium cation. As result of that compact arrangement, diaspore has greater density than boehmite [66].

Though, the use of diaspore bauxite rocks for the production of alumina via Bayer or sintering process is possible. But, the use of gibbsite bauxite rocks for alumina production is more common due to the lower requirements in processing temperatures [64-65].

I.2.3 Alumina gels

They are colloidal hydroxides highly varied in particular by their crystal structures. They can be amorphous in particular when they are freshly precipitated or not well-crystallised or evolved in hydroxide or oxy-hydroxide with a definite structure. However, they can be prepared by using either mineral salts or sol-gel methods [63]. Though, sol-gel method appears to be the best way of preparing alumina gels since it enables to obtain products endowed with high homogeneity and purity, at relatively low temperature as compared to other methods [63].

Alumina gels are among the best absorbing substances used in several domains of applications [63].

I.2.4 Transition aluminas

They are also called metastable alumina polymorphs. They are all synthetic products obtained by heating aluminium hydroxide or oxy-hydroxide compounds as shown in Equation (E2) [22]:

Aluminium hydroxides or oxy-hydroxides $\longrightarrow$ transition aluminas $\longrightarrow$ $\alpha\text{-}Al_2O_3$ (E2)

However, alpha-alumina ($\alpha\text{-}Al_2O_3$) cannot be considered as a polymorph form of aluminium hydroxide or oxy-hydroxide since it is the stable form (thermodynamically) generally observed at elevated temperatures and unstable at low temperatures [63]. Though, it was observed that between the temperatures of dehydroxylation of either aluminium hydroxides or oxy-hydroxides and the alpha-alumina first crystallization, a number of well

characterised and reproducible intermediate crystalline alumina structures are formed [22]. Each one has a stable different crystal structure at a given temperature range and with just one exception which is amorphous. The type or structure of each alumina and its temperature range of existence are determined by the structure of the starting hydroxide precursor. They are different for gibbsite, bayerite, nordstrandite, boehmite or diaspore. Extensive literature exists on the dehydroxylation of crystalline hydroxides, in particular on gibbsite because it is the phase formed in the industrial Bayer Process. So, transition aluminas have received Greek letters to identify them such as: gamma, delta, theta, kappa, chi, eta and rho [22]. Figure 16 is adapted from the most recent review of the thermal transformation sequence of aluminium hydroxides and oxy-hydroxides [22].

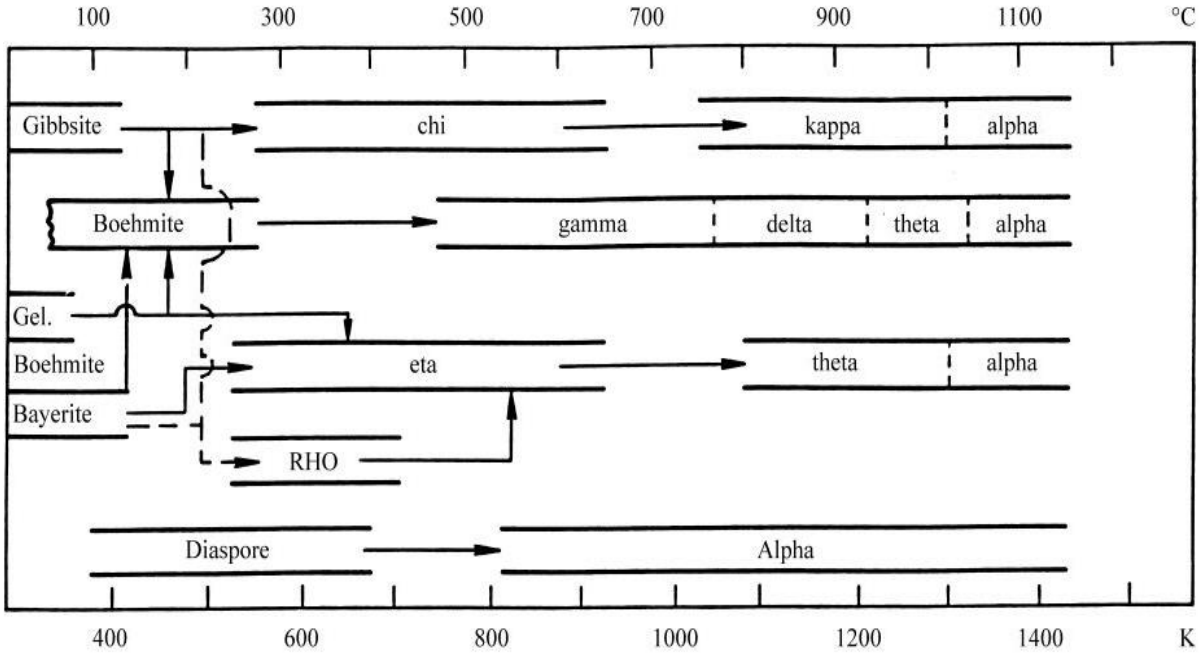

Figure 16: Thermal transformation sequence of aluminium hydroxides and oxy-hydroxides [22].

Hence, transition aluminas have uses in ceramics, particularly as adsorbents, catalysts, coatings and soft abrasives [63-64].

I.2.5 Calcined aluminas

They are aluminas in which α-Al_2O_3 phase begin to appear with a transformation rate ranging between 5 and 100 % [63]. At the end of calcination, the complement mostly composed of transition alumina disappears completely as result of its transformation into α-Al_2O_3. However, if gibbsite is used as starting hydroxide precursor, its transformation into α-Al_2O_3 is done with significant mass loss in term of water vapour between 200 and 400 °C

[67]. In practice, the high pressure of water vapour created at the level of grain as result of the thermal transformation induced the formation of boehmite as shown in Equation (E3) [63, 67]:

gibbsite $\longrightarrow$ boehmite $\longrightarrow$ γ-Al_2O_3 $\longrightarrow$ δ-Al_2O_3 $\longrightarrow$ θ-Al_2O_3 $\longrightarrow$ α-Al_2O_3. (E3)

Though, these calcinations are generally done in a rotary kiln. Calcined aluminas represent the one-quarter of the production of alumina. They are used in the manufacturing of cements, glasses, enamels, refractories, mineral fibbers such as mullite. Also, they found specific applications in the production of polishing, trimming of brakes and bio-compatible prostheses [63-64].

I.2.6 Sintered aluminas

They are ceramics of calcined alumina sintered between 1600 and 1900 °C [64]. The precursor used is composed of alumina spheres (2 cm in diameter) calcined and crushed, initially formed by agglomeration or extrusion and most often by adding organic binder which is being released upon heating. The elaboration process consists of continuous sintering of these spheres in a vertical kiln of several meters of height equipped with gas-burners. Evidently, big crystal of 50 to 300 μm of α-Al_2O_3 with high purity is obtained in form of hexagonal tablets elongated and this justifies the designation tabular aluminas given to this type of aluminas [63]. Therefore, sintered aluminas are available after crushing and sieving in various granulometric classes. The properties of these products are at the same time related those of α-Al_2O_3 and those of ceramics especially with high density (3400-3600 Kg / m^3), low porosity and good abrasive resistance for loads and thermal shocks [63]. They represent 10 % of the overall production of aluminas.

Though, the major uses of sintered aluminas are found in the domains of refractories, ceramics, filters for melted metals, mineral charges for resins, supports for catalysts and thermal interchangers [63-64].

I.2.7 Molten aluminas or corundums

Corundum is the hardest natural mineral known after diamond. However, alumina melts at around 2040 °C and boils at around 3500 °C [63]. Upon cooling, alumina solidifies in big crystal as the gradient of temperature becomes weak. The nature possesses natural resources of melted alumina such as corundum (pure state), emery which is an impure form

containing 30 up to 40 % of magnetite (Fe_3O_4) and different precious stones which are the different varieties of corundum coloured with small quantity of metallic oxides such as Cr^{3+} for ruby, Fe^{2+} and Ti^{4+} for sapphire [63-64]. These natural resources are now insufficient to cover the industrial demand in molten aluminas. Nevertheless, there exist two possibilities for their production. The first one is by melting calcined alumina leading to obtain white corundum while the second one is by direct treatment of bauxite which represents 80 % of the overall production leading to obtain brown corundum.

Regarding white corundum, it is produced by melting calcined alumina in an electric furnace. As-prepared specimens in form of breads are heated at 2100 °C by regularly supplying the kiln with alumina. After cooling and fragmentation, it is possible to separate the middle of each bread rich in β-Al_2O_3. The purity of white corundum obtained is 99.5 % in Al_2O_3 of which 95 % in α-Al_2O_3 [63].

As for brown corundum, its production is based on melting and reducing bauxite with coke thanks to an electric furnace. The obtained brown corundum contained approximately 97 % of α-Al_2O_3, 2 % of unreduced TiO_2 and marks of SiO_2 and Fe_2O_3 [63].

Though, molten aluminas are tenacious, chemically inert along with good mechanical resistance and dimensional stability at elevated temperatures. They are used in the fields of abrasives and refractories as well as mineral charge [64].

I.2.8 Ultrapure aluminas

The purity of these aluminas (99.99 %) is achieved either by using the road of alcoolate production of gel from high purity aluminium followed by distillation of the obtained aluminium alcoolate or by purifying gibbsite obtained from Bayer process [63]. In one way, it can be done by redissolution of gibbsite using sulphuric acid (H_2SO_4), followed by neutralization with ammonia (NH_4OH) in order to obtain alum ($NH_4Al(SO_4)_2$, $12H_2O$) which is then calcined. In another way, gibbsite can be re-crystallised after dissolution into aluminate or proceeding by re-crystallisation of aluminium chloride hexa-hydrate ($AlCl_3$, $6H_2O$). In all cases, the operations end by a calcination above 1000 °C [63].

Though, approximately 1000 tons of ultrapure alumina is produced annually for the manufacture of monocrystals of sapphire used in jewelry and in advance technology such as optical laser [64]. Also, they are applied for other applications such as polishing and cleaning of optical materials or electronics [63].

I.3 Characterisation methods of raw materials and alkali-aluminosilicate products

I.3.1 Particle size distribution

Particle size analysis is used to characterise the size distribution of particles in a given sample. It can be applied to solid materials, suspensions, emulsions and even aerosols. There are several methods used to measure particle size. Some particle sizing methods can be used for a wide range of samples, but some can only be used for specific applications. It is quite important to select the most suitable method for different samples as different methods can produce quite different results for the same material. Particle size analysis is a very important test and it is used for quality control in many industries. Indeed, in an industry where milling or grinding is used, particle size is a critical factor for determining the efficiency of manufacturing processes and performance of final product [37]. Some industries and product types where particle sizing is used includes: pharmaceuticals, building materials, paints and coatings, food and beverages, aerosols, etc.

However, one basic problem with particle size analysis is characterising particles using just one number. Most particle sizing techniques aim report particle size distributions on a two-dimensional graph with particle size on the x-axis and quantity of material on the y-axis. The difficulty with this technique is that there is only one shape that can be described by a single unique number and that is the sphere. Only a sphere measures the same across every dimension. If we say we have a 100 μ sphere, this describes it exactly. We cannot say the same for a cube, where the 100 μ may describe the length of one edge, or even a diagonal transect. For this reason, all particle sizing techniques measure a one-dimensional property of a particle and relate this to the size of an equivalent sphere. One example is to measure the surface area of a particle and then report the size of sphere which has the same surface area. Probably, the most convenient method is to measure the volume of each particle in a sample and report the size of a sphere which has the same volume as the particles being measured. Therefore, the laser diffraction has become one of the most commonly used particle sizing methods, especially for particles in the range of 0.5 to 1000 μ. It works on the principle that when a beam of a laser light is scattered by a group of particles, the angle of light scattering is inversely proportional to particle size meaning that the smaller the particle size, the larger the angle of light scattering [38]. This method has become very popular because it can be applied to many different sample types. It is also a very fast, reliable and reproducible technique and can measure over a very wide size range. Nevertheless, there are many other methods for analysing particle size. Sieving is one of the oldest particle sizing methods and is still widely

used for relatively large particles (Ø > 1 mm). When measuring very small particles (Ø < 0.5 μm), Dynamic Light Scattering is by far the easiest methods to use. If you need to measure morphological properties of particles such as shape and size, then image analysis methods are the only way to gain the extra information.

I.3.2 Specific surface area

The state of splitting of a solid material can be quantified by the value of its specific surface area, which corresponds to the overall surface of grains per unit masse. The specific surface area can be determined thanks to Blaine permeability or BET (Brunauer, Emmett and Teller) method [38]. The apparatus used to determine Blaine permeability is quite simple to use and mostly employed in cement industries. The principle of determining specific surface area thanks to Blaine permeability is based on the fact that the time necessary to cross one layer of powder by a given volume of air is function of the overall surface of particles composing the powder [38]. However, Blaine method measures the permeability of the air of a pressurized layer of powder with respect to a given procedure, the air being at atmospheric pressure with a known temperature. Nevertheless, the most commonly used method to determine the specific surface area of materials is BET method [68]. This method describes the physical adsorption of adsorbates and is based on three principal hypotheses [68]:

- the enthalpy of adsorption of molecules other than those of the first layer is equal to the enthalpy of liquefaction;
- there is no interaction between adsorbed molecules;
- the number of adsorbed layers becomes infinite at the saturating vapour pressure.

As previously indicated, the principle is based on the physical adsorption phenomenon of a gas at a temperature neighbouring its boiling point. The determination of the quantity of a gas adsorbed necessary to cover the surface of the sample to be analysed with a mono-layer enables to calculate its specific surface area. The quantity of gas adsorbed at constant temperature is function of its relative pressure. The BET adsorption model is therefore described by the following Equation (E4) [68]:

$$P / V (P_0-P) = 1 / VmC + P (C-1) / P_0VmC \quad \text{(E4)}$$

P: pressure of gas;

P_0: saturating vapour pressure of the adsorbent;

V: volume of gas adsorbed per gram of solids (m^3);

Vm: volume of gas necessary to obtain a mono-layer per gram of solids (m^3)

C: constant describing the interactions adsorbent-adsorbate.

Though, the plotting of the graph $P / V(P_0-P)$ as function of P / P_0 enables to obtain the value of the volume (Vm) of the mono-layer, which is the inverse of the slope and the value of Vm is directly proportional to the specific surface $S = \boldsymbol{\sigma}\, NVm / V_M$, where:

$\boldsymbol{\sigma}$: surface occupied by one molecule of adsorbate (m^2);

N: Avogadro number (mol^{-1});

V_M: molar volume of the adsorbate (m^3).

Furthermore, it is worth recalling that this technique is applied when the fineness of powder is high [38].

I.3.3 Chemical analysis

Chemical analysis is the study of chemical composition and structure of substances [69]. Globally, it may be considered the corpus of all techniques whereby any exact chemical information is obtained. There are two branches in analytical chemistry: qualitative and quantitative analyses [38]. Qualitative analysis is the determination of those elements and compounds that are present in a given sample of unknown material. Quantitative analysis is the determination of the amount by weight of each element or compound present. The procedures by which these aims may be achieved include testing for the chemical reaction of a putative constituent with an admixed reagent or for some well-defined physical property of the putative constituent. Classical methods include the use of analytical balance, gas manometer, burette and visual inspection of colour change. Gas and paper chromatography are particularly important modern methods. Physical techniques such as mass spectrometer are also employed. For samples in the gaseous state, optical spectroscopy provides the best technique for determining which atomic and molecular species are present [69].

I.3.4 Fourier Transformed Infrared Spectroscopy

It involves the absorption of electromagnetic radiation in the infrared region of the spectrum which results in changes in the vibrational energy of molecule. Since, usually all molecules will be having vibrations in the form of stretching, bending, etc., the absorbed energy will be utilised in changing the energy levels associated with them. It is a valuable and formidable tool in identifying organic compounds which have polar chemical bonds (such as O-H, N-H, C-H, etc.) with good charge separation (strong dipoles) [69]. It was originally designed as a double beam spectrophotometer comprising IR source (red hot ceramic material), grating monochromator, thermocouple detector, cells made of either sodium

chloride or potassium bromide materials, etc. In this process, the light is dispersed by the monochromator. But, this type of basic design for IR measurements has been outdated. Instead, a newer technique termed Fourier Transform Infrared spectroscopy (FTIR) has been in practice. This technique utilises a single beam of un-dispersed light and has instrument components similar to the previous one. In FTIR, the un-dispersed light beam is passed through the sample and the absorbances at all wavelengths are received at the detector simultaneously. A computerised mathematical manipulation known as Fourier Transform is performed on this data, to obtain absorption data for each and every wavelength. To perform this type of calculations interference of light pattern is required for which the FTIR instrumentation contains two mirrors, one fixed and one moveable with a beam splitter in between them (Figure 17). Before scanning the sample, a reference or a blank scanning is required [69]. FTIR spectroscopy finds extensive use in the identification and structural analysis of organic compounds, natural products, polymers, etc.

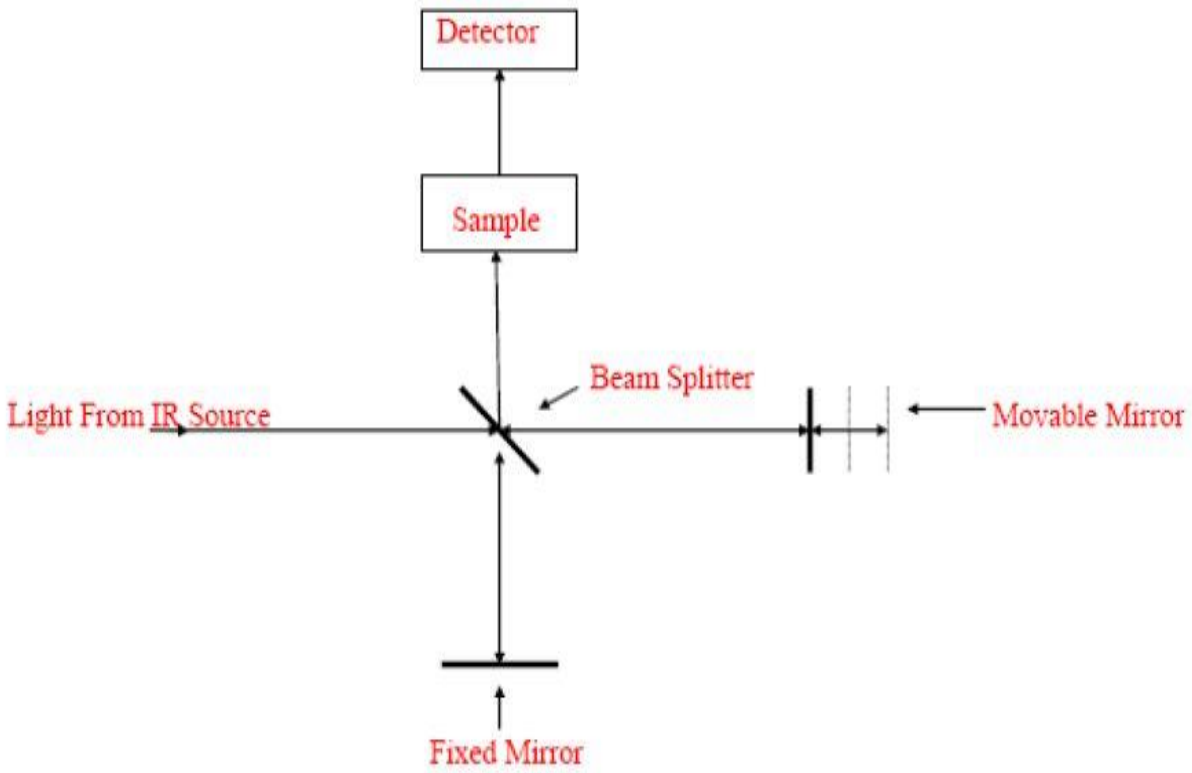

Figure 17: Principle of FTIR spectroscopy analysis [69].

I.3.5 X-Ray Diffractometry

In this technique, the primary X-rays are made to fall on the sample under study. Because of its wave nature, like light waves, it gets diffracted to a certain angle. This angle of diffraction, which differs from that of the incident beam, will give the information regarding

the crystal nature of the substance. The wavelength of the X-rays can be varied for the application by using a grating plate. The instrumentation consists of X-ray tube for the source, monochromator and a rotating detector (Figure 18). In crystals, the ions or molecules are arranged in well-defined positions in planes in three dimensions. The impinging X-rays are reflected by each crystal plane. Since the spacing between the atoms and hence the planes cannot be same or identical for any two chemical substances, this technique provides vital information regarding the arrangement of atoms and the spacing in between them and also to find out the chemical compositions of crystalline substances. The sample under study can be of either a thin layer of crystal or in a powder form. Since, the power of a diffracted beam is dependent on the quantity of the corresponding crystalline substance, it is also possible to carry out quantitative determinations. As application, the X-ray diffraction is a good tool to study the nature of crystalline substances [69].

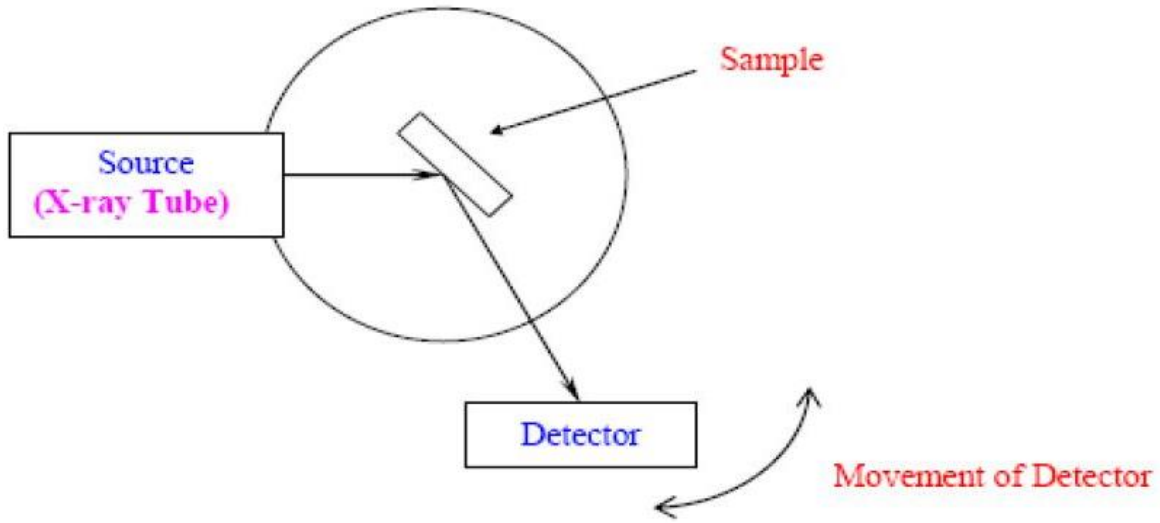

Figure 18: Principle of X-Ray Diffractometry [69].

I.3.6 Scanning Electron Microscopy (SEM)

In this technique, an electron beam is focused onto the sample surface kept in a vacuum by electro-magnetic lenses since electron possesses dual nature with properties of both particle and wave. An electron beam can be focused or condensed like an ordinary light. The beam is then rastered or scanned over the surface of the sample. The scattered electron from the sample is then fed to the detector and then to a Cathode Ray Tube (CRT) through an amplifier, where the images are formed, which gives the information on the surface of the sample [69]. The instrument used comprises a heated filament as source of electron beam, condenser lenses, aperture, evacuated chamber for placing the sample, electron detector,

amplifier, CRT with image forming electronics, etc. (Figure 19). As applications, Scanning Electron Microscopy has been applied to the surface studies of metals, ceramics, polymers, composites and biological materials for both topography as well as compositional analysis. An extension or sometimes conjunction to SEM of this technique is Electron Probe Micro Analysis (EPMA), where the emission of X-rays, from the sample surface, is studied upon exposure to a beam of high energy electrons. Depending on the type of detectors used, this method is classified into two as follows: Energy Dispersive Spectrometry (EDS) and Wavelength Dispersive Spectrometry (WDS). This technique is used extensively in the analysis of metallic and ceramic inclusions, inclusions in polymeric materials, diffusion profiles in electronic components. The major drawback of this analysis is that the instrumentation is complicated and needs high vacuum for optimum performance [69].

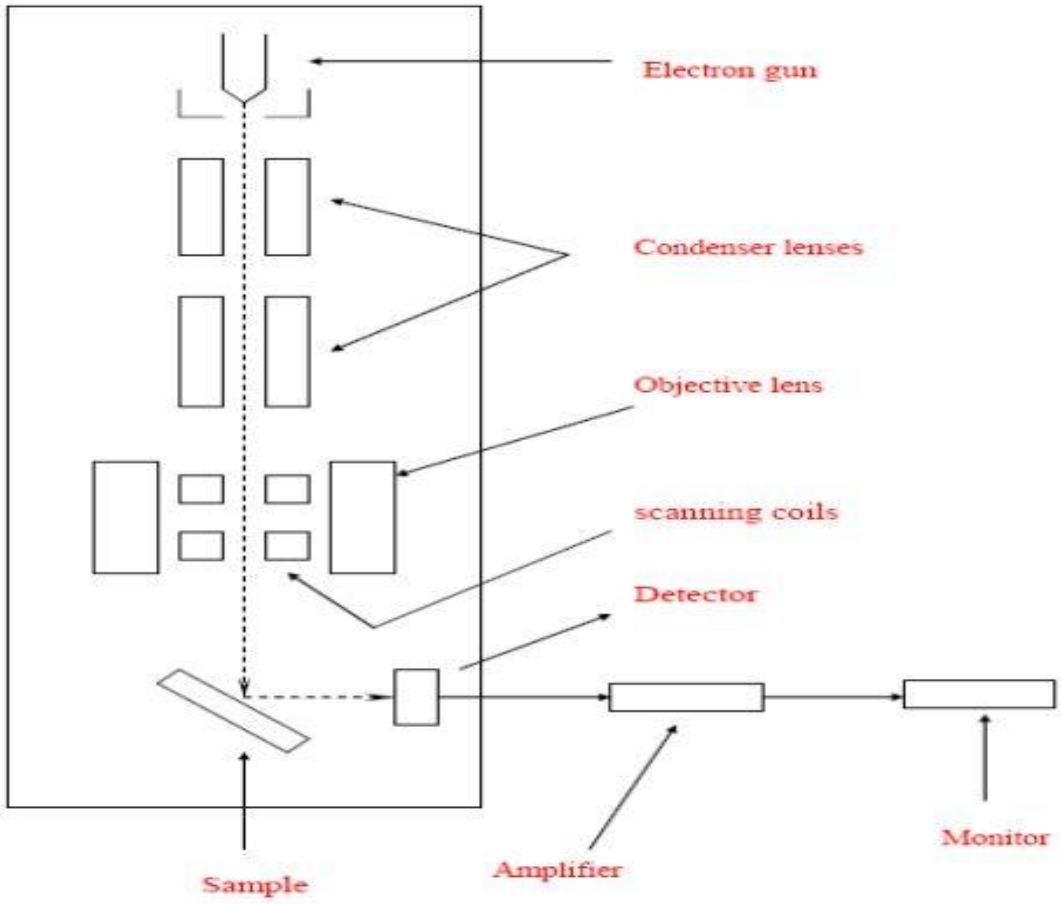

Figure 19: Principle of Scanning Electron Microscopy analysis [69].

I.3.7 Drying and thermal shrinkage

The shrinkage is the reduction of dimensions of a material compared to its initial dimensions [38]. This is due to the presence of capillary forces developed during the

formation of meniscus when water contained in capillary is evacuated. However, the shrinkage is obtained by measuring the dimensions of specimens at a given day or after thermal treatment (curing or heating). There exist many types of shrinkage [38]:

- the shrinkage before setting, attributed to the premature loss of a part of water by evaporation due to mixing;
- the hydraulic shrinkage, which is firstly assigned to le Chatelier contraction and finally to drying shrinkage. This shrinkage ranges between 0.2 to 0.4 % for concretes;
- the thermal shrinkage which is ascribed to the contraction of concretes during its cooling.

I.3.8 Thermal analysis

Thermal analysis actually comprises a series of methods, which detect the changes in the physical and mechanical properties of a given substance by application of heat or thermal energy [69]. The physical properties include mass, temperature, enthalpy, dimension, dynamic characteristics, etc. It finds its application in finding the purity, integrity, crystallinity and thermal stability of the chemical substances under study. Most often, it is used in the determination of the composition of complex mixtures. This technique has been adopted as testing standard in quality control in the production field, process control and material inspection. It is applied in wide range of fields including polymers, glasses, ceramics, metals, explosives, semiconductors, medicines and foods [69]. The following are the popular methods under this technique: Thermogravimetric Analysis (TGA), Differential Thermal Analysis (DTA), Differential Scanning Calorimetry (DSC), Thermo-mechanical Analysis (TMA) and Dilatometry.

I.3.8.1 Thermogravimetric Analysis (TGA)

In this technique (TGA), the change in sample weight is measured while the sample is heated at a constant rate or at constant temperature, under air or inert atmosphere (N_2). This technique is effective for quantitative analysis of thermal reactions that are accompanied by mass changes, such as evaporation, decomposition, gas absorption, desorption and dehydration [38]. The simplified diagram for this instrumentation is presented in Figure 20. The micro-balance plays a significant role during measurement since the change in sample mass affects the equilibrium of the balance. This imbalance is fed back to a force coil, which generates additional electromagnetic force to recover equilibrium. The amount of additional

electromagnetic force is proportional to the mass change. During the heating process, the temperature may go as high as 1500 °C inside the furnace [69].

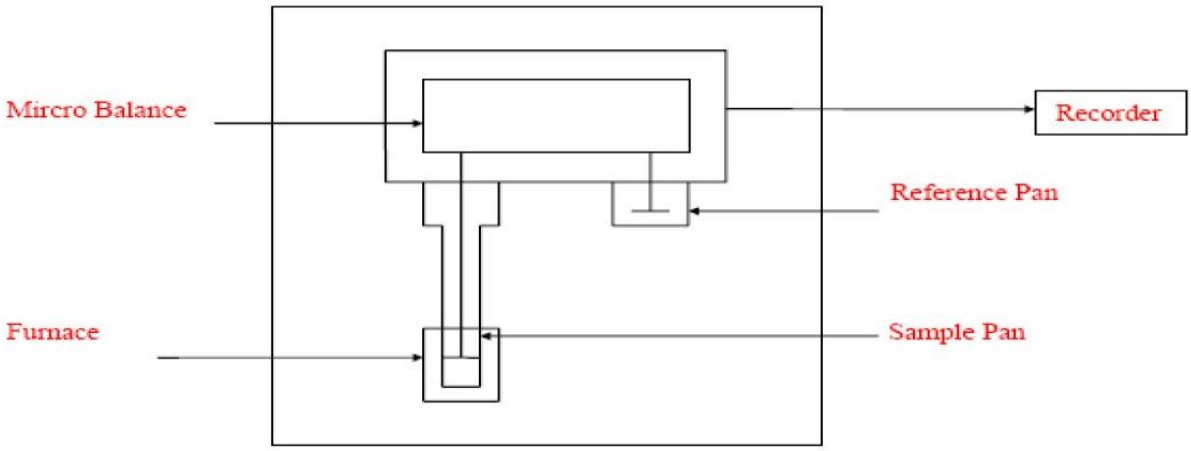

Figure 20: Principle of Thermogravimetric Analysis (TGA) [69].

I.3.8.2 Differential Thermal Analysis (DTA)

This technique measures the temperature difference between a sample and a reference material as a function of temperature as they are heated or cooled or kept at a constant temperature [38]. Here, the sample and the reference material are simultaneously heated or cooled at a constant rate. Reaction or transition temperatures are then measured as a function of the temperature difference between the sample and the reference. It provides vital information of the materials regarding their endothermic and exothermic behaviour at high temperatures [69]. It finds most of its applications in analysing and characterising clay materials, ceramic, ores, etc.

I.3.8.3 Differential Scanning Calorimetry (DSC)

This technique is more or less similar to DTA except that it measures the amount of heat absorbed or released by a sample as it is heated or cooled or kept at constant temperature [38]. Here, the sample and the reference material are simultaneously heated or cooled at a constant rate. The difference in temperature between them is proportional to the difference in heat flow from the heating source (furnace) between the two materials [69]. It is the well-suited technique in the detection and further studies of liquid crystals. This technique is applied to most of polymers in evaluating the curing process of thermoset materials as well as in determining the heat of melting and melting point of thermoplastic polymers, glass transition temperature (Tg), endothermic and exothermic behaviours. Through, the adjunct process of isothermal crystallisation, it provides information regarding the molecular weight

and structural differences between very similar materials. The instrumentation (Figure 21) is exactly similar to that of DTA except for the difference in obtaining the results [69].

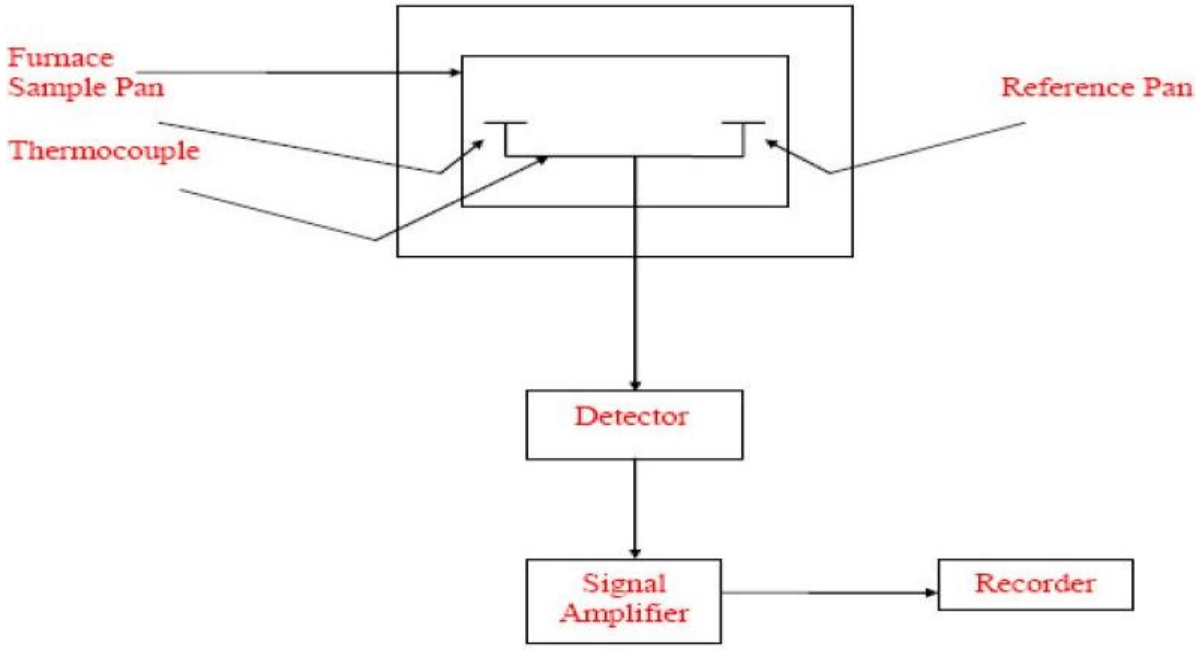

Figure 21: Principle of DSC / DTA Analyses [69].

I.3.8.4 Thermo-mechanical Analysis (TMA)

TMA is the measurement of behaviour of materials such as expansion or contraction when temperature and load are applied. A scan of dimensional changes related to temperature at constant load or load at constant temperature provides valuable information about the mechanical properties of samples [69]. One of the most important applications of TMA is the characterisation of composite and laminate materials, through the study of glass transition temperature and expansion coefficient. Another application is in the quantitative measurement of extension and contraction observed in textile fibbers, thin films and similar materials [69].

I.3.8.5 Dilatometry

Dilatometry deals with the determination of length or volume as a function of temperature. Actually, dilatometry is quite different from TMA because TMA is generally carried out under tension or load [69]. Historically, dilatometry and TMA date back to ancient metrology. Obvious length measurements are made through side-by-side comparison with a standard whereas obvious volume measurements are through comparison with the content of a standard vessel. Dilatometry is also applied to determine the coefficient of thermal expansion of solid material [38]. Indeed, when a new phase has a different coefficient of thermal

expansion, its formation may be recognised on a dilatometry curve. When two neighbouring phases have similar coefficients of thermal expansion, the method is not sensitive. The precision of this technique is generally not better than several percent. Nevertheless, the highest precision of length measurement can be achieved by interferometry whereas volume determination can be obtained thanks to pycnometers [69].

I.3.9 Physical properties

Apparent porosity, water absorption, apparent specific gravity and bulk density are primary physical properties of fired refractory bricks and cement products [70]. These properties are widely used in the evaluation and comparison of the product quality and as part of the criteria for selection and use of products in a variety of industrial applications. These test methods are used for determining any or all of these properties. These test methods are primary standard methods which are suitable for use in quality control, research and development, establishing criteria for evaluating compliance with specifications and providing data for design purposes [71]. Fundamental assumptions inherent in these test methods are that the test specimens are not attacked by water, the test specimens conform to the requirements for size, configuration, and original faces, the open pores of the test specimens are fully impregnated with water during the boiling treatment, and the blotting of the saturated test specimens is performed as specified in a consistent and uniform manner to avoid withdrawing water from the pores. Deviation from any of these assumptions adversely affects the test results. Certain precautions must be exercised in interpreting and using results from these test methods. All four property values are interrelated by at least two of the three base data values generated during testing. Thus, an error in any base data value will cause an error in at least three of the property values for a given test specimen. Some of these properties (apparent specific gravity and bulk density) are functions of other factors such as product composition, compositional variability within the same product, impervious porosity and total porosity [71]. Generalisations on or comparisons of property values should only be judiciously made between like products tested by these test methods or with full recognition of potentially inherent differences between the products being compared or the test method used.

I.3.10 Mechanical strength

The most important characteristic of hardened paste, mortar and concrete is the compressive strength at a given age. When they are under load, hardened paste, mortar and concrete usually behave as brittle materials. On one hand, their rupture is not preceded of important deformations. On the other hand, their tensile strength is as much lower than their compressive strength [38]. The parameters such as permeability and durability are less important compared to compressive strength. However, the strength of mortar or concrete depends on a certain number of parameters such as the dosage of raw materials used, the degree and the processing condition. Additionally, the strength of mortar or concrete is independent of the class of cement employed. Notwithstanding that, the aggregates should be properly selected (shape and size) in order to optimize the final characteristics of as-obtained products (mortars and concretes) [38].

I.4 Summary and motivations of the thesis

Recently, thermal resistance of calcined-clay based-geopolymers was extensively reported but there is lack of data in regard with the thermal resistance of kaolin-based geopolymers. It is worth recalling that the use of kaolin for alkaline activation is limited as result of its low reactivity and this study will help to fill the gap. Also, there are not enough data in regard with thermal stability of alkali-activated volcanic scoria and this work will help to bring more knowledge on this issue. Moreover, it was observed that heating metakaolin-based geopolymers induces the formation of cracks which limit its residual mechanical strength. An attempt to improve the thermal stability of kaolin and metakaolin-based geopolymers as well as alkali-activated volcanic scoria specimens obtained with partial replacement of aluminium hydroxide compounds as mineral additives is reported in this thesis.

Chapter II: Materials and experimental methods

This chapter reports a detailed description on raw materials and experimental methods employed. Firstly, it describes the sources of kaolin and volcanic scoria as well as their respective locations of collection. Secondly, a description of mineral additives, reagents, the procedure used for preparing the alkaline activator along with a brief description of condition of synthesis of geopolymers and alkali-activated binders is provided. Finally, the characteristics of analytical instruments used to characterise the raw materials and the resulting binders along with their heated products are reported.

II.1 Materials and processing

II.1.1 Aluminosilicates

Two types of aluminosilicate sources were used in this study: kaolin and volcanic scoria. The kaolin sample referenced as K in this study was supplied in its natural form by the group Nubru Holding which operates on the valorisation of certain local raw materials for the production of ceramics and other related materials in Cameroon [20]. As for the volcanic scoria sample, it was collected along the "Cameroon volcanic line" at the locality of Galim (Latitude 5°40'05"; Longitude 10°23'10"; Altitude: 1143 m), Bamboutos Division, West Region of Cameroon [38]. A partial view of volcanic scoria deposit of Galim is presented in Figure 22.

Figure 22: Partial view of volcanic scoria deposit of Galim [38].

The particles of volcanic scoria collected from Galim deposit are highly vesicular with larger vesicles and are black in colour [37] and they are referenced as Z in this study. However, these volcanic scoriae are locally used as aggregates to produce concrete for construction purpose and civil engineering applications [37].

Once collected, the as-received kaolin (K) and volcanic scoria (Z) were processed respectively prior to be used as starting materials for the synthesis of alkaline cements.

Regarding the kaolin sample (K), it was purified by wet sieving using Stock's law thanks to a 100 μm mesh-sifter [38]. This method was actually based on the difference of density of each mineral contained in the raw material. To that end, the material was introduced in a big bucket containing enough tap water and allowed to wet for at least 24 h. After this, a second bucket filled with enough tap water and a 100 μm mesh-sifter were required for the washing process. The impurities and solid particles with low densities were maintained on the surface whereas the small particles such as clay minerals (diameter < 2 μm) were held in solution and allowed to be deposited after some times. After separation of impurities and solid particles thanks to a 100 μm mesh-sifter along with water, the obtained slurry was enriched in clay minerals and firstly dried over sun in order to accelerate the evaporation process. Thereafter, the as-obtained kaolin powder (K) was secondly oven dried in the electrical oven (Heraeus, type VT 5042 EK) (Annex) to remove absorbed water molecules in order to facilitate further sieving process. The obtained kaolin sample (K) was then sieved at 90 μm and the resulting powders were kept in a sealed bucket out of moisture prior to be used.

Once obtained, the kaolin powder (K) was divided into two sets. One portion was kept as-obtained in a sealed bucket prior to be used as starting material for the synthesis of alkaline cements. Another portion was thermally treated in the programmable electric furnace (Nabertherm, Mod. LH 60/14) for 4 h at 700 °C [72] at heating rate of 1 °C / min [73] in order to obtain a suitable reactive metakaolin referenced as MK in this study.

To that end, the program of calcination presented in Figure 23 was used.

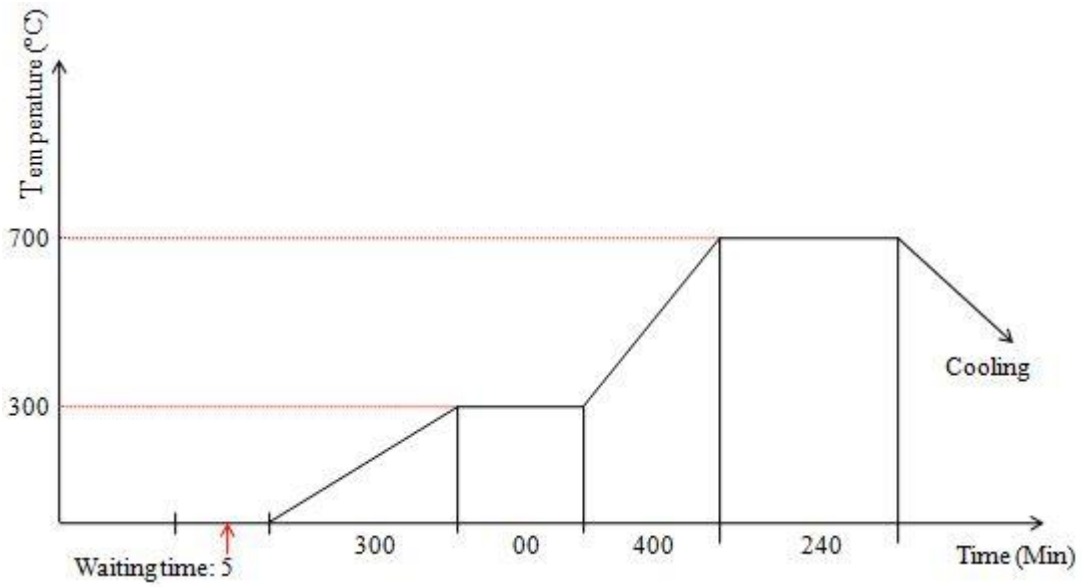

Figure 23: Temperature cycle in the furnace during calcination of kaolin sample (K).

Actually, the calcination was carried out in four stages:

- weighing of certain mass of the kaolin sample and charging in the electrical furnace;
- rising in temperature controlled by stages (Figure 23);
- holding the temperature at the stage of amorphisation (700 °C) for 4 h;
- cooling up to ambient temperature of the laboratory after some times and discharging.

It is worth recalling that within the framework of this study, the choice of the amorphisation temperature of the kaolin sample (K) at 700 °C was due the previous work carried out by Elimbi et *al*. [72], who had shown that at that particular temperature, the obtained metakaolin (MK) exhibits maximum disorder, thus very reactive. Additionally, the heating rate of 1 °C / min along with the 4 h (240 min) of amorphisation used was due to the previous work done by Kenne et *al*. [73] who had also shown that when the heating rate of a kaolinitic clay is very slow, the resulting metakaolin is very reactive accordingly. Thus, the resulting metakaolin was then kept in a sealed bucket out of moisture prior to be used as starting material for the synthesis of alkaline cements.

As for the volcanic scoria sample (Z), it was firstly washed with tap water in order to remove the impurities and organic matters and secondly dried at 105 ° C for 24 h in an electrical oven (Heraeus, type VT 5042 EK) prior to be grounded. Thereafter, the volcanic scoria (Z) was introduced in a porcelain jar along with high alumina balls as grinding medium. The material was ball milled for 4 h (Annex), sieved at 90 µm mesh-sifter and the resulting powders were kept in a sealed bucket out of moisture prior to be used as starting material for the synthesis of alkaline cements.

II.1.2 Mineral additives

Two types of alumina sources supplied by the company Sigma Aldrich were used in this study. On one hand, amorphous aluminium hydroxide referenced as A was provided in its powder form and use as-received. This material was kept as-received prior to be used as partial replacement for the synthesis of alkaline cements. On the other hand, the semi-crystalline aluminium oxy-hydroxide referenced as B was supplied in granular form with average diameter of spheres ranging between 3-6 mm. However, it was firstly ground using a porcelain mortar and pestle. Secondly, the obtained powder was then sieved at 90 µm mesh-sifter and the resulting powder was kept in a sealed bucket out of moisture prior to be used as partial replacement for the synthesis of alkaline cements.

II.1.3 Preparation of the alkaline activator solution

Commercial sodium silicate solution (density of 1400 Kg / m^3 and silicic moduli of 3.22), sodium hydroxide pellets and distilled water were used. The activator was prepared by mixing sodium hydroxide (99 % by mass of NaOH) solution and commercial sodium silicate (% by mass: SiO_2 (28.7), Na_2O (8.9), H_2O (62.4)) in order to get the following molar ratios: SiO_2 / Na_2O =1.45 and H_2O / Na_2O =16. Prior to be used, the obtained solution was sealed and stored at least for 24 h at ambient temperature (24 ± 3 °C) of the laboratory in order to allow full silicate depolymerisation.

II.2 Experimental methods

II.2.1 Elaboration of formulations

Mixtures of powders were obtained by partially replacing each aluminosilicate source (kaolin (K), metakaolin (MK) or volcanic scoria (Z)) by 0, 10, 20 and 30 % by mass by each alumina source (amorphous aluminium hydroxide (A) or aluminium oxy-hydroxide (B)) respectively as presented in Table I.

Table I: Mix proportions in alkaline cement pastes (% by mass).

Formulations	Aluminosilicates (K or MK or Z)	Replacements (A or B)	L / S mass ratio
GK	100	00	0.86
GK_B^{10}	90	10	0.86
GK_B^{20}	80	20	0.86
GK_B^{30}	70	30	0.86
GK_A^{10}	90	10	1.17
GK_A^{20}	80	20	1.51
GK_A^{30}	70	30	1.84
GMK	100	00	1.13
GMK_B^{10}	90	10	1.13
GMK_B^{20}	80	20	1.13
GMK_B^{30}	70	30	1.13
GMK_A^{10}	90	10	1.20
GMK_A^{20}	80	20	1.68
GMK_A^{30}	70	30	2.01
GZ	100	00	0.84
GZ_B^{10}	90	10	0.84
GZ_B^{20}	80	20	0.84
GZ_B^{30}	70	30	0.84
GZ_A^{10}	90	10	0.96
GZ_A^{20}	80	20	1.13
GZ_A^{30}	70	30	1.34

In each mixture, dried powders were initially mixed in the Hobart mixer (M & O model N50-G) (Annex) for 5 min. Then, the alkaline activator was gradually added for other 5 min. In each mixture, liquid to solid mass ratio (L / S) was done as given in Table I.

Fresh alkaline cement pastes obtained were poured into cylindrical moulds (height: 46 mm; diameter: 23 mm) and covered with a thin film of polyethylene, vibrated for 5 min

thanks to the electrical vibrating table (M & O, type 202, No. 106) (Annex) in order to remove entrapped air bubbles.

II.2.2 Conditioning of alkaline cement specimens

Once obtained, the as-produced specimens resulting from kaolin were cured at 60 °C in the oven (Heraeus, type VT 5042 EK) for 7 days in order to accelerate the hardening or setting process before demoulding. After demoulding, the as-obtained specimens denoted respectively as GK, GK_A^{10}, GK_A^{20}, GK_A^{30}, GK_B^{10}, GK_B^{20} and GK_B^{30} were maintained in the same oven at the same temperature prior to be characterised. Conversely, specimens resulting from metakaolin (GMK, GMK_A^{10}, GMK_A^{20}, GMK_A^{30}, GMK_B^{10}, GMK_B^{20} and GMK_B^{30}) as well as those obtained from volcanic scoria (GZ, GZ_A^{10}, GZ_A^{20}, GZ_A^{30}, GZ_B^{10}, GZ_B^{20} and GZ_B^{30}) were sealed in black plastic and cured at ambient temperature of laboratory for at least 24 h prior to be demoulded. After demoulding, these specimens were maintained in the same black plastic and cured at ambient temperature of the laboratory for 28 days prior to be characterised as well.

II.2.3 Thermal treatment of alkaline cement specimens

The as-obtained specimens were divided into 7 batches. The first batch (GK, GK_A^{10}, GK_A^{20}, GK_A^{30}, GK_B^{10}, GK_B^{20}, GK_B^{30}, GMK, GMK_A^{10}, GMK_A^{20}, GMK_A^{30}, GMK_B^{10}, GMK_B^{20}, GMK_B^{30}, GZ, GZ_A^{10}, GZ_A^{20}, GZ_A^{30}, GZ_B^{10}, GZ_B^{20} and GZ_B^{30}) was characterised as-obtained whereas the six other batches were firstly oven dried (Heraeus, type VT 5042 EK) at 105 °C for at least 24 h in order to minimize the level of formation of cracks due to water evaporation during further heating at elevated temperatures. Finally, they were respectively heated at 300, 700, 900, 1100, 1150 and 1200 °C for 2 h in the programmable electric furnace (Nabertherm, Mod.LH60/14) at heating rate of 5 °C / min thanks to the program of calcination presented in Figure 24 and by using the various values of holding time summarised in Table II.

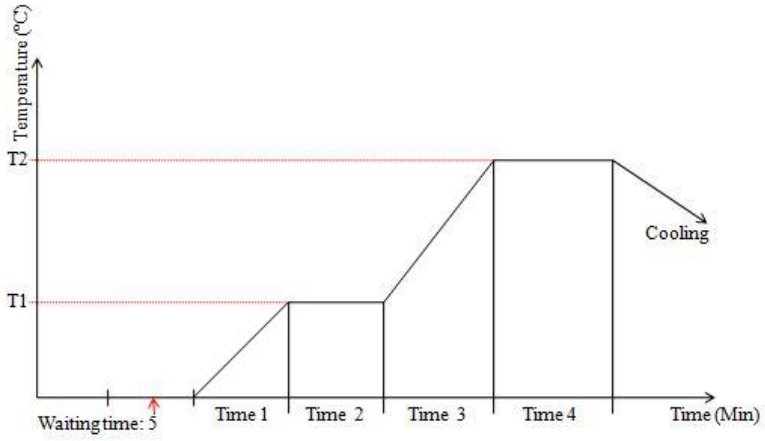

Figure 24: Temperature cycle in the furnace during calcination of specimens.

Table II: Values of holding time used for calcination of specimens.

Heating temperatures (°C)	Temperature of stages (°C)	Time 1 (min)	Time 2 (min)	Time 3 (min)	Time 4 (min)
300	T1: 300	60	00	/	/
	T2: 300	/	/	00	120
700	T1: 300	60	00	/	/
	T2: 700	/	/	80	120
900	T1: 300	60	00	/	/
	T2: 900	/	/	120	120
1100	T1: 300	60	00	/	/
	T2: 1100	/	/	160	120
1150	T1: 300	60	00	/	/
	T2: 1150	/	/	170	120
1200	T1: 300	60	00	/	/
	T2: 1200	/	/	180	120

(T1: temperature at the first stage of heating; T2: temperature at the second stage of heating)

II.2.4 Characterisation of alkaline cements along with their heated products

II.2.4.1 Thermal behaviour of hardened alkaline cement products

It is worth recalling that a substance subjected to heat treatment can undergo transformations of phase, modification of structure, decomposition and variation of volume [38]. Thermal analysis appears as a useful tool to observe these modifications thanks to the

temperature. Among these techniques, Differential Thermal Analysis (DTA) and Thermogravimetric Analysis (TGA) are usually used. Additionally, these two types of thermal analyses are most often carried out simultaneously in the same apparatus.

Within the framework of this study, the selected alkaline cements (GK, GK_A^{10}, GK_B^{30}, GMK, GMK_A^{10}, GMK_B^{30}, GZ, and GZ_B^{30}) initially cured either at ambient temperature of the laboratory or oven dried at 60 °C depending on the formulations, were crushed thanks to a porcelain mortar and pestle, and then sieved at 90 µm mesh-sifter. The resulting powders of each formulation (< 1 g) were subjected to thermal analyses (TGA and DTA) using a TGA / DSC 3^+ device of the Company Mettler Toledo as from 20 to 1200 °C in a self-generated atmosphere of air at heating rate of 5 °C / min. Actually, this analysis was done in the Laboratory of Materials of the European Ceramic Centre in France.

II.2.4.2 Morphological observation

The appearance of hardened alkaline cement specimens was visualised before and after heating. To that end, both volume stability and cracks development were used as a tool to assess the macro-scale thermal stability of specimens after thermal treatment. Additionally, the determination of the colour of specimens was carried out thanks to the Munsel Code [74]. This variation was observed on the unheated and heated specimens by comparing their colours with those contained and indexed in the Munsel code.

II.2.4.3 Evaluation of thermal shrinkage

The shrinkage is the reduction in dimensions of a specimen compared to its initial values as result of either curing or heat treatment. However, when the variation is related in only one dimension, it is called linear shrinkage [38].

It is worth pointing out that within the framework of this study, thermal shrinkage was determined on the length of cylindrical specimens according to ASTM C 267 standard [75] using a digital calliper (Annex). Thermal shrinkage (TS) was calculated thanks to the Equation (E5):

$$TS = \frac{L_0 - L_T}{L_O} \times 100\ (\%) \qquad \text{(E5)}$$

L_0: length before heating (mm);

L_T: length after heating (mm);

TS: thermal shrinkage (%).

II.2.4.4 Evaluation of physical properties

Physical properties such as water absorption, open porosity and bulk density of hardened alkaline cement specimens along with their heated products were determined by using Archimedes principles according to ASTM Standards C20 / 2010 [70].

However, the density of a porous material is known to be the ratio between its dry mass over its apparent volume [71]. The procedure of this method is described as followed. Firstly, the specimen is weighed (M_1) using a balance before being introduced into a vacuum bell-jar. Then, the vacuum is created after 2 h thanks to a vacuum pump. While maintaining the vacuum in the setup, the specimen is immersed in distilled water and heated for 2 h. Secondly, after 24 h, it is removed from the liquid of immersion with density denoted as $\rho_{(liquid)}$ and then placed in the basket and the weight under water (M_2) is collected. Finally, the specimen is removed from the water, sponged slightly with wet linen in order not to empty open porosities and the mass M_3 (wet mass) is measured [70]. The calculation of bulk density (BD), open porosity (OP) and water absorption (WA) of specimens was done thanks to the following formulas:

- $BD = \frac{M_1}{M_3 - M_2} \times \rho_{(liquid)}$ (E6)

- $OP = \frac{M_3 - M_1}{M_3 - M_2} \times 100$ (E7)

- $WA = \frac{M_3 - M_1}{M_1} \times 100$ (E8)

Actually, these measurements were done in the Laboratory of Structural Mechanic and Civil Engineering, Polytechnic University of Mons, Belgium.

II.2.4.5 Evaluation of compressive strength

It was measured on hardened alkaline cement specimens initially cured at ambient temperature of laboratory and aged 28 days or oven dried at 60 °C for 7 days along with all their heated products according to EN 196.1 Standard [76]. The test consisted for placing the cylindrical specimen on the plate of the electro-hydraulic press (M & O, type 11.50, N0° 21) (Annex) and then subjected to a continuous and progressive force (charge) at an average

speed of 3 mm / min until the specimen is crushed. However, the surfaces of the various cylinders should be polished using abrasive papers in a manner that they become parallel in order to avoid non-uniform force or charge [38]. Compressive strength is therefore the ratio of the maximum force or charge supported by the cylinder in the course of the test over its initial surface area. By using **d** to designate the diameter of a cylindrical specimen measured thanks to a digital calliper and F the maximum force (charge) that it can withstand before breaking, the compressive strength (CS) is calculated using the Equation (E9):

$$CS = \frac{4000 \times F}{\pi d^2} \quad \text{(E9)}$$

F (KN)

d (m)

CS (MPa).

II.2.5 Mineralogical and microstructural characterisations of starting materials and synthesised products

II.2.5.1 Particle size distribution

Particle size analysis of the starting materials (K, MK, Z, A and B) was carried out using a laser particle size analyzer (MASTERSIZER S, Malvern, UK). The procedure involved passing of dilute well-dispersed slurry of each starting material through a flow cell positioned in the path of the laser beam to generate a scattering pattern. 0.1 % of sodium hexa-metaphosphate was used as a dispersant and ultrasonic vibration for 2 min was applied to avoid agglomeration [37]. The processing of data collected thanks to a computer helps to draw the particles size distribution of the starting materials expressed on the volume basis. However, the software used assimilates the grains as spheres whose values of diameters are reported on the X-axis [38]. Actually, this analysis was carried out in the Laboratory of Materials of the European Ceramic Centre in France.

II.2.5.2 Specific surface area

Measurement of specific surface area of powders of the starting materials (K, MK, Z, A and B) allows to determine the overall surface of a set of particles, including that of open pores accessible to external gases. Actually, it is based on the measurement of the quantity of gas adsorbed (nitrogen) by a powder sample. Knowing the quantity of adsorbate, the dimension of adsorbed molecules and their possible of arrangements, the surface of the solid

responsible for adsorption is evaluated using the model of calculation known as BET (Brunauer, Emmett and Teller) method [68]. This method requires a pre-processing of samples through the removing of gas and dehydration in between 150 and 300 °C in order to evacuate all molecules initially adsorbed by the solid. The apparatus used was a Micromeritics Tristar II 3020. This analysis was done in the Laboratory of Materials of the European Ceramic Centre in France.

II.2.5.3 Chemical compositions

Chemical analysis of the starting materials (K, MK, Z, A and B) were done in order to determine the percentage (by mass) of elements expressed in term of their most stable oxides. However, this analysis exhibits two advantages:

- qualitative analysis since it gives the nature of various chemical species contained in the sample;
- quantitative analysis because it allows to determine the amount of major elements [38].

Chemical compositions of the starting materials were measured by Inductively Coupled Plasma and Optical Emission Spectroscopy (ICP-OES) using an Optima™ 7000 DV ICP-OES (PerkinElmer) device equipped with a CCD sensor. Each analysis composition was subjected to an acid dilution of at least 2 % in pure nitric acid (more if necessary to obtain a pH lower than 3) [77]. This analysis was done in the Laboratory of Materials and Durability of Constructions, INSA Toulouse, France.

II.2.5.4 Thermal analyses

Thermal behaviour of the starting materials (K, Z, A and B) were also followed by TGA / DTA thanks to the apparatus and the procedure previously described in the session II.2.4.1.

II.2.5.5 Fourier Transform Infrared Spectroscopy analysis

This analysis is based on the absorption phenomenon that occurs when the infrared radiation crosses the material to be analysed. The radiation is absorbed selectively according to the vibrations excited from the material. Indeed, each molecule or functional groups constituting the materials have levels of vibrations corresponding to precise energies. When the molecule is excited to its Eigen vibration energy, it absorbs the incidental energy and thus

enabling the study of various connections present in the material. Alkaline cements are mainly composed of silicon, aluminium and alkaline cations (M^+). The presence of these three elements will induce a great number of possible connections (Si-O-Si, Si-O-Al, Si-O, Si-O-M, O-Si-O) having each various vibrational modes. Globally, for alkaline cements, the vibrational modes most detectable are symmetric and asymmetric stretching vibrations as well as bending vibration in the plane [78].

However, within the framework of this study, approximately 1 mg of the powder of material to be analysed was placed on the surface of diamond crystal ATR (Attenuated Total Reflection). After pull down the crank to cover the sample, the recording process of the spectrum was directly carried out. This analysis was done thanks to the Bruker Alpha-p Spectrophotometer in the Laboratory of Analytical Chemistry, University of Yaoundé I, Cameroon.

II.2.5.6 XRD analysis

This analysis helps to determine the mineralogical composition of a given sample of unknown material. Indeed, the crystalline phases are identified by comparing the obtained patterns with the Powder Diffraction File (PDF) standards from the International Centre for Diffraction Data (ICDD).

Approximately 2 mg of each powder of material was introduced in a cylindrical mould, then compacted so that the specimen to be analysed showed a maximum size of 40 mm of diameter and 5 mm of height. Then, the specimen was placed on the stand of the Brucker D8 diffractometer, irradiated with a beam of parallel and monochromatic X-ray of known wavelength (1.5405 Å). Actually, the beam was produced thanks to the copper anticathode having the energy of radiation of 8047 eV. This analysis was done in the Belgian Ceramic Research Centre Laboratory and in the Geology Laboratory of the Liege University, Belgium.

II.2.5.7 Scanning Electron Microscopy analysis

Microscopic observations were performed using two types of Scanning Electron Microscope: the JEOL JSM-IT300 and the FEI Quanta FEG 450 ESEM.

Concerning the JEOL IT300, it was equipped with a detector made with standard semiconductors on low vacuum models, with high sensitivity to weak voltage or fast rate of scanning. It functions under high vacuum with accelerating voltage ranging between 0.3 KV

and 15 KV along with a growth ranging between 5x and 300 000x. This apparatus was used for microscopic observations of selected metakaolin and volcanic scoria-based specimens along with their heated products. It was done in the Laboratory of Materials and Durability of Constructions, INSA Toulouse, France.

Regarding the FEI Quanta FEG 450 ESEM, it was equipped with detectors of secondary electrons made with semiconductors and various detectors of secondary electrons gas. The accelerating voltage here can reach 30 KV and it functions under vacuum. This apparatus was used for microscopic observations of selected kaolin-based specimens along with their heated products. Actually, it was done in the Laboratory of Materials at the European Ceramic Centre in France.

Chapter III: Results and discussion

This chapter reports the results and detailed discussions of the investigations described in chapter II. Firstly, the characterisation of the starting materials and the mineral additives used for alkaline activation is reported. Secondly, the influence of mineral additives replacements on thermal stability of the resulting kaolin and metakaolin-based geopolymers as well as alkali-activated volcanic scoria specimens is critically examined. Finally, the thermal stabilities of resulting products are compared based on their thermal behaviours and residual compressive strengths.

III.1 Characterisation of the starting materials

III.1.1 Particle size distribution

The curves (Figures 25-29) present the volume distributions by each class of particles and the corresponding cumulative volumes of K, MK, Z, A and B respectively. Thanks to the cumulative volume curves (blue curves), the maximum diameter corresponding at 10 % (d_{10}), 50 % (d_{50}) and 90 % (d_{90}) of particles was evaluated for each starting material as well as the corresponding span (standard deviation) [79]. The obtained results are summarised in Table III.

Table III: Granulometric characteristics of the starting materials.

Starting materials	d_{10} (µm)	d_{50} (µm)	d_{90} (µm)	$(d_{90}-d_{10}) / d_{50}$
K	5.24	12.31	47.29	3.42
MK	5.42	12.62	46.92	3.29
Z	1.31	6.80	22.01	3.04
A	2.47	6.51	21.25	2.88
B	1.68	8.46	46.03	5.24

However, the particle size distribution of K (Figure 25) ranges as from 1 to 229 µm with the mean particle diameters at d_{10}=5.24 µm; d_{50}=12.31 µm and d_{90}=47.29 µm. Additionally, the volume distribution of K (red curve) shows that the powder of kaolin has a bimodal distribution with the span value of 3.42 (Table III) and mostly composed of particles having small sizes. The first population varies as from 1 to 29.9 µm with the largest particle having a size of 11.57 µm whereas the second population varies as from 29.9 to 229 µm.

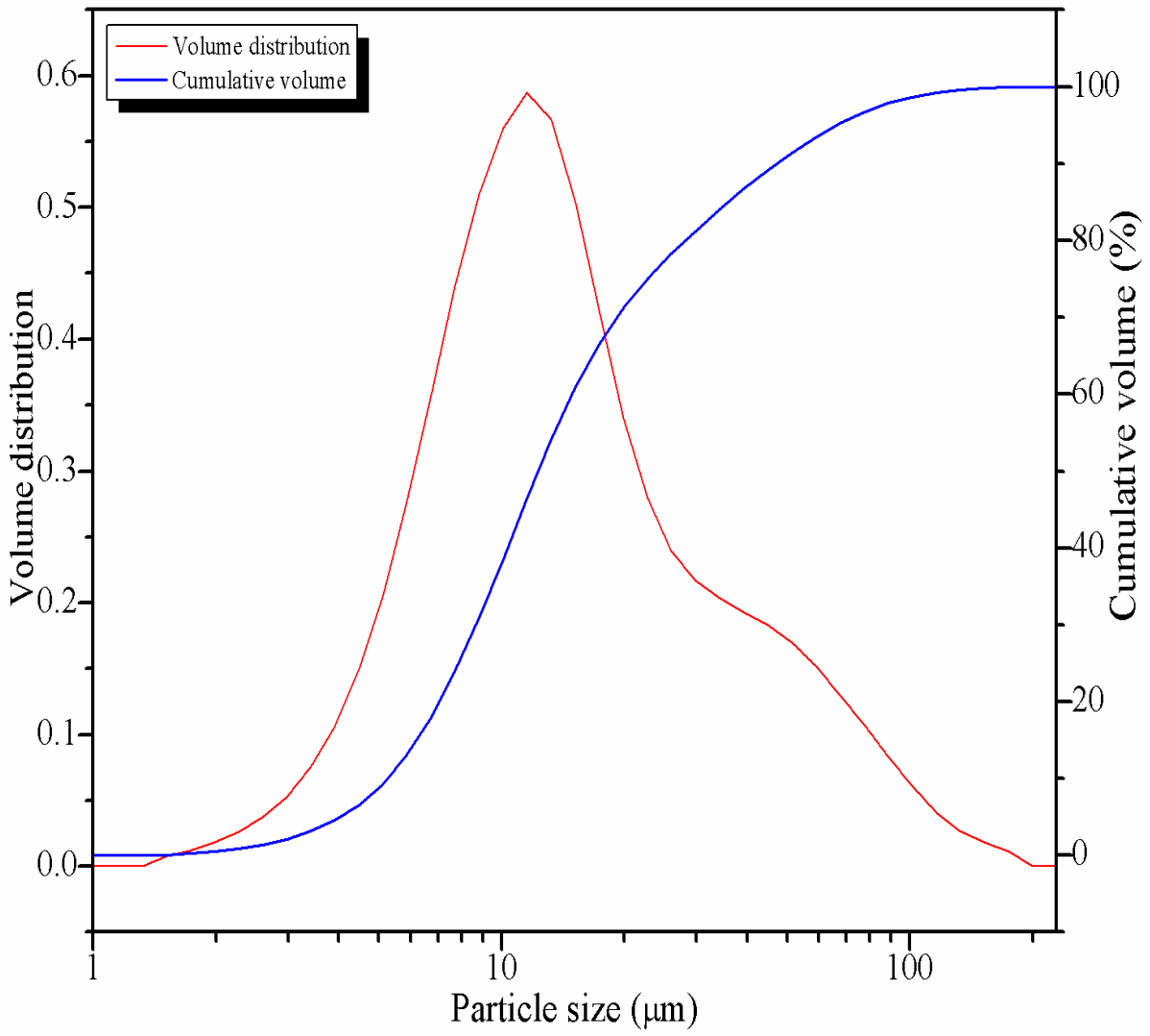

Figure 25: Particle size distribution of the kaolin (K).

Concerning the particle size distribution of MK as presented in Figure 26, it ranges as from 1 to 300 μm with the mean particle diameters at d_{10}=5.42 μm; d_{50}=12.62 μm and d_{90}=46.92 μm. Moreover, the volume distribution of MK (red curve) shows that the powder of metakaolin also has a bimodal distribution with the span value of 3.29 (Table III). The first mode varies as from 1 to 29.9 μm with the largest particle having a size of 11.57 μm whereas the second mode varies as from 29.9 to 300 μm. From the above, it appears that the distributions of both kaolin and metakaolin seem to be alike. They are mainly constituted of particles having small sizes, which are characteristics of clay minerals [80].

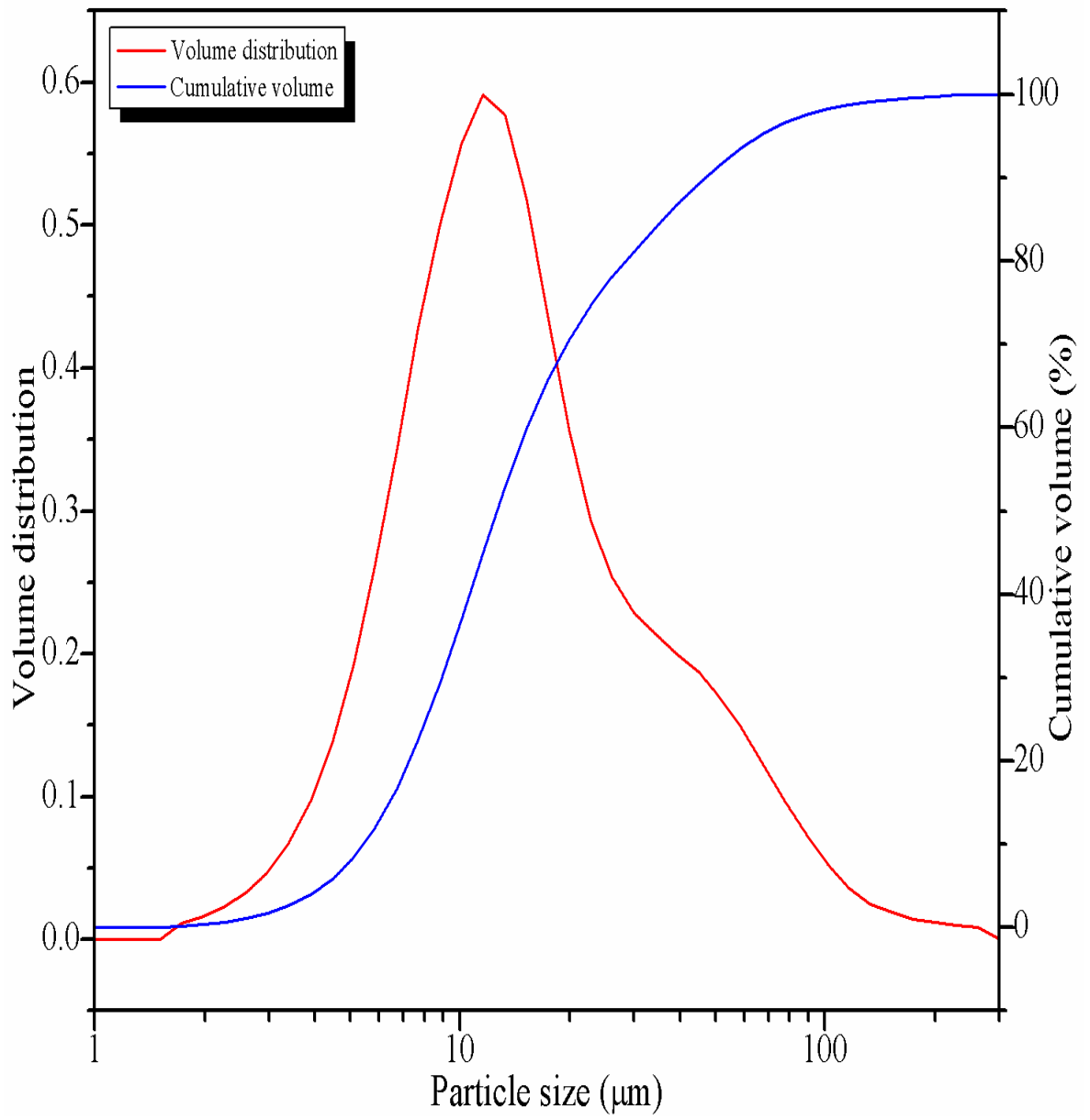

Figure 26: Particle size distribution of the metakaolin (MK).

As for the particle size distribution of Z as shown in Figure 27, it ranges as from 1 to 68 μm with the mean particle diameters at d_{10}=1.31 μm; d_{50}=6.80 μm and d_{90}=22.01 μm. In addition, the volume distribution of Z (red curve) shows that the powder of the volcanic scoria has a bimodal distribution with the span value of 3.04 (Table III). The first population varies as from 1 to 34 μm whereas the second population varies as from 34 to 68 μm with the largest particle having a size of 45 μm. Compared with kaolin and metakaolin distributions, it appears that the powder of volcanic scoria is mostly composed of particles having bigger sizes. Basically, kaolin and metakaolin could be more reactive than volcanic scoria during alkaline activation based on their particle size distributions [79].

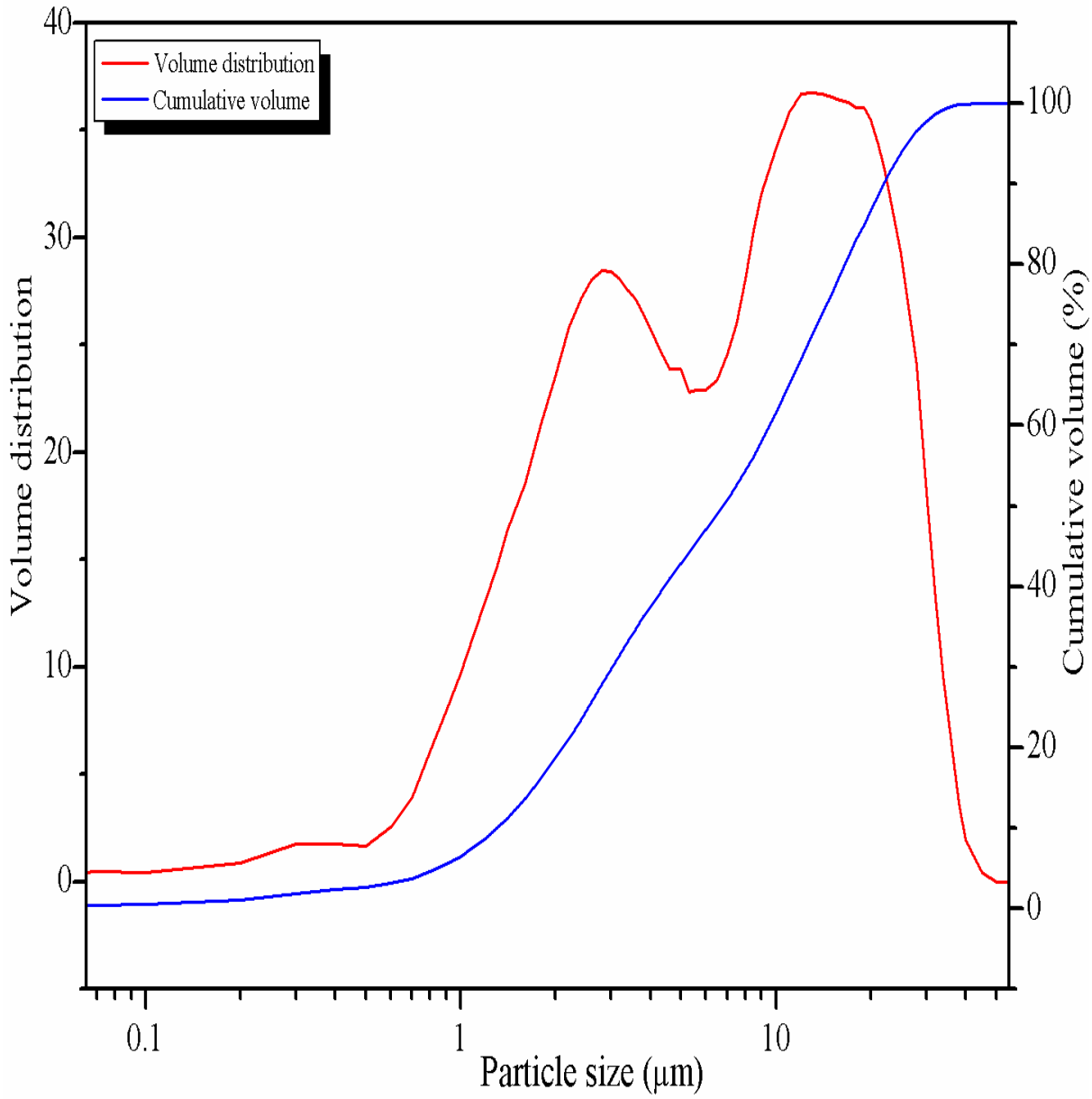

Figure 27: Particle size distribution of the volcanic scoria (Z).

Regarding the particle size distribution of A as presented in Figure 28, it ranges as from 0.1 to 262 µm with the mean particle diameters at d_{10}=2.47 µm; d_{50}=6.51 µm and d_{90}=21.25 µm. Besides, the volume distribution of A (red curve) shows that the powder of the amorphous aluminium hydroxide has a bimodal distribution with the span value of 2.88 (Table III). The first mode varies as from 0.1 to 26.11 µm with the largest particles having a size of 8.82 µm whereas the second mode varies as from 26.11 to 262 µm. This indicates that the amorphous aluminium hydroxide is mainly composed of particles having small sizes such as clay minerals [80].

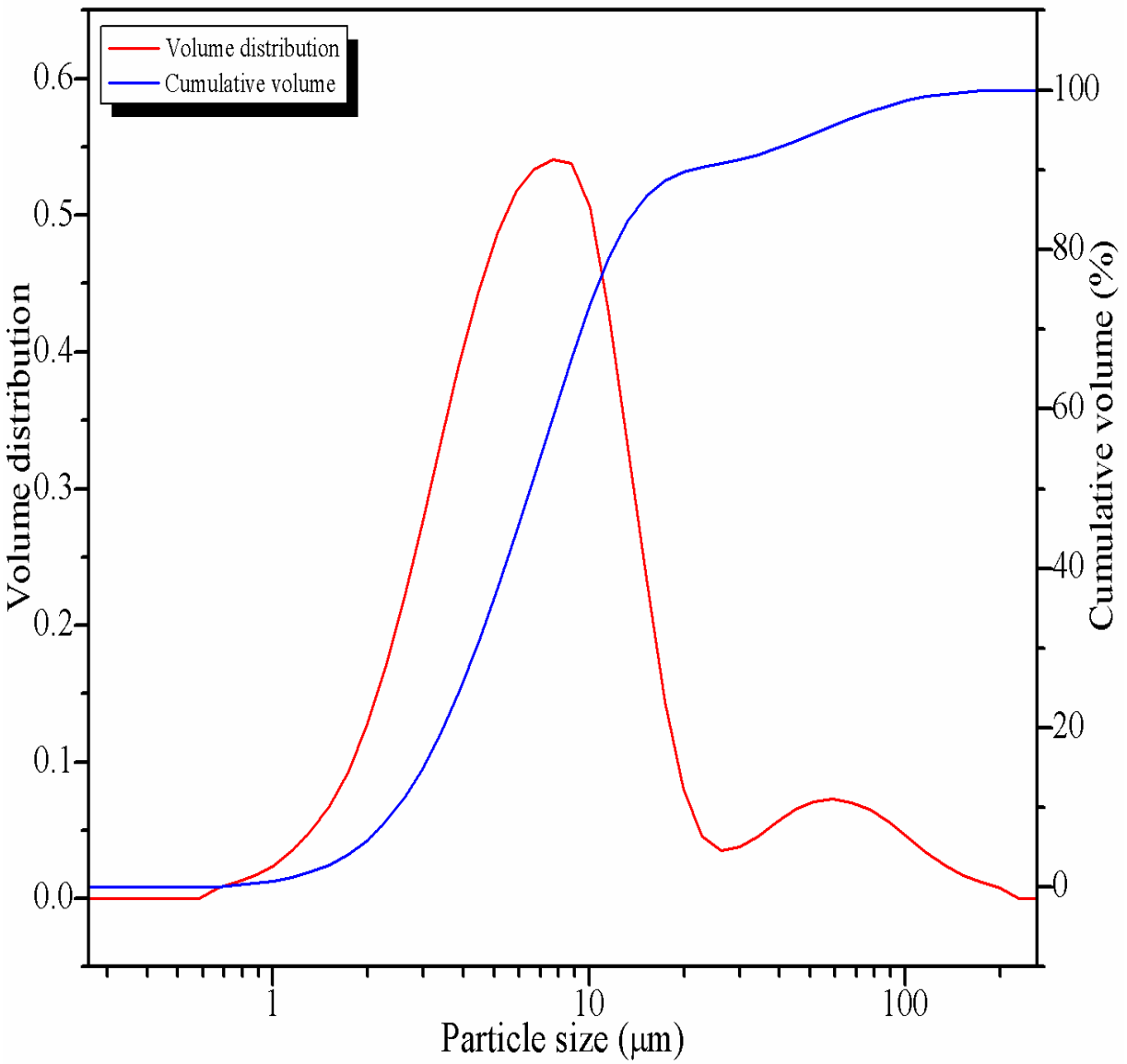

Figure 28: Particle size distribution of the amorphous aluminium hydroxide (A).

Referring to the particles size distribution of B (Figure 29), it ranges as from 0.1 to 344 μm with the mean particle diameters at d_{10}=1.68 μm; d_{50}=8.46 μm and d_{90}=46.03 μm. Also, the volume distribution of B (red curve) shows that the powder of the aluminium oxy-hydroxide has a tri-modal distribution with the span value of 5.24 (Table III). The first population varies as from 0.1 to 6.72 μm with the largest particles having a size of 2.98 μm. The second population varies as from 6.72 to 17.40 μm whereas the third population varies as from 17.40 to 344 μm with the largest particles having a size of 34.25 μm. Compared to the amorphous aluminium hydroxide, aluminium oxy-hydroxide is mostly composed of particles having bigger sizes as previously observed for the volcanic scoria sample.

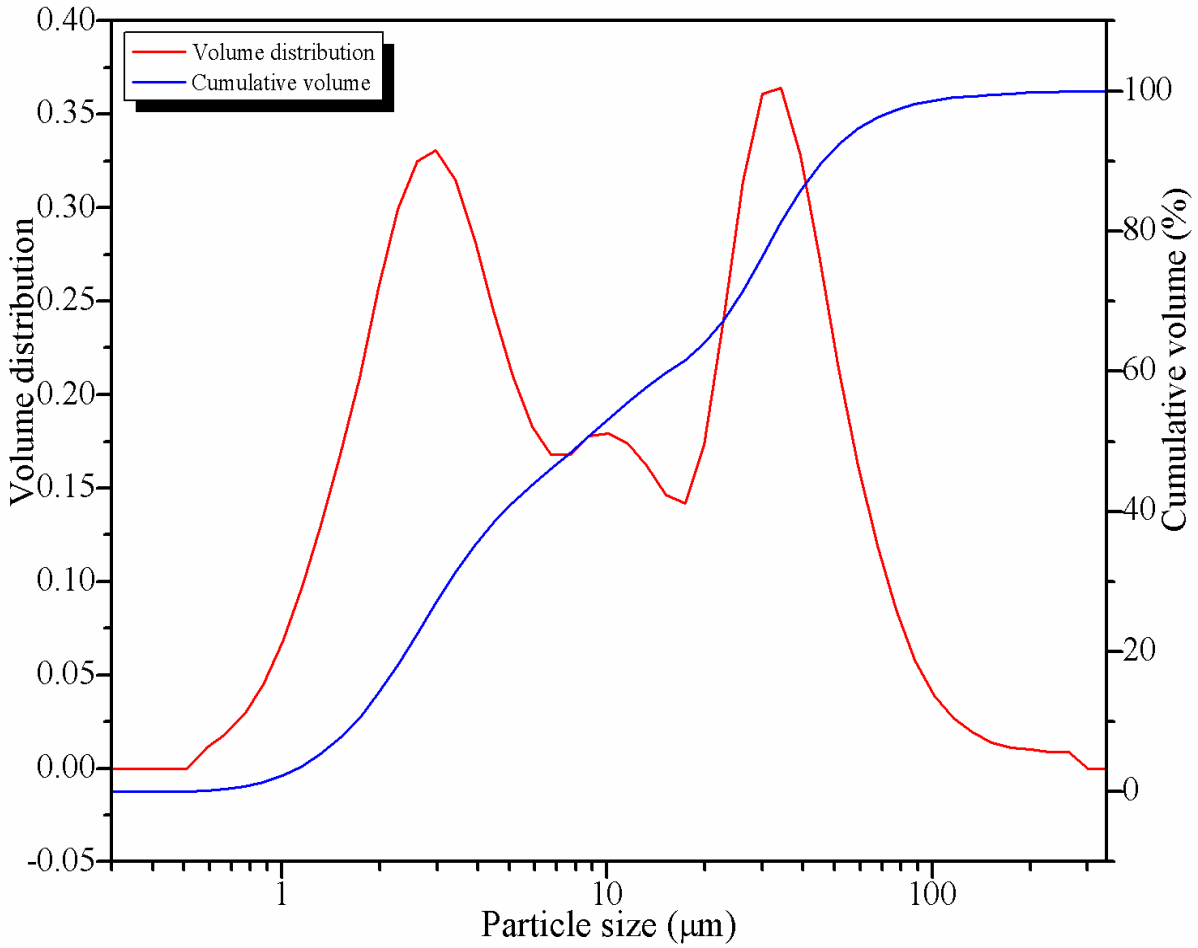

Figure 29: Particle size distribution of the aluminium oxy-hydroxide (B).

III.1.2 Specific surface area

The specific surface areas of the starting materials (K, MK, Z, A and B) determined thanks to the BET method are reported in Table IV. Pertaining to the aluminosilicate precursors, the specific surface areas of K, MK and Z are respectively 22.6; 28.2 and 15.7 m^2 / g. It appears that the specific surface area of MK is higher than those of K and Z respectively. It is worth recalling that the specific surface area of a material is a characteristic that has an influence on its degree of reactivity [81]. Thus, MK will be more reactive than K whereas K will be more reactive than Z, based on the specific surface area results. Additionally, these observations are in accordance with the particle size distributions.

As for alumina sources, the specific surface areas of A and B are respectively 60.9 and 286.2 m^2 / g. Theoretically, this shows that aluminium oxy-hydroxide could be approximately five times more reactive than amorphous aluminium hydroxide. Furthermore, the specific surface areas of alumina sources are higher than those of aluminosilicate precursors.

Thus, from the obtained results reported in Figures 25-29 and Table IV respectively, it appears that there is a correlation between particles size distributions and specific surface areas of the starting materials. So, as the particles size of a material is small, the corresponding specific surface area is high accordingly [82]. It is important to highlight that both particle size distribution and specific surface area of an aluminosilicate material have an impact during its alkaline activation. This is most likely due to the fact that a significant part of the reaction occurs at the particle-liquid interface [58]. As result of that, the smaller the particle size of a material, the higher the resulting specific surface area, the more the material is to be likely to react in the presence of an alkaline activator [38].

Table IV: Specific surface area of the starting materials.

Starting materials	Specific surface area (m^2 / g)
K	22.6
MK	28.2
Z	15.7
A	60.9
B	286.2

III.1.3 Chemical composition

The composition of the starting materials (K, MK, Z, A and B) determined by ICP / OES is reported in Table V.

Concerning K, its composition shows respectively SiO_2 and Al_2O_3 as major oxides, with the sum of SiO_2 + Al_2O_3 equals to 78.10 % by mass along with the molar ratio SiO_2 / Al_2O_3 of 1.61. This composition is suitable for using kaolin as feedstock for the synthesis of geopolymers as it is among the range of basic ingredients of raw materials required for alkaline activation [37, 83]. The minor oxides present are CaO, Fe_2O_3, Na_2O, K_2O, MgO, TiO_2, SO_3, P_2O_5 and Cr_2O_3 with a total sum of 2.36 % by mass. The presence of 1.10 % by mass of TiO_2 allows expecting that K may contain either rutile or anatase [84]. The little amount of K_2O (0.24 % by mass) indicates the presence of micaceous mineral (illite or muscovite) [85]. The value of the loss on ignition (18.75 % by mass) is above the theoretical value generally encountered for typical kaolinitic clay (13.96 % by mass) [23]. This shows that in addition to kaolinite mineral, K also contains aluminium hydroxide or oxy-hydroxide

compound due to the great amount of Al_2O_3 (40.10 % by mass) which accounts for the excess value of the loss on ignition (4.79 % by mass) [84].

As for MK, it also exhibits SiO_2 and Al_2O_3 as major oxides, with the sum of SiO_2 + Al_2O_3 equals to 93.50 % by mass along with the molar ratio SiO_2 / Al_2O_3 of 1.58. This enables metakaolin to be considered as good feedstock for the synthesis of geopolymers [37, 83]. The minor oxides present are CaO, Fe_2O_3, Na_2O, K_2O, MgO, TiO_2, SO_3, P_2O_5 and Cr_2O_3 with a total sum of 3.29 % by mass. The loss on ignition (2.81 % by mass) observed can be due either to the moisture as result of the fineness of metakaolin particles (Figure 26) or to the structural water of micaceous mineral [81, 86-87].

Regarding to Z, its chemical composition reveals that it is a basaltic material of scoria type as the SiO_2 content is less than 52.5 % by mass [37, 83]. The major oxides are SiO_2, Al_2O_3 and Fe_2O_3, with the sum of SiO_2+ Al_2O_3+ Fe_2O_3 equals to 69.90 % by mass and the molar ratio of SiO_2 / Al_2O_3 of 4.18. This composition is as well suitable for using it as feedstock for the synthesis of alkaline cements as it is among the range of basic ingredients of raw materials required for alkaline activation [37, 83]. The minor oxides present are CaO, Na_2O, K_2O, MgO, TiO_2, P_2O_5 and Mn_2O_3 with a total sum of 16.90 % by mass. The loss on ignition (11.10 % by mass) along with the undetermined (2.10 % by mass) can be attributed to the presence of organic matter and clay minerals [84].

Referring to A, its chemical composition shows that it is mainly composed of Al_2O_3 (57.40 % by mass) as major oxide associated among other with minor oxides such as SiO_2, Na_2O and P_2O_5 with a total sum of 1.37 % by mass. The loss on ignition evaluated at 41.23 % by mass is not very far from the theoretical value (34.62 % by mass) encountered for standard aluminium hydroxide [23]. Despite, the difference between the obtained and the theoretical values (6.61 % by mass) may be attributed to the amorphous nature of aluminium hydroxide along with the fact that it is mostly composed of particles having small sizes (Figure 28) which enables to capture the moisture [88-89].

Pertaining to B, it contains 81.38 % by mass of Al_2O_3 as major oxide associated among other with minor oxides such as SiO_2, Na_2O, SO_3 and P_2O_5 with a total sum of 1.52 % by mass. Its loss on ignition is 17.10 % by mass which is not very far from the theoretical value (15 % by mass) encountered for pure aluminium oxy-hydroxide [66]. Despite, the excess amount (2.10 % by mass) observed can be attributed to the fineness of the particles of aluminium oxy-hydroxide which enables to capture the moisture [66].

From the above, both A and B can be used to replace the aluminosilicate precursors (K, MK and Z) so as to vary the SiO_2 / Al_2O_3 molar ratio in order to obtain mixtures whose

alkaline activation can converts into a binder with improved characteristics either after ambient temperature curing or after elevated temperature exposure [82, 90].

Table V: Chemical composition of starting materials (LOI: Loss On Ignition at 1000 °C).

Oxides	K	MK	Z	A	B
SiO_2	38.00	45.10	40.10	0.21	1.02
Al_2O_3	40.10	48.40	16.30	57.40	81.38
Fe_2O_3	0.70	0.86	13.50	-	-
CaO	0.05	0.63	6.30	-	-
Na_2O	0.04	0.03	0.80	0.95	0.30
K_2O	0.24	0.25	0.50	-	-
MgO	0.13	0.17	5.30	-	-
TiO_2	1.10	1.23	3.20	-	-
SO_3	0.01	0.01	-	-	0.08
P_2O_5	0.07	0.09	0.60	0.11	0.06
Cr_2O_3	0.02	0.02	-	-	-
Mn_2O_3	-	-	0.20	-	-
LOI	18.75	2.81	11.10	41.23	17.10
$SiO_2 + Al_2O_3$	78.10	93.50	56.40	57.61	82.40
Total	99.21	99.60	97.90	99.90	99.96

III.1.4 Mineralogical composition

The XRD patterns of the starting materials (K, MK, Z, A and B) determined by X-ray powder diffraction between 5 and 70 ° (2θ) are shown in Figure 30.

Concerning K, it contains the following crystalline phases: kaolinite [$Al_2Si_2O_5(OH)_4$: PDF# 14–164]; gibbsite [$Al(OH)_3$: PDF# 33–18]; quartz [SiO_2: PDF# 46–1045]; anatase [TiO_2: PDF# 21–1272] and illite -2M1 [$(K,H_3O)(Al,Mg,Fe)_2(Si,Al)_4O_{10}[(OH)_2,(H_2O)]$]: PDF# 26–911)].

As for MK which is the output product of thermal treatment of the kaolin (K), it contains quartz, anatase and illite as crystalline phases. Besides, the halo peak observed between 15-40 ° 2θ is characteristic of the reactive amorphous phase contained into the metakaolin [79]. Though, the absence of both kaolinite and gibbsite minerals is attributed to their thermal transformations [84]. Conversely, the presence of illite in MK accounts for the loss on ignition observed on its chemical composition (Table V) [87].

Regarding to Z, it contains the following crystalline phases: forsterite ferroan [$Mg_{1,42}Fe_{0,58}(Si_{0,99}Al_{0,01})O_4$: PDF# 87-0619)]; anorthite ordered [$Ca_{0,66}Na_{0,34}Al_{1,66}Si_{2,34}O_8$: PDF# 12-0301]; anorthoclase [$Na_{0,85}K_{0,15}(AlSi_3O_8$): PDF# 75-1635]; diopside [$(Ca_{0,89}Mg_{1,11}Si_2O_6)$: PDF# 87-0698]; augite [$(Ca,Na)(Mg,Fe,Al)(Si,Al)_2O_6$: PDF# 24-201]; hematite [Fe_2O_3: PDF# 89-0596]; maghemite [γ-Fe_2O_3: PDF# 89-5894]; allophane [$SiO_2.Al_2O_3.H_2O$: PDF#02-0039] and anatase [TiO_2: PDF# 21–1272]. The broad hump observed between 20-45 ° 2θ is characteristic of the glassy phase contained into the volcanic scoria [37].

Pertaining to alumina sources, amorphous aluminium hydroxide (A) is totally amorphous whereas aluminium oxy-hydroxide (B) is semi-crystalline and mainly contains boehmite [γ-AlO(OH): PDF# 21–1307] as crystalline phase.

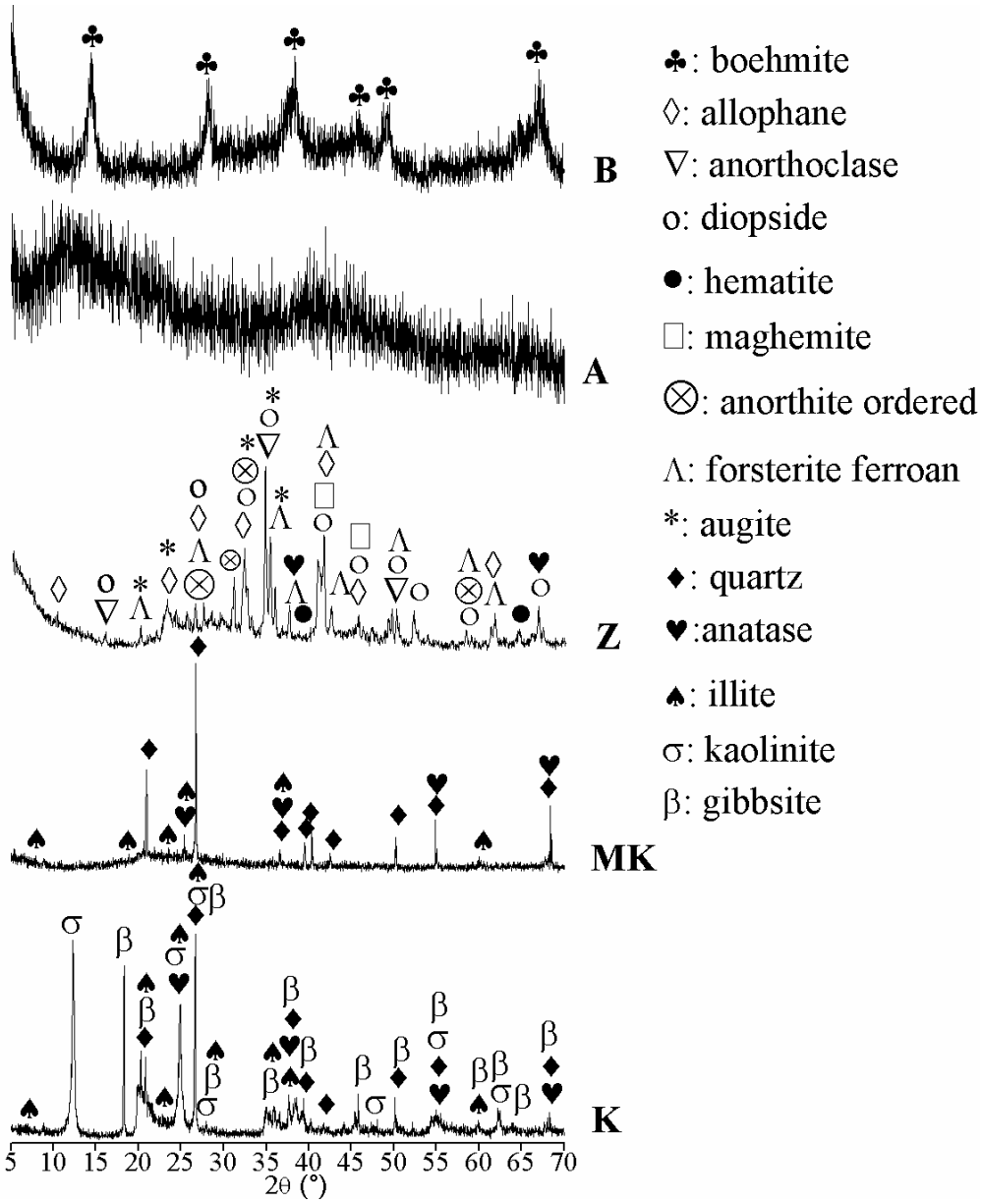

Figure 30: XRD patterns of the starting materials (K: kaolin; MK: metakaolin; Z: volcanic scoria; A: amorphous aluminium hydroxide; B: aluminium oxy-hydroxide).

III.1.5 FTIR spectra

FTIR spectra of the starting materials (K, MK, Z, A and B) are presented in Figure 31.

Pertaining to K, the peaks observed within the range of 3688–3625 cm^{-1} are attributed to the stretching vibrations of structural –OH groups of kaolinite network [91-92]. Those appearing around 3520, 3488 and 3421 cm^{-1} respectively are associated with the structural -OH stretching vibration modes of gibbsite [66, 93]. The band around 1042 cm^{-1} is attributed to the Si-O-Si in-plane stretching vibration of kaolinite network [93]. The peak around 909 cm^{-1} is attributed to the Al(VI)–OH stretching vibration of kaolinite network [81] whereas the one around 794 cm^{-1} is attributed to the Al(IV)–O stretching vibration of gibbsite network [94]. The peaks at the range of 726–677 cm^{-1} are attributed to Si–O–Si and Si–O–Al symmetric stretching vibrations of the kaolinite network [94]. The absorption peak around 549 cm^{-1} is attributed to Al-OH vibrations of Al in six fold coordination, probably due to the presence of illite [95-96] whereas those appearing at the range of 471–431 are attributed to Si–O–Si and O–Si–O bending vibrations of quartz [97]. These absorptions peaks confirm the crystalline phases observed on the mineralogical composition of the kaolin sample (Figure 30).

As for MK, the absence of the structural O–H stretching vibrations initially observed at the range of 3688–3625 cm^{-1} and 3520–3421 cm^{-1} for both kaolinite and gibbsite networks respectively, confirms that the dehydroxylation occurs during thermal activation of the kaolin sample [66, 81, 84]. Nevertheless, the weak bands around 3400 cm^{-1} and 1680 cm^{-1} are attributed to the O-H stretching and bending vibrations respectively of absorbed water molecules [97-98]. This is due to the high fineness and sheet-like structure of metakaolin particles and the corresponding high specific surface area which enables to capture the moisture [86]. The peak around 1077 cm^{-1}characteristic of Si–O–Si stretching vibration has become broad, indicating the presence of amorphous silica [97, 99]. The peak around 794 cm^{-1} characterising the Al(IV)–O stretching vibration has also become broad, showing the efficiency of thermal activation to convert Al(VI) contained in the kaolin sample into Al(IV) in high concentration in the resulting reactive metakaolin [80, 97]. The peak around 462 cm^{-1} is attributed to Si–O–Si and O–Si–O bending vibrations of quartz, showing that it is not significantly affected by thermal activation [94].

Regarding to Z, the peaks appearing at the range of 3700–3622 cm^{-1} are attributed to the structural O–H stretching vibrations as result of the existence of phyllosilicates such as

allophane present in the volcanic scoria sample [100]. The bands around 3420 and 1631 cm^{-1} are characteristic stretching and bending vibrations, respectively, of O–H bonds of silanol and absorbed water molecules [37, 83]. The band located around 1037 cm^{-1} is ascribed to Si–O–T (T: Si or Al) of aluminosilicate framework [83]. The peak around 909 cm^{-1} is attributed to Al(VI)–OH stretching vibration whereas the one around 545 cm^{-1} is assigned to Si–O–Al(VI) bending vibration of silicate network [97]. The peak located at 469 cm^{-1} corresponds to the bending vibration of Si–O–Fe bond [51, 83].

Referring to A, the significant broad band at 3480 cm^{-1} is due to the hydrogen bonding between adjacent layers of aluminium hydroxide framework, thereby justifying its amorphous nature [101]. The broad band appearing around 1630 and 1526 cm-^{1} are characteristic of H–O–H bending vibration bonds of absorbed water molecules whereas the one around 1426 cm^{-1} is attributed to asymmetric vibration of Al–O bonds [20]. The peak located at 857 cm^{-1} is attributed to the out-of-phase v(OH) bending vibration whereas the one at 562 cm^{-1} is attributed to the bending vibration mode of AlO_6 unit [66, 101].

Regarding to B, the significant broad band around 3420 cm^{-1} is attributed to the hydrogen bonding between adjacent layers of aluminium oxy-hydroxide (boehmite) network [101]. The peak appearing around 3085 cm^{-1} is ascribed to v(OH) stretching vibration of boehmite network [101]. The peak located at 1637 cm^{-1} corresponds to O–H bending vibration of absorbed water molecules whereas the one around 1390 cm^{-1} is assigned to the asymmetric vibration of Al–O [20]. The peak observed at 1080 cm^{-1} corresponds to Al–OH bending vibration, characteristic of boehmite [66, 101]. The peak located at 731 cm^{-1} corresponds to the out-of-plane v(OH) bending vibration whereas those at 603 and 485 cm^{-1} respectively are attributed to the bending vibration modes of AlO_6 units [101].

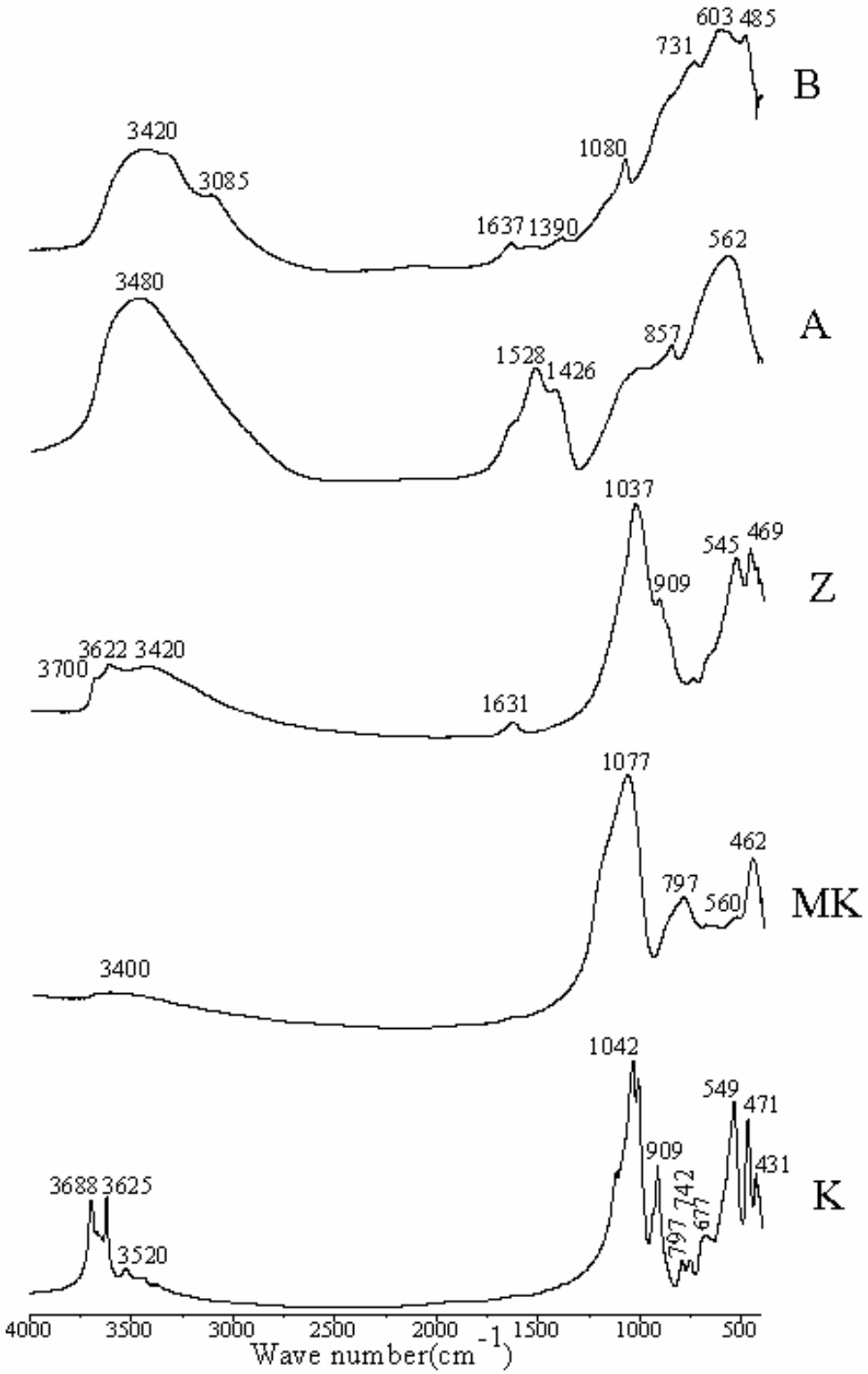

Figure 31: IR spectra of the starting materials.

III.1.6 Thermal behaviour

The thermal behaviour followed by DTA / TG / DTG analyses of the starting materials (K, Z, A and B) are presented in Figures 32-35 respectively.

Concerning K as presented in Figure 32, its DTA curve (black curve) exhibits three endothermic phenomena and one exothermic phenomenon whereas TG / DTG curves (red / blue curves) show three mass losses. The first one corresponds to the loss of free water and it is expressed by an endothermic peak with maximum around 42 °C [84]. The second one refers to thermal decomposition of gibbsite (Equation (E10)) and this is expressed by an endothermic peak around 274 °C [23, 88, 101]. The third mass loss (~10.5 % by mass) accounts for the dehydroxylation of kaolinite to form metakaolinite (Equation (E11)) which is expressed by an endothermic peak with maximum around 500 °C [72, 81]. Additionally, metakaolinite is exothermically transformed into mullite / spinel phase (Equation (E12)) around 975 °C [23, 81, 102-103]. DTA / TG / DTG analyses allow to confirm that kaolinite and gibbsite minerals are the major phases in the kaolin sample (K).

$$Al_2O_3.3H_2O \longrightarrow Al_2O_3 + 3H_2O \quad \text{(E10)}$$

$$2SiO_2.Al_2O_3.2H_2O \longrightarrow 2SiO_2.Al_2O_3 + 2H_2O \quad \text{(E11)}$$

$$2SiO_2.Al_2O_3 \longrightarrow 1/3(3Al_2O_3.2SiO_2) + 4/3SiO_2 \quad \text{(E12)}$$

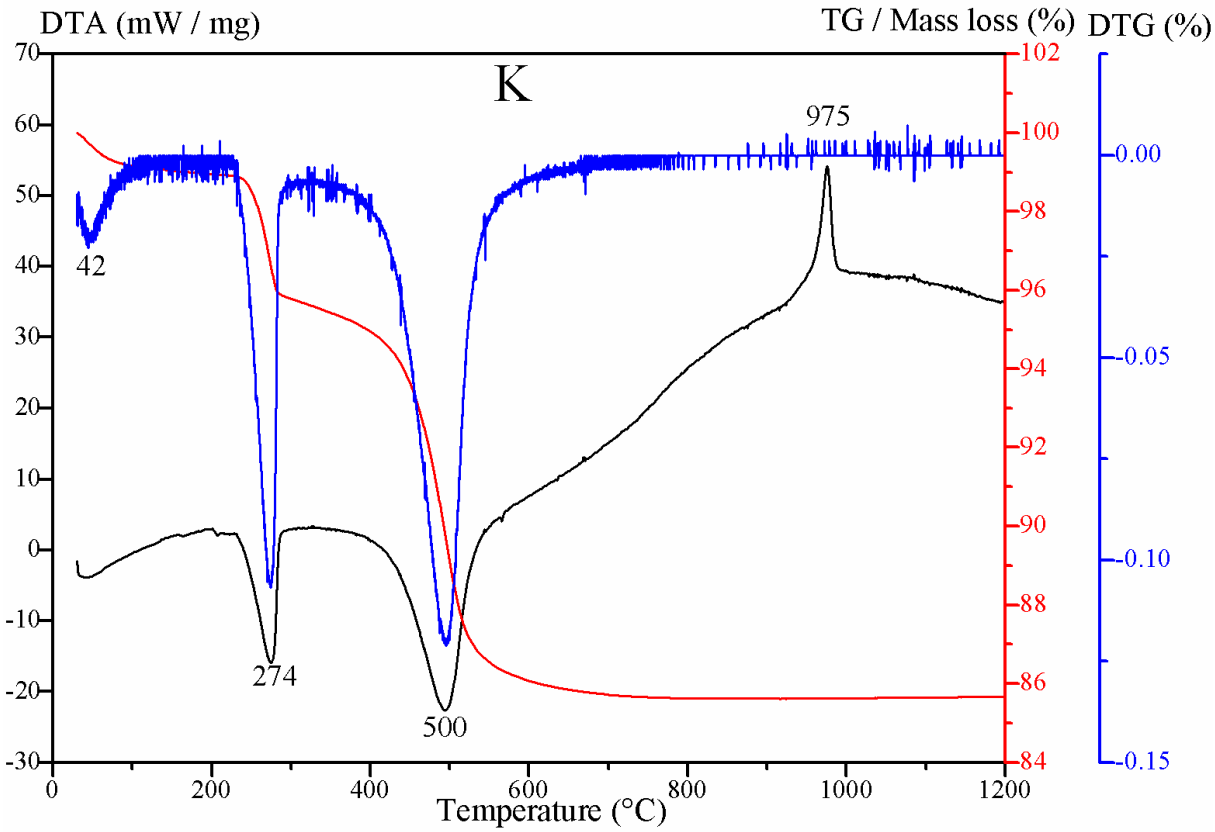

Figure 32: DTA / TG / DTG curves of the kaolin sample (K).

As for Z as shown in Figure 33, its DTA curve (black curve) shows three endothermic phenomena and two exothermic phenomena whereas TG / DTG curves (red / blue curves) exhibit two mass losses. The first one is attributed to the loss of free water which is very common in the aluminosilicate glasses and it is expressed by an endothermic peak with maximum around 64 °C [37]. The second one corresponds to the thermal decomposition of organic matter which is expressed by a broad exothermic band with maximum around 300 °C [84]. The third one is assigned to the thermal decomposition of allophane (second mass loss) (Equation (E13)) and this is expressed by an endothermic peak with maximum around 425 °C [104]. The fourth one corresponds to the densification of the volcanic scoria thanks to the increase melting of alkali and this is expressed by a broad exothermic phenomenon with maximum around 875 °C [15]. The fifth one is attributed to the melting of the volcanic scoria and this expressed by an endothermic peak observed as from 950 to 1200 °C [105]. DTA / TG / DTG analyses allow to confirm that allophane is the only hydrated crystalline phase as initially observed on the mineralogical composition of the volcanic scoria sample (Figure 30).

$$SiO_2.Al_2O_3.H_2O \longrightarrow SiO_2.Al_2O_3 + H_2O \qquad \text{(E13)}$$

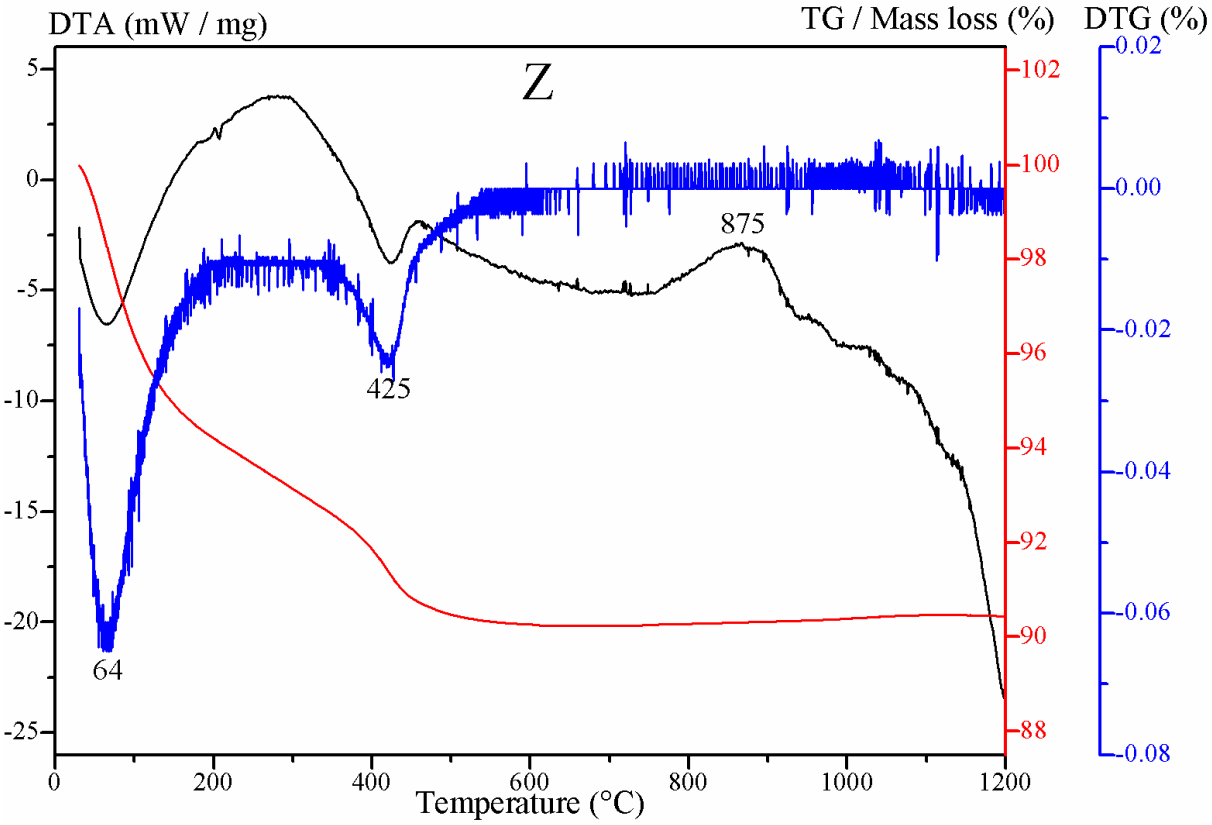

Figure 33: DTA / TG / DTG curves of the volcanic scoria sample (Z).

Regarding to A as depicted in Figure 34, its DTA curve (black curve) exhibits three endothermic phenomena and one exothermic phenomenon whereas TG / DTG curves (red / blue curves) show two mass losses. The first mass loss is of about 35 % by mass and is very close to 34.6 % by mass which is the theoretical value for typical pure aluminium hydroxide [23]. The latter is related to hydration, zeolithic and structural water as consequence of its transformation into aluminium oxy-hydroxide (Equation (E14)) and this is expressed by a large endothermic signal observed between 50 and 300 °C with maximum around 124 °C [20, 103, 106-107]. The second one testifies the presence of aluminium oxy-hydroxide formed as an intermediate and this is expressed by an endothermic dome displayed between 350 and 750 °C on the DTA curve [107]. The third one (beginning at 776 °C on DTG curve) accounts for the final dehydroxylation of aluminium oxy-hydroxide (~5 % by mass of mass loss) to give $\gamma - Al_2O_3$ (Equation (E15)) and this is expressed by an endothermic peak observed with maximum around 878 °C [101]. The fourth one is attributed to the thermal transformation of the obtained $\gamma - Al_2O_3$ into α-Al_2O_3 (corundum) (Equation (E16)) and this is established by the broad exothermic band on DTA with maximum around 1050 °C [23, 101]. Thus, DTA / TG / DTG analyses of amorphous aluminium hydroxide shows that its thermal transformation leads to the most stable form of aluminium oxide (α-Al_2O_3) known as corundum as from 900 to 1200 °C [22-23].

$$Al_2O_3.3H_2O \longrightarrow \gamma Al_2O_3.2H_2O + H_2O \quad \text{(E14)}$$

$$\gamma Al_2O_3.2H_2O \longrightarrow \gamma Al_2O_3 + 2\,H_2O \quad \text{(E15)}$$

$$\gamma Al_2O_3 \longrightarrow \alpha Al_2O_3 \quad \text{(E16)}$$

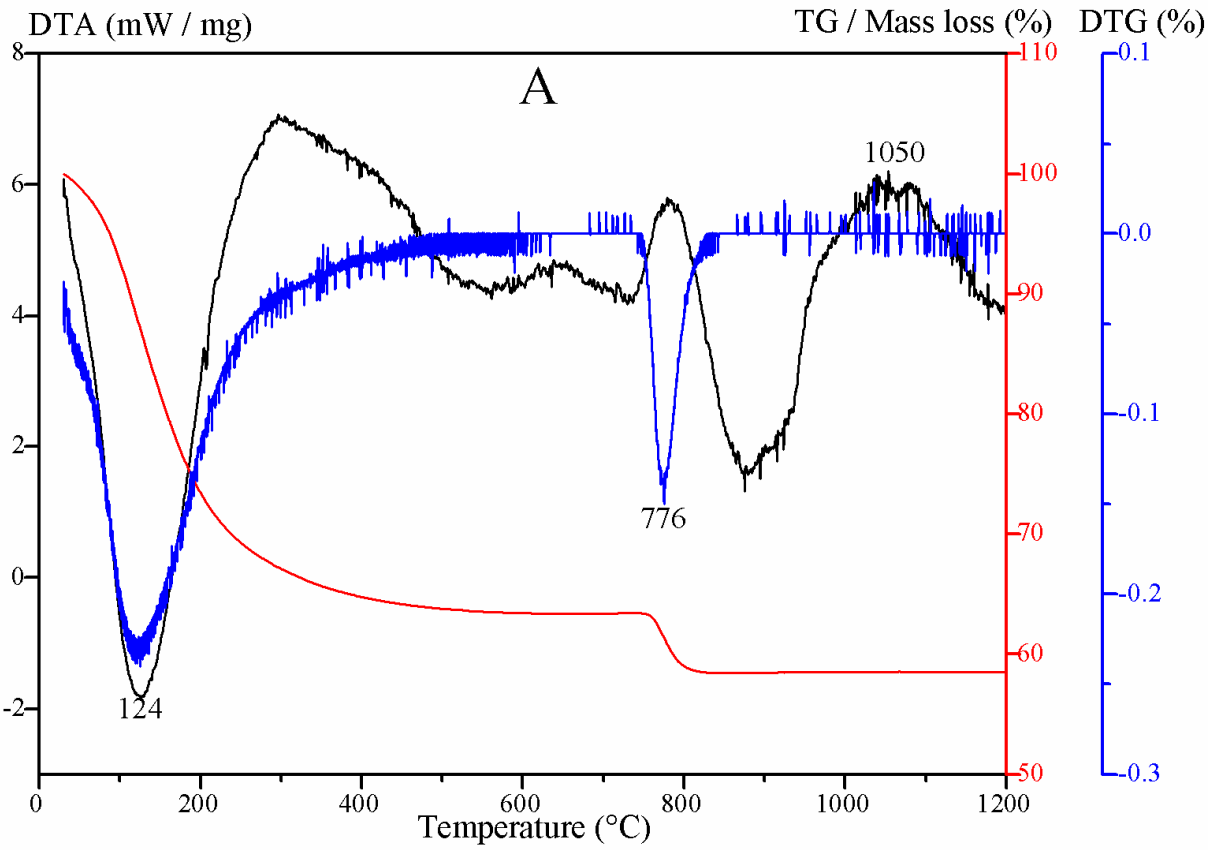

Figure 34: DTA / TG / DTG curves of the amorphous aluminium hydroxide (A).

Referring to B presented in Figure 35, its DTA curve (black curve) presents three endothermic phenomena and one exothermic phenomenon whereas TG / DTG curves (red / blue curves) exhibit two major mass losses. The first one (~10 % by mass of mass loss) corresponds to hydration and bound water expressed by the presence of an endothermic peak with maximum around 60 °C [84, 103]. The second one is attributed the onset loss of structural water from aluminium oxy-hydroxide and this is expressed by an endothermic peak with maximum observed around 210 °C [107]. The third one (~7 % by mass of mass loss) is ascribed for the final dehydroxylation of aluminium oxy-hydroxide (B) to give $\gamma - Al_2O_3$ (Equation (E15)) and this is established by an endothermic peak observed with maximum around 430 °C [88, 103]. The fourth one corresponds to the thermal transformation of the obtained $\gamma - Al_2O_3$ into α-Al_2O_3 (corundum) (Equation (E16)) between 900 and 1200 °C and this is established by a broad exothermic band on DTA curve with maximum around 1050 °C [23, 101]. Thus, the thermal transformation of aluminium oxy-hydroxide also leads to the most stable form of aluminium oxide (α-Al_2O_3) known as corundum as from 900 to 1200 °C [22-23].

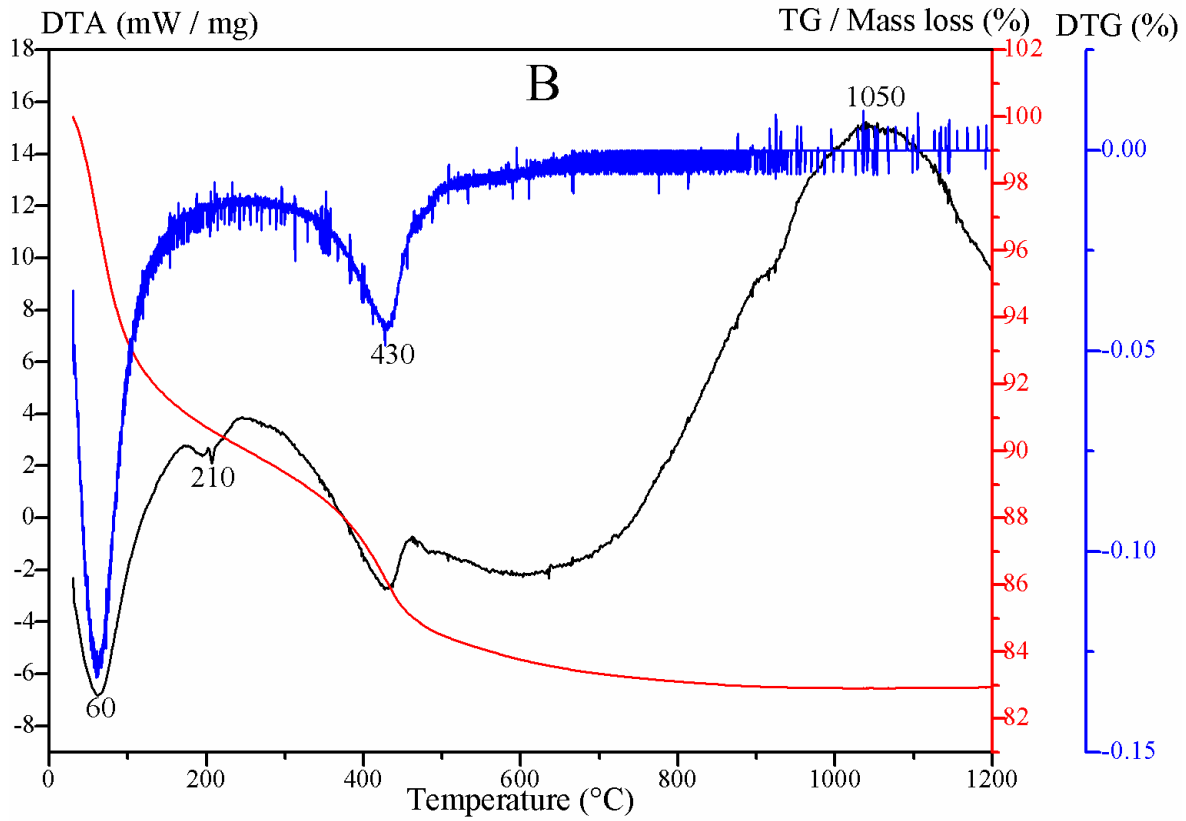

Figure 35: DTA / TG / DTG curves of the aluminium oxy-hydroxide (B).

III.1.7 Conclusion

The aim of this first section was to characterise the starting materials in order to determine their suitability to be used as feedstock materials for the synthesis of alkaline cements. Particle size distribution and specific surface area revealed that kaolin, metakaolin and amorphous aluminium hydroxide contained great amount of fine particles as compared to volcanic scoria and aluminium oxy-hydroxide which instead showed great amount of bigger particles. Moreover, chemical and mineralogical analyses revealed that kaolin and metakaolin as result of their high amount of SiO_2 and Al_2O_3 (>70 % by mass) appear to be good feedstock materials for the synthesis of alkaline cements compared to volcanic scoria (56.40 % by mass). However, the use of alumina sources as result of their high content of Al_2O_3 as partial replacements can help to compensate this deficiency so as to obtain a binder material endowed with improved fired characteristics.

III.2 Influence of amorphous aluminium hydroxide and aluminium oxy-hydroxide on the thermal stability of kaolin-based geopolymers

III.2.1 Flowability behaviour of kaolin-based geopolymer pastes

Figure 36 depicts the flowability of kaolin-based geopolymer pastes expressed in terms of replacement content and liquid to solid mass ratio (L / S). L / S of 0.86 was suitable for GK which was considered as the reference mixture. The same value of liquid to solid mass ratio was suitable for the mixtures GK_B^{10}, GK_B^{20} and GK_B^{30} with aluminium oxy-hydroxide as replacement. They displayed good flowability and were consistent and homogeneous mixtures of particles during and after moulding. As for the mixtures with amorphous aluminium hydroxide as replacement, L / S of 1.17 was suitable for GK_A^{10} whereas L / S of 1.51 and 1.84 were respectively tested for GK_A^{20} and GK_A^{30} but this did not allow consolidated specimens. Actually, the difference between the two replacements pertaining to the mass ratio L / S can be ascribed either to the particle size distribution or to the ability of particles to absorb the activating solution. For instance, the particle size distribution of amorphous aluminium hydroxide shows the presence of great amount of fine particles (Figure 28) as compared to that of aluminium oxy-hydroxide (Figure 29), meanwhile contact angle of the former is smaller than the latter, thereby requiring greater amount of activating solution to achieve good wettability. It is worth noting that the specimens of GK_A^{20} and GK_A^{30} were not well consolidated even after 7 days of curing at 60 °C. This suggested that excess of amorphous aluminium hydroxide may hinder the extent of the formation of the polysialate network [59, 85].

Hence, partial replacement of kaolin by 30 % by mass of aluminium oxy-hydroxide or by 10 % by mass of amorphous aluminium hydroxide gave suitable mix designs that led to consolidated kaolin-based geopolymers with good flowability. For further assessment in this study, microstructural and mineralogical characterisations were performed only for GK, GK_A^{10} and GK_B^{30}.

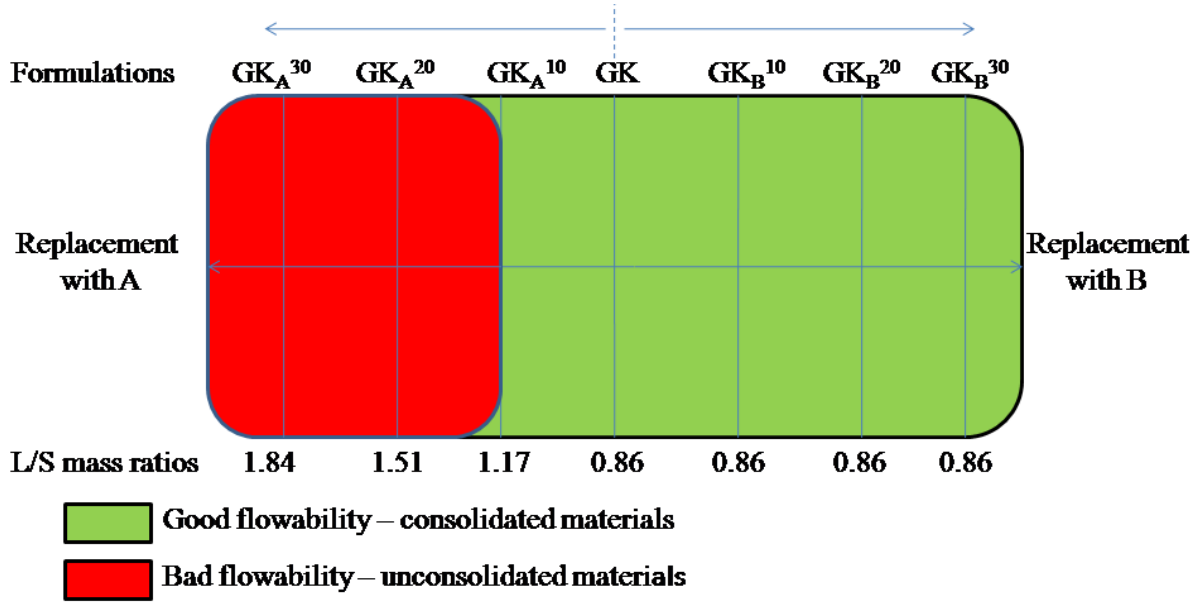

Figure 36: Flowability of the kaolin-based geopolymer pastes.

III.2.2 Thermal behaviour of hardened kaolin-based geopolymers

Thermal behaviour followed by DTA / TG / DTG analyses of the selected hardened kaolin-based geopolymers (GK, GK_A^{10} and GK_B^{30}) are presented in Figures 37-39 respectively.

TG / DTG curves of the kaolin-based geopolymers (GK, GK_A^{10} and GK_B^{30}) present three mass losses (Figures 37-39). The first mass loss is attributed to free water absorbed or entrapped in large cavities of geopolymer framework and this is highlighted by an endothermic peak at the range of 85-90 °C [20, 60]. The second one is assigned to thermal decomposition of gibbsite, combined with partial dehydration and dehydroxylation of replacements (A or B) highlighted by an endothermic peak at the range of 263-270 °C which is very close to the value observed with typical pure gibbsite [73, 95]. The third mass loss is related to both the breakdown of residual kaolinite network and the complete transformation of aluminium oxy-hydroxide formed as an intermediate to give $\gamma - Al_2O_3$ [67, 101]. The broad endothermic peaks observed between 350 and 700 °C account for dehydration of geopolymer gel and dehydroxylation of the replacements (A and B) respectively [101, 103]. Referring to GK, GK_A^{10} and GK_B^{30}, the above-mentioned phenomena show a maximum at around 621, 575 and 473 °C respectively on their DTG curves. This is due to the thermal decomposition of the intermediate aluminium oxy-hydroxide of the amorphous aluminium hydroxide (A) along with the residual kaolinite [67, 101]. Between 900 and 1200 °C, the DTA curves of the kaolin-based geopolymers exhibit a broad exothermic dome without mass change, related to structural reorganisation along with crystallisation of phases such as mullite

and corundum which are respectively classical output products of thermal treatment of the starting materials (K, A and B), coupled to sintering / densification [61, 103, 108]. Regarding the samples GK_A^{10} and GK_B^{30}, the intensity of their peaks which are characteristic of maximum packing of particles is more pronounced [61]. This evidences the presence of thermal inert phases (mullite and corundum) in large quantity which contribute in improving their microstructures [23]. Conversely with GK (Figure 37), the intensity of its dome is weak, attesting low amount of thermal inert phases. Moreover, the dome of GK undergoes a deflection around 1120 °C which is ascribed to excessive sintering along with possible melting [18, 20], which induces cracks, warping, swelling and this could lead to damaged structure. Conversely, GK_A^{10} and GK_B^{30} are thermally stable between 900-1200 °C as illustrated by the thermal behaviour (Figures 38-39). Hence, using either amorphous aluminium hydroxide or aluminium oxy-hydroxide as replacements for the synthesis of kaolin-based geopolymers allows improvement of thermal stability of the heated products.

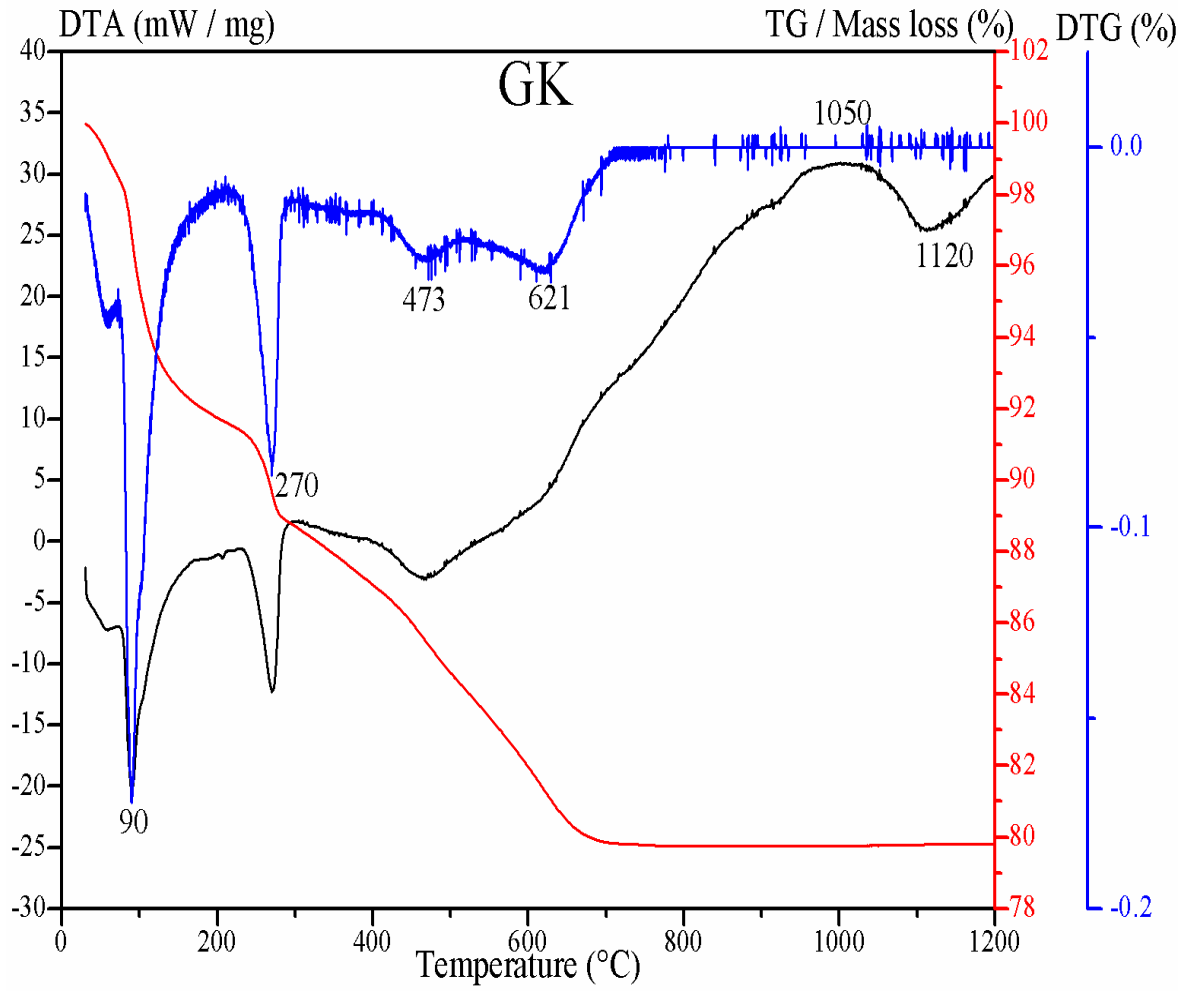

Figure 37: DTA / TG / DTG curves of the kaolin-based geopolymer (GK) initially cured at 60 °C.

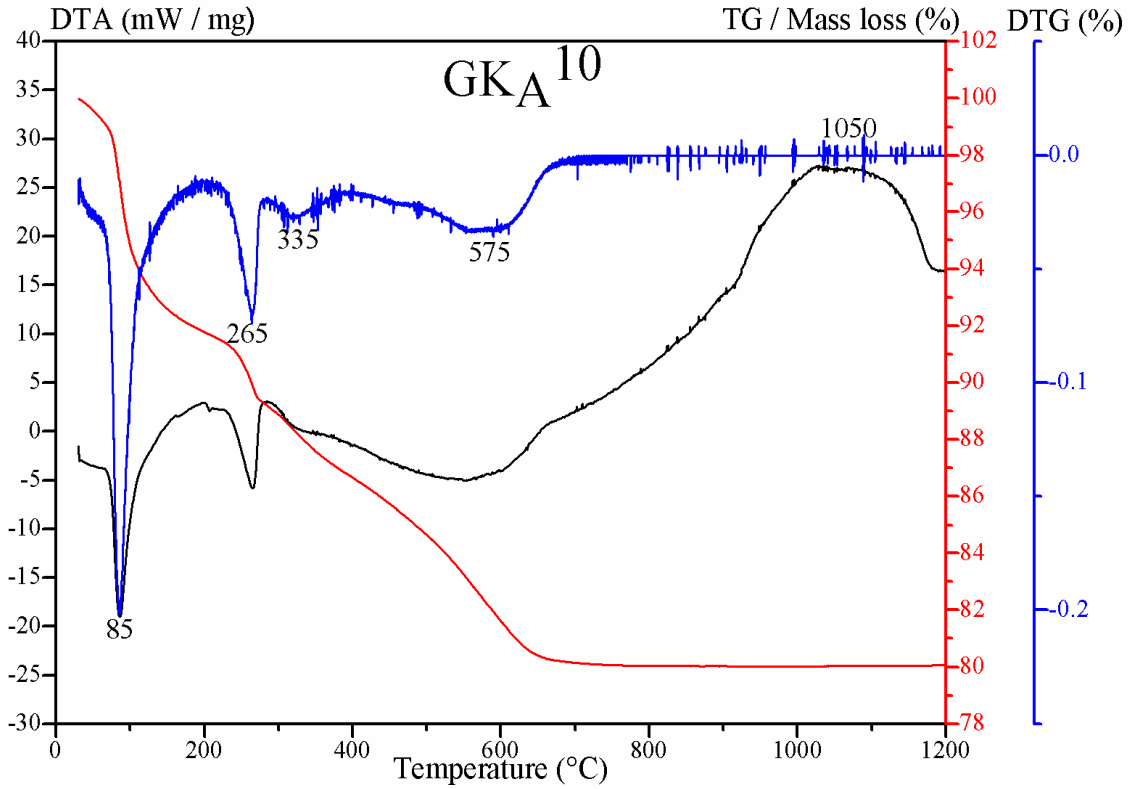

Figure 38: DTA / TG / DTG curves of the kaolin-based geopolymer obtained with partial replacement of amorphous aluminium hydroxide (GK_A^{10}) initially cured at 60 °C.

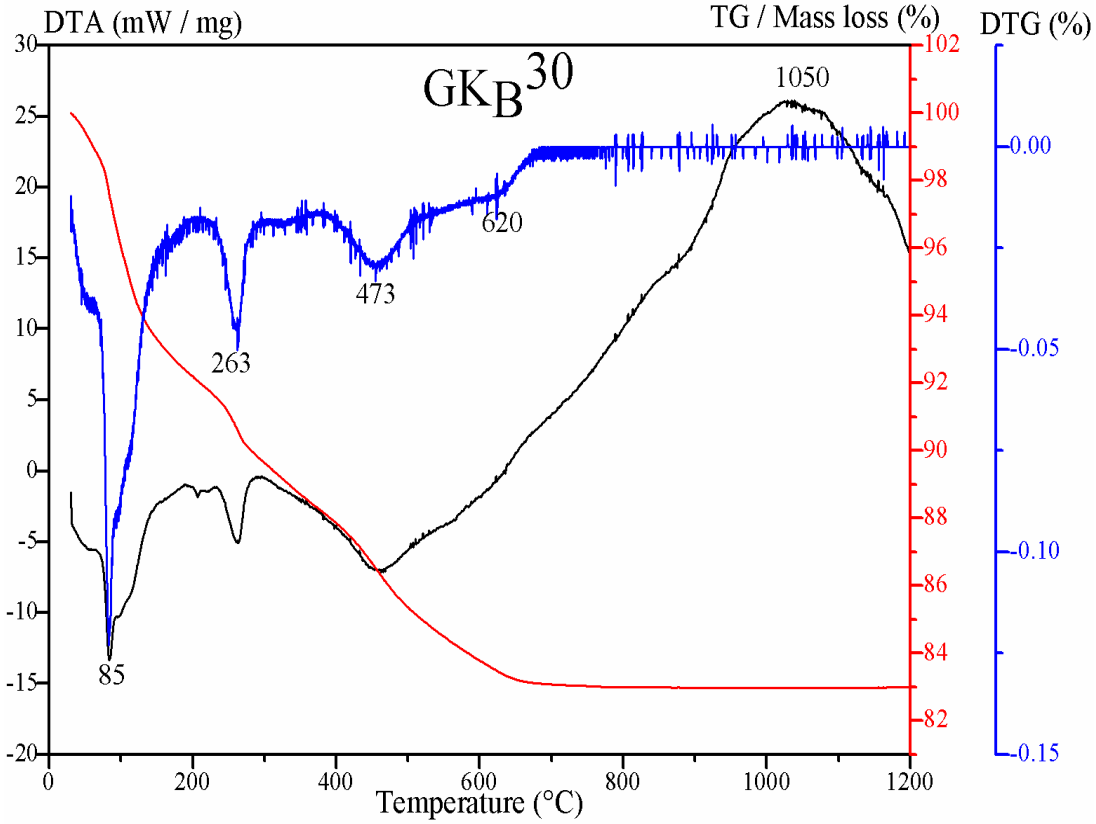

Figure 39: DTA / TG / DTG curves of the kaolin-based geopolymer obtained with partial replacement of aluminium oxy-hydroxide (GK_B^{30}) initially cured at 60 °C.

III.2.3 Morphological observation

Visual aspects of unheated and heated kaolin-based geopolymer specimens are shown in Figure 40 and the resulting colour change of bodies are summarised in Table VI. Globally, unheated and heated specimens at 900 °C exhibited good volume stability without apparent cracks, with the colour of bodies varying from light greenish gray to pale yellow. At 1100 °C, GK showed poor volume stability (weak swelling) compared to GK_A^{10} and GK_B^{30}. Moreover, GK specimens heated at 1150 °C exhibited cracks, swelled and the volume shrinkage was negative (-14.59 %). Conversely, GK_A^{10} and GK_B^{30} did not show cracks but rather good volume stability at 1150 and 1200 °C respectively. Between 1100 and 1200 °C, the colour of bodies varied from pale / light yellow, light gray and white (Table VI). This can be attributed to the mix design in formulations and the heating temperatures used. Thus, with a determined liquid to solid mass ratio, amorphous aluminium hydroxide and aluminium oxy-hydroxide allowed improvement of thermal stability of kaolin-based geopolymer specimens.

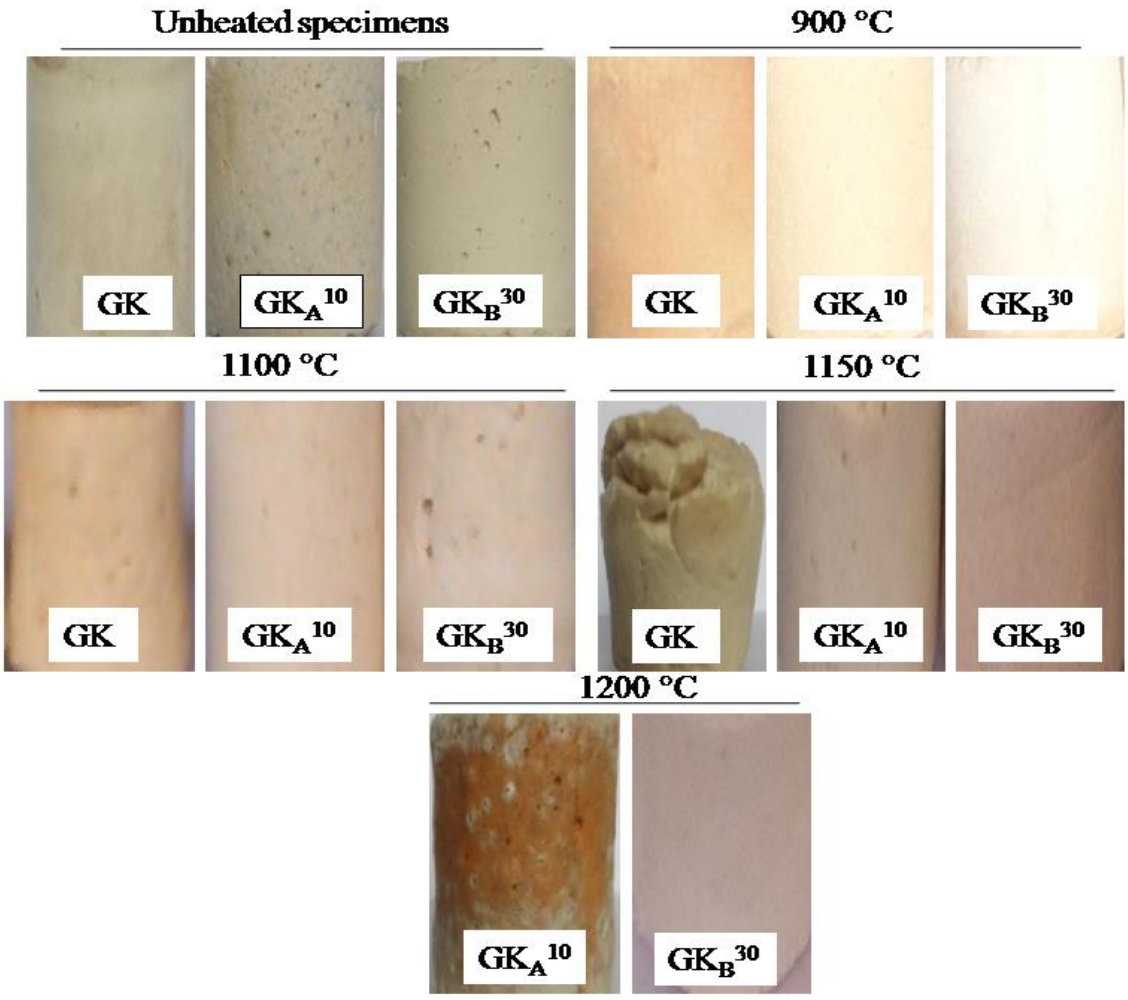

Figure 40: Visual aspect of the kaolin-based geopolymers and their heated products.

Table VI: Colour change of the kaolin-based geopolymers versus heating temperature.

Formulations	Temperatures / Colours	(24 ±3) °C	900 °C	1100 °C	1150 °C	1200 °C
GK	Munsell code	5GY8/2	2.5Y8/4	5Y8.5/4	5Y8/4	/
	Visual colour	Light greenish gray	Pale yellow	Pale yellow	Pale yellow	/
GK_A^{10}	Munsell code	5GY8/2	5Y9/4	5Y8/2	5Y7/2	5Y8.5/4
	Visual colour	Light greenish gray	Pale yellow	Light yellow	Light gray	Pale yellow
GK_B^{30}	Munsell code	5GY8/2	5Y9/2	5Y8/2	5Y7/2	5Y8/1
	Visual colour	Light greenish gray	Pale yellow	Pale yellow	Light gray	White

III.2.4 Thermal shrinkage

Figure 41 presents the thermal shrinkage (TS) of the selected heated kaolin-based geopolymer specimens (GK, GK_A^{10} and GK_B^{30}). It can be observed that between 300 and 700 °C, the presence of the replacements in the specimens of GK_A^{10} and GK_B^{30} leads to slight reduction of TS as compared to GK. Indeed, the presence of either amorphous aluminium hydroxide or aluminium oxy-hydroxide as replacement enables to weaken the specimens, thereby accounting for low reactivity [59]. Notwithstanding that, the TS of GK, GK_A^{10} and GK_B^{30} increases consistently as from 300 to 900 °C, as result of dehydration and dehydroxylation of the polysialate gel and the replacements along with onset of sintering / densification of specimens [15]. At 1100 °C, the specimens of GK show poor volume retention as result of weak expansion, leading to damaged structure with an important negative volume shrinkage (-14.59 %) at 1150 °C as initially observed in the visual aspects (Figure 42). Conversely, the specimens of GK_B^{30} and GK_A^{10} exhibit highest TS at 1100 and 1150 °C respectively followed by slight reduction of TS at 1200 °C. Indeed, the highest TS developed either at 1100 °C for GK_B^{30} or 1150 °C for GK_A^{10} accounts for high densification as result of maximum particles packing whereas the lessening of TS can be attributed to the partial dissolution of certain neo-formed aluminosilicate phases which causes slight expansion of specimens [15]. Thus, both amorphous aluminium hydroxide and aluminium oxy-

hydroxide used in certain proportions can help to control the TS of heated kaolin-based geopolymers.

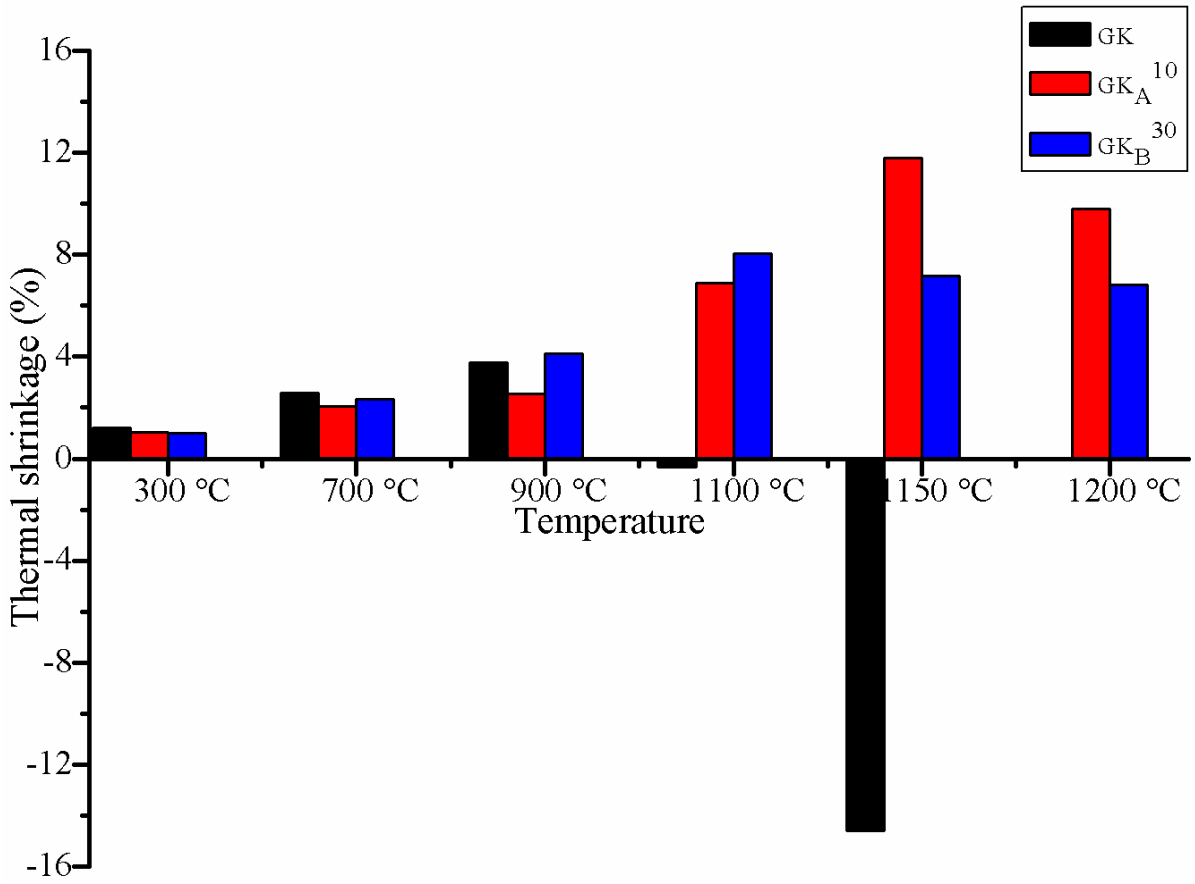

Figure 41: Thermal shrinkage of the selected heated kaolin-based geopolymer specimens.

III.2.5 Physical properties

Physical properties such as water absorption, open porosity and bulk density of kaolin-based geopolymers along with their heated products were assessed.

III.2.5.1 Water absorption

Figure 42 presents the variation of water absorption (WA) versus temperature for the kaolin-based geopolymers and their heated products. For the kaolin-based geopolymers, WA increases with the increase of replacements which may show that the aluminium hydroxides do not or weakly take part in geopolymerisation [95]. Indeed, kaolin contributes significantly to the formation of geopolymer gel (sample GK) whereas the replacements behave as fillers (GK_A^{10} and GK_B^{30}) [59, 85]. When comparing the geopolymers initially cured at 60 °C, WA has increased consistently at 300 °C most likely due to gradual transformation of geopolymer gel. Moreover, the loss of water of both gibbsite and replacements (Figures 37-39) generates

pores which contribute to raise WA [19]. Between 700 and 900 °C, WA of GK is reduced as result of the onset of densification thanks to the melting of non reacted alkaline activator. Concerning GK_A^{10} and GK_B^{30} heated respectively at 700 and 900 °C, WA still increases because of weak densification. In fact for these temperatures, replacements delay the densification process [61, 106]. WA of GK heated at 1100 °C remains slightly constant showing that its maximum densification is achieved. As for GK_A^{30} and GK_B^{30}, WA is reduced at 1100 °C as compared to 900 °C. The difference between the behaviour of the former (GK) and the latter (GK_A^{30} and GK_B^{30}) is attributed to various mix proportions of the binder (kaolin) and the replacements (Table I). Referring to GK_A^{10} and GK_B^{30}, WA is the lowest after heating at 1150 and 1200 °C respectively. In fact, the transformation of the binder has provoked the collapse of pores hence lessening of WA [109].

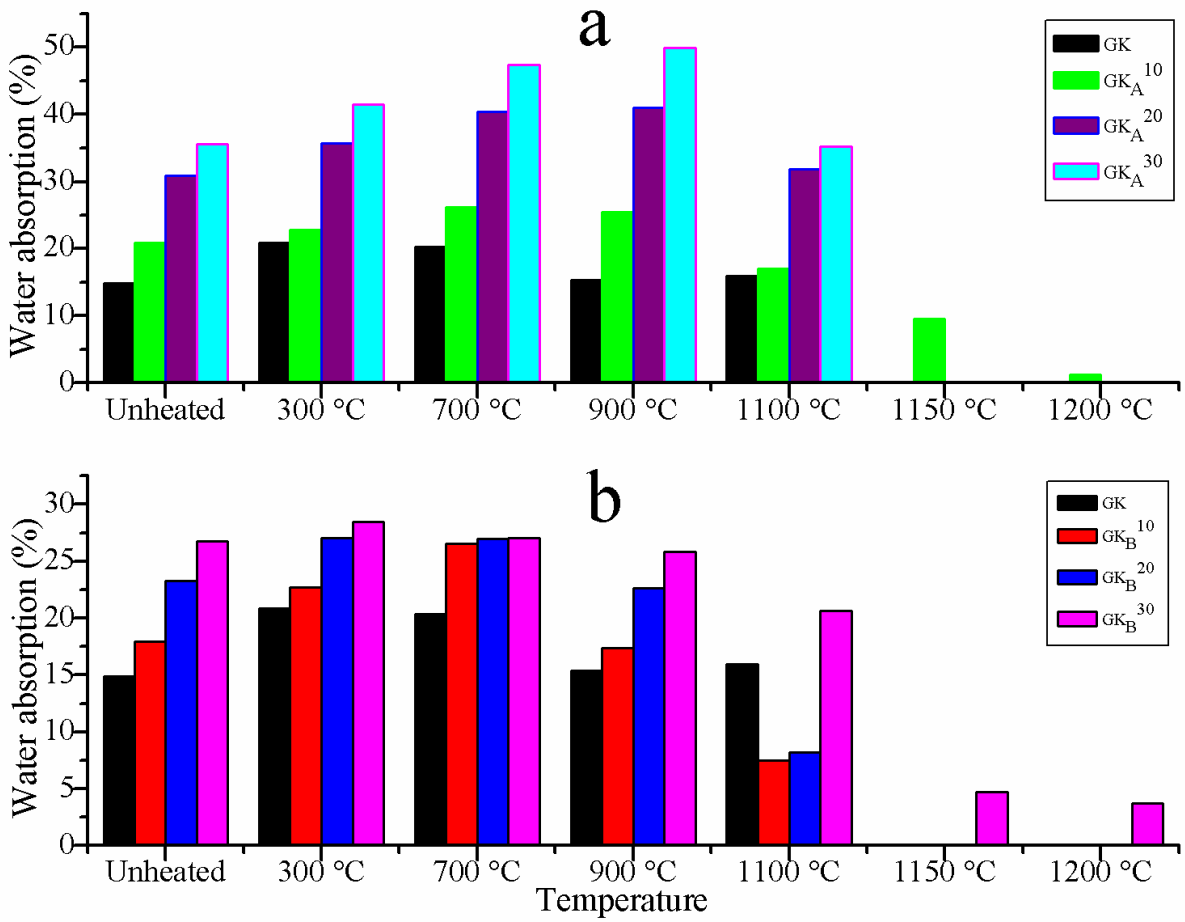

Figure 42: Water absorption of the kaolin-based geopolymers and their heated products.

III.2.5.2 Open porosity

The evolution of the open porosity (OP) of the selected kaolin-based geopolymers (GK, GK_A^{10} and GK_B^{30}) and their heated products is shown in Figure 43. Concerning the

unheated specimens, the partial replacement of the kaolin sample (K) with either amorphous aluminium hydroxide (A) or aluminium oxy-hydroxide (B) leads to products with an increase OP (GK_A^{10} and GK_B^{30}) compared to the reference specimen (GK). This is in accordance with the fact that the replacements do not or weakly take part in alkaline activation. Conversely, the OP of GK decreases consistently after heating up to 1100 °C, as result of the sintering / densification. However, the OP of the specimens of GK_A^{10} and GK_B^{30} increase after heating at 900 °C as result of the loss of structural water from both the replacements and polysialate matrix which generates the pores. Thereafter, a consistent lessening of the OP for both GK_A^{10} and GK_B^{30} specimens is observed up to 1200 °C, most likely attributed to the improvement of sintering / densification which enable the collapse of pores.

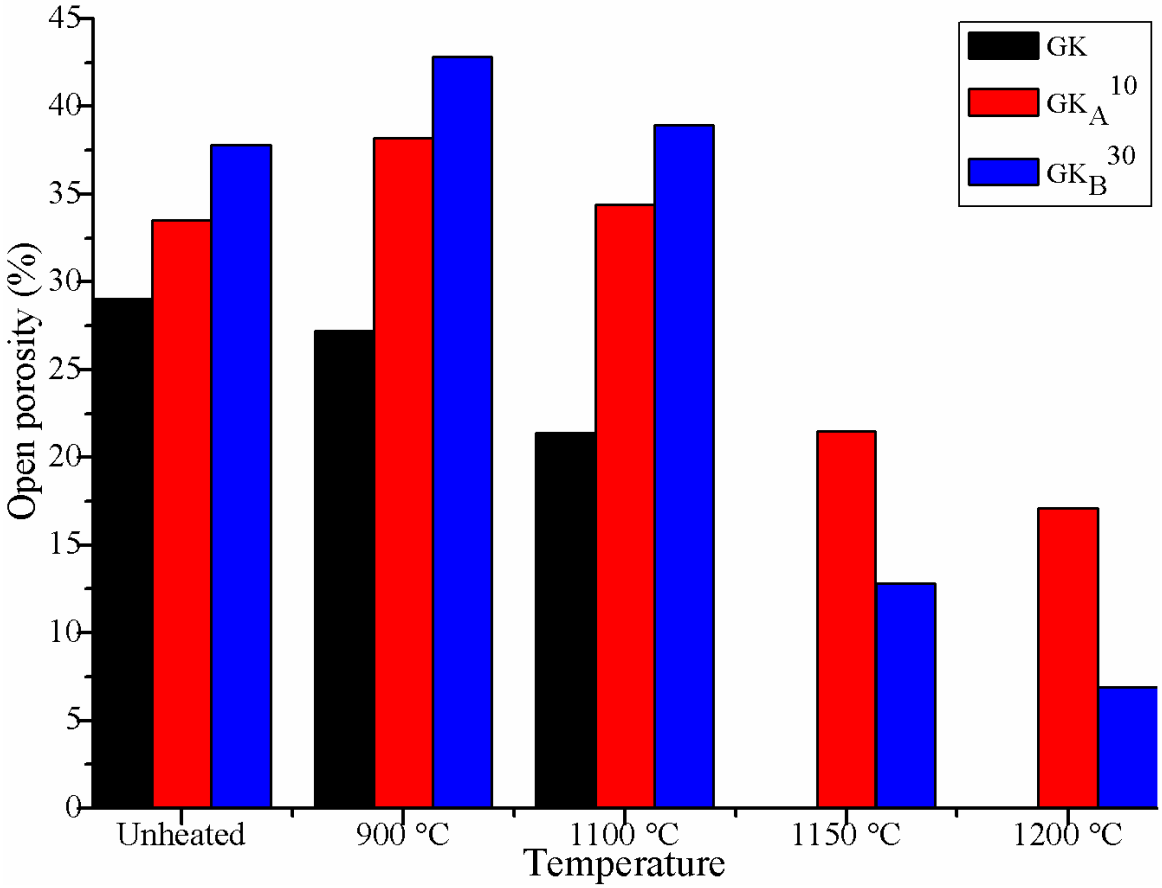

Figure 43: Open porosity of the kaolin-based geopolymers and their heated products.

III.2.5.3 Bulk density

The evolution of the bulk density (BD) of the selected kaolin-based geopolymer specimens (GK, GK_A^{10} and GK_B^{30}) and of their heated products is presented in Figure 44. It can be observed that the unheated specimens show different values of BD as result of the difference in density for both the kaolin and each replacement (amorphous aluminium

hydroxide or aluminium oxy-hydroxide) [110] along with the mix design used (Table I). After heating at 1100 °C, the BD of the specimens of GK is reduced slightly as compared to its initial value, which could be due to the formation of closed pores within the matrix. Conversely, the BD for the specimens of GK_A^{10} and GK_B^{30} is increased consistently after heating up to 1200 °C. This accounts for the fact that heating help to improve the sintering / densification which leads to an enhancement of BD of resulting products.

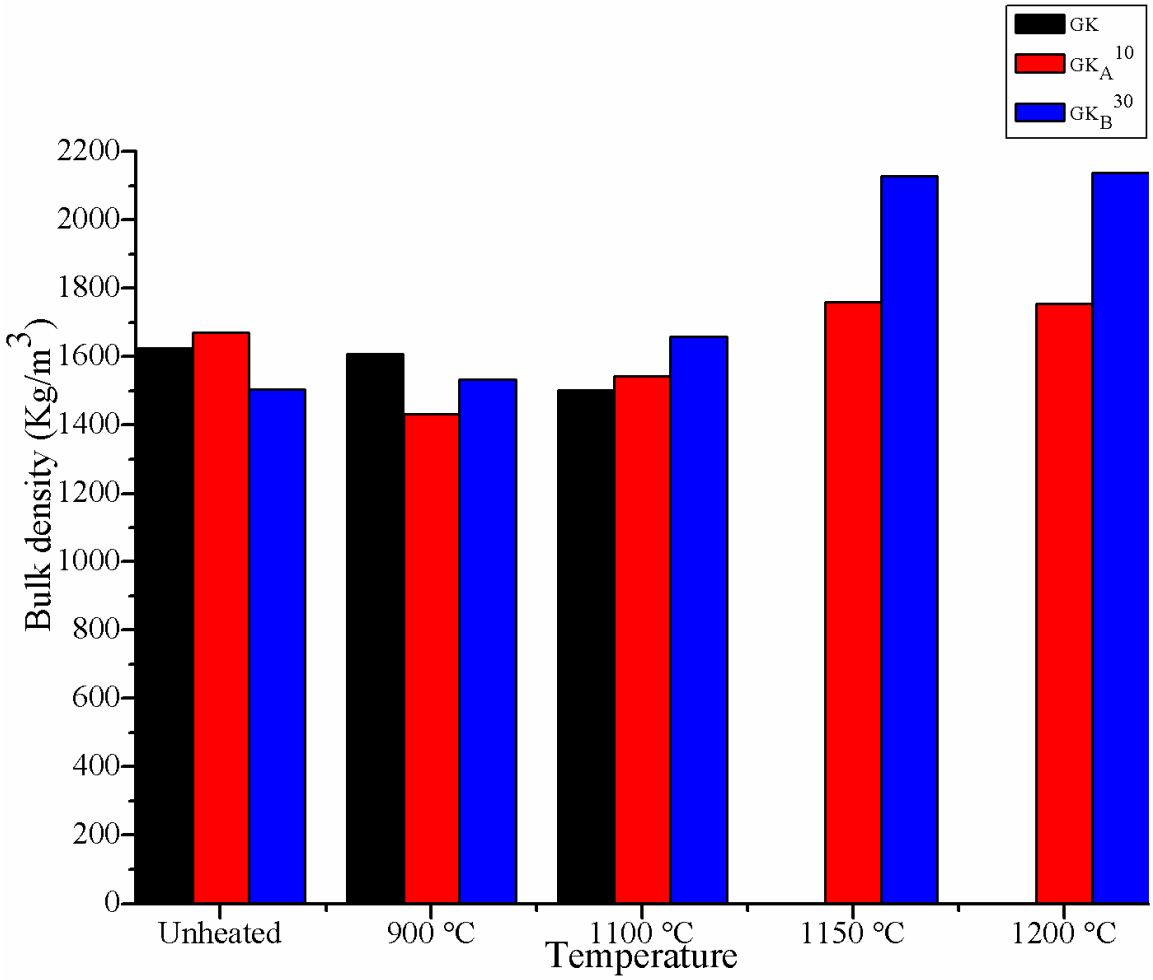

Figure 44: Bulk density of the kaolin-based geopolymers and their heated products.

III.2.6 Compressive strength

Compressive strength (CS) of the kaolin-based geopolymers and of their heated products versus temperature is given in Figure 45. For the kaolin-based geopolymers, there is decrease of CS with the increase of replacements. Indeed, CS are 22.6, 14.1 and 9.7 MPa respectively for GK, GK_A^{10} and GK_B^{30} which shows that replacements contribute to reduce CS. This decrease is also observed for the kaolin-based geopolymers heated at 300 °C, as result of gradual transformation of the geopolymer gel [15, 21] which is in accordance with

the increase of water absorption (Figure 42). However, CS of GK heated between 300 and 900 °C almost remains constant whereas that of specimens with replacement (GK_A^{10} and GK_B^{30}) increases weakly as result of weak densification of the latter [61, 111-112]. Conversely, after heating at 1100 °C, there is significant increase of CS for GK_A^{10} and GK_B^{30} as compared to that of GK. This could be related to the formation of new crystalline phases. Indeed, as compared with GK heated at 1100 °C, the CS of GK_B^{30} has increased of about 41.5 % (Figure 45b) whereas that of GK_A^{10} has increased of about 19.5 % (Figure 45a). Furthermore, the highest CS is obtained at 1150 °C for GK_A^{10} (60.2 MPa) and is reduced at 1200 °C (40.0 MPa). This is due to the fact that at 1150 °C, its compactness has improved thanks to densification which contributes to gather and wrap up stable crystalline phases [84]. Additionally, GK_B^{30} heated at 1150 and 1200 °C respectively leads to constant compressive strength value (12.0 MPa) which is low as compared to the value at 1100 °C (29.1 MPa). The decrease of CS at 1200 °C for GK_A^{10} and GK_B^{30} could be probably due to partial dissolution of Al-Si minerals such as nepheline and carnegieite which allows the creation of closed pores within the microstructure [15]. Hence, replacement of amorphous aluminium hydroxide (10 % by mass) or aluminium oxy-hydroxide (30 % by mass) in alkaline activation of kaolin is an interesting process to get heated products with improved volume stability and CS.

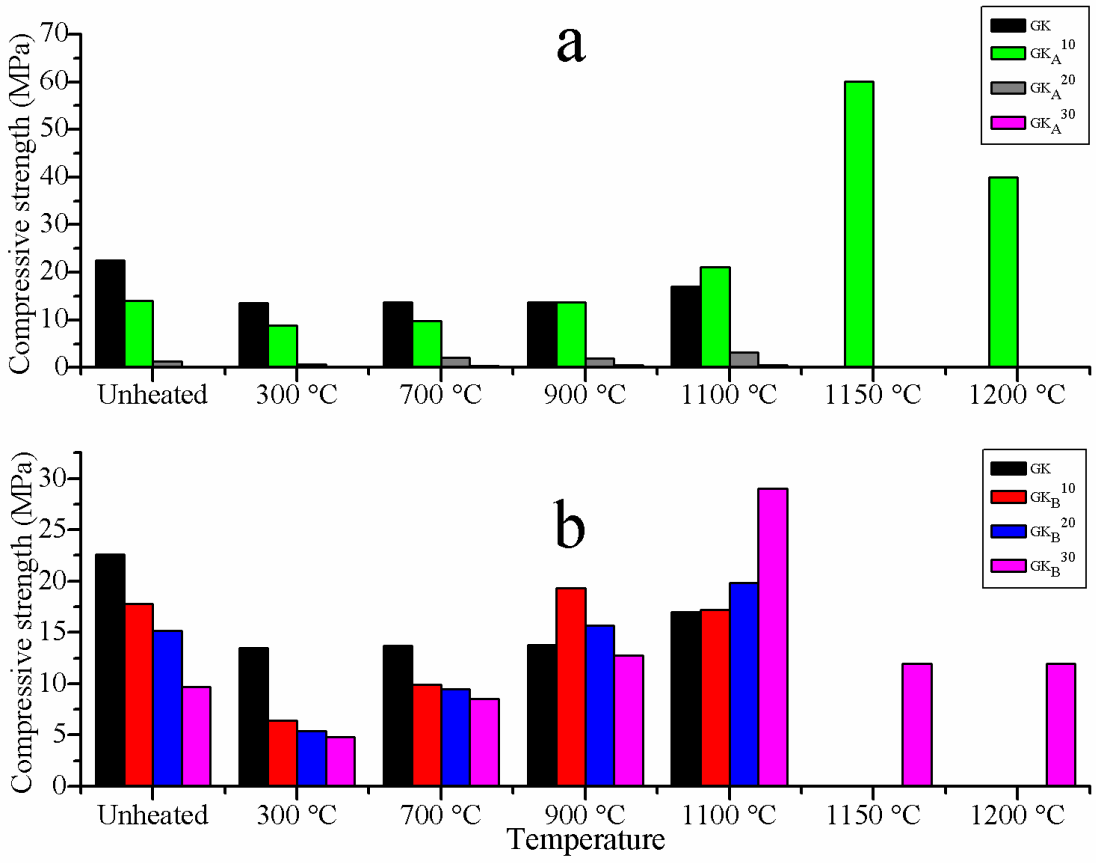

Figure 45: Compressive strength of the kaolin-based geopolymers and their heated products.

III.2.7 Microstructure

Mineralogical and microstructural characterisations of the selected kaolin-based geopolymers (GK, GK_A^{10} and GK_B^{30}) along with their heated products were assessed thanks to XRD, FTIR spectroscopy and SEM analyses.

III.2.7.1 Mineralogical composition and phase evolution

XRD (Figures 46-48) between 5 and 70° (2θ) were done in order to get better understanding on phase evolution of the kaolin-based geopolymers before and after heating at elevated temperatures.

However, the kaolin-based geopolymers such as GK and GK_A^{10} (Figures (46-48) contained kaolinite [$Al_2Si_2O_5(OH)_4$: PDF# 14-164], gibbsite [$Al(OH)_3$: PDF# 33-18], quartz [SiO_2: PDF# 46-1045], illite - 2M1 [$(K,H_3O)(Al,Mg,Fe)_2(Si,Al)_4O_{10}[(OH)_2,(H_2O)]$: PDF# 26-911] and anatase [TiO_2: PDF# 21-1272]. In addition to the above-mentioned crystalline phases, the sample GK_B^{30} contained boehmite [γ-AlO(OH): PDF# 21-1307] from the semi-crystalline aluminium oxy-hydroxide (Figure 48). This reveals the low reactivity of the above-mentioned minerals in alkaline medium as shown by the intensities of their peaks.

Conversely, all the heated kaolin-based geopolymer specimens (Figures 46-48) contained: mullite [$Al_6Si_2O_{13}$: PDF# 15-776]; corundum [α-Al_2O_3: PDF# 10-173]; rutile [TiO_2: PDF# 21-1276]; quartz [SiO_2: PDF# 46-1045]; tridymite [SiO_2: PDF# 18-1170]; nepheline [$(Na,K)AlSiO_4$: PDF# 89-8763] and carnegieite [$NaAlSiO_4$: PDF# 44-1496] as crystalline phases.

It is worth pointing out that the absence of kaolinite, illite, gibbsite and boehmite is attributed to their thermal transformations [84] as result of heating. Moreover, the intensities of the peaks related to nepheline and carnegieite are greater in GK_A^{10} and GK_B^{30} than in GK. Since the formation of nepheline and carnegieite is generally attributed to the transformation of amorphous phase of geopolymer, it can be concluded that the presence of replacements (A and B) have improved the yield of their formations. This is in accordance with the improvement of residual compressive strength observed at elevated temperatures (Figure 45). Notwithstanding that, the lessening of residual compressive strength observed at 1200 °C (Figures 47-48) is linked to the partial dissolution of nepheline and carnegieite [15].

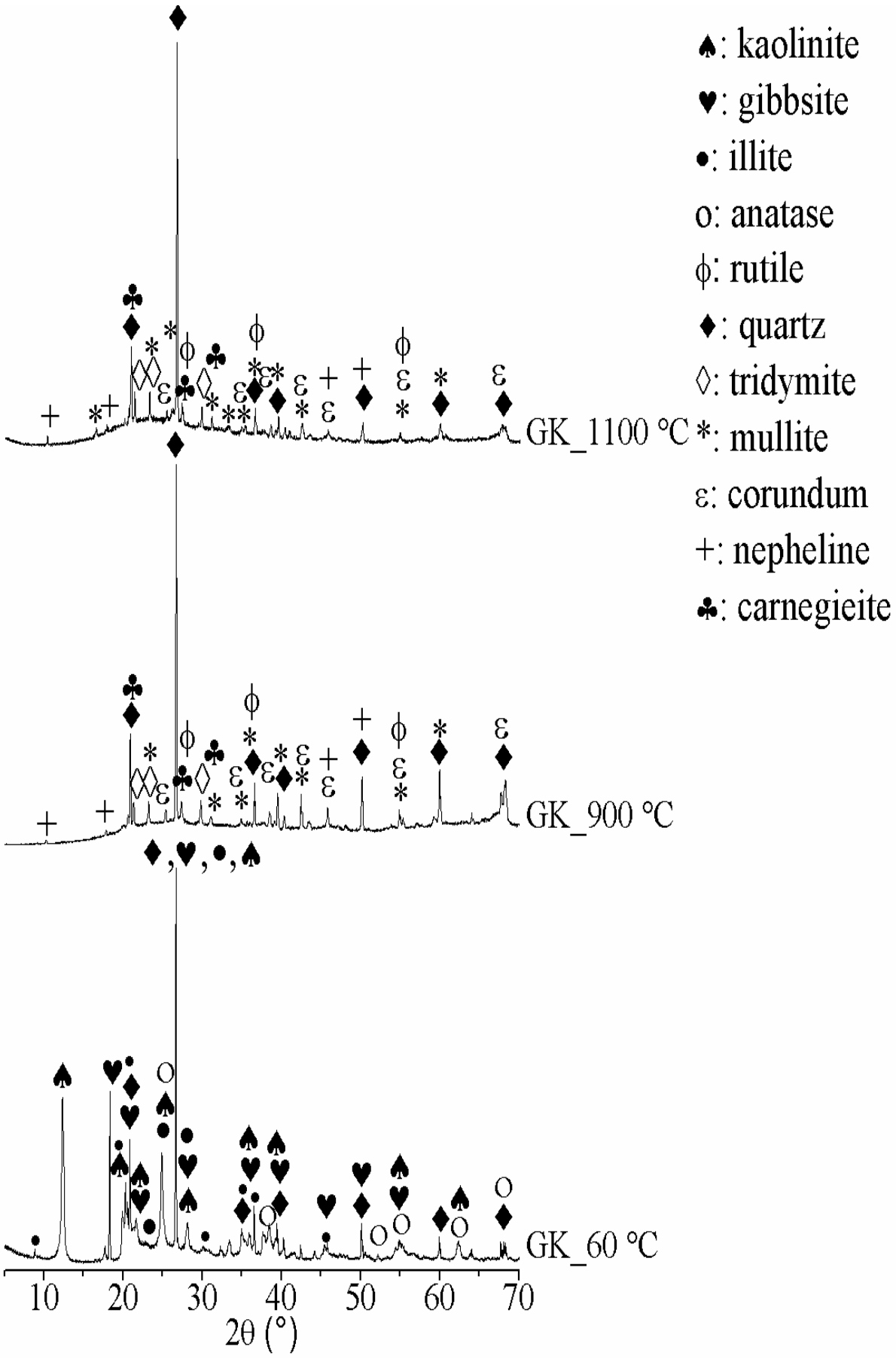

Figure 46: XRD patterns of the kaolin-based geopolymers (GK) and their heated products.

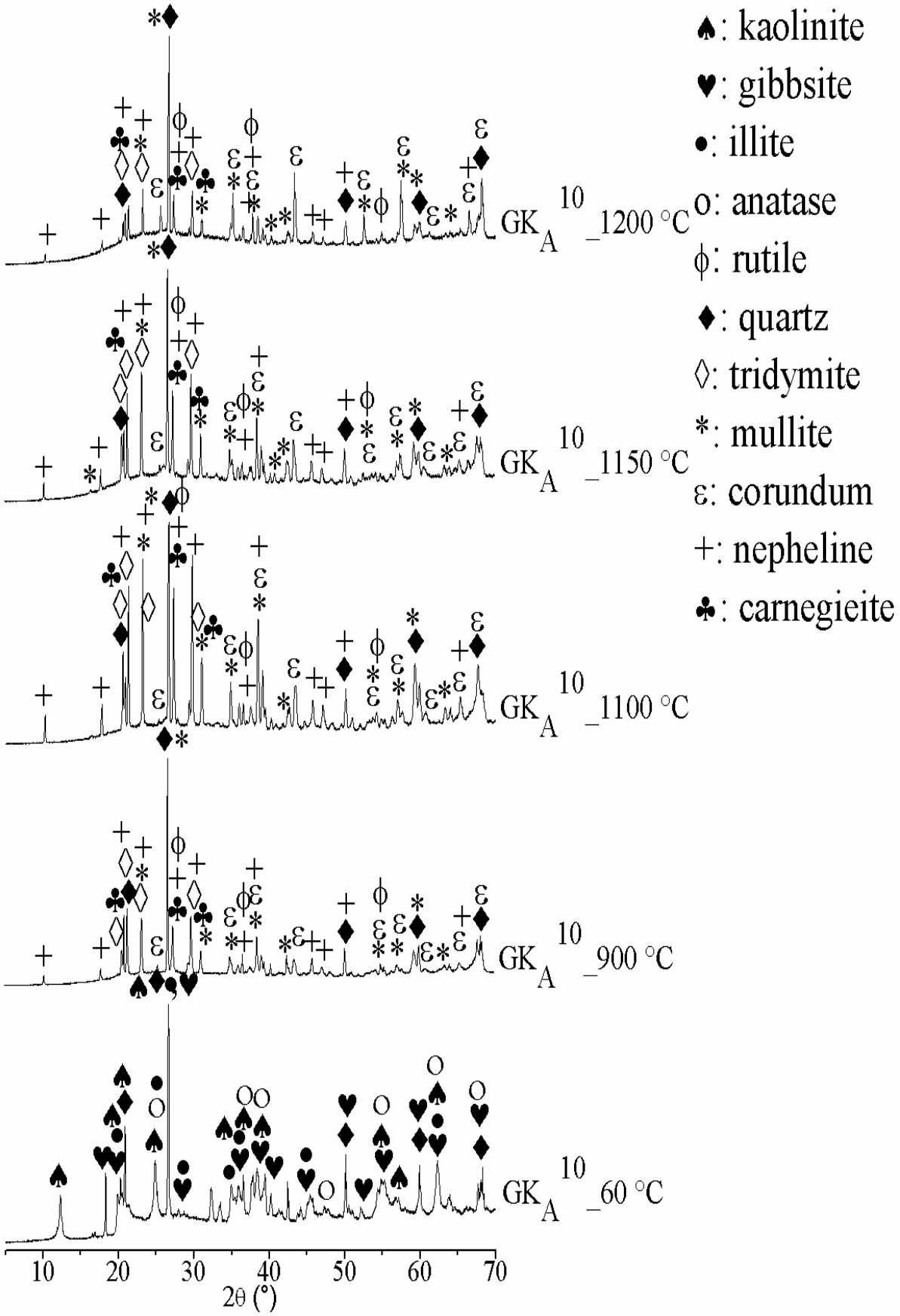

Figure 47: XRD patterns of the kaolin-based geopolymers obtained with partial replacement of amorphous aluminium hydroxide (GK_A^{10}) and their heated products.

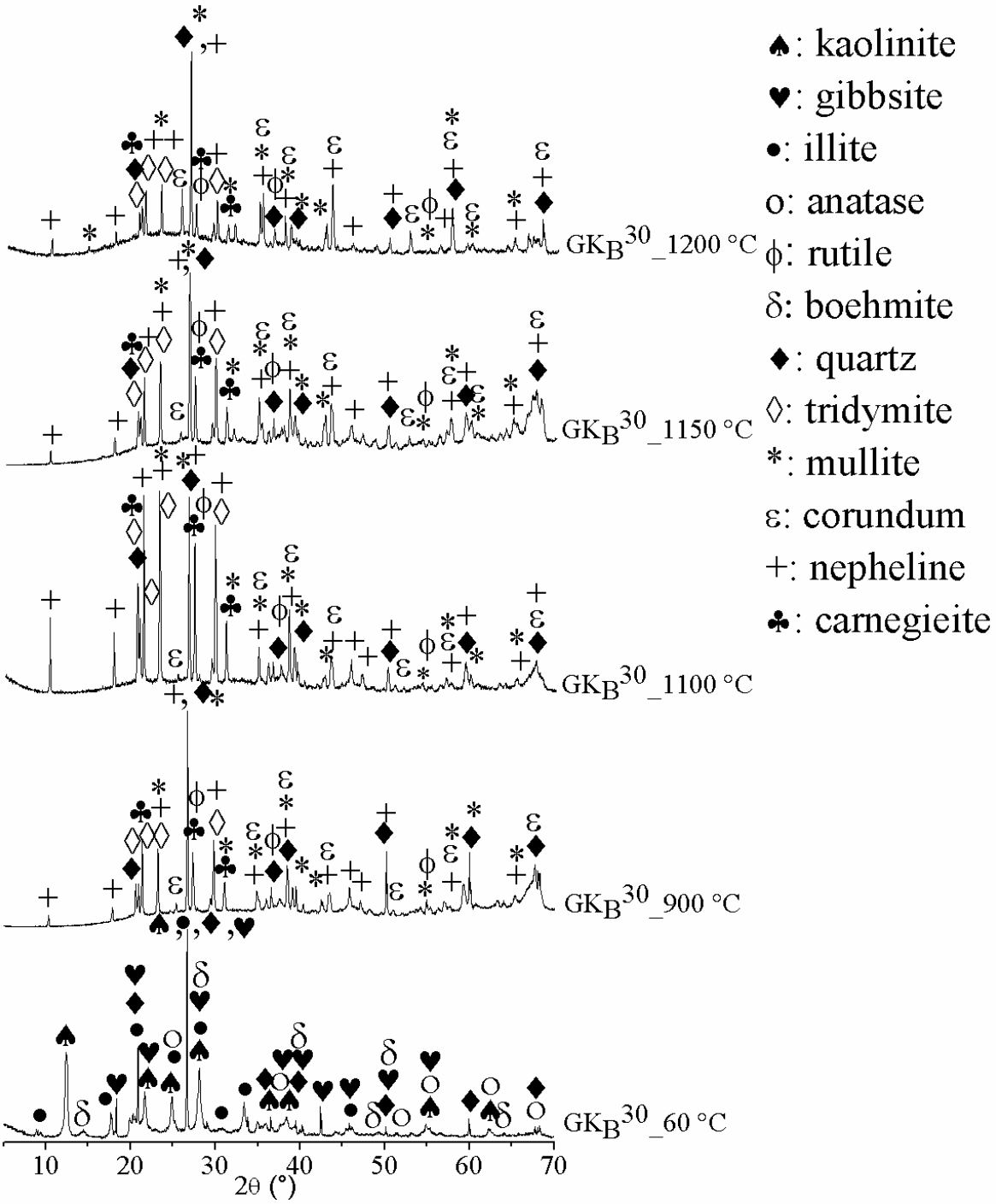

Figure 48: XRD patterns of the kaolin-based geopolymers obtained with partial replacement of aluminium oxy-hydroxide (GK_B^{30}) and their heated products.

III.2.7.2 FTIR spectra

FTIR spectra of the kaolin-based geopolymers (GK, GK_A^{10} and GK_B^{30}) initially cured at 60 °C along with their heated products (900-1200 °C) are shown in Figure 49.

Concerning the specimens initially cured at 60 °C, the peaks observed around 3688 cm^{-1} and 3621 cm^{-1} are attributed to the structural -OH groups of the kaolinite network

whereas the one appearing around 3514 cm^{-1} is ascribed to the structural –OH group of the gibbsite network [93, 113]. This confirms the presence of kaolinite and gibbsite as they were already observed in the XRD patterns of the kaolin-based geopolymers (Figures 46-48), thereby accounting for their low reactivity. The broad band observed around 3400 cm^{-1} is attributed to the stretching vibration of O-H bonds whereas the one located at 1644 cm^{-1} is attributed to bending vibration of H-O-H which expresses surface absorbed or entrapped water in large cavities of geopolymer framework [58, 94, 114]. The band at 1464 cm^{-1} is ascribed to stretching vibration of C-O bond as consequence of the existence of efflorescence on geopolymers [72] whereas the one at 1388 cm^{-1} is attributed to asymmetric vibration of Al-O and Si-O bonds [20]. However, the intensity of the latter vibration band is reduced for GK_A^{10} and GK_B^{30} as consequence of presence of replacements, evidencing the decrease of the extent of cross-linking. The bands at 790 and 743 cm^{-1} are attributed to Si-O-Al vibrations [94]. The band at 911 cm^{-1} refers to Al-OH bending vibration, those observed within the range of 1025 and 999 cm^{-1} are related to Si-O-Si in-plane vibration whereas the one at 1113 cm^{-1} is assigned to apical Si-O stretching vibration of kaolinite network showing its low reactivity in strong alkaline medium [81, 93, 115]. The main band observed at 999 cm^{-1} corresponds to symmetric and asymmetric stretching vibrations of Si-O-T (T: Si or Al) of geopolymer network [94, 116], related to the formation of polysialate gel which is the fingerprint of geopolymer matrix [58, 116]. The peak at 848 cm^{-1} is related to non-condensed Si-OH bending vibration in GK_A^{10} and GK_B^{30}, suggesting the occurrence of further condensation at elevated temperature and which could also contribute to the formation of geopolymer network [60]. The band at 790 cm^{-1} is assigned to AlO_4 vibration units of geopolymers [94]. The weak band around 663 cm^{-1} is attributed to symmetric stretching vibrations of Si-O-Al and Si-O-Si groups of geopolymers [82, 94]. The peak around 530 cm^{-1} is attributed to bending vibration of Si–O-Al($_{VI}$) bonds whereas the one located at 460 cm^{-1} is assigned to the bending vibration of Si-O-Si and O-Si-O bonds of quartz, showing that it remains unreacted in the matrix after alkaline activation [92, 94].

As for the spectra of the heated kaolin-based geopolymers (900-1200 °C), there is a shoulder at 1100 cm^{-1} attributed to stretching vibration of Si-O in tetrahedron along with vibration band around 688 cm^{-1} attributed to Si-O of quartz and the peak at 513 cm^{-1} assigned to Si-O-Al bending vibration [18, 21, 81]. In fact, the latter appearance may account for new formed Al-Si minerals such as nepheline / carnegieite (Figures 46-48), originating from the transformation of amorphous phase of geopolymer [15, 18]. The major broad band observed within the range of 982 and 979 cm^{-1} are related to Si-O-T (T: Si or Al) stretching vibrations

[116]. The bands observed within the range of 471 and 452 cm^{-1} are attributed to Si-O-Si and O-Si-O bending vibrations of quartz, showing that either it remains unreacted in strong alkaline medium or it has partially reacted during heating up to 1200 °C [20, 94]. At 1200 °C, GK_A^{10} and GK_B^{30} show three supplementary peaks. The peak at around 840 cm^{-1} is attributed to Al(IV)-O bonds [19, 96]. The peaks at around 634 cm^{-1} and 568 cm^{-1} are related to the IR characteristics of Al-O octahedrons (hexa-coordinated Al) in corundum, α-Al_2O_3 [19, 96].

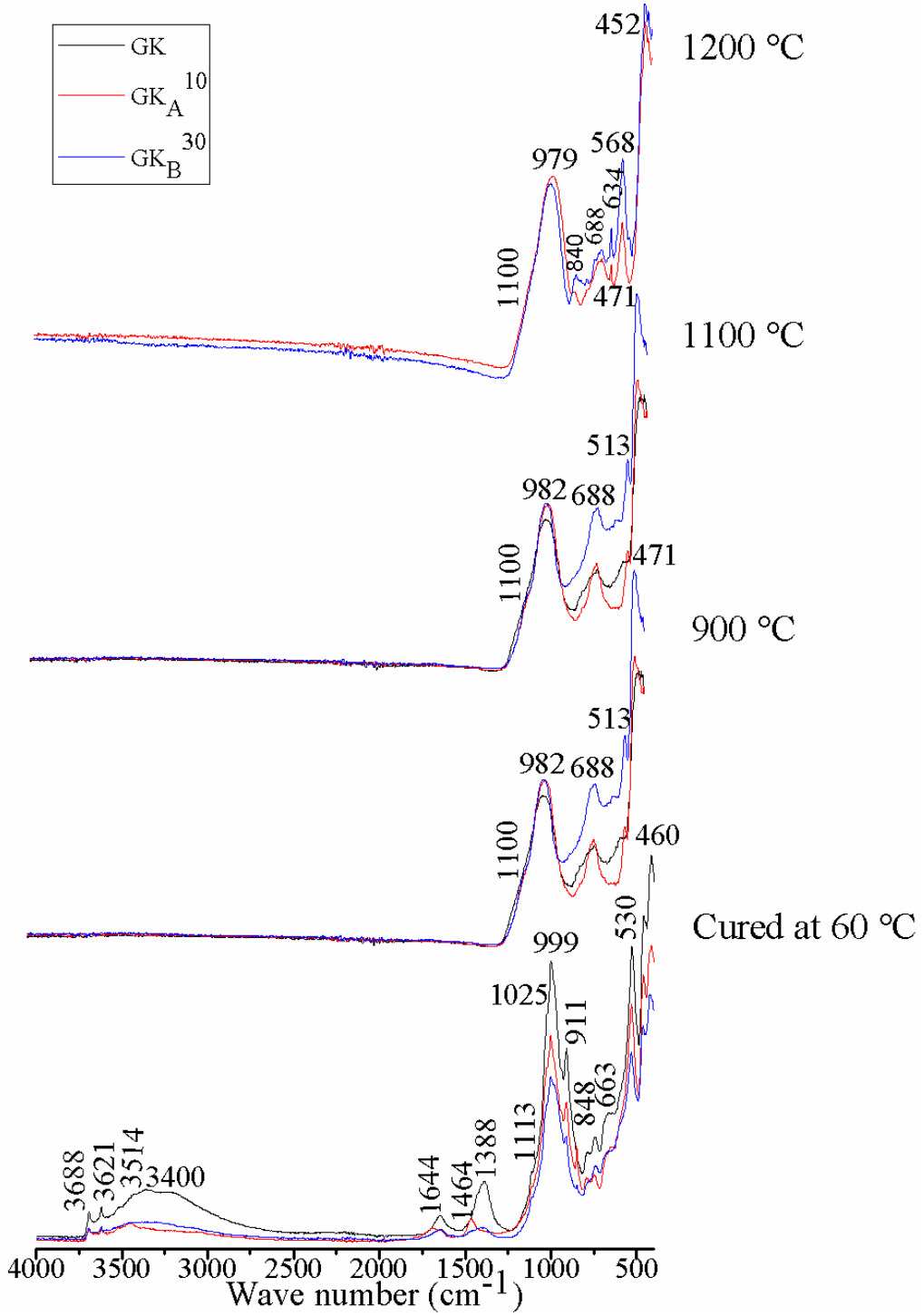

Figure 49: FTIR spectra of the kaolin-based geopolymers and their heated products.

III.2.7.3 SEM analysis

Figure 50 shows the microstructure of the selected kaolin-based geopolymers (GK, GK_A^{10} and GK_B^{30}) along with their heated products. Unheated GK micrograph shows interlocked-like fibbers close one to another which makes the whole compact enough material whereas unheated GK_A^{10} and GK_B^{30} are sponge-like with white aspect in certain areas, reminding the presence of the replacement. Heated at 900 °C, GK is compact whereas GK_A^{10} and GK_B^{30} are sponge-like showing that replacements delay the densification [61]. At 1100 °C, the compactness of GK has increased which may be due to the increase of melting of residual alkali from the activator [11]. Also, at 1100 °C, GK_A^{10} is compact in spite of the presence of some closed pores whereas the compactness of GK_B^{30} has increased but it still remains sponge-like. These differences may be ascribed to the high alumina content in GK_A^{10} and GK_B^{30}. Between 1150 and 1200 °C, the compactness of GK_A^{10} and GK_B^{30} has improved. Yet, GK_B^{30} displays some closed pores probably due to partial dissolution of nepheline and carnegieite [15].

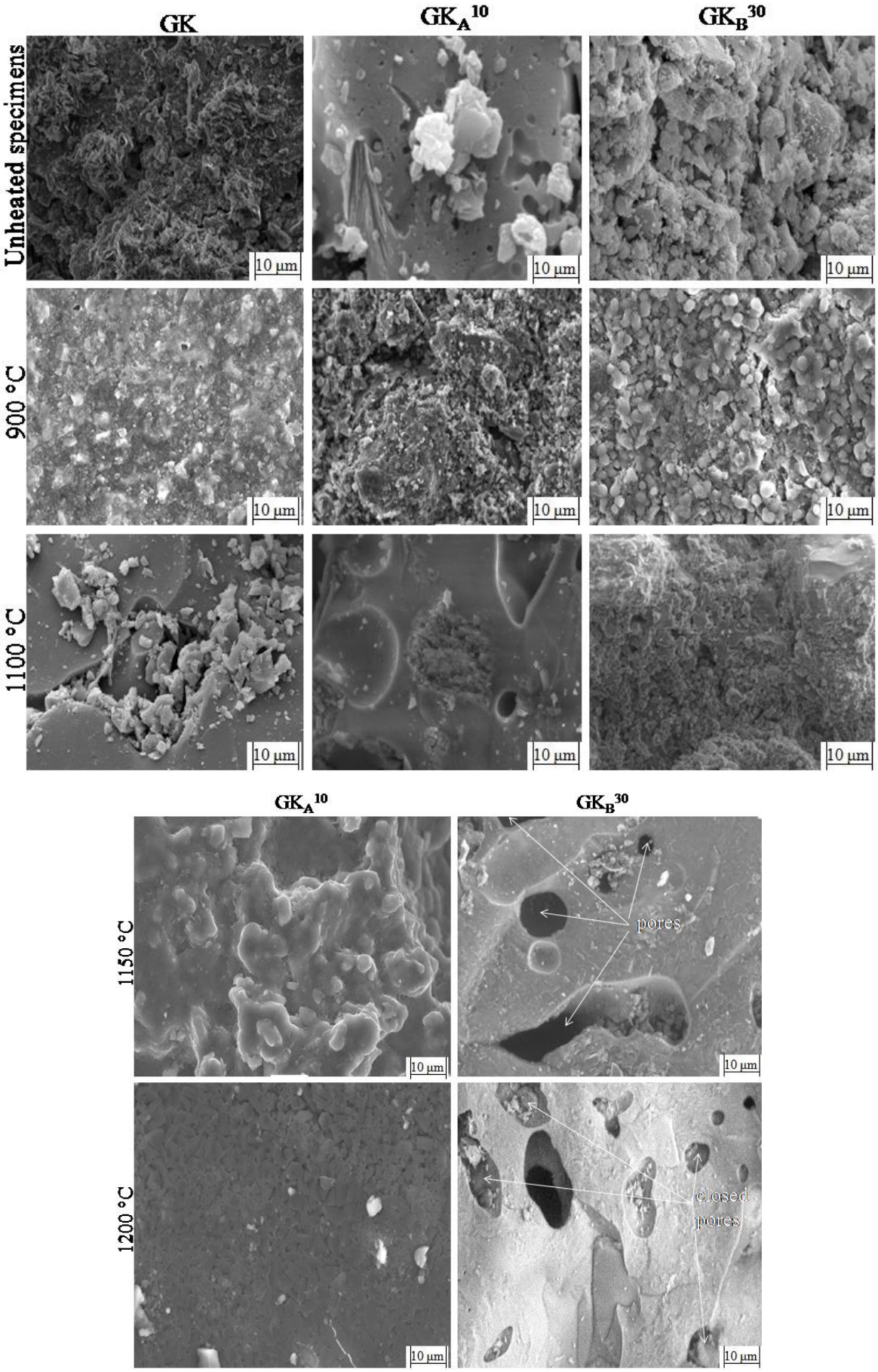

Figure 50: SEM images of the kaolin-based geopolymers and their heated products.

III.2.8 Conclusion

Amorphous aluminium hydroxide and aluminium oxy-hydroxide were used as partial replacements for the synthesis of kaolin-based geopolymers cured at 60 °C and exposed at elevated temperatures (300-1200 °C). Kaolin-based geopolymers with amorphous aluminium hydroxide of 10 % by mass or with aluminium oxy-hydroxide of 30 % by mass exhibit low compressive strength compared to the reference geopolymer (GK). At 1100 °C, compressive strength of heated geopolymers with replacements is improved due to the formation of stable crystalline phases (mullite, corundum, nepheline and carnegieite) and to densification. Further heating of reference kaolin-based geopolymer (GK) at 1150 °C leads to damaged structure ascribed to both excessive sintering and swelling due to the transition of a part of quartz into tridymite. Conversely, specimens with 10 % by mass of amorphous aluminium hydroxide or 30 % by mass of aluminium oxy-hydroxide exhibit good volume stability up to 1200 °C. This is ascribed to the thermal transformation of the replacements and to their contribution to form Al-Si minerals (nepheline and carnegieite). Unfortunately, at 1200 °C partial dissolution of nepheline and carnegieite provokes the formation of closed pores which lessens residual compressive strength. Used as replacements in certain percentages, amorphous aluminium hydroxide and aluminium oxy-hydroxide can successfully help to get heated kaolin-based geopolymers thermally stable and endowed with high residual compressive strength.

III.3Influence of amorphous aluminium hydroxide and aluminium oxy-hydroxide on the thermal stability of metakaolin-based geopolymers

III.3.1 Flowability behaviour of metakaolin-based geopolymer pastes

The flowability of the metakaolin-based geopolymer pastes expressed in terms of replacement content and liquid to solid mass ratio (L / S) is presented in Figure 51. L / S of 1.13 was suitable for GMK which was considered as the reference mixture. The same value of liquid to solid mass ratio was suitable for the mixtures GMK_B^{10}, GMK_B^{20} and GMK_B^{30} with aluminium oxy-hydroxide as replacement. They displayed good flowability and were consistent and homogeneous mixtures of particles during and after moulding. As for the mixtures with amorphous aluminium hydroxide as replacement, L / S of 1.20 was suitable for GMK_A^{10} whereas L / S of 1.68 and 2.01 were respectively tested for GMK_A^{20} and GMK_A^{30} but this did not allow consolidated specimens. Actually, the difference between the two replacements pertaining to the L / S mass ratio can be ascribed either to the particle size distribution or to the ability of particles to absorb the activating solution. For instance, the

particle size distribution of amorphous aluminium hydroxide shows the presence of greater amount of fine particles (Figure 28) as compared to that of aluminium oxy-hydroxide (Figure 29), meanwhile the contact angle of the former is smaller than the latter, thereby requiring greater amount of activating solution to achieve good wettability. It is worth pointing out that the specimens of GMK_A^{20} and GMK_A^{30} were not well consolidated even after 28 days of curing at ambient temperature of the laboratory. This suggested that excess of amorphous aluminium hydroxide may hinder the extent of the formation of the polysialate framework [59, 85].

Hence, partial replacement of metakaolin with 30 % by mass of aluminium oxy-hydroxide or with 10 % by mass of amorphous aluminium hydroxide gave suitable mix designs that led to consolidated metakaolin-based geopolymers with good flowability. For further assessment in this study, microstructural and mineralogical characterisations were performed only for GMK, GMK_A^{10} and GMK_B^{30}.

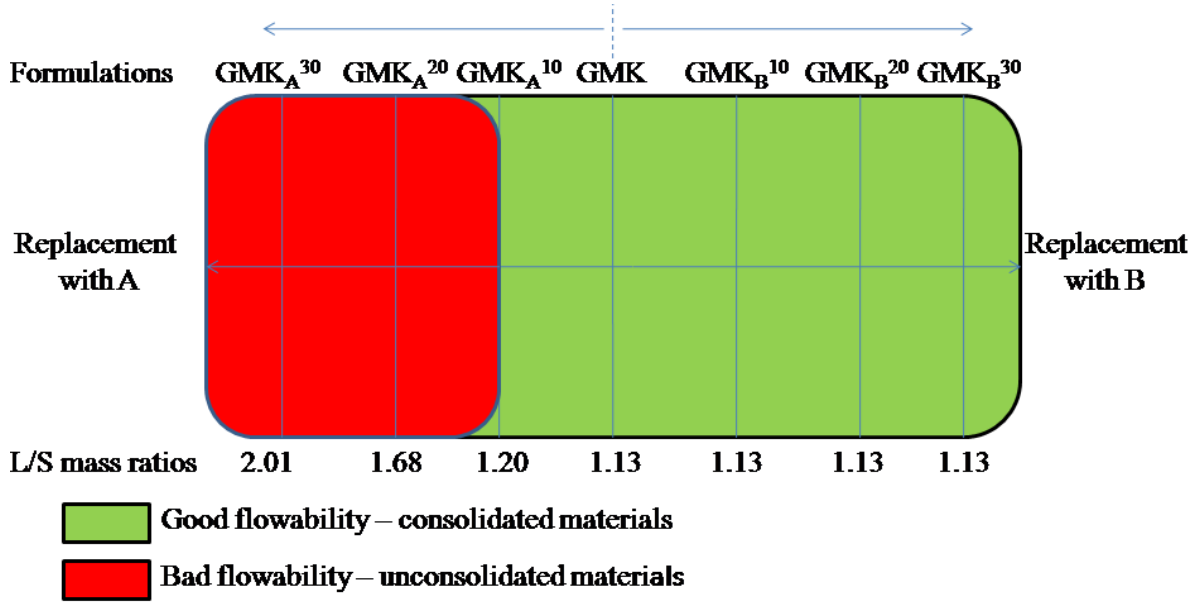

Figure 51: Flowability of the metakaolin-based geopolymer pastes.

III.3.2 Thermal behaviour of hardened metakaolin-based geopolymer pastes

Figures 52-54 show the thermal behaviour followed by TG / DTG and DTA analyses of the selected metakaolin-based geopolymer specimens (GMK, GMK_A^{10} and GMK_B^{30}) initially cured at ambient temperature and aged 28 days. The major mass loss is observed between ambient temperature and 250 °C as depicted by the first broad endothermic peaks observed in DTA curves. Indeed, the specimens of GMK, GMK_A^{10} and GMK_B^{30} show 13.7, 14.8 and 14.6 % of mass loss respectively. This mass loss is attributed to the removal of physically absorb water, interstitial and chemically bound water respectively from polysialate

network, amorphous aluminium hydroxide and aluminium oxy-hydroxide [19, 60-61]. Additionally, the amount of water released in these metakaolin-based geopolymer specimens is much, indicating high condensed structure accordingly [60]. This is due to the high fineness of metakaolin particles which require greater amount of alkaline activator to achieve good workability. The second minor mass loss of 2.4, 2.9 and 3.6 % respectively for GMK, GMK_A^{10} and GMK_B^{30}, which occurs between 250 and 700 °C is mostly attributed to the hydroxyl water from both the polysialate gel and the replacements (A and B) [20, 67, 76]. Between 800 and 1200 °C, the TG / DTG curves do not show mass loss whereas DTA ones display respectively broad exothermic bands (GMK, GMK_A^{10} and GMK_B^{30}). This thermal phenomenon corresponds to the crystallisation of new phases. Hence, partial replacement with either amorphous aluminium hydroxide or aluminium oxy-hydroxide is beneficial to prevent the early melting of metakaolin-based geopolymer specimens. Additionally, the crystallisation of new phases is observed between 900-1100 °C for GMK whereas there is a sliding to higher temperatures (1100-1200 °C) for both GMK_A^{10} and GMK_B^{30} specimens. The latter observations show that partial replacement with either amorphous aluminium hydroxide or aluminium oxy-hydroxide lengthens the thermal stability of metakaolin-based geopolymer specimens.

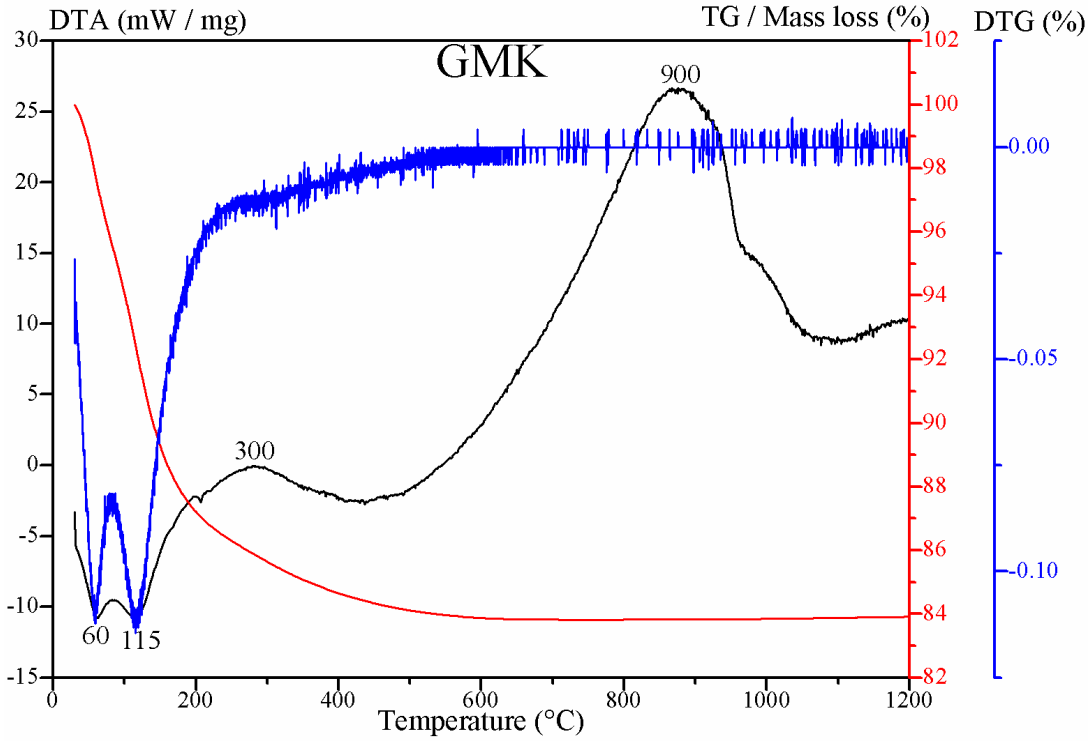

Figure 52: DTA / TG / DTG curves of the metakaolin-based geopolymer (GMK) initially cured at ambient temperature.

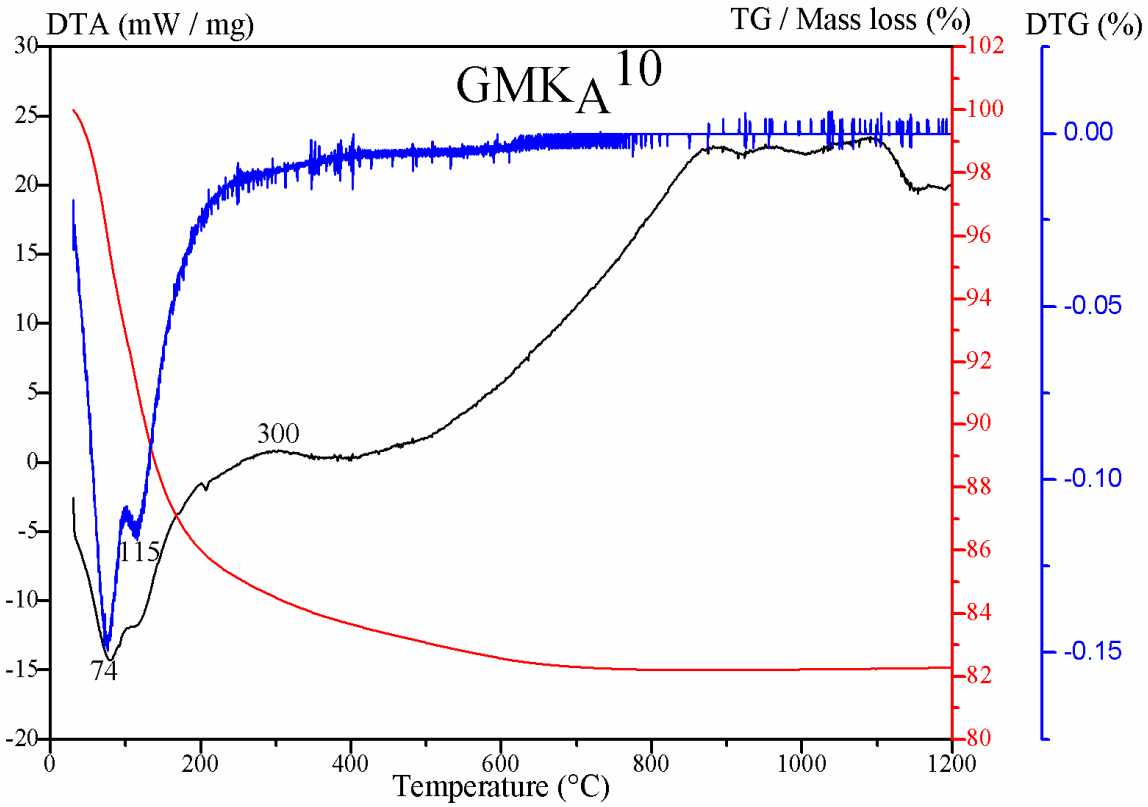

Figure 53: DTA / TG / DTG curves of the metakaolin-based geopolymer obtained with amorphous aluminium hydroxide (GMK_A^{10}) and initially cured at ambient temperature.

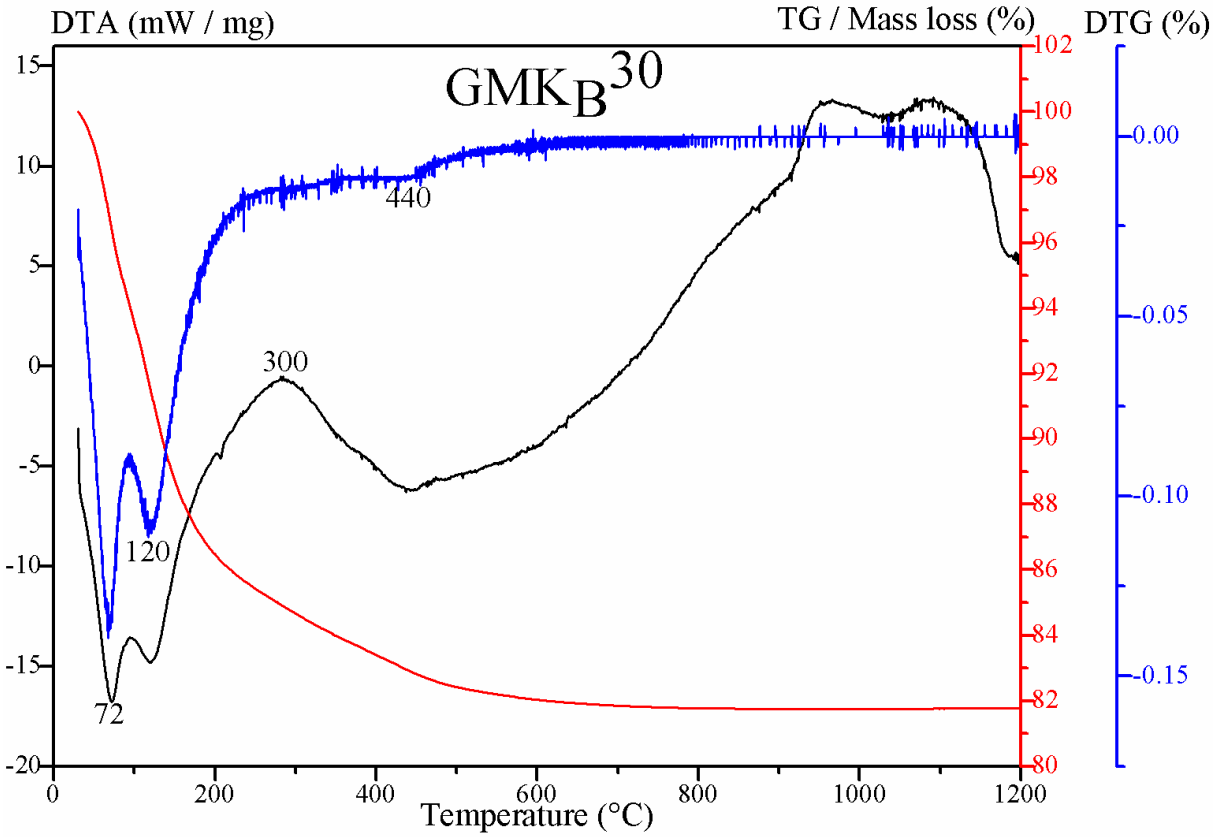

Figure 54: DTA / TG / DTG curves of the metakaolin-based geopolymer obtained with aluminium oxy-hydroxide (GMK_B^{30}) and initially cured at ambient temperature.

III.3.3 Morphological observation

The appearance of the selected metakaolin-based geopolymer specimens (GMK, GMK_A^{10} and GMK_B^{30}) along with their heated products is shown in Figure 55 whereas the resulting colour change of bodies are summarised in Table VII. Globally, unheated and heated metakaolin-based geopolymer specimens at 900 °C show good volume stability with no apparent cracks, in which the colour of bodies vary from yellow, pale yellow and light yellowish brown (Table VII). Conversely, there are cracks when GMK specimens are heated at 1100 °C, which result from both expansion of quartz [19] and low thermal stability whereas GMK_A^{10} and GMK_B^{30} specimens heated at 1200 °C rather show good volume stability and absence of cracks. This is attributed to the presence of the replacements (A or B) which hinder the formation of cracks probably due to their refractoriness [61]. Additionally, the colour of bodies between 1100 and 1200 °C vary from pale yellow to light yellow, most likely attributed to the mix designs along with the heating temperatures employed. Hence, as result of their refractoriness, partial replacement of metakaolin by either amorphous aluminium hydroxide (10 % by mass) or aluminium oxy-hydroxide (30 % by mass) in alkaline activation leads to products endowed with good volume stability up to 1200 °C.

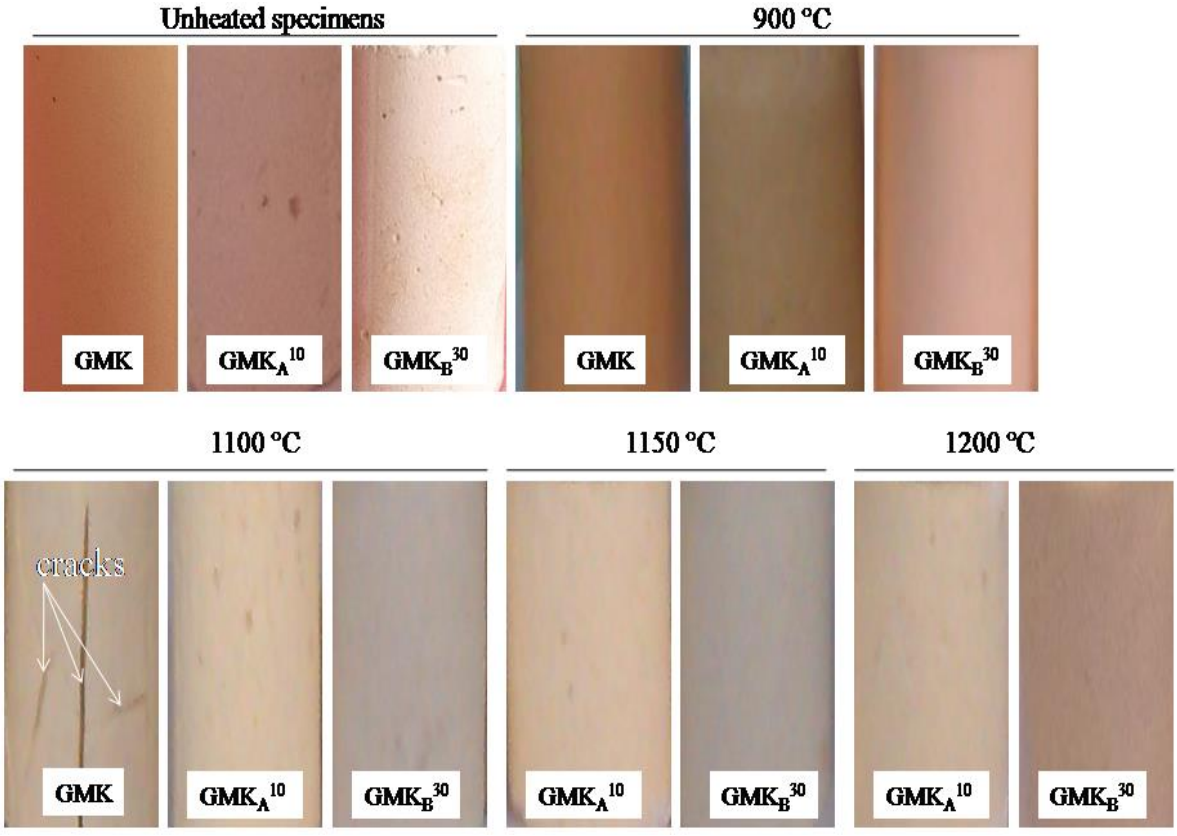

Figure 55: Visual aspect of the metakaolin-based geopolymers and their heated products.

Table VII: Colour change of the metakaolin-based geopolymers versus heating temperature.

Formulations	Temperatures / Colours	(24 ±3) °C	900 °C	1100 °C	1150 °C	1200 °C
GMK	Munsell code	10YR8/8	2.5Y7/10	5Y9/4	/	/
	Visual colour	Yellow	Pale yellow	Pale yellow	/	/
GMK_A^{10}	Munsell code	5Y8.5/2	10YR6/4	2.5Y9/4	2.5Y9/4	2.5Y9/4
	Visual colour	Pale yellow	Light yellowish brown	Light yellow	Light yellow	Light yellow
GMK_B^{30}	Munsell code	5Y8/4	2.5Y9/2	7.5Y9/2	5Y9/2	5Y9/2
	Visual colour	Pale yellow	Yellow	Light yellow	Light yellow	Pale yellow

III.3.4 Thermal shrinkage

Figure 56 depicts the thermal shrinkage (TS) of the selected heated metakaolin-based geopolymer specimens (GMK, GMK_A^{10} and GMK_B^{30}) versus heating temperature. Between 300 and 900 °C, partial replacement of metakaolin with either amorphous aluminium hydroxide or aluminium oxy-hydroxide leads to the reduction of shrinkage of the resulting heated metakaolin-based geopolymer specimens, as it was already observed in the literature [59]. In fact, this is attributed to both the low reactivity and the refractoriness of the replacements (A and B) which contribute to delay the densification process of specimens in that range of heating temperature [61]. However, the TS of GMK specimens is greater at 900 °C as compared to those of GMK_A^{10} and GMK_B^{30}, showing that the sintering / densification of the former is already achieved. At 1100 °C, the TS of GMK specimen is reduced as compared to the value observed at 900 °C. This is probably ascribed to the weak volume expansion of the specimen as result of quartz transition (quartz $\alpha \longrightarrow$ quartz $\beta \longrightarrow$ tridymite) [19] which generates cracks as previously observed on visual aspects (Figure 55). As for the specimens obtained from partial replacement with either amorphous aluminium hydroxide or aluminium oxy-hydroxide, GMK_A^{10} specimens show highest TS at 900 °C whereas the ones of GMK_B^{30} is recorded at 1150 °C. This can be attributed to the mix designs used along with the refractory nature of each replacement. A moderate lessening of TS is observed at 1200 °C, as result of the onset of partial dissolution of Al-Si minerals such as nepheline and carnegieite which induces slight expansion of specimens [15].

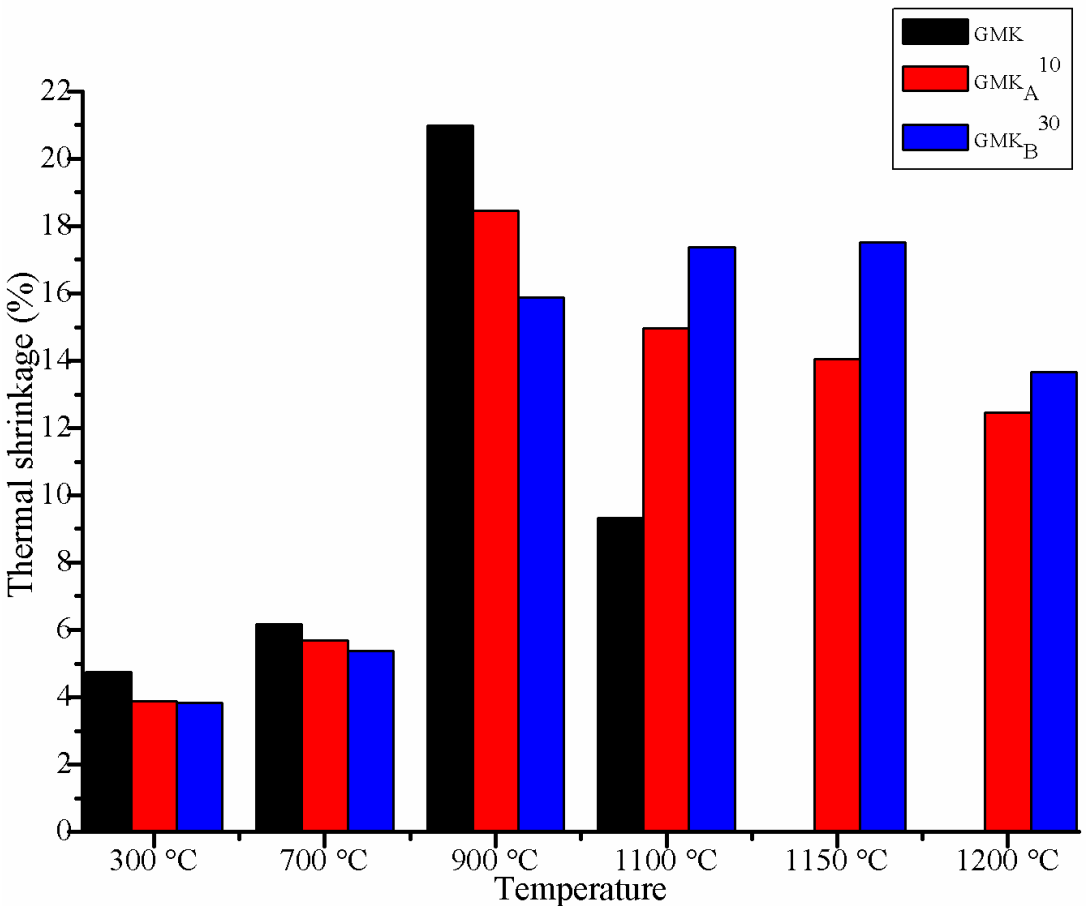

Figure 56: Thermal shrinkage of the heated metakaolin-based geopolymer specimens.

III.3.5 Physical properties

Physical properties such as water absorption, open porosity and bulk density of the metakaolin-based geopolymer specimens along with their heated products were assessed.

III.3.5.1 Water absorption

The variation of water absorption (WA) of the metakaolin-based geopolymer specimens versus heating temperature is presented in Figure 57. WA of unheated metakaolin-based geopolymer specimens increased with increasing amount of replacement. This may indicate that amorphous aluminium hydroxide and aluminium oxy-hydroxide have not yet reacted chemically or behave as fillers [95]. Compared to unheated specimens, the WA of specimens heated at 300 °C is increased as result of the transformation of geopolymer gel along with the loss of absorbed water which generates pores. It worth pointing out that both the unheated and heated specimens of GMK_A^{20} and GMK_A^{30} at 300 °C, were unconsolidated and decomposed during the boiling process. At 700 °C, there is slight decreased of WA for all specimens as result of the onset of sintering / densification caused by the non-reacted alkaline

activator [15]. Between 900 and 1100 °C, WA is the lowest for GMK as compared to GMK_A^{30} and GMK_B^{30} specimens. This may arise from the great L / S mass ratio (1.13) such as the non-reactive amount of activator enhances the sintering so as to achieve the densification [84]. Conversely, the fact that the WA for GMK_A^{30} and GMK_B^{30} specimens is still high accounts for the fact that the presence of the replacements delays the densification as result of their refractoriness [61]. Between 1150 and 1200 °C, the WA of GMK_A^{10} (Figure 57a) remains slightly constant whereas that of GMK_B^{30} (Figure 57b) decreases most likely due to the improvement of densification thanks to further heating, which enables the collapse of pores, hence lessening of WA [109].

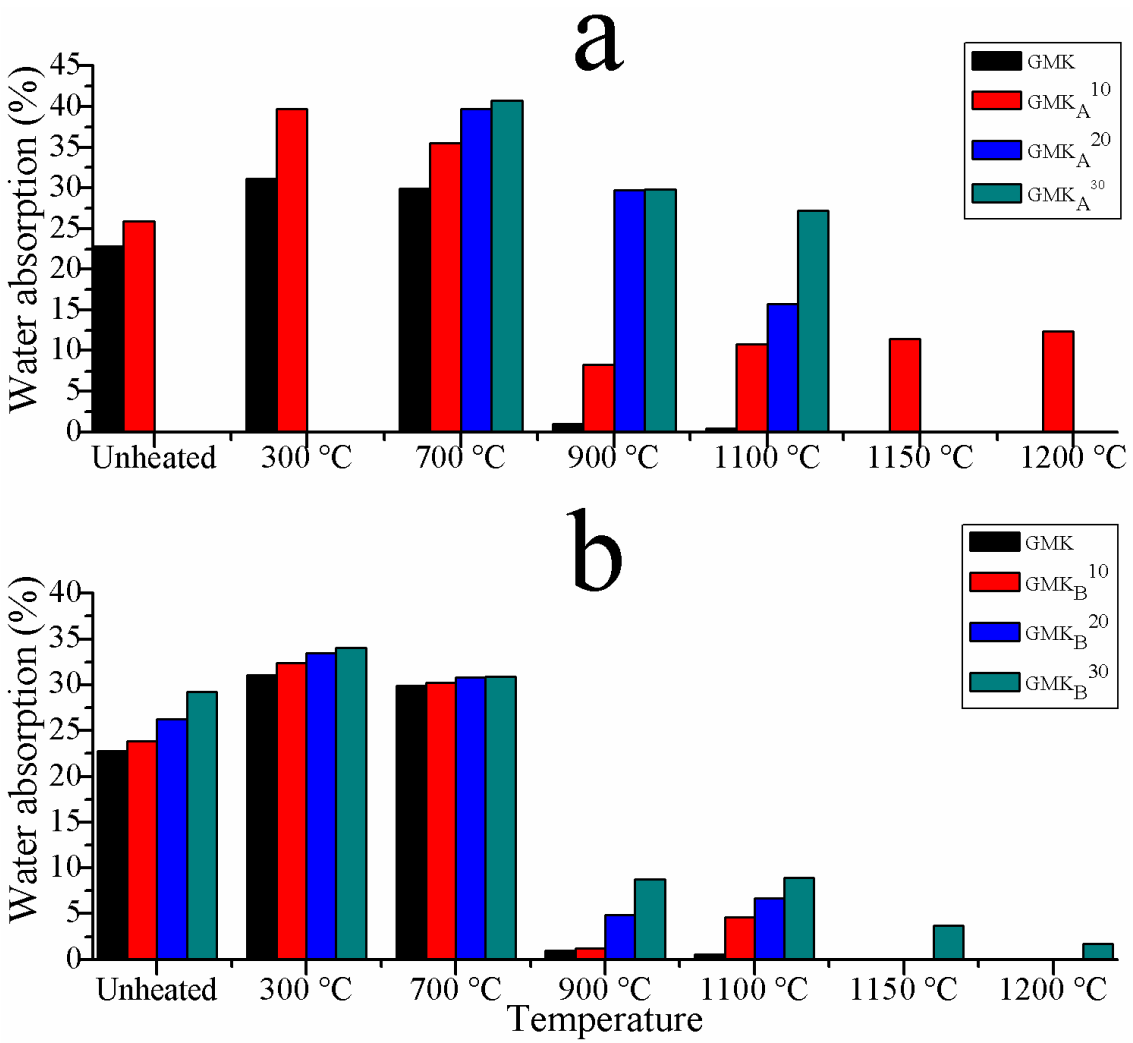

Figure 57: Water absorption of the metakaolin-based geopolymers and their heated products.

III.3.5.2 Open porosity

Figure 58 presents the open porosity (OP) of the selected metakaolin-based geopolymer specimens (GMK, GMK_A^{10} and GMK_B^{30}) along with their heated products. It

appears that the OP of unheated products increases with the increase amount of replacement and this is in accordance with the water absorption results (Figure 57). Indeed, this may shows that amorphous aluminium hydroxide and aluminium oxy-hydroxide are either non-reactive or behave as fillers during alkaline activation of metakaolin. As for the heated specimens, the OP of GMK is the lowest between 900 and 1100 °C as compared to those of GMK_A^{10} and GMK_B^{30}. This is most likely attributed to the densification which enables the collapse of pores, hence lessening of the OP accordingly. Conversely, the high OP observed for GMK_A^{10} and GMK_B^{30} specimens (900 and 1100 °C) correlates with the fact that the presence of the replacements (A and B) delays the densification process. Between 1150 and 1200 °C, the OP of GMK_A^{10} remains slightly constant whereas that of GMK_B^{30} is the lowest as result of the improvement of densification due to further heating, which causes the collapse of pores, hence lessening of the OP of the resulting products.

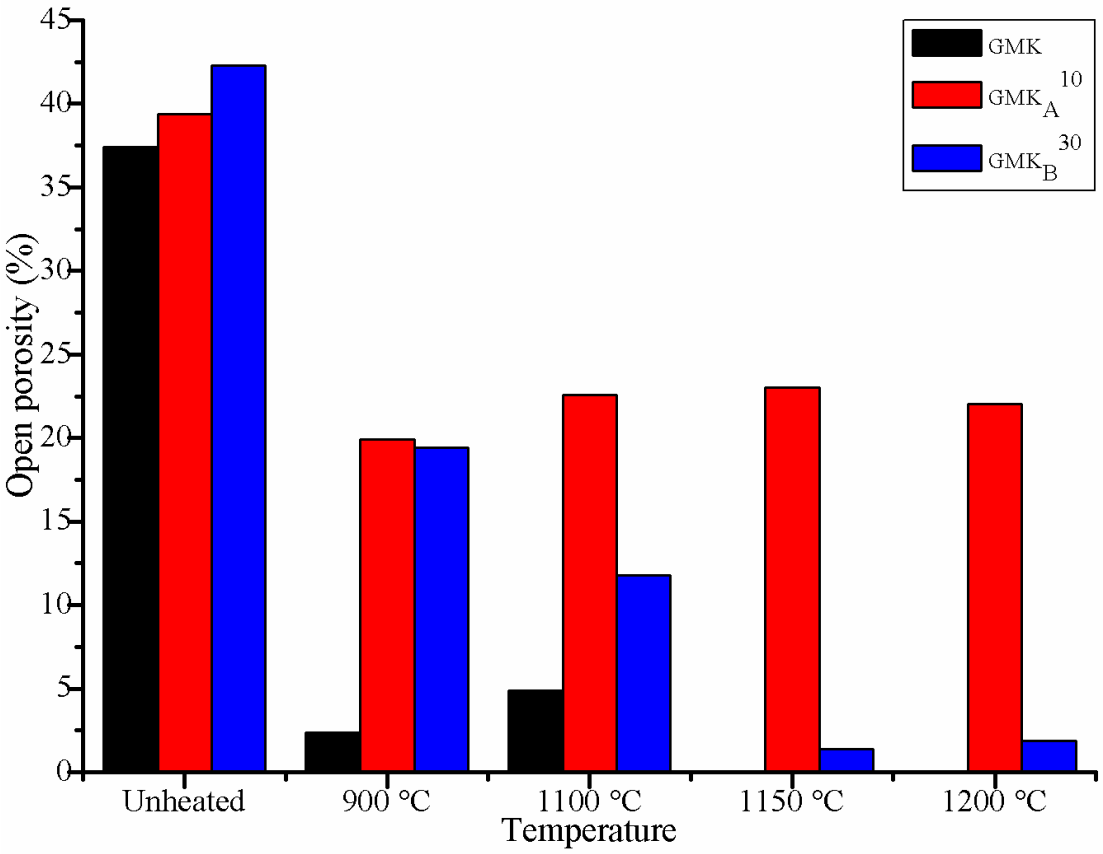

Figure 58: Open porosity of the selected metakaolin-based geopolymers and their heated products.

III.3.5.3 Bulk density

The evolution of the bulk density (BD) of the selected metakaolin-based geopolymer specimens (GMK, GMK_A^{10} and GMK_B^{30}) along with their heated products is shown in Figure

59. The BD of the unheated specimens increases with the increase amount of replacement, most likely attributed to the difference of density of each starting material used (metakaolin and replacements) [110]. At 900 °C, GMK specimens exhibit the highest BD as compared to those of GMK_A^{10} and GMK_B^{30}. This shows that the densification of the former is already achieved whereas those of GMK_A^{10} and GMK_B^{30} specimens are still ongoing most likely due to the refractoriness of the replacements. Nevertheless, the lowering of the BD observed for GMK specimens at 1100 °C could be connected to the presence of closed pores within its microstructure. As for the specimens obtained from partial replacement, the highest BD of GMK_A^{10} is achieved at 900 °C whereas that of GMK_B^{30} is obtained at 1100 °C due to the sintering / densification. Between 1100 and 1200 °C, the BD of GMK_A^{10} specimens remains slightly constant whereas that of GMK_B^{30} decreases, probably due to partial dissolution of Al-Si minerals (nepheline and carnegieite) which generates closed pores within its microstructure.

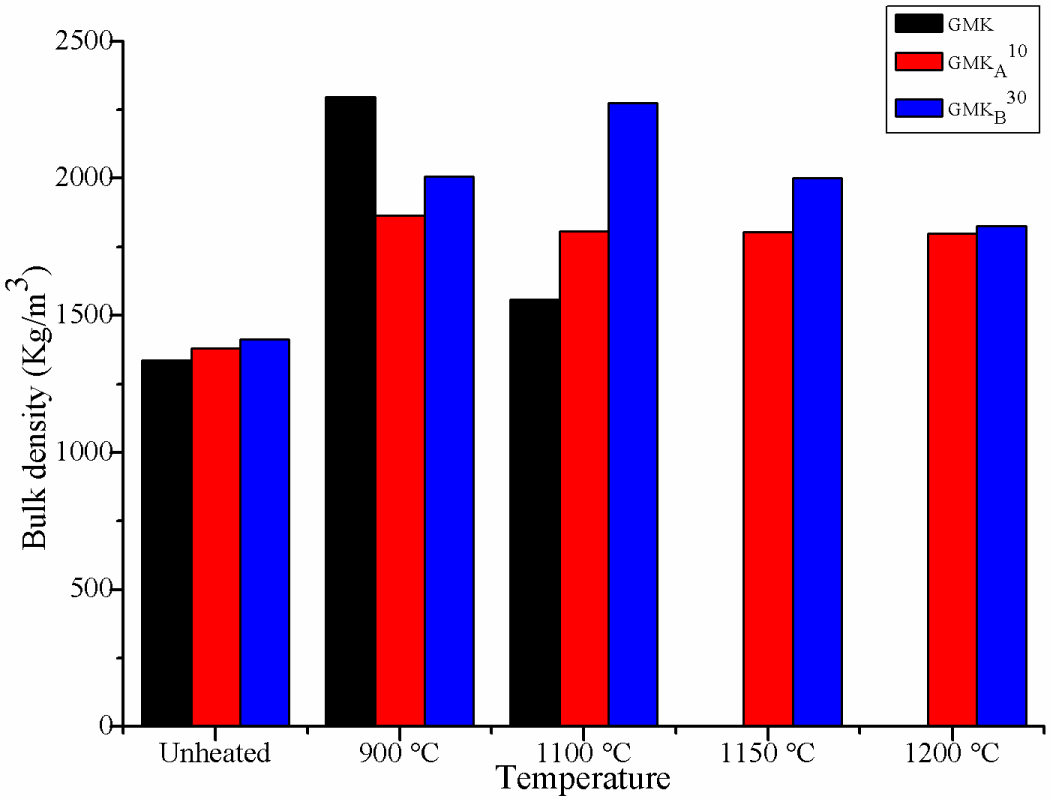

Figure 59: Bulk density of the selected metakaolin-based geopolymers and their heated products.

III.3.6 Compressive strength

Figure 60 exhibits the compressive strength (CS) of the metakaolin-based geopolymer specimens along with their heated products. It appears that CS of the unheated

specimens decreases with the increase amount of replacement. This is due to the fact that, gradual increase of either amorphous aluminium hydroxide or aluminium oxy-hydroxide weakened the strength of specimens since the replacements have not yet reacted chemically. However, CS values of the metakaolin-based geopolymer specimens obtained with partial replacement of amorphous aluminium hydroxide were too low (Figure 60a) as compared to those obtained with aluminium oxy-hydroxide as replacement (Figure 60b). This accounts for the low reactivity of the replacements (A and B) during alkaline activation [38, 58]. At 300 °C, the CS of GMK specimens is reduced as compared to the value observed for the unheated ones, most likely attributed to the gradual transformation of the polysialate gel [15, 21] which is in accordance with the increase of water absorption (Figure 57). As for the specimens obtained from partial replacement with alumina sources, the CS remains slightly constant since the replacements have not yet reacted chemically at that temperature. Between 700 and 900 °C, the CS of all the specimens has increased consistently as result of further geopolymerisation along with the onset of sintering / densification [15]. It is worth pointing out that the enhancement of CS observed for the reference GMK specimens at 900 °C, can be attributed to the presence of great amount of gibbsite in the kaolin sample (Figure 30), which is being transformed into corundum (α-Al_2O_3) at elevated temperatures (900-1100 °C) [23]. Corundum as result of its refractoriness and hardness helps to reinforce and strengthen the microstructure, thereby improving CS [62]. As for the specimens obtained from partial replacement with alumina sources, the CS has increased consistently but remains lower than that of GMK specimens, attesting that the presence of the replacements delays the densification process as result of their refractoriness [61]. At 1100 °C, the CS of GMK specimens has reduced as compared to the value observed at 900 °C, most likely due to the presence of cracks (Figure 55) generated by quartz phase transition(quartz $\alpha \rightarrow$ quartz $\beta \rightarrow$ tridymite) [19, 103]. Conversely, the CS of GMK_A^{10} and GMK_B^{30} specimens has improved, due to the improvement of densification. However, the CS of GMK_A^{10} specimens remains slightly constant at 1150 °C whereas that of GMK_B^{30} specimens exhibits the highest value of CS (76.7 MPa), attributed to both densification and crystallisation of new stable phases [16, 62]. Nevertheless, the decrease of CS recorded at 1200 °C can be attributed to partial dissolution of Al-Si minerals such as nepheline and carnegieite [15].

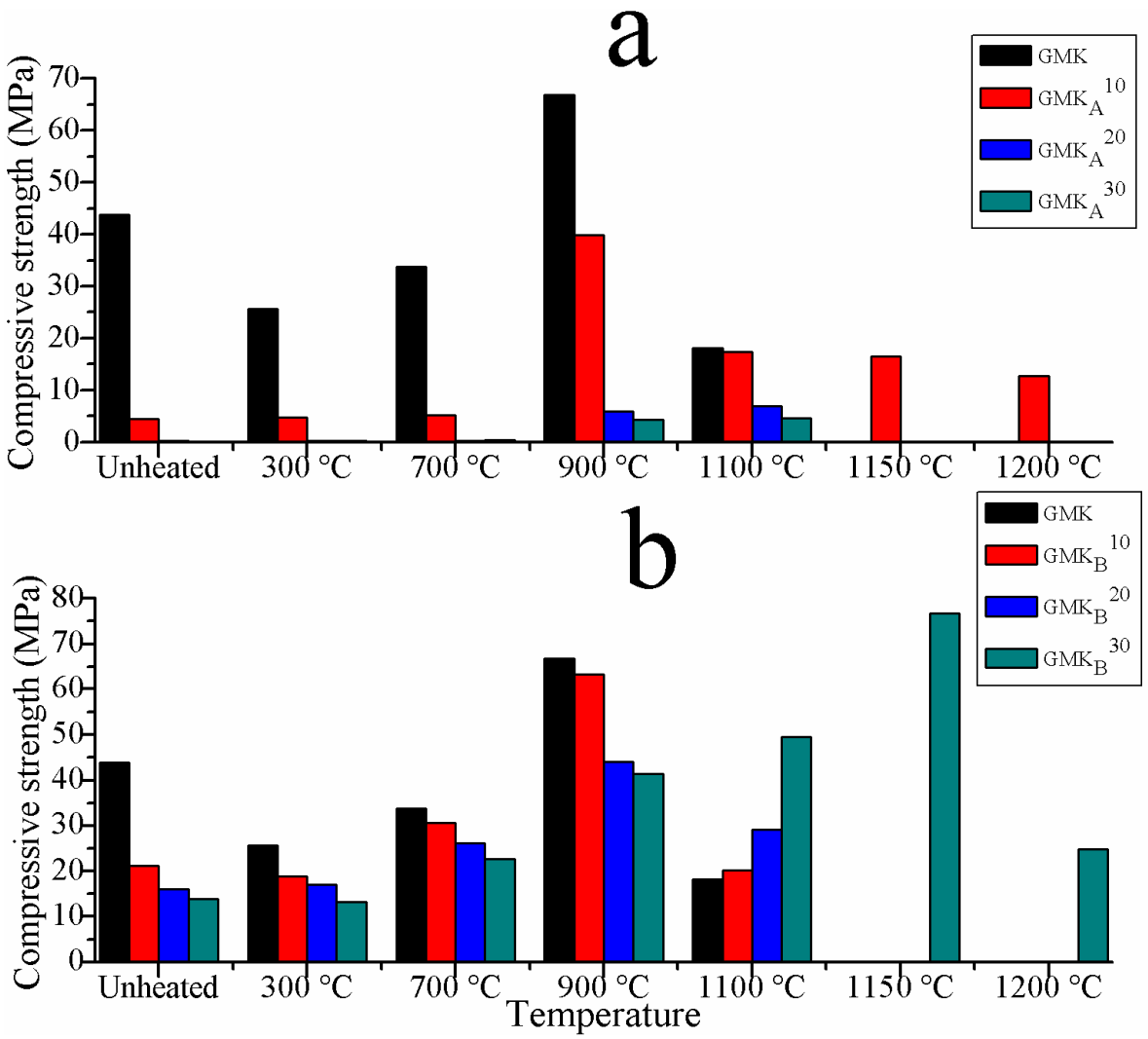

Figure 60: Compressive strength of the metakaolin-based geopolymers and their heated products.

III.3.7 Microstructure

Mineralogical and microstructural characterisations of the selected metakaolin-based geopolymers (GMK, GMK_A^{10} and GMK_B^{30}) along with their heated products were assessed thanks to XRD, FTIR spectroscopy and SEM analyses.

III.3.7.1 Mineralogical composition and phase evolution

XRD (Figures 61-63) between 5 and 70 ° (2θ) were done so as to get better understanding on phase evolution of the selected metakaolin-based geopolymers (GMK, GMK_A^{10} and GMK_B^{30}) before and after thermal exposure (900-1200 °C).

Concerning unheated specimens, GMK and GMK_A^{10} contained illite – 2M1 [$(K,H_3O)(Al,Mg,Fe)_2(Si,Al)_4O_{10}[(OH)_2,(H_2O)]$: PDF# 26-911], anatase [TiO_2: PDF# 21–

1272] and quartz [SiO_2: PDF# 46–1045]. In addition to the latter mentioned crystalline phases, the unheated GMK_B^{30} contains boehmite [γ-AlO(OH): PDF# 21–1307] originating from aluminium oxy-hydroxide. The presence of these crystalline phases as initially observed on mineralogical composition of the starting materials (Figure 30) accounts for both the low reactivity during alkaline activation and for the resulting low compressive strength obtained.

As for the heated specimens, they contained mullite [$Al(Al_{0.83}Si_{1.08}O_{4.85})$: PDF# 89–2814], corundum [α-Al_2O_3: PDF# 10–173], rutile [TiO_2: PDF# 21-1276], quartz and tridymite [SiO_2: PDF# 18–1170], nepheline [(Na,K)$AlSiO_4$: PDF# 89–8763] and carnegieite [$NaAlSiO_4$: PDF# 44–1496]. The presence of these crystalline phases along with sintering / densification helps to reinforce and strengthen the matrix so as to obtain a dense microstructure which exhibits improved compressive strength and enhanced thermal stability.

However, it is interesting to mention that on both the unheated and heated GMK XRD patterns (Figure 61), the order of magnitude of the diffuse halo characteristic of the amorphous phase ($17 ° < 2\theta < 38°$) is well pointed up contrarily to those of the unheated and heated GMK_A^{10} and GMK_B^{30} ones, in which this halo is slightly reduced as result of the presence of the replacement (A or B). Yet, in the heated metakaolin-based geopolymers obtained from partial replacement (GMK_A^{10} and GMK_B^{30}), the main peak intensities of nepheline and carnegieite are highest at 1100 and 1150 °C respectively. This is in accordance with the enhancement of residual compressive strength recorded. Conversely, at 1200 °C, partial dissolution of the latter neo-formed crystalline phases as indicated by the decrease of their main peak intensities (Figures 62-63) accounts for the decrease of residual compressive strength observed.

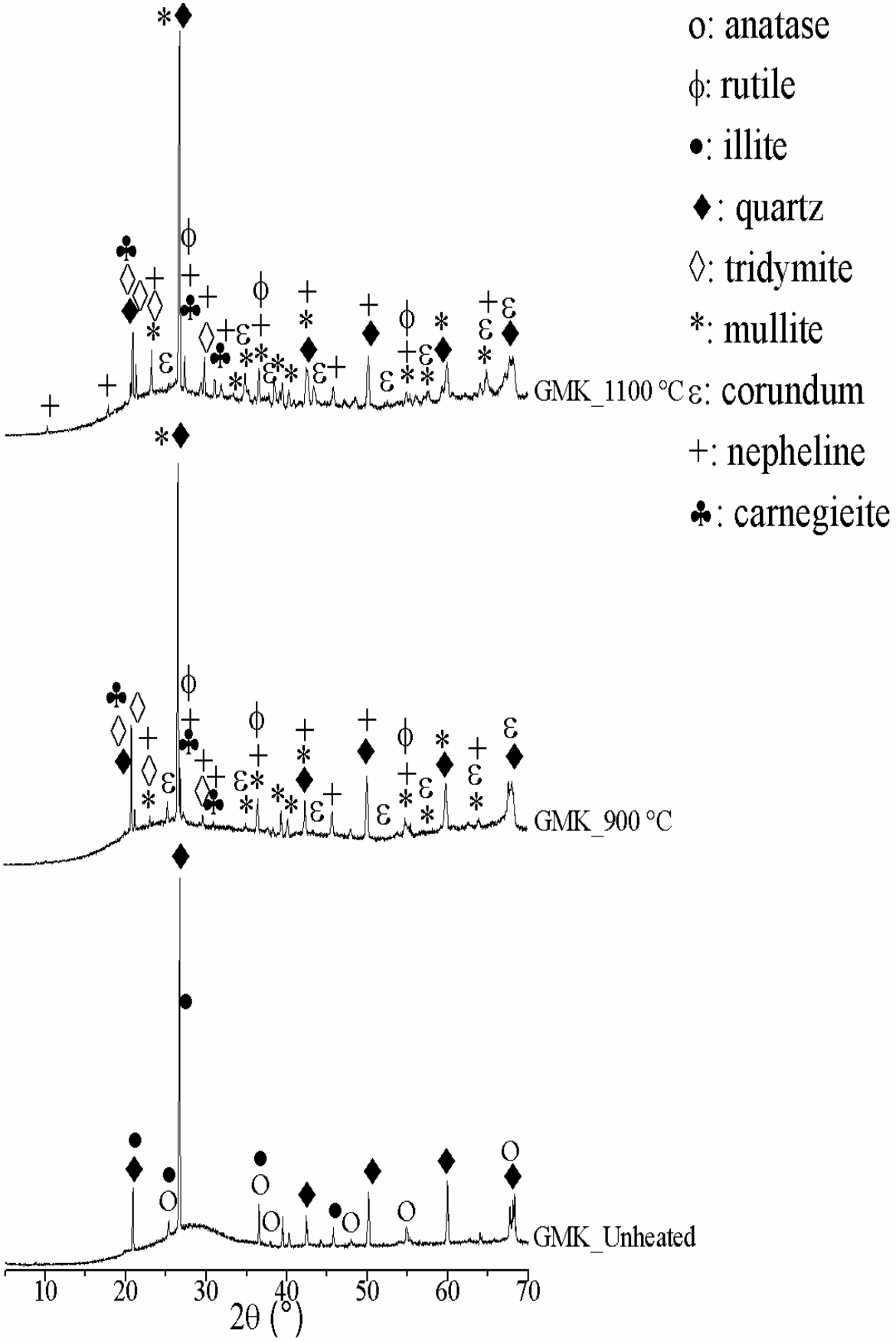

Figure 61: XRD patterns of the metakaolin-based geopolymers (GMK) and their heated products.

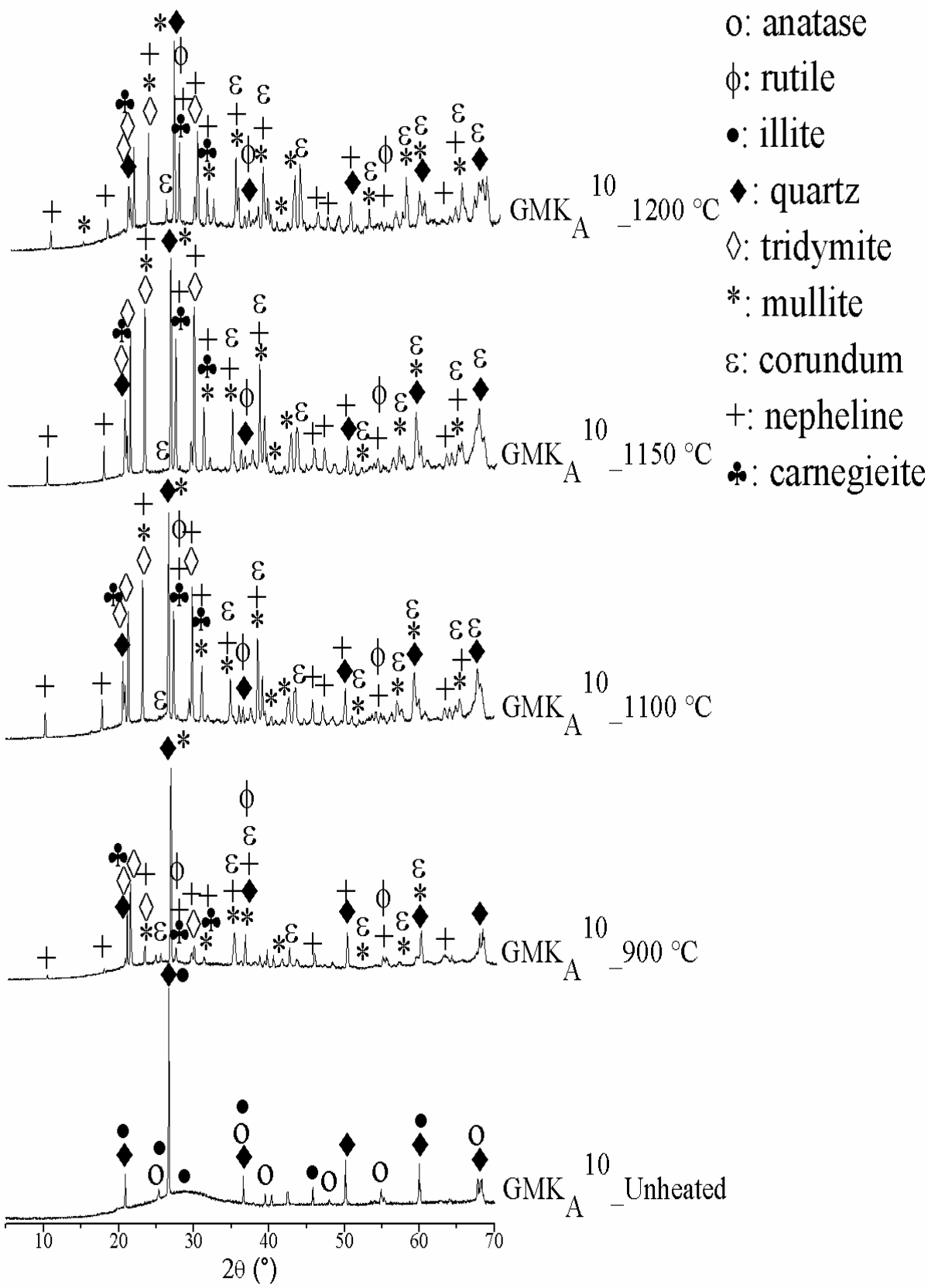

Figure 62: XRD patterns of the metakaolin-based geopolymers obtained with partial replacement of amorphous aluminium hydroxide (GMK_A^{10}) and their heated products.

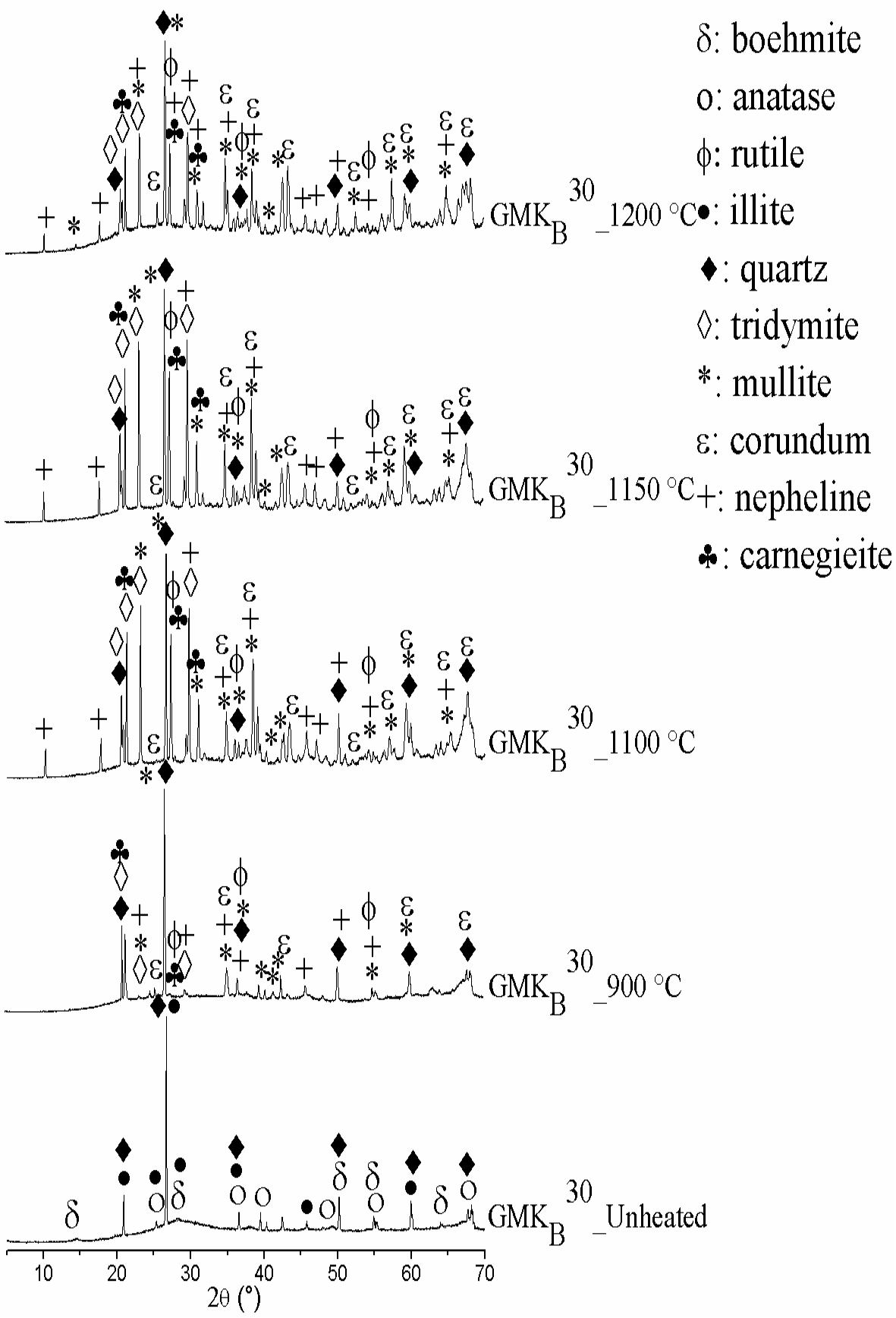

Figure 63: XRD patterns of the metakaolin-based geopolymers obtained with partial replacement of aluminium oxy-hydroxide (GMK_B^{30}) and their heated products.

III.3.7.2 FTIR spectra

FTIR spectra of the selected metakaolin-based geopolymers (GMK, GMK_A^{10} and GMK_B^{30}) along with their heated products are shown in Figure 64.

Concerning unheated and heated specimens, the band around 976 cm^{-1} refers to asymmetric stretching vibration of Si–O–T (T: Si or Al) and T–O–M (M: Na+ or K+), characteristic of the polysialate network [59]. Its progressive shift to low wave numbers indicates better development of polysialate network [59, 78]. Yet, the accurate position of vibration observed within the range of 992–976 cm^{-1} is sensitive to both the length and the angle of Si–O–Si bonds, which is mostly affected by local network and next-nearest neighbours [78]. For unheated specimens, significant broad band located at 3400 cm^{-1} as result of O–H stretching vibration and H–O–H bending vibration around 1648 cm^{-1} are characteristic of surface adsorbed or entrapped water in large cavities of polysialate network [9]. Also, the band around 1391 cm^{-1} is attributed to asymmetric vibration of Al–O and Si–O bonds, indicating the cross-linking in metakaolin-based geopolymers [20]. The peak located at 859 cm^{-1} is attributed to the non-condensed Si–OH bending vibration of silanol [19, 58, 60] suggesting the occurrence of further condensation (geopolymerisation) at elevated temperature, hence building of the polysialate network [60]. At 1200 °C, the specimens of GMK_A^{10} and GMK_B^{30} present three supplementary peaks. The peak around 833 cm^{-1} is attributed to Al(IV)-O bonds [19, 96]. The peaks around 633 cm^{-1} and 568 cm^{-1} are related to the IR characteristics of Al-O octahedrons (hexa-coordinated Al) in corundum, α-Al_2O_3 [19, 96]. The bands within the range of 701–678 cm^{-1} are attributed to symmetric stretching vibration of Si–O–Si and Si–O–Al bonds [94]. Also, the bands within the range of 540–510 cm^{-1} are attributed to bending vibration of Si–O-Al($_{VI}$) bonds [117]. The peak around 450 cm^{-1} is attributed to Si–O–Si or O–Si–O bending vibrations of quartz, showing that either it remains unreacted in strong alkaline medium or it has partially reacted during heating at elevated temperatures (900-1200 °C) to give tridymite [20, 94]. As for the spectra of heated metakaolin-based geopolymers (900-1200 °C), there is a small shoulder around 1100 cm^{-1} attributed to stretching vibration of Si-O in tetrahedron [18, 21, 81]. In fact, the latter appearance may account for new formed Al-Si minerals such as nepheline / carnegieite (Figures 61-63), originating from the transformation of amorphous phase of geopolymer [15, 18]. Additionally, the broadness of these peaks observed within the range of 992-979 cm^{-1} are linked with the high content of nepheline and carnegieite in the specimens of GMK_A^{10} and GMK_B^{30} [18].

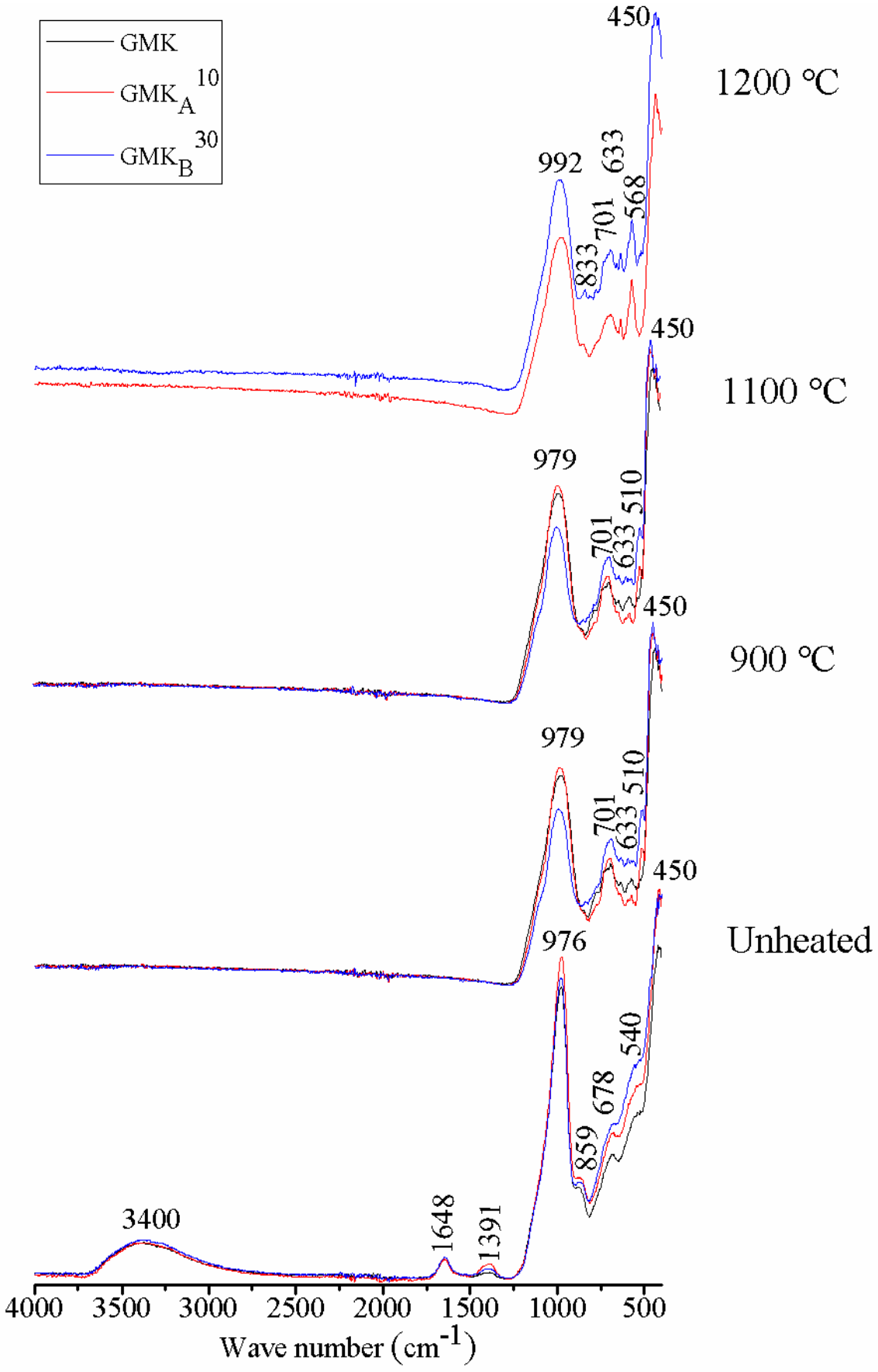

Figure 64: FTIR spectra of the metakaolin-based geopolymers and their heated products.

III.3.7.3 SEM analysis

Figure 65 shows the micrographs of the selected metakaolin-based geopolymer specimens (GMK, GMK_A^{10} and GMK_B^{30}) along with their heated products.

Concerning unheated specimens, the micrograph of GMK shows interlocked-like fibbers, close one to another which makes the whole compact enough material whereas the unheated specimens of GMK_A^{10} and GMK_B^{30} are sponge-like with white aspect in certain areas, reminding the presence of the replacement (Figure 63).

At 900 °C, the micrograph of GMK appears very smooth and shows great compactness [42] whereas those of GMK_A^{10} and GMK_B^{30} exhibit porous features, showing that the replacements delay the densification process due to their refractoriness. At 1100 °C, the micrograph of GMK shows the presence of closed pores and cracks. Inversely, the micrograph of both GMK_A^{10} and GMK_B^{30} show smooth feature with few pores, indicating that the densification process is not yet finished. At 1150 and 1200 °C respectively, the micrographs of GMK_A^{10} and GMK_B^{30} appear highly compact and smooth due to the improvement of densification.

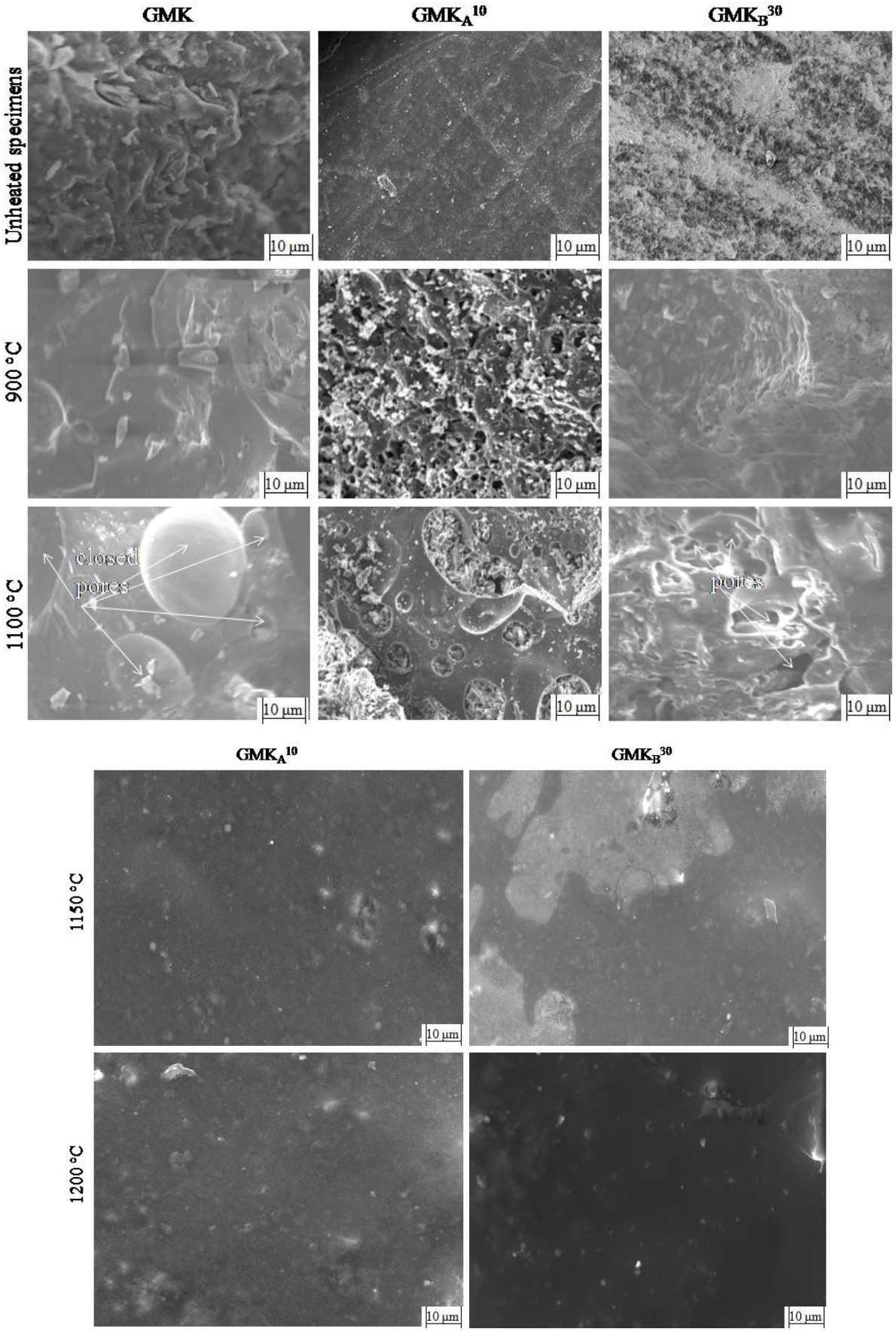

Figure 65: SEM images of the metakaolin-based geopolymers and their heated products.

III.3.8 Conclusion

Amorphous aluminium hydroxide and aluminium oxy-hydroxide partially replace metakaolin during alkaline activation. The as-obtained metakaolin-based geopolymer specimens along with their heated products (300-1200 °C) were characterised. Globally, the unheated products obtained from partial replacement with alumina sources show low compressive strength as compared to those without replacements. This was due to the fact that the replacements have not yet reacted chemically or behaved as fillers. However, thermal behaviour revealed that the presence of replacement lengthens the stability of heated products up to 1200 °C. Thus, without replacement, specimens of metakaolin-based geopolymers showed visible cracks at 1100 °C as result of quartz phase transition. Conversely, the heated ones obtained from partial replacement with alumina sources exhibited good volume stability up to 1200 °C. This was attributed to the refractoriness of replacement along with their contribution to form thermally stable minerals (corundum, mullite). Also, at 1150 °C, specimens obtained with 30 % by mass of aluminium oxy-hydroxide showed highest residual compressive strength of 76.7 MPa, due to the great content of thermally stable minerals (corundum and mullite) coupled with densification. Unfortunately, at 1200 °C, residual compressive strength of specimens dropped as result of partial dissolution of nepheline and carnegieite which generated closed pores within their microstructure. Hence, partial replacement of metakaolin with 30 % by mass of aluminium oxy-hydroxide or 10 % by mass of amorphous aluminium hydroxide during alkaline activation is a suitable process to get thermally stable products endowed with high residual compressive strength.

III.4 Influence of amorphous aluminium hydroxide and aluminium oxy-hydroxide on the thermal stability of alkali-activated volcanic scoria

III.4.1 Flowability behaviour of alkali-activated volcanic scoria pastes

Figure 66 depicts the flowability of alkali-activated volcanic scoria pastes expressed in terms of replacement content and liquid to solid mass ratio (L / S).

However, the L / S of 0.84 was suitable for GZ which was considered as the reference mixture. The same value of liquid to solid mass ratio was suitable for the mixtures GZ_B^{10}, GZ_B^{20} and GZ_B^{30} with aluminium oxy-hydroxide as replacement. They displayed good flowability and were consistent and homogeneous mixtures of particles during and after moulding.

As for the mixtures with amorphous aluminium hydroxide as replacement, L / S of 0.96, 1.13 and 1.34 were respectively tested for GZ_A^{10}, GZ_A^{20} and GZ_A^{30} but this did not allow consolidated specimens. Actually, the difference between the two replacements pertaining to the mass ratio L / S can be ascribed either to the particle size distribution or to the ability of particles to absorb the activating solution. For instance, particle size distribution of amorphous aluminium hydroxide (Figure 28) exhibits a great amount of fine particles as compared to that of aluminium oxy-hydroxide (Figure 29), meanwhile the contact angle of the former is smaller than the latter, thereby requiring a greater amount of activating solution to achieve good wettability. It is worth noting that the specimens of GZ_A^{10}, GZ_A^{20} and GZ_A^{30} were not well consolidated even after 28 days of curing at ambient temperature of the laboratory. This suggested that amorphous aluminium hydroxide may hinder the extent of the formation of the polysialate network [59, 85].

Hence, partial replacement of volcanic scoria by 10; 20 and 30 % by mass of aluminium oxy-hydroxide gave suitable mix designs that led to consolidated alkali-activated volcanic scoria with good flowability. For further assessment in this study, microstructural and mineralogical characterisations were performed only for GZ and GZ_B^{30} which are the two extreme formulations.

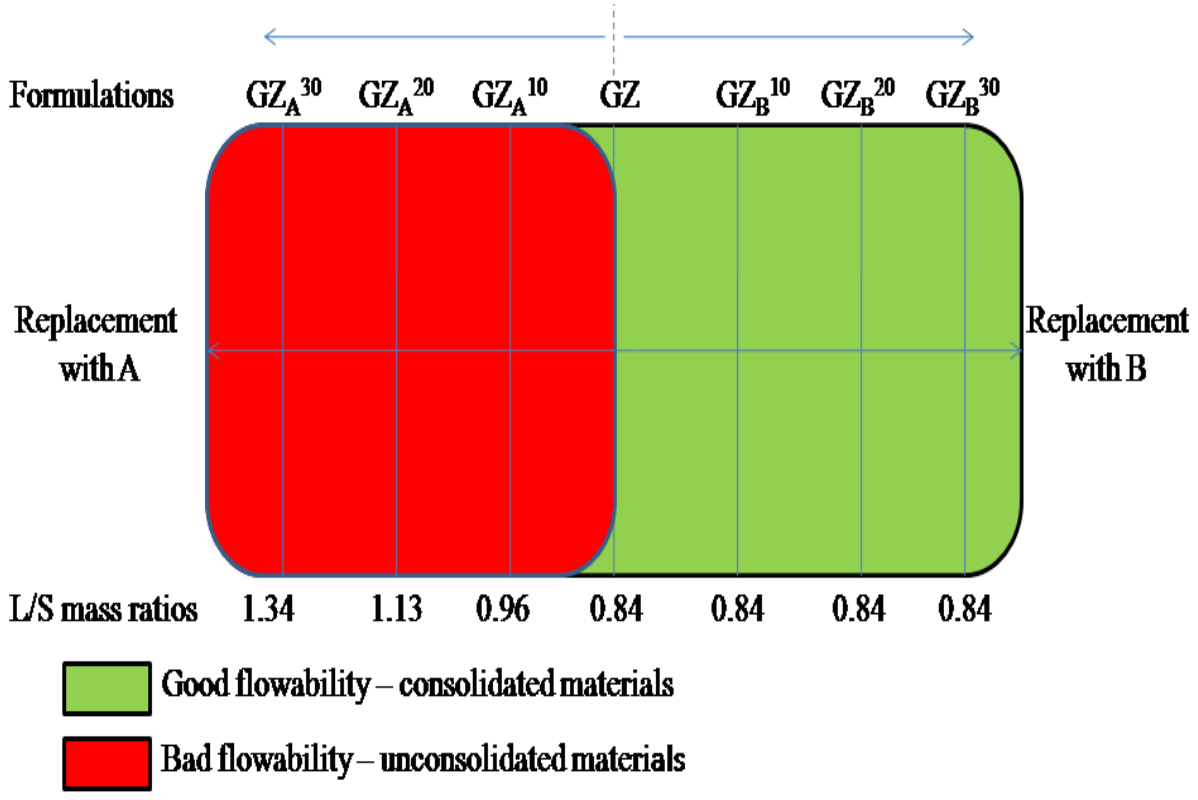

Figure 66: Flowability of alkali-activated volcanic scoria pastes.

III.4.2 Thermal behaviour of hardened alkali-activated volcanic scoria pastes

Thermal behaviour followed by TG / DTG and DTA analyses of the selected hardened alkali-activated volcanic scoria specimens (GZ and GZ_B^{30}) initially cured at ambient temperature and aged 28 days are presented in Figures 67 and 68 respectively.

It appears that each TG / DTG curve exhibits two mass losses. The major mass loss is observed between ambient temperature and 250 °C as depicted by the first broad endothermic peaks with maximum around 90 °C for both GZ and GZ_B^{30} specimens. Indeed, the specimens of GZ and GZ_B^{30} show 8.5 and 9.8 % of mass loss respectively. These mass losses are attributed to the removal of physically absorb water, interstitial and chemically bound water respectively from the polysialate network and aluminium oxy-hydroxide [19, 60-61]. The second minor mass loss (3.6 and 5.0 % respectively for GZ and GZ_B^{30}) which occurred between 250 and 700 °C was attributed to the hydroxyl water from the polysialate gel and aluminium oxy-hydroxide [20, 67, 107] along with the structural water of allophane [104].

Between 800 and 1200 °C, the TG / DTG curves did not show mass loss whereas the DTA ones displayed respectively broad exothermic band for GZ_B^{30} (Figure 68) and broad endothermic peak for GZ (Figure 67). These thermal phenomena corresponded respectively to the crystallisation of new phases for GZ_B^{30} and melting for GZ around 1140 °C [61, 105]. Hence, partial replacement with aluminium oxy-hydroxide is beneficial to prevent the early melting of alkali-activated volcanic scoria specimens. Additionally, thermal behaviour revealed that replacement with aluminium oxy-hydroxide lengthened the thermal stability of alkali-activated volcanic scoria specimens.

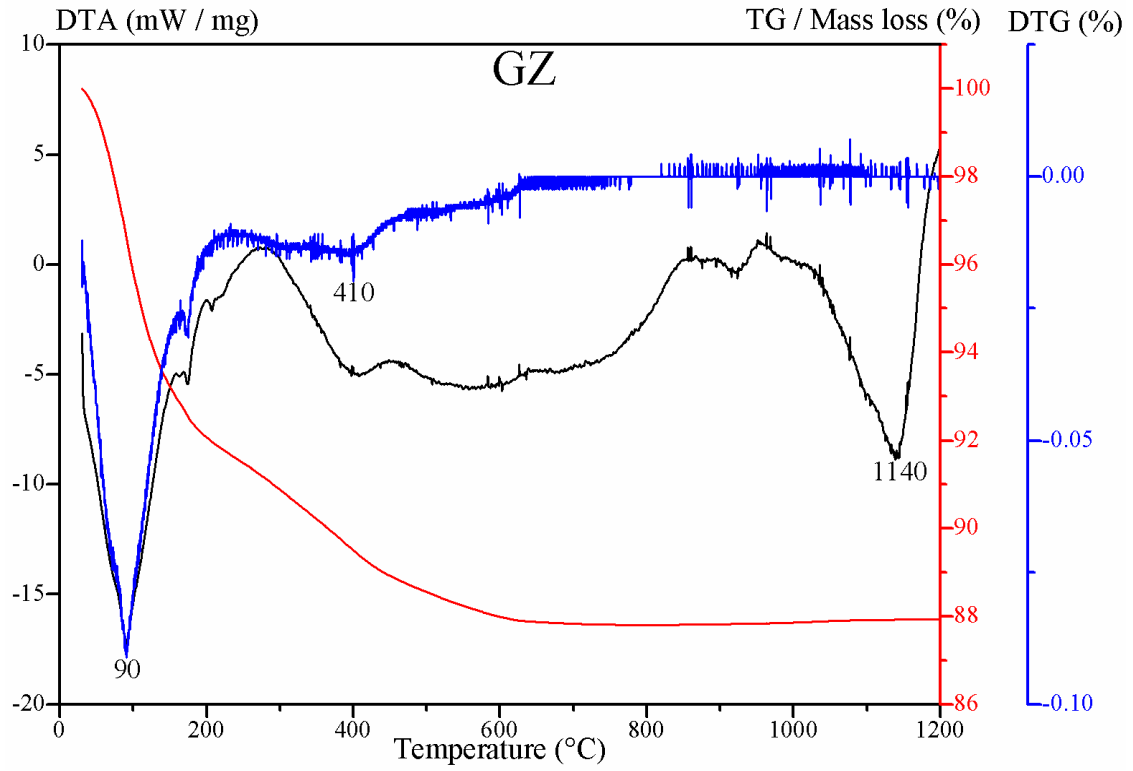

Figure 67: DTA / TG / DTG curves of the alkali-activated volcanic scoria (GZ) initially cured at ambient temperature and aged 28 days.

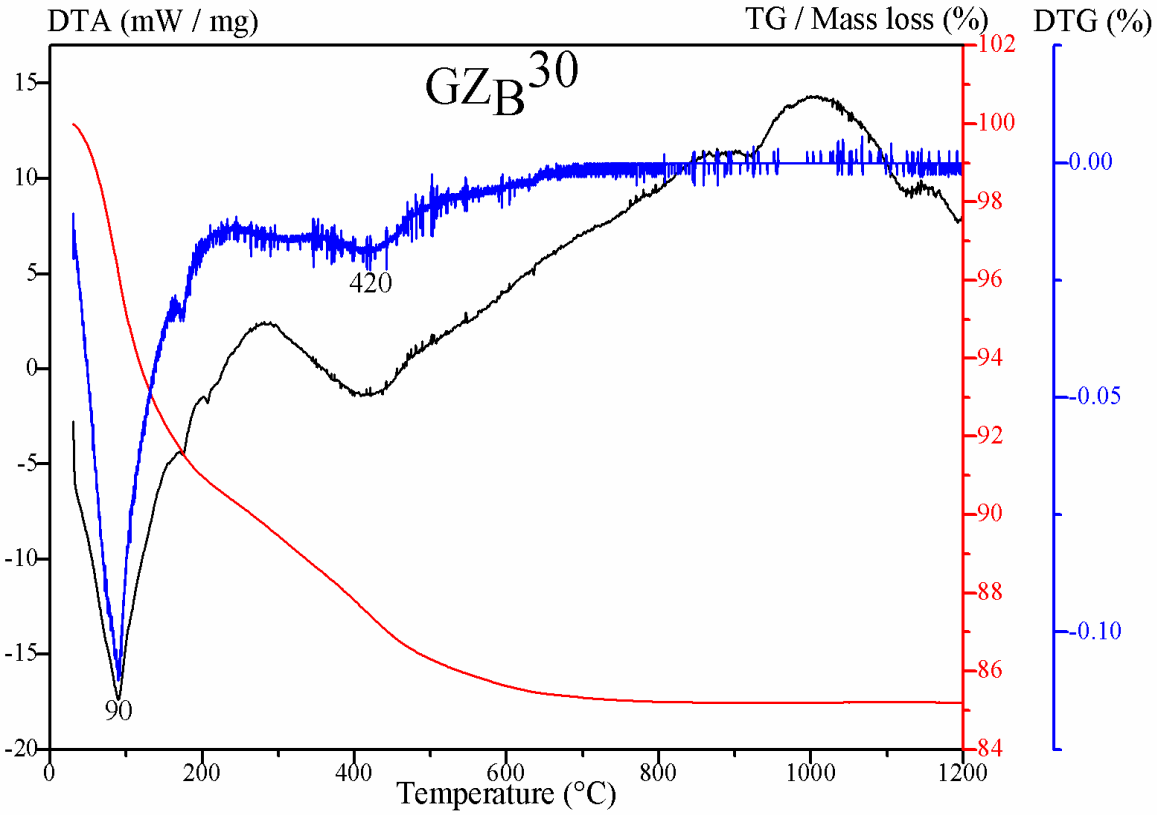

Figure 68: DTA / TG / DTG curves of the alkali-activated volcanic scoria obtained with partial replacement of aluminium oxy-hydroxide (GZ_B^{30}) initially cured at ambient temperature and aged 28 days.

III.4.3 Morphological observation

Visual aspects of the unheated and heated alkali-activated volcanic scoria specimens (GZ and GZ_B^{30}) are shown in Figure 69 and the resulting colour change of bodies are summarised in Table VIII. Globally, the unheated and heated alkali-activated volcanic scoria specimens at 900 °C showed good volume stability without apparent cracks. Additionally, the colours of bodies vary from pale yellow (unheated) to yellowish red (GZ) and reddish yellow (GZ_B^{30}) after heating at 900 °C (Table VIII). This is due to the presence of great content of Fe_2O_3 (13.50 %) and TiO_2 (3.20 %) contained in the chemical composition of the volcanic scoria (Table V) which greatly influence the colour of bodies after heating [84]. At 1100 °C, GZ specimens blacken, exhibit swellings and melt at 1150 °C. Moreover, the colours of bodies vary from yellowish brown to black, most likely attributed to the melting of iron containing minerals. Inversely, GZ_B^{30} specimens heated at least at 1150 °C show good volume stability and there is neither swelling nor crack. Additionally, the colours of bodies vary from brownish yellow to yellowish brown and pale olive at 1200 °C. Hence, as result of its refractoriness, partial replacement of volcanic scoria with aluminium oxy-hydroxide during alkaline activation leads to products endowed with good volume stability up to 1200 °C. This is in accordance with the thermal behaviour results (Figures 67-68).

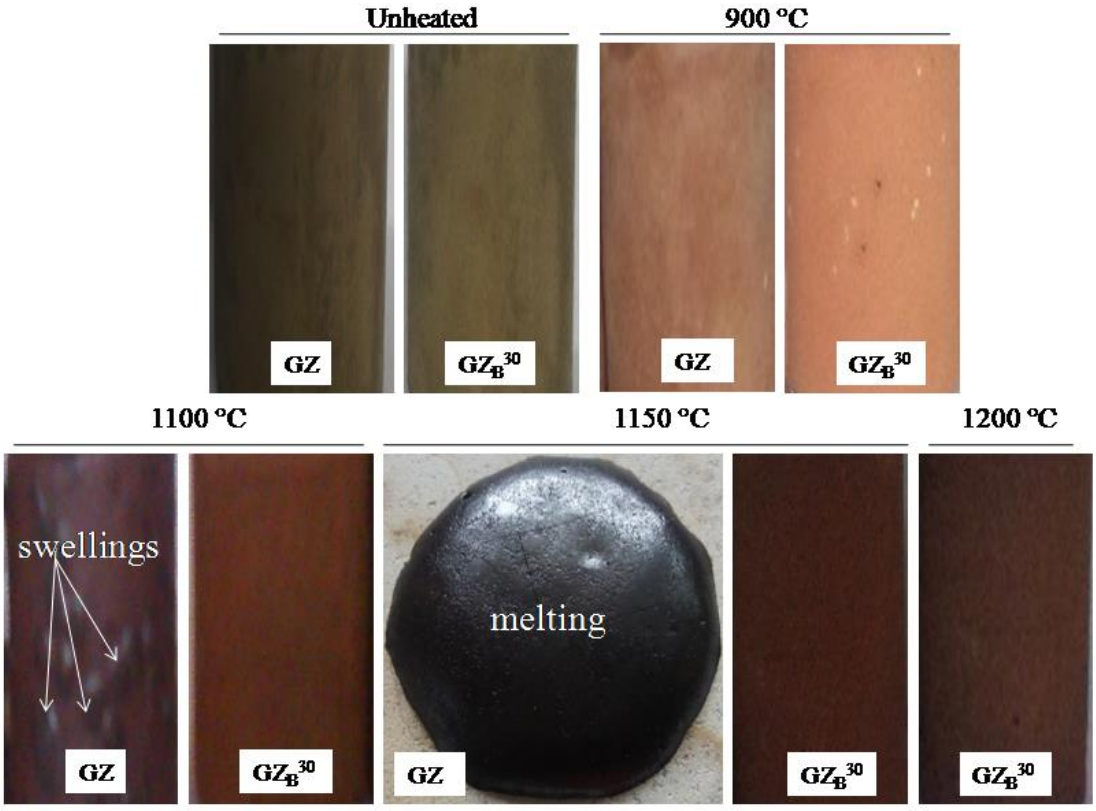

Figure 69: Visual aspect of the alkali-activated volcanic scoria and their heated products.

Table VIII: Colour change of the alkali-activated volcanic scoria versus heating temperature.

Formulations	Temperatures / Colours	(24 ±3) °C	900 °C	1100 °C	1150 °C	1200 °C
GZ	Munsell code	5Y7/4	5YR5/6	10YR5/6	10YR1/2	/
	Visual colour	Pale yellow	Yellowish red	Yellowish brown	Black	/
GZ_B^{30}	Munsell code	5Y7/4	7.5YR8/8	10YR6/6	10YR5/6	5Y6/4
	Visual colour	Pale yellow	Reddish yellow	Brownish yellow	Yellowish brown	Pale olive

III.4.4 Thermal shrinkage

Figure 70 depicts the thermal shrinkage (TS) of the selected heated alkali-activated volcanic scoria specimens (GZ and GZ_B^{30}) versus heating temperature. At 300 °C, partial replacement of volcanic scoria with aluminium oxy-hydroxide leads to the reduction of TS of the resulting alkali-activated volcanic scoria specimens (GZ_B^{30}) as it was already reported in the literature [59]. This can be attributed to the fact that the replacement with aluminium oxy-hydroxide weakens the strength of specimen since the latter has not yet reacted chemically, thereby showing its low reactivity during alkaline activation. Between 700 and 1100 °C, the TS of GZ specimens increase consistently as result of the increasing melting of both the non-reacted activator and alkalis which enable to improve the sintering effect leading to the densification at 1100 °C [15]. As for GZ_B^{30} specimens heated in the same range, the TS increases consistently but with reduced values as compared to those of GZ specimens. This is due to the refractoriness of the replacement that delays the densification process of specimens [61]. Additionally, the highest TS for GZ_B^{30} specimens is obtained at 1150 °C, showing the high reactivity of both volcanic scoria and aluminium oxy-hydroxide as result of the improvement of densification thanks to heating. Nevertheless, the lowering of the TS for GZ_B^{30} specimens at 1200 °C is due to the onset of partial dissolution of Al-Si minerals such as nepheline and carnegieite which induces slight expansion of specimens [15]. Globally, partial replacement of volcanic scoria with aluminium oxy-hydroxide during alkaline activation leads to products endowed with low TS (~ 6 %) after heating at elevated temperatures (1200 °C). This can be technologically applied for structural engineering applications [42, 61].

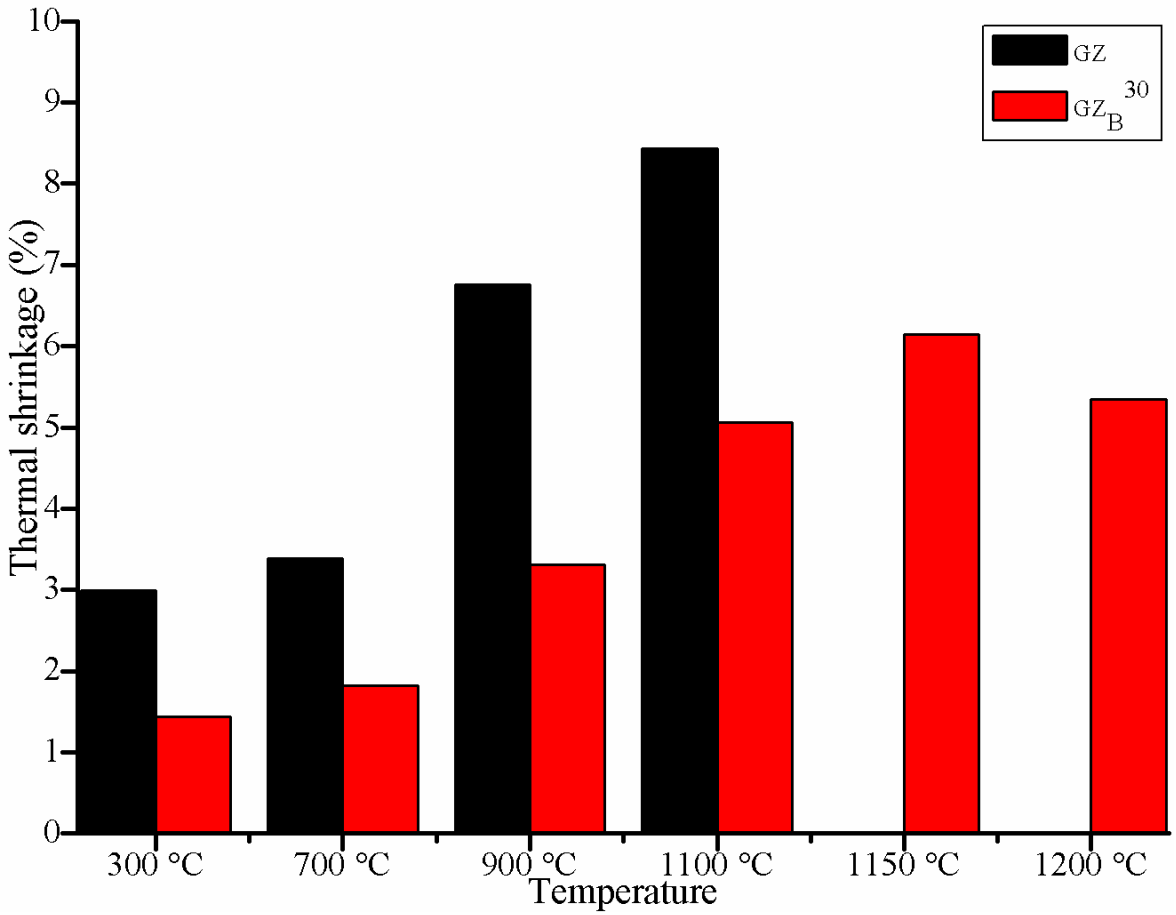

Figure 70: Thermal shrinkage of the heated alkali-activated volcanic scoria specimens.

III.4.5 Physical properties

Physical properties such as water absorption, open porosity and bulk density of alkali-activated volcanic scoria specimens along with their heated products were assessed.

III.4.5.1Water absorption

The variation of water absorption (WA) versus heating temperature of alkali-activated volcanic scoria along with their heated products is presented in Figure 71. WA for unheated alkali-activated volcanic scoria specimens increases with the increase amount of replacement, which may indicate that amorphous aluminium hydroxide and aluminium oxy-hydroxide are either non-reactive or behave as fillers [95]. When comparing with unheated alkali-activated volcanic scoria specimens, WA has increased consistently at 300 °C most likely due to the gradual transformation of the polysialate gel. Moreover, the onset loss of structural water from both the replacements and allophane generates pores which contribute to raise WA [19]. Between 700 and 900 °C, there is slight decreased of WA of specimens as result of the onset of sintering due to the increasing melting of non-reacted alkaline activator

along with alkalis [15, 84]. At 1100 °C, WA of GZ specimens is the lowest (< 2 %) as result of the improvement of sintering leading to the densification. WA for alkali-activated volcanic scoria specimens that initially contain aluminium oxy-hydroxide (GZ_B^{10}-GZ_B^{30}) is slightly reduced (Figure 71b) compared to that observed at 900 °C. This is most likely attributed to the sintering effect [61]. Regarding the alkali-activated volcanic scoria specimens that initially contain amorphous aluminium hydroxide (GZ_A^{10}-GZ_A^{30}), WA is the lowest at 1100 °C (Figure 71a) as result of the high L / S mass ratios used (Figure 66) which enable to enhance the sintering process. Compared with the values obtained at 1100 °C, WA at 1150 °C for GZ_B^{30} has decreased moderately and this was due to the improvement of densification. Due to the good thermal stability (Figure 69), GZ_B^{30} was heated at 1200 °C and it appeared that WA values decreased as result of the onset melting of certain Al-Si minerals which generates vitreous phase [109].

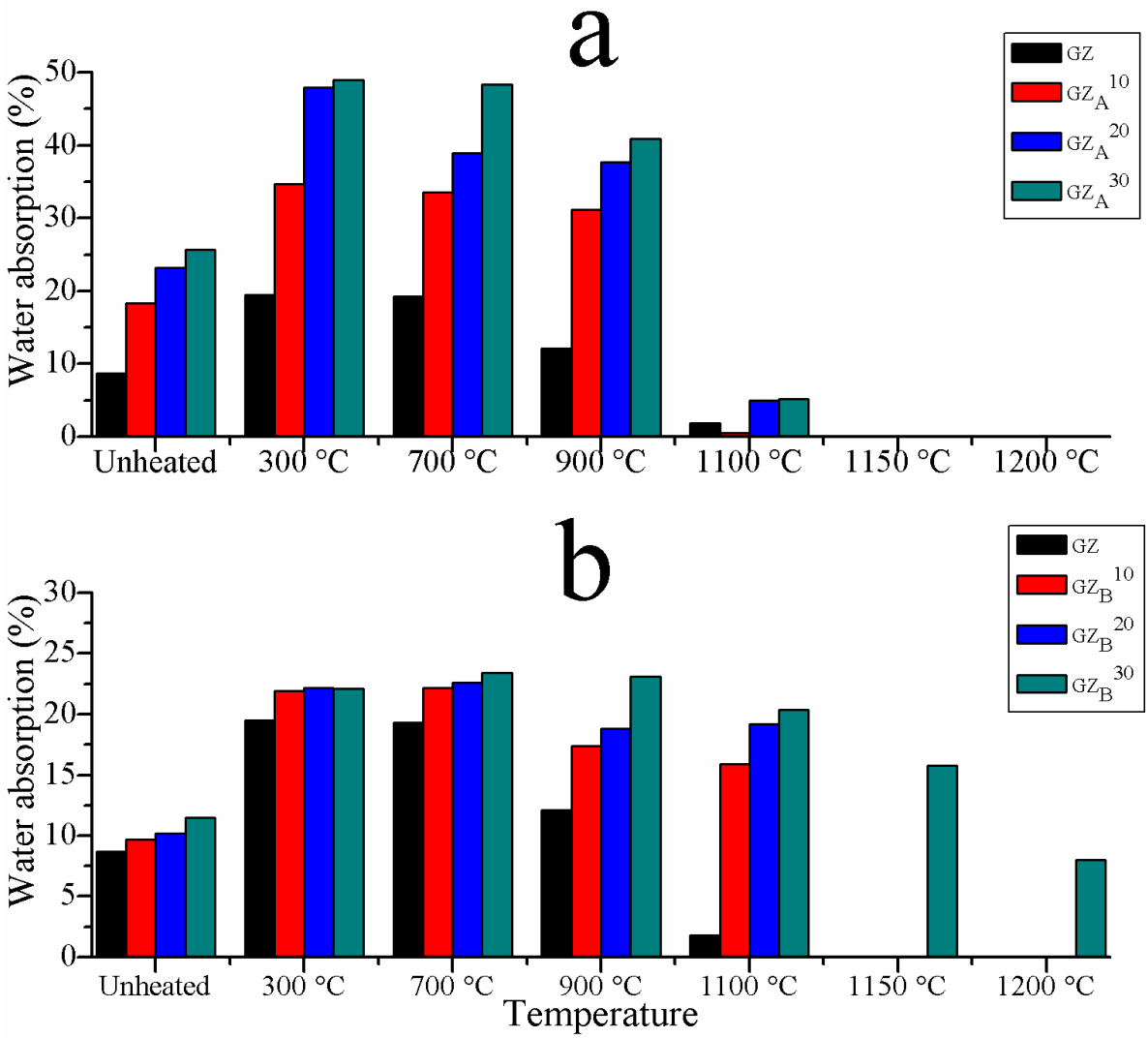

Figure 71: Water absorption of the alkali-activated volcanic scoria and their heated products.

III.4.5.2 Open porosity

Figure 72 shows the variation of open porosity (OP) of the selected alkali-activated volcanic scoria specimens (GZ and GZ_B^{30}) along with their heated products. Concerning unheated specimens, partial replacement of volcanic scoria by aluminium oxy-hydroxide (30 % by mass) during alkaline activation leads to products endowed with increased OP (GZ_B^{30}) as compared to the reference specimens (GZ). This is in accordance with the increase of water absorption as previously observed (Figure 71), probably due to the fact that the replacement has not yet reacted chemically or behaves as filler [95]. After heating at elevated temperatures (900-1100 °C), there is a consistent decreased of OP for the reference specimens (GZ). This is connected to the improvement of sintering effect brought about by the non-reacted alkaline activator along with the increase melting of alkalis [15]. As for the specimens of GZ_B^{30} heated at 900 °C, the OP is increased consistently as result of the presence of the replacement which delays the densification process due to its refractoriness [61]. Conversely, between 1100 and 1200 °C, there is consistent decreased of OP for the specimens of GZ_B^{30} thanks to the improvement of densification along with the onset melting of certain Al-Si minerals which enables the collapse of pores, hence lowering the resulting OP [109].

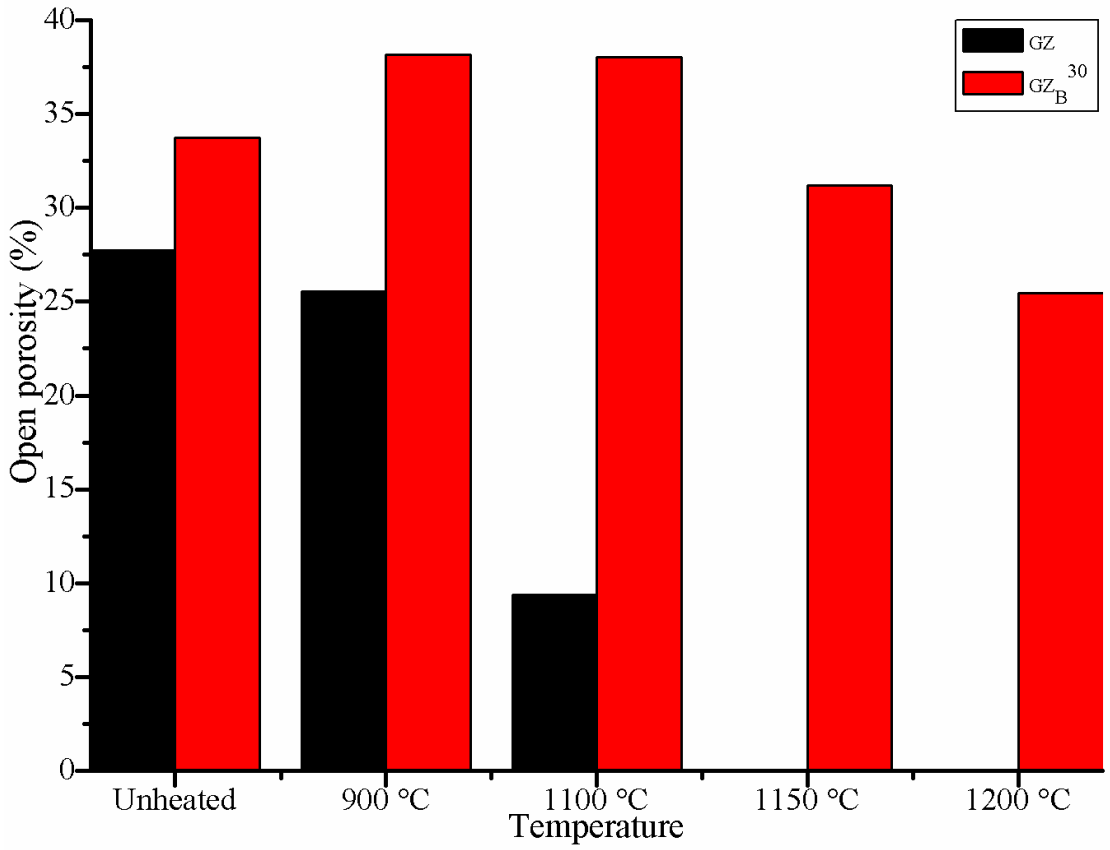

Figure 72: Open porosity of the alkali-activated volcanic scoria and their heated products.

III.4.5.3 Bulk density

The evolution of bulk density (BD) of the selected alkali-activated volcanic scoria specimens (GZ and GZ_B^{30}) along with their heated products is shown in Figure 73. Regarding unheated specimens, the BD is increased in the specimens that contained replacement (GZ_B^{30}) as compared to the reference ones (GZ). This can be explained by the fact that a less dense raw material (volcanic scoria) was replaced by a dense raw material (aluminium oxy-hydroxide) during the synthesis, so as the resulting products exhibited high bulk density [110]. As for heated products, the BD for GZ is increased consistently between 900 and 1100 °C as result of the improvement of densification thanks to sintering effect. Conversely, the BD for GZ_B^{30} is slightly decreased at 900 °C before being increased consistently up to 1200 °C. Indeed, the decrease is due to the presence of the replacement which delays the densification process of specimens heated at 900 °C along with the presence of pores. Nevertheless, further heating at elevated temperatures (1100-1200 °C) is therefore required to improve the densification process in order to achieve a dense structure.

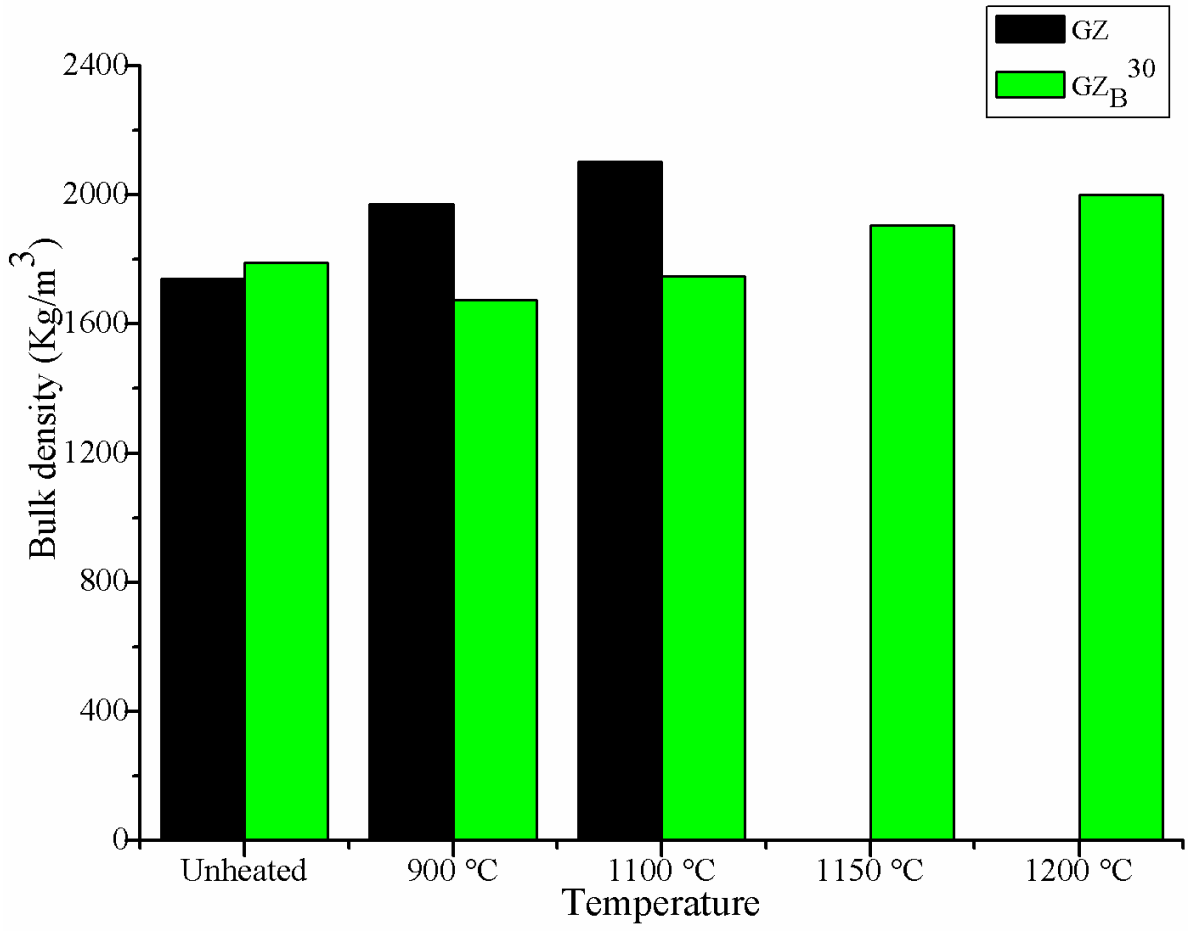

Figure 73: Bulk density of the alkali-activated volcanic scoria and their heated products.

III.4.6 Compressive strength

Figure 74 presents compressive strength (CS) versus temperature of the alkali-activated volcanic scoria along with their heated products. CS of unheated and specimens heated at 300 °C decreases with the increase of replacement. This is due to the fact that, gradual increase of either amorphous aluminium hydroxide or aluminium oxy-hydroxide weakened the strength of specimens since the replacements have not yet reacted chemically. However, it is worth pointing out that CS values of alkali-activated volcanic scoria are too weak as result of the low reactivity of both volcanic scoria and the replacements in alkaline medium [38, 58]. Between 700 and 900 °C, there was improvement of CS for some formulations. This was ascribed to the formation of new crystalline phases along with the onset of densification via the polysialate matrix [21, 46]. Globally, specimens with replacement exhibited lower CS values than those without replacement. Indeed, CS for GZ_A^{10}, GZ_A^{20} and GZ_A^{30} (Figure 74a) were too low for both unheated and specimens heated up to 900 °C as predicted by the flowability behaviour (Figure 66). This was ascribed to the fact that the replacement delayed the densification process thanks to its refractoriness [61]. At 1100 °C, CS values of all the alkali-activated volcanic scoria specimens remained improved as result of the improvement of densification thanks to heating along with the crystallisation of new phases. It is worth pointing out that the enhancement of CS for GZ_A^{10}, GZ_A^{20} and GZ_A^{30} observed at 1100 °C was assigned to great amount of alkaline activator used (Figure 66) for these formulations which reacts as fluxing agent thereby improving the sintering process. At 1150 °C, GZ_B^{30} specimens exhibited highest residual compressive strength of 35.0 MPa (Figure 74b) as result of both densification and greatest content of new formed crystalline phases [46, 109]. As result of their good thermal stability, the specimens of GZ_B^{30} were further heated at 1200 °C. Unfortunately, they exhibited important CS loss of about 62 % which was attributed to partial dissolution of certain Al-Si minerals such as nepheline and carnegieite [15].

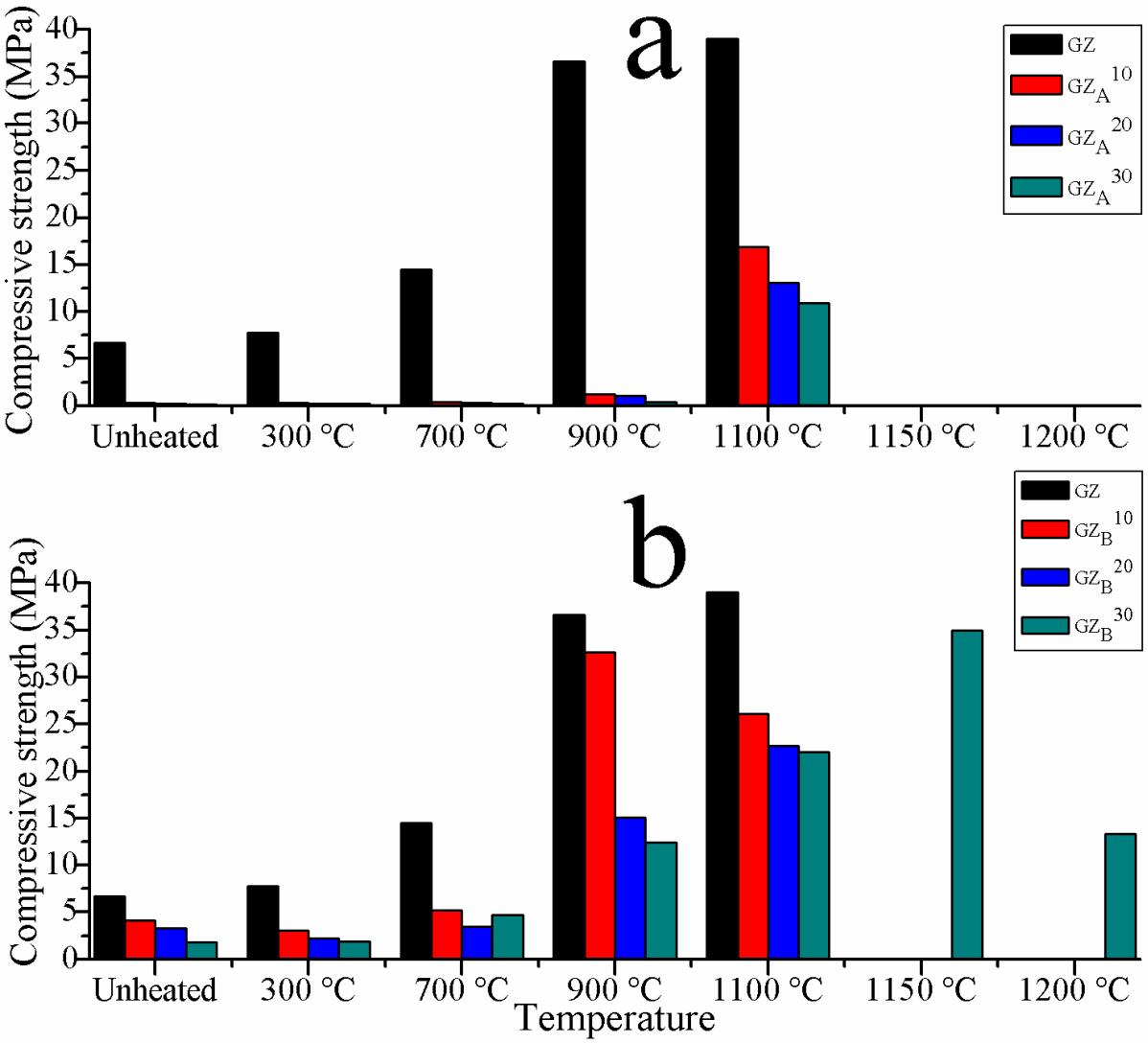

Figure 74: Compressive strength of the alkali-activated volcanic scoria and their heated products.

III.4.7 Microstructure

Mineralogical and microstructural characterisations of the selected alkali-activated volcanic scoria (GZ and GZ_B^{30}) along with their heated products were assessed thanks to XRD, FTIR spectroscopy and SEM analyses.

III.4.7.1 Mineralogical composition and phase evolution

XRD (Figures 75-76) between 5-70 ° (2θ) were done in order to get better understanding on mineralogical composition of the selected alkali-activated volcanic scoria (GZ and GZ_B^{30}) before and after thermal exposures (900-1200 °C).

Pertaining to unheated alkali-activated volcanic scoria, GZ (Figure 75) contains minerals such as forsterite ferroan [$Mg_{1,42}$ $Fe_{0,58}(Si_{0,99}Al_{0,01})O_4$: PDF# 87-0619)], anorthite ordered

[$Ca_{0,66}Na_{0,34}Al_{1,66}Si_{2,34}O_8$: PDF# 12-0301], anorthoclase [$Na_{0,85}K_{0,15}(AlSi_3O_8$): PDF# 75-1635], diopside [$(Ca_{0,89}Mg_{1,11}Si_2O_6)$: PDF# 87-0698], augite [(Ca,Na)(Mg,Fe,Al)$(Si,Al)_2O_6$: PDF# 24-201], hematite [Fe_2O_3 : PDF# 89-0596], maghemite [γ-Fe_2O_3 : PDF# 89-5894], allophane [$SiO_2.Al_2O_3.H_2O$: PDF#02-0039] and anatase [TiO_2: PDF# 21–1272]. In addition to the latter crystalline phases, unheated GZ_B^{30} (Figure 76) contains boehmite [γ-AlO(OH): PDF# 21–1307] originating from aluminium oxy-hydroxide. The presence of crystalline phases such as augite, diopside, hematite, maghemite, forsterite ferroan, anorthite ordered, anorthoclase, allophane, anatase and boehmite in the specimens of unheated alkali-activated volcanic scoria shows their low reactivity during alkaline medium [2, 56]. This accounts for the low compressive strength recorded with unheated alkali-activated volcanic scoria specimens (Figure 74).

However, heated alkali-activated volcanic scoria specimens (GZ and GZ_B^{30}) contain mullite [$Al(Al_{0.83}Si_{1.08}O_{4.85})$: PDF# 89–2814], corundum [α-Al_2O_3: PDF# 10–173], nepheline [(Na,K)$AlSiO_4$: PDF# 89–8763], carnegieite [$NaAlSiO_4$: PDF# 44–1496], hematite, augite, diopside and rutile [TiO_2: PDF# 21-1276]. The absence of allophane, boehmite and other minerals is attributed to their thermal transformations. It is worth pointing out that in the heated alkali-activated volcanic scoria specimens, there is gradual transformation of both the amorphous phase ($17° \leq 2\theta \leq 38°$) and boehmite probably into Al-Si minerals such as nepheline, carnegieite, mullite and corundum. Additionally, the presence of the latter mentioned crystalline phases contributes to reinforce and strengthen the polysialate matrix and which leads to improve residual compressive strength of heated products (Figure 74).

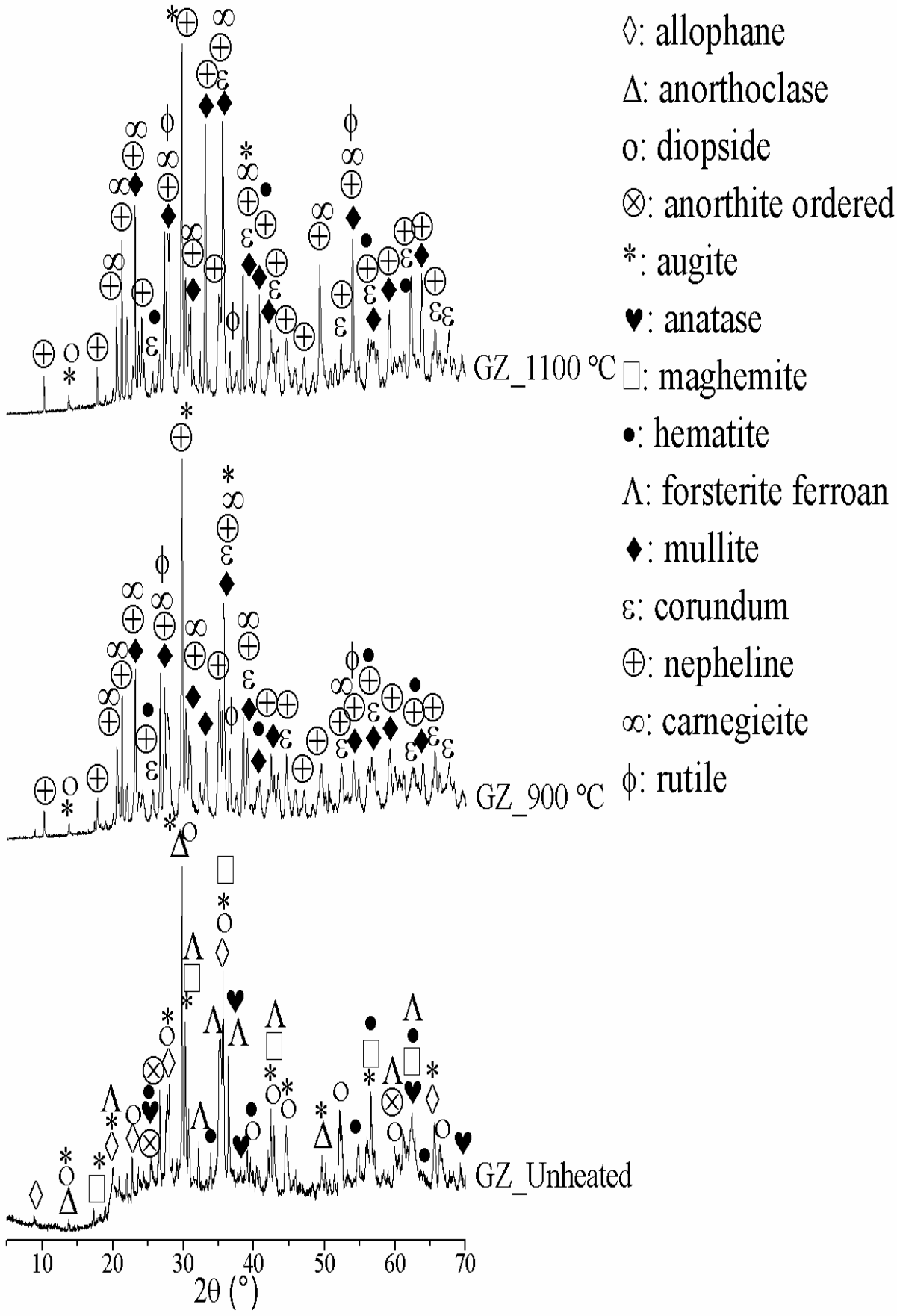

Figure 75: XRD patterns of the alkali-activated volcanic scoria (GZ) and their heated products.

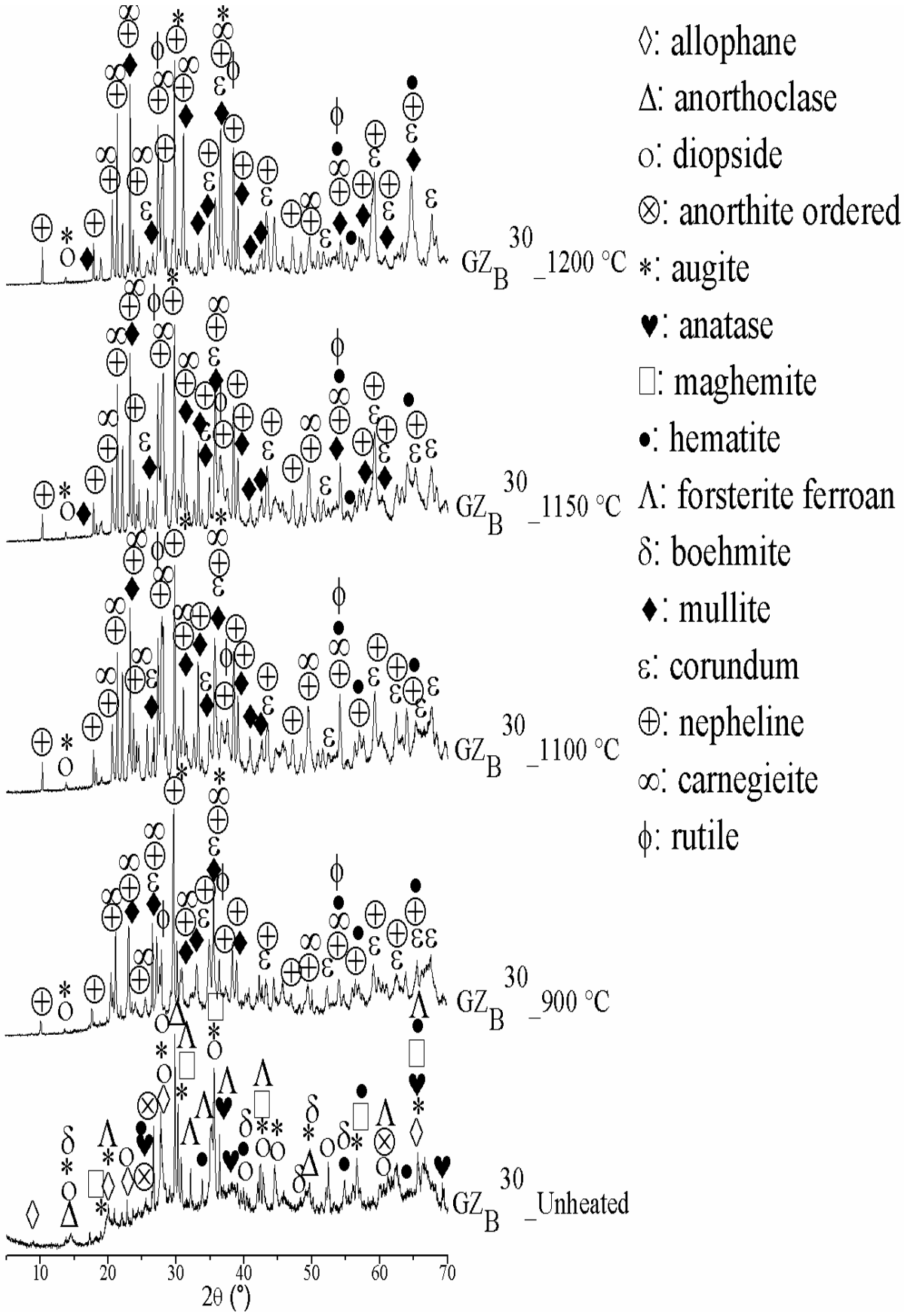

Figure 76: XRD patterns of the alkali-activated volcanic scoria obtained with partial replacement of aluminium oxy-hydroxide (GZ_B^{30}) and their heated products.

III.4.7.2 FTIR spectra

FTIR spectra of the selected alkali-activated volcanic scoria (GZ and GZ_B^{30}) along with their heated products are shown in Figure 77. Referring to unheated alkali-activated volcanic scoria specimens, the narrow peaks around 995 cm^{-1} refer to asymmetric stretching vibration of Si–O–T (T: Si or Al) and T–O–M (M: Na+ or K+), characteristic of the polysialate network [59, 118]. Its progressive shift to low wave numbers usually indicates better development of the polysialate network [59, 78]. Yet, the accurate position of vibration observed within the range of 995–979 cm^{-1} for unheated and heated specimens, is sensitive to both the length and the angle of Si–O–Si bonds, which is mostly affected by local network and next-nearest neighbours [78]. Additionally, the shoulder located at 1100 cm^{-1} along with the peaks observed around 979 cm^{-1} for heated specimens have become broad as result of the presence of great content of Al-Si minerals such as nepheline and carnegieite resulting from the crystallisation of the amorphous phase, as observed in the mineralogical compositions (Figures 75-76) [18]. For unheated specimens, significant broad band around 3400 cm^{-1} as result of O–H stretching vibration and H–O–H bending vibration at 1641 cm^{-1} are characteristic of surface adsorbed or entrapped water in large cavities of the polysialate network [9, 118]. Also, the bands within the range of 1489–1420 cm^{-1} are attributed to stretching vibrations of O–C–O bonds which highlight the existence of efflorescence due to atmospheric carbonation of the alkali-activated volcanic scoria specimens [9, 59]. The peaks within the range of 730–688 cm^{-1} are attributed to symmetric stretching vibration of Si–O–Si and Si–O–Al bonds [94]. For heated specimens, the peaks around 584 cm^{-1} and 572 cm^{-1} are related to the IR characteristics of Al-O octahedrons (hexa-coordinated Al) in corundum, α-Al_2O_3 [19, 96]. Also, the bands within the range of 513–510 cm^{-1} are attributed to bending vibrations of Si–O-Al($_{VI}$) bonds [117]. The peaks within the range of 468–440 cm^{-1} are attributed to Si–O–Si or O–Si–O bending vibrations of silica [20, 94].

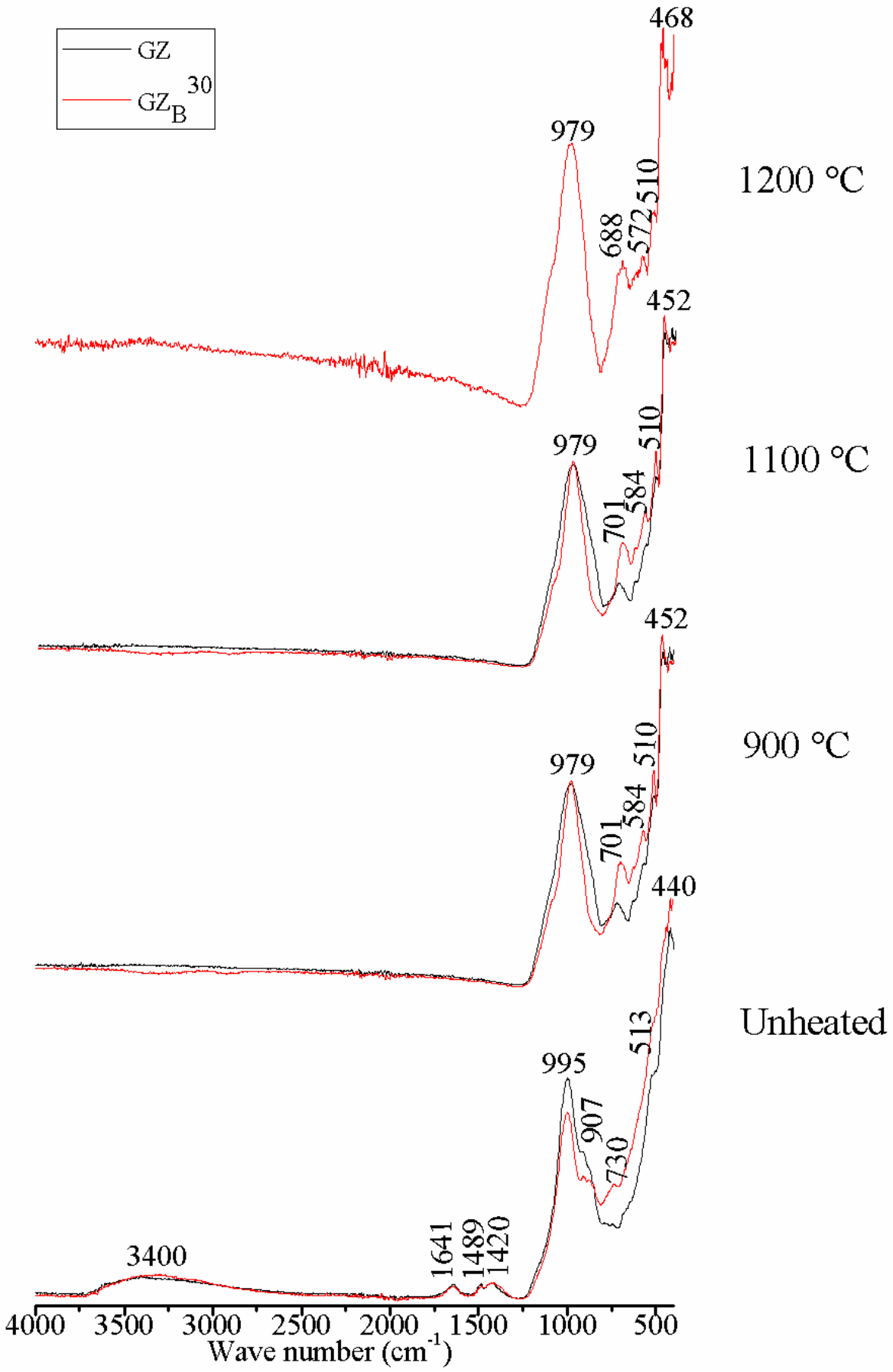

Figure 77: FTIR spectra of the alkali-activated volcanic scoria and their heated products.

III.4.7.3 SEM analysis

Figure 78 shows the micrographs of the selected alkali-activated volcanic scoria (GZ and GZ_B^{30}) along with their heated products. The micrographs of the unheated GZ and GZ_B^{30} exhibit heterogeneous feature with visible unreacted particles probably attributed to the low reactivity of both volcanic scoria and aluminium oxy-hydroxide during alkali-activation. At 900 °C, the micrographs of both GZ and GZ_B^{30} remain porous and compared to the unheated ones, the particles are closer one to another. Additionally, the matrix of GZ is more compact than that of GZ_B^{30} showing that the replacement delays the densification process due to its refractoriness. At 1100 °C, the micrograph of GZ displays smooth and compact feature though there are abundant large closed pores in comparison to the micrograph of GZ_B^{30} which exhibits compactness and very small pores. At 1150 °C, the micrograph of GZ_B^{30} appears highly compact due to the improvement of densification. At 1200 °C, the compactness for GZ_B^{30} begins to be partially deteriorated due the presence of closed pores probably generated by partial dissolution of crystalline phases such as nepheline and carnegieite [15].

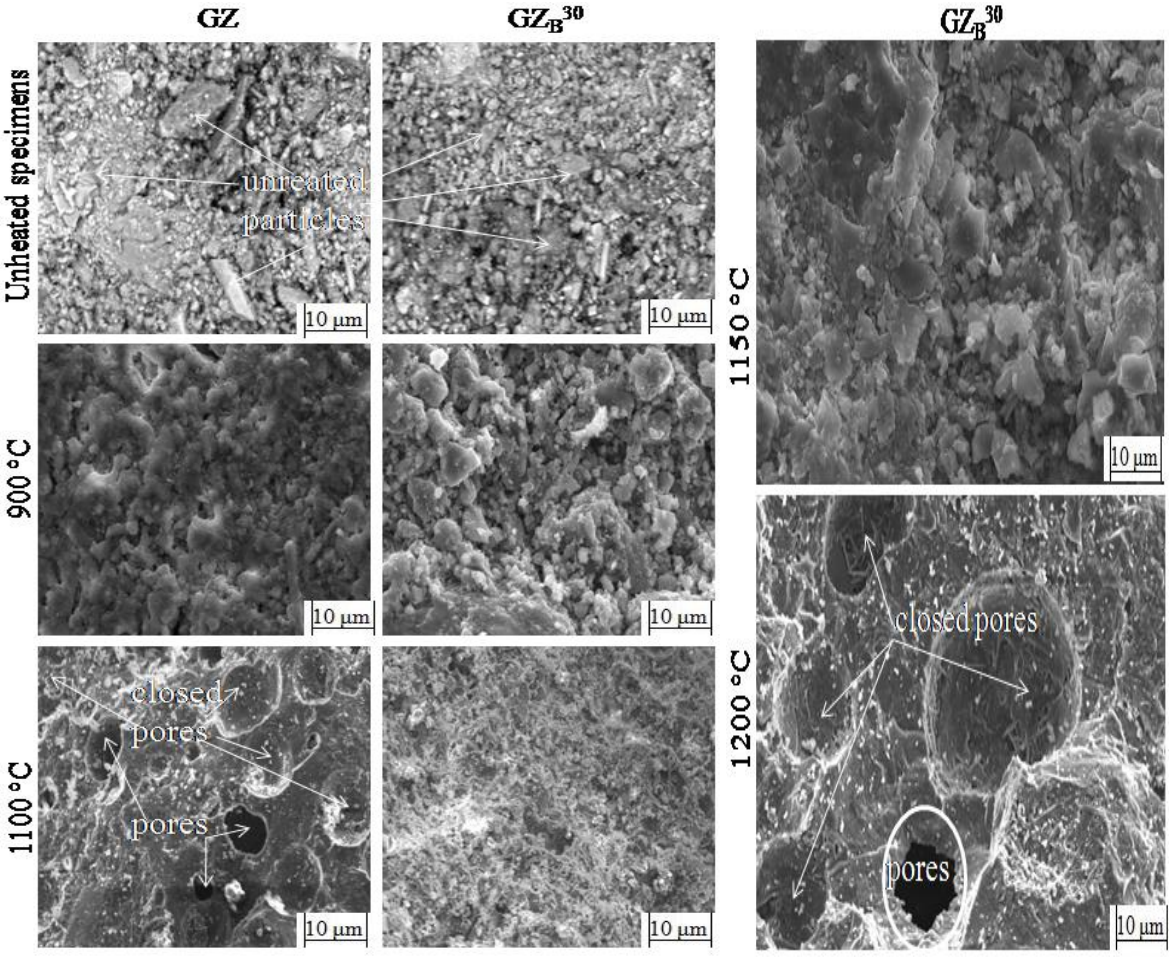

Figure 78: SEM images of the alkali-activated volcanic scoria and their heated products.

III.4.8 Conclusion

Amorphous aluminium hydroxide and aluminium oxy-hydroxide partially replace volcanic scoria during alkaline activation. The as-obtained specimens along with their heated products (300-1200 °C) were characterised. Unheated alkali-activated volcanic scoria specimens that contained replacements showed low compressive strength as compared to those without replacements. This was due to the fact the replacements have not yet reacted chemically, so they behaved as fillers. As for heated specimens, thermal behaviour revealed that the presence of aluminium oxy-hydroxide improved thermal stability of heated alkali-activated volcanic scoria up to 1200 °C as compared to those without replacement. Indeed, without aluminium oxy-hydroxide, specimens of alkali-activated volcanic scoria exhibited swelling at 1100 °C and melted at 1150 °C. Conversely, heated specimens of alkali-activated volcanic scoria with aluminium oxy-hydroxide led to good volume stability up to 1200 °C. This was attributed to the refractoriness of the replacement along with its contribution to the formation of thermally stable minerals (corundum, mullite). Also, at 1150 °C, specimens with 30 % by mass of aluminium oxy-hydroxide showed highest residual compressive strength of 35 MPa due to both increasing content of thermally stable minerals (corundum and mullite) and sintering. Unfortunately, residual compressive strength of alkali-activated specimens with aluminium oxy-hydroxide that were heated at 1200 °C dropped as result of partial dissolution of nepheline and carnegieite which generated closed pores within their microstructure. Hence, partial replacement of volcanic scoria with up to 30 % by mass of aluminium oxy-hydroxide during alkaline activation is a suitable process to get thermally stable products.

III.5 Comparison of thermal stability of resulting alkali-aluminosilicate products

This comparison was done thanks to both thermal behaviours and residual compressive strengths of resulting heated products.

III.5.1 Thermal behaviour of resulting products

DTA curves (between 20 and 1200 °C) of the selected hardened alkali-aluminosilicate products (GK, GK_A^{10}, GK_B^{30}, GMK, GMK_A^{10}, GMK_B^{30}, GZ and GZ_B^{30}) are summarised in Figure 79. Globally, all curves show broad exothermic bands within the range of 800 and 1200 °C as result of densification along with the crystallisation of new phases as previously discussed. However, the broad exothermic bands in the reference specimens obtained without replacements (GK, GMK and GZ) are followed by broad endothermic peaks

around 1150 °C most likely attributed to the onset melting of certain Al-Si minerals available in low amount. Conversely, the counterpart obtained from partial replacement with alumina sources (GK_A^{10}, GK_B^{30}, GMK_A^{10}, GMK_B^{30} and GZ_B^{30}) do not show broad endothermic bands but they rather present broad exothermic bands which are lengthened up to 1200 °C. This is mostly ascribed to the presence of the replacements which enables the crystallisation of new stable phases such as mullite, corundum, nepheline and carnegieite in greater amount. These crystalline phases contribute to reinforce the sintered matrix, thereby improving thermal stability of resulting products. Thus, used in certain proportions, both amorphous aluminium hydroxide and aluminium oxy-hydroxide lengthened the thermal stability of kaolin and metakaolin-based geopolymers respectively as well as alkali-activated volcanic scoria specimens up to 1200 °C.

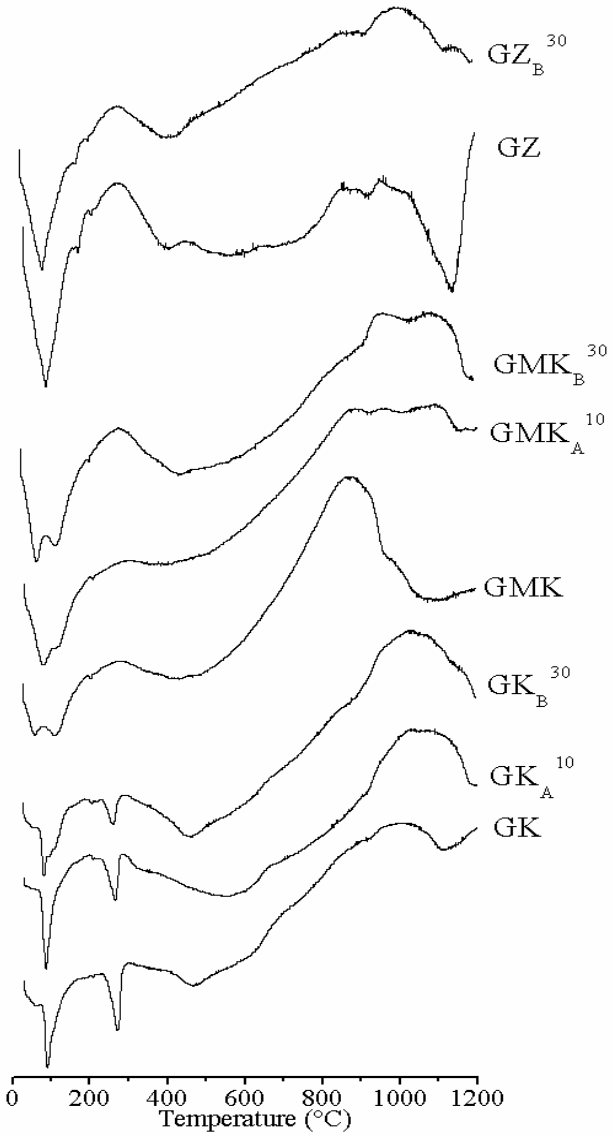

Figure 79: DTA curves of the selected hardened alkali-aluminosilicate products.

III.5.2 Residual compressive strength after thermal exposure

Figure 80 presents residual compressive strength of the selected alkali-aluminosilicate products initially exposed at elevated temperatures (900-1200 °C). Basically, it can be observed that residual compressive strength depends on both the mix designs and the heating temperature. However, for refractory or elevated temperature applications requiring the temperature around 900 °C, the specimens of GMK, GMK_A^{10}, GMK_B^{30} and GZ as result of their high residual compressive strength can be used rather than other formulations. But, if the required temperature is extended around 1100 °C, the most convenient formulations to be used are GMK_B^{30}, GZ and GK_B^{30}. Moreover, if the required temperature is around 1150 °C, the formulations to be used are GMK_B^{30}, GK_A^{10} and GZ_B^{30}. Additionally, if the required temperature is around 1200 °C, the most indicated formulations to be used are GK_A^{10} and GMK_B^{30} thanks to the enhance thermal stability and high residual compressive strength.

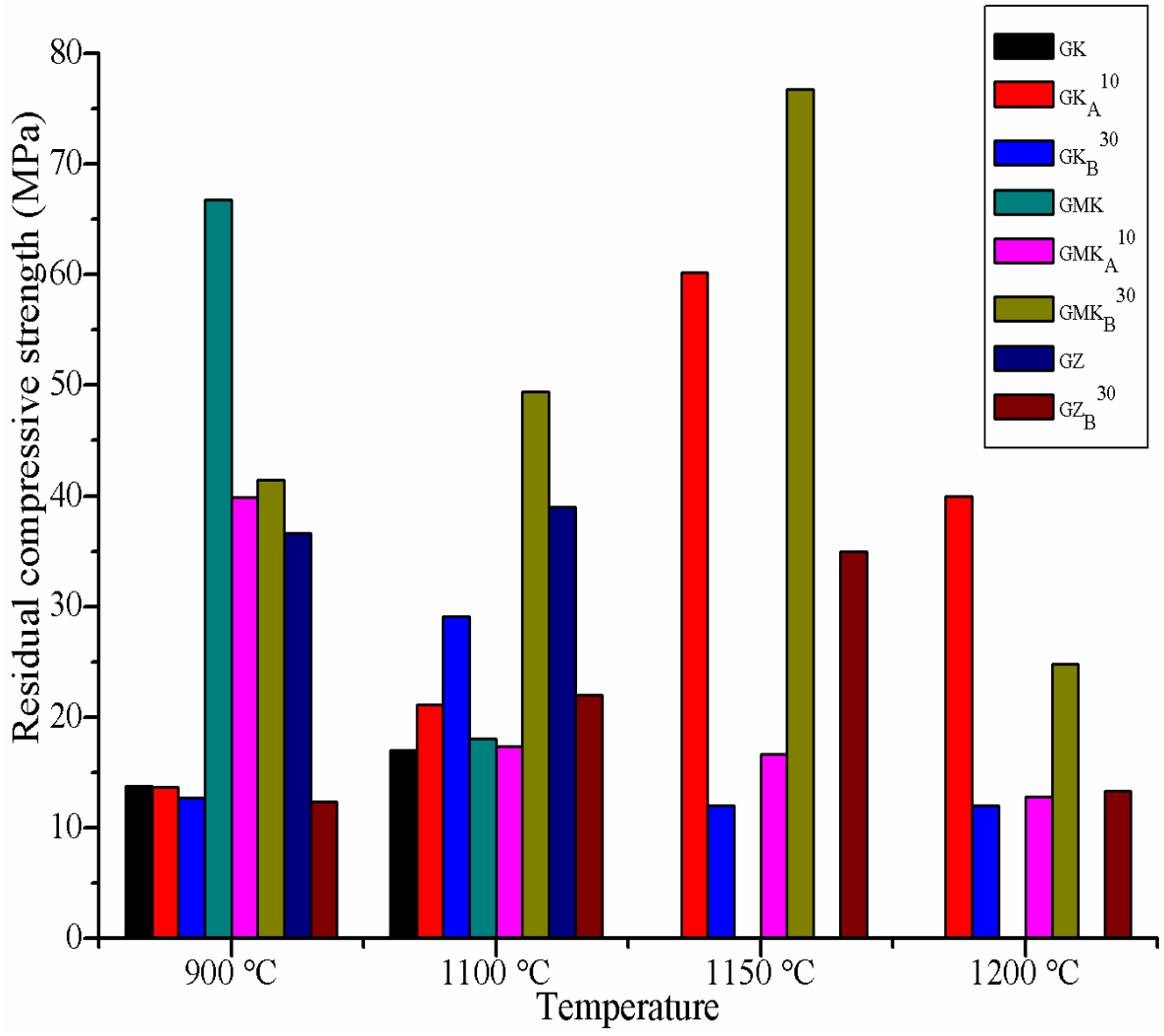

Figure 80: Residual compressive strength of heated alkali-aluminosilicate products.

III.5.3 Conclusion

Thermal behaviour revealed that the use of amorphous aluminium hydroxide or aluminium oxy-hydroxide in certain proportions as partial replacement during alkaline activation of kaolin, metakaolin and volcanic scoria led to lengthen the thermal stability of products up to 1200 °C as compared to those without replacements. This was due to the crystallisation on new stable phases such as mullite, corundum, nepheline and carnegieite in greater amount which helped to reinforce and strengthen the sintered matrix, thereby improving the residual compressive strength. The latter can be technologically applied at elevated temperatures or for structural refractory applications.

General conclusion and perspectives

The aim of this research was to study the thermal stability of cements resulting from alkaline activation of kaolin, metakaolin and volcanic scoria respectively with partial replacement of amorphous aluminium hydroxide and aluminium oxy-hydroxide. To this end, mixtures obtained by partially replacing each aluminosilicate precursor by 0, 10, 20 and 30 % by mass by each replacement were alkali-activated. After curing, each formulation was divided into 7 batches. One portion was kept as-obtained whereas others were heated at elevated temperatures (300-1200 °C). Depending on the starting raw materials and the synthesised products, the following characteristics were assessed: morphological observation, thermal behaviour (DTA / TG / DTG), thermal shrinkage, water absorption, open porosity, bulk density and compressive strength. Chemical compositions of starting materials were done by ICP / OES whereas the physical characteristics were assessed thanks to particle size analysis and BET method. Microstructural characterisations were carried out by XRD, FTIR spectroscopy and SEM analyses.

Pertaining to characterisation of the starting materials, chemical and mineralogical analyses revealed that both kaolin and metakaolin as result of their high amount of SiO_2 and Al_2O_3 (>70 % by mass), appear to be good feedstock materials for the synthesis of alkaline cements as compared to volcanic scoria (56.40 % by mass). However, alumina sources as result of their high Al_2O_3 content can be potentially used as partial replacements to compensate this deficiency in order to improve the fired characteristics of resulting products. Concerning unheated products resulting from alkaline activation, all specimens obtained with 10 % by mass of amorphous aluminium hydroxide or 30 % by mass of aluminium oxy-hydroxide exhibited low compressive strength as compared to those without replacements. Globally, this was due to fact that the replacements behaved as fillers since they have not yet chemically reacted. However, when heated at elevated temperatures, both residual compressive strength and volume stability of specimens with replacements were improved as compared to those without replacements. Indeed, without replacements, kaolin and metakaolin-based geopolymer specimens exhibited respectively poor volume stability (weak swelling) and cracks whereas alkali-activated volcanic scoria ones exhibited swelling at 1100 °C. Additionally, at 1150 °C, kaolin-based geopolymer specimens were morphologically damaged whereas alkali-activated volcanic scoria ones melted. Conversely, the specimens with 10 % by mass of amorphous aluminium hydroxide or 30 % by mass of aluminium oxy-hydroxide showed good volume stability up to 1200 °C without apparent cracks and swellings. Additionally, kaolin-based geopolymers with 30 % by mass of aluminium oxy-hydroxide that were heated at 1100 °C showed residual compressive strength of 29.1 MPa

whereas those obtained with 10 % by mass of amorphous aluminium hydroxide gave 60.2 MPa at 1150 °C. Also, at 1150 °C, metakaolin-based geopolymers and alkali-activated volcanic scoria obtained with 30 % by mass of aluminium oxy-hydroxide showed residual compressive strength of 76.7 and 35.0 MPa respectively. This was attributed to the improvement of compactness of specimens thanks to densification along with the formation of stable new crystalline phases such as mullite, corundum, carnegieite and nepheline. Yet, heating kaolin and metakaolin-based geopolymers respectively as well as alkali-activated volcanic scoria specimens at 1200 °C led to partial dissolution of nepheline and carnegieite which generates closed pores within their microstructure, hence decrease of residual compressive strength. Furthermore, thermal behaviour also revealed that the use of amorphous aluminium hydroxide or aluminium oxy-hydroxide in certain proportions as partial replacement during alkaline activation of kaolin, metakaolin and volcanic scoria led to the lengthening of thermal stability of resulting products up to 1200 °C as compared to those without replacements. Additionally, these products are thermally stable and endowed with high residual compressive strength. Hence, they can technologically be applied at elevated temperatures or for structural refractory applications.

Further research is required for this study. Firstly, replacement of synthetic alumina sources by natural bauxites mainly rich in gibbsite and boehmite during alkaline activation of aluminosilicates involved in this study. Finally, the assessment of thermal stability of the resulting alkali-activated aluminosilicate pastes and with mortars and concretes obtained respectively by adding fine and coarse sand aggregates.

References

[1] A.M. Rashad, Alkali-activated metakaolin: A short guide for civil Engineer – An overview, *Constr. Build. Mater*. **41** (2013) 751–765.

[2] J. Baenla, J.B. Bike Mbah, I.B. Djon Li Ndjock, A. Elimbi, Partial replacement of low reactive volcanic ash by cassava peel ash in the synthesis of volcanic ash based geopolymer, *Constr. Build. Mater*. **227** (2019) 116689.

[3] J. Davidovits, Properties of geopolymer cements, in *First International Conference on Alkaline Cements and Concretes, Scientific Research Institute on Binders and Materials , Kiev State Technical University, Kiev, Ukraine* (1994) 131-149.

[4] C.N. Bewa, H.K. Tchakouté, D. Fotio, C.H. Rüscher, E. Kamseu, C. Leonelli, Water resistance and thermal behavior of metakaolin-phosphate-based geopolymer cements, *J. Asian Ceram. Soc.* **6** (3) (2018) 271–283.

[5] J.L. Provis, Geopolymers and other alkali activated materials: why, how, and what?, *Mater. Struct.* **47** (2014) 11–25.

[6] J. Davidovits, Geopolymers - Inorganic polymeric new materials, *J. Therm. Anal.* **37** (1991) 1633–1656.

[7] P. Duxson, The structure and thermal evolution of metakaolin geopolymers, PhD Thesis, University of Melbourne, 2006.

[8] C. Nicholson, R. Fletcher, N. Miller, C. Stirling, J. Morris, S. Hodges, K. MacKenzie, M. Schmücker, Building Innovation through Geopolymer Technology, *Chem. New Zeal.* (2005) 10–12.

[9] X. Jiao, Y. Zhang, T. Chen, Thermal stability of a silica-rich vanadium tailing based geopolymer, *Constr. Build. Mater.* **38** (2013) 43–47.

[10] M. Zhang, M. Zhao, G. Zhang, D. Mann, K. Lumsden, M. Tao, Durability of red mud-fly ash based geopolymer and leaching behavior of heavy metals in sulfuric acid solutions and deionized water, *Constr. Build. Mater.* **124** (2016) 373–382.

[11] D.L.Y. Kong, J.G. Sanjayan, K. Sagoe-Crentsil, Comparative performance of geopolymers made with metakaolin and fly ash after exposure to elevated temperatures, *Cem. Concr. Res.* **37** (2007) 1583–1589.

[12] J. Temuujin, A. Minjigmaa, W. Rickard, A. van Riessen, Thermal properties of spray-coated geopolymer-type compositions, *J. Therm. Anal. Calorim.* **107** (2012) 287–292.

[13] D.L.Y. Kong, J.G. Sanjayan, Damage behavior of geopolymer composites exposed to elevated temperatures, *Cem. Concr. Compos.* **30** (2008) 986–991.

[14] D.L.Y. Kong, J.G. Sanjayan, Effect of elevated temperatures on geopolymer paste, mortar and concrete, *Cem. Concr. Res.* **40** (2010) 334–339.

[15] C. Kuenzel, L.M. Grover, L. Vandeperre, A.R. Boccaccini, C.R. Cheeseman, Production of nepheline / quartz ceramics from geopolymer mortars, *J. Eur. Ceram. Soc.* **33** (2013) 251–258.

[16] Z. Sun,H. Cui, H. An, D. Tao, Y. Xu, J. Zhai, Q. Li, Synthesis and thermal behavior of geopolymer-type material from waste ceramic, *Constr. Build. Mater.* **49** (2013) 281–287.

[17] H. Cheng-yong, L. Yun-ming, M. Mustafa, M.M.A.B. Abdullah, K. Hussin, Thermal resistance variations of fly ash geopolymers: foaming responses, *Sci. Rep.* **7** (2017) 45355.

[18] M. Lahoti, K.K. Wong, E. Yang, K.H. Tan, Effects of Si / Al molar ratio on strength endurance and volume stability of metakaolin geopolymers subject to elevated temperature, *Ceram. Int.* **44** (2018) 5726–5734.

[19] J. Ye, W. Zhang, D. Shi, Effect of elevated temperature on the properties of geopolymer synthesized from calcined ore-dressing tailing of bauxite and ground-granulated blast furnace slag, *Constr. Build. Mater.* **69** (2014) 41–48.

[20] A. Elimbi, H.K. Tchakouté, M. Kondoh, J.D. Manga, Thermal behavior and characteristics of fired geopolymers produced from local Cameroonian metakaolin, *Ceram. Int.* **40** (2014) 4515–4520.

[21] P.N. Lemougna, K.J.D. Mackenzie, U.F.C. Melo, Synthesis and thermal properties of inorganic polymers (geopolymers) for structural and refractory applications from volcanic ash, *Ceram. Int.* **37** (2011) 3011–3018.

[22] P.S. Santos, H.S. Santos, S.P. Toledo, Standard Transition Aluminas. Electron Microscopy Studies, *Mater. Res.* **3** (4) (2000) 104–114.

[23] H.S. Santos, T.W. Campos, P.S. Santos, P.K. Kiyohara, Thermal phase sequences in gibbsite / kaolinite clay: electron microscopy studies, *Ceram. Int.* **31** (2005) 1077–1084.

[24] C.N. Djangang, E. Kamseu, M.K. Ndikontar, G.L.L. Nana, J. Soro, U.C. Melo, A. Elimbi, P. Blanchart, D. Njopwouo, Sintering behaviour of porous ceramic kaolin – corundum composites : Phase evolution and densification, *Mater. Sci. Eng. A* **528** (2011) 8311– 8318.

[25] C.N. Djangang, A.B. Tchamba, E. Kamseu, U.C. Melo, A. Elimbi, A.M. Ferrari, C. Leonelli, Reaction sintering and microstructural evolution in metakaolin-metastable alumina composites, *J. Therm. Anal. Calorim.* **117** (2014) 1035–1045.

[26] C.N. Djangang, C. Tealdi, A.S. Cattaneo, P. Mustarelli, E. Kamseu, C. Leonelli, Cold-

setting refractory composites from cordierite and mullite-cordierite design with geopolymer paste as binder: Thermal behavior and phase evolution, *Mater. Chem. Phys.* **154** (2015) 66–77.

[27] J.L. Provis, J.S.J. van Deventer, *Alkali Activated Materials: State-of-the-Art Report, RILEM TC 224-AAM;* Springer, 2014.

[28] S.A. Bernal, R.M. De Gutierrez, E.D. Rodríguez, Alkali-activated materials: cementing a sustainable future, *Ing. Compet.* **15** (2) (2013) 211–223.

[29] F. Pacheco-torgal, J. Castro-Gomes, S. Jalali, Alkali-activated binders: A review Part 1. Historical background, terminology, reaction mechanisms and hydration products, *Constr. Build. Mater.* **22** (2008) 1305–1314.

[30] F. Pacheco-Torgal, J. Castro-Gomes, S. Jalali, Alkali-activated binders: A review. Part 2. About materials and binders manufacture, *Constr. Build. Mater.* **22** (2008) 1315–1322.

[31] R. Onori, Alkaline activation of incinerator bottom ash for use in structural applications, PhD Thesis, Sapienza University of Rome, 2011.

[32] V.B. Thapa, D. Waldmann, A short review on alkali-activated binders and geopolymer binders, in *Contribution à des ouvrages collectifs*, 2018, 576–591.

[33] N.R. Rakhimova, R.Z. Rakhimov, Reaction products, structure and properties of alkali-activated metakaolin cements incorporated with supplementary materials – a review, *J. Mater. Res. Technol.* **8** (1) (2019) 1522–1531.

[34] M. Cyr, Peut-on formuler un géopolymere ou un liant alcali-activé comme un ciment Portland ? in *Conférence Internationale Francophone NoMaD, Université de Liège, Liège, Belgique 8-9 Novembre* (2018) 1–11.

[35] J. Davidovits, Geopolymers and geopolymeric materials, *J. Therm. Anal.* **35** (1989) 429–441.

[36] J. Davidovits, 30 Years of Successes and Failures in Geopolymer Applications. Market Trends and Potential Breakthroughs, in *Geopolymer 2002 Conference, October 28-29, 2002, Melbourne, Australia* (2002) 1–16.

[37] J.N.Y. Djobo, Synthesis factors, characteristics and durability of volcanic ash-based geopolymer cements, PhD Thesis, University of Yaoundé I, 2017.

[38] H.K. Tchakouté, Elaboration et caractérisation de ciments géopolymères à base de scories volcaniques, Thèse de doctorat PhD, Université de Yaoundé I, 2013.

[39] J. Davidovits, R. Davidovits, Ferro-sialate geopolymers, *Technical papers* **27** (2020) 1-6.

[40] G. Engelhardt, E. Lohse, A. Samoson, M. Mägi, M. Tarmak, E. Lippmaa, High resolution ^{29}Si n.m.r of dealuminated and ultrastable Y-zeolites, *Zeolites* **2** (1982) 59–

62.

[41] A. Favier, Mécanisme de prise et rhéologie de liants géopolymères modèles, Thèse de doctorat PhD, Université Paris-Est, 2013.

[42] P. Rovnaník, K. Šafránková, Thermal behaviour of metakaolin / fly ash geopolymers with chamotte aggregate, *Materials* **9** (2016) 535.

[43] V.F.F. Barbosa, K.J.D. MacKenzie, C. Thaumaturgo, Synthesis and characterisation of materials based on inorganic polymers of alumina and silica: sodium polysialate polymers, *Int. J. Inorg. Mater.* **2** (2000) 309–317.

[44] P. Duxson, A. Fernandez-Jiménez, J.L. Provis, G.C. Lukey, A. Palomo, J.S.J. van Deventer, Geopolymer technology: the current state of the art, *J. Mater. Sci.* **42** (2007) 2917–2933.

[45] C. Li, H. Sun, L. Li, A review: The comparison between alkali-activated slag (Si+Ca) and metakaolin (Si+Al) cements, *Cem. Concr. Res.* **40** (2010) 1341–1349.

[46] Y. Ding, J.G. Dai, C.J. Shi, Mechanical properties of alkali-activated concrete: A state-of-the-art review, *Constr. Build. Mater.* **127** (2016) 68–79.

[47] L.N. Tchadjié, S.O. Ekolu, Enhancing the reactivity of aluminosilicate materials toward geopolymer synthesis, *J. Mater. Sci.* **53** (7) (2017) 4709–4733.

[48] A. Palomo, P. Krivenko, I. Garcia-Lodeiro, E. Kavalerova, and O. Maltseva, A. Fernández-Jiménez, A review on alkaline activation: new analytical perspectives, *Mater. Construcc.* **64** (315) (2014) 1–24.

[49] M. Torres-Carrasco, F. Puertas, Alkaline activation of different aluminosilicates as an alternative to Portland cement : alkali activated cements or geopolymers, *Rev. Ing. Construcc*. **32** (2) (2017) 5–12.

[50] L.M. Murillo, S. Delvasto, M. Gordillo, A study of a hybrid binder based on alkali-activated ceramic tile wastes and Portland cement, in *Sustainable and Nonconventional Construction Materials using Inorganic Bonded Fiber Composites*, Elsevier Ltd, 2017, 291–311.

[51] R.C. Kaze, L.M.B. Moungam, M.L.F. Djouka, A. Nana, E. Kamseu, U.F.C. Melo, C. Leonelli, The corrosion of kaolinite by iron minerals and the effects on geopolymerization, *Appl. Clay Sci.* **138** (2017) 48–62.

[52] J.N.Y. Djobo, A. Elimbi, H.K. Tchakouté, S. Kumar, Mechanical activation of volcanic ash for geopolymer synthesis: effect on reaction kinetics, gel characteristics, physical and mechanical properties, *RSC Adv.* **6** (2016) 39106–39117.

[53] L.N. Tchadjié, J.N.Y. Djobo, N. Ranjbar, H.K. Tchakouté, B.B.D. Kenne, A. Elimbi, D.

Njopwouo, Potential of using granite waste as raw material for geopolymer synthesis, *Ceram. Int.* **42** (2) (2015) 3046–3055.

[54] D. Khale, R. Chaudhary, Mechanism of geopolymerization and factors influencing its development: a review, *J. Mater. Sci.* **42** (2007) 729–746.

[55] J.N.Y. Djobo, A. Elimbi, H.K. Tchakouté, S. Kumar, Volcanic ash-based geopolymer cements / concretes: the current state of the art and perspectives, *Environ. Sci. Pollut. Res.* **24** (5) (2016) 4433–4446.

[56] I.B. Djon Li Ndjock, A. Elimbi, M. Cyr, Rational utilization of volcanic ashes based on factors affecting their alkaline activation, *J. Non. Cryst. Solids* **463** (2017) 31–39.

[57] H.K. Tchakouté, A. Elimbi, J.A. Mbey, C.J.N. Sabouang, D. Njopwouo, The effect of adding alumina-oxide to metakaolin and volcanic ash on geopolymer products : A comparative study, *Constr. Build. Mater.* **35** (2012) 960–969.

[58] J.N.Y. Djobo, L.N. Tchadjié, H.K. Tchakouté, B.B.D. Kenne, A. Elimbi, D. Njopwouo, Synthesis of geopolymer composites from a mixture of volcanic scoria and metakaolin, *J. Asian Ceram. Soc.* **2** (2014) 387–398.

[59] J.N.Y. Djobo, A. Elimbi, J.D. Manga, I.B. Djon Li Ndjock, Partial replacement of volcanic ash by bauxite and calcined oyster shell in the synthesis of volcanic ash-based geopolymers, *Constr. Build. Mater.* **113** (2016) 673–681.

[60] H.K. Tchakouté, C.H. Ruscher, S. Kong, E. Kamseu, Thermal behavior of metakaolin-based geopolymer cements using sodium waterglass from rice husk ash and waste glass as alternative activators, *Waste Biomass Valor.* **8** (3) (2016) 573–584.

[61] E. Kamseu, A. Rizzuti, C. Leonelli, D. Perera, Enhanced thermal stability in K_2O-metakaolin-based geopolymer concretes by Al_2O_3 and SiO_2 fillers addition, *J. Mater. Sci.* **45** (2010) 1715–1724.

[62] P. Rovnaníková, P. Bayer, P. Rovnaník, J. Novak, Properties of alkali-activated aluminosilicate materials with fire-resistant aggregate after high temperature loading, *Cem. Comb. Durable Concr.* (2005) 277–286.

[63] R. Perrin, J.P. Scharff, *Chimie Industrielle, 2eme édition*. Paris, Dunod, 2002.

[64] P. Boch,J.C. Niepce, *Ceramic Materials: Processes, properties and applications*. ISTE Ltd, 2007.

[65] A.K. Karamalidis, D.A. Dzombak, *Surface complexation modeling: Gibbsite*. John Wiley & Sons, Inc., Hoboken, New Jersey, 2010.

[66] J.T. Kloprogge, H.D. Ruan, R.L. Frost, Thermal decomposition of bauxite minerals: infrared emission spectroscopy of gibbsite, boehmite and diaspore, *J. Mater. Sci.* **37** (6)

(2002) 1121–1129.

[67] K.J.D. Mackenzie, J. Temuujin, K. Okada, Thermal decomposition of mechanically activated gibbsite, *Thermochim. Acta* **327** (1999) 103–108.

[68] N.S. Soro, Influence des ions fer sur les transformations thermiques de la kaolinite, Thèse de doctorat PhD, Université de Limoges, 2003.

[69] D. Rajarathnam, *Instrumental chemical analysis: Basic principles and techniques*, Laboratory Manual.

[70] S.A. Ghonaim, H.B.G. Ghazal, M.F. Abadir, Effect of the Type of Aggregate on the Properties of Alumina Refractory Concrete, *J. Am. Sci.* **6** (12) (2010) 673–684.

[71] **ASTM C20**, Standard Test Methods for Apparent Porosity, Water Absorption, Apparent Specific Gravity and Bulk Density of Burned Refractory Brick and Shapes by Boiling Water, 2010.

[72] A. Elimbi, H.K. Tchakouté, D. Njopwouo, Effects of calcination temperature of kaolinite clays on the properties of geopolymer cements, *Constr. Build. Mater.* **25** (2011) 2805–2812.

[73] B.B.D. Kenne, A. Elimbi, M. Cyr, J.D. Manga, H.K. Tchakouté, Effect of the rate of calcination of kaolin on the properties of metakaolin-based geopolymers, *J. Asian Ceram. Soc.* **3** (2015) 130–138.

[74] *Munsell Soil Color Charts, Washable.* Maryland, USA, 2000.

[75] **ASTM C 267**, Standard test methods for length change of hardened hydraulic cement, mortar and concrete, 2008.

[76] R. Dupain, J.C. Lanchon, J.C. Saint Arroman, *Granulats, sols, ciments et betons*. Casteilla, Paris, 2000.

[77] R. Pouhet, Formulation and durability of metakaolin-based geopolymers, PhD Thesis, University of Toulouse III - Paul Sabatier, 2015.

[78] E. Kamseu, M.C. Bignozzi, U.C. Melo, C. Leonelli, V.M. Sglavo, Design of inorganic polymer cements: Effects of matrix strengthening on microstructure, *Constr. Build. Mater.* **38** (2013) 1135–1145.

[79] D. Mierzwinski, M. Łach, M. Hebda, J. Walter, M. Szechynska-Hebda, J. Mikuła, Thermal phenomena of alkali-activated metakaolin studied with a negative temperature coefficient system, *J. Therm. Anal. Calorim.* **138** (2019) 4167–4175.

[80] A.Z. Khalifa, Ö. Cizer, Y. Pontikes, A. Heath, P. Patureau, S.A. Bernal, A.T.M. Marsh, Advances in alkali-activation of clay minerals, *Cem. Concr. Res.* **132** (2020) 106050.

[81] C. Bich, J. Ambroise, J. Péra, Influence of degree of dehydroxylation on the pozzolanic

activity of metakaolin, *Appl. Clay Sci.* **44** (2009) 194–200.

[82] H.K. Tchakouté, A. Elimbi, E. Yanne, C.N. Djangang, Utilization of volcanic ashes for the production of geopolymers cured at ambient temperature, *Cem. Concr. Compos.* **38** (2013) 75–81.

[83] J.N.Y. Djobo, A. Elimbi, H.K. Tchakouté, S. Kumar, Reactivity of volcanic ash in alkaline medium, microstructural and strength characteristics of resulting geopolymers under different synthesis conditions, *J. Mater. Sci.* **51** (22) (2016) 10301–10317.

[84] E. Tiffo, A. Elimbi, J.D. Manga, A.B. Tchamba, Red ceramics produced from mixtures of kaolinite clay and waste glass, *Brazilian J. Sci. Technol.* **2** (4) (2015) 1–13.

[85] M. Monneron-Gyurits, E. Joussein, M. Soubrand, P. Fondanèche, S. Rossignol, Valorization of mussel and oyster shells toward metakaolin-based alkaline activated material, *Appl. Clay Sci.* **162** (2018) 15–26.

[86] J. Ninov, Hygroscopic sorption properties of metakaolin, *J. Univ. Chem. Technol. Metall.* **45** (1) (2010) 47–52.

[87] P.T. Tanev, L.T. Vlaev, Effect of grain size on the synthesis of active alumina from gibbsite by flash calcination and rehydration, *Catal. Lett.* **19** (1993) 351–360.

[88] T. Ondro, O. Al-shantir, F. Obert, A. Trník, Non-isothermal kinetic analysis of illite dehydroxylation, in *Central European Symposium on Thermophysics 2019 (CEST)*, **2133** (2019) 20036, 1–6.

[89] E.Yusiharni, R. Gilkes, Rehydration of heated gibbsite, kaolinite and goethite: An assessment of properties and environmental significance, *Appl. Clay Sci.* **64** (2012) 61–74.

[90] H.K. Tchakouté, A. Elimbi, B.B.D. Kenne, J.A. Mbey, D. Njopwouo, Synthesis of geopolymers from volcanic ash via the alkaline fusion method: Effect of Al_2O_3 / Na_2O molar ratio of soda – volcanic ash, *Ceram. Int.* **39** (2013) 269–276.

[91] B.J. Saikia, G. Parthasarathy, Fourier Transform Infrared Spectroscopic Characterization of Kaolinite from Assam and Meghalaya, Northeastern India, *J. Mod. Phys.* **1** (2010) 206–210.

[92] M.M. Qtaitat, I.N. Al-Trawneh, Characterization of kaolinite of the Baten El-Ghoul region / south Jordan by infrared spectroscopy, *Spectrochim. Acta. A.* **61** (2005) 1519–1523.

[93] H. Cheng, J. Yang, Q. Liu, J. Zhang, R.L. Frost, A spectroscopic comparison of selected Chinese kaolinite, coal bearing kaolinite and halloysite — A mid-infrared and near-infrared study, *Spectrochim. Acta Part A Mol. Biomol. Spectrosc.* **77** (2010) 856–861.

[94] D. Panias, I.P. Giannopoulou, T. Perraki, Effect of synthesis parameters on the mechanical properties of fly ash-based geopolymers, *Colloids Surfaces A Physicochem. Eng. Asp.* **301** (2007) 246–254.

[95] H.K. Tchakouté, C.H. Rüscher, J.N.Y. Djobo, B.B.D. Kenne, D. Njopwouo, Influence of gibbsite and quartz in kaolin on the properties of metakaolin-based geopolymer cements, *Appl. Clay Sci.* **107** (2015) 188–194.

[96] X.H. Jin, L. Gao, J.K. Guo, The structural change of diphasic mullite gel studied by XRD and IR spectrum analysis, *J. Eur. Ceram. Soc.* **22** (2002) 1307–1311.

[97] I. Lancellotti, M. Catauro, C. Ponzoni, F. Bollino, C. Leonelli, Inorganic polymers from alkali activation of metakaolin: Effect of setting and curing on structure, *J. Solid State Chem.* **200** (2013) 341–348.

[98] H.K. Tchakouté, C.H. Rüscher, S. Kong, E. Kamseu, C. Leonelli, Geopolymer binders from metakaolin using sodium waterglass from waste glass and rice husk ash as alternative activators: A comparative study, *Constr. Build. Mater.* **114** (2016) 276–289.

[99] A. Tironi, M.A. Trezza, E.F. Irassar, A.N. Scian, Thermal Treatment of Kaolin: Effect on the Pozzolanic Activity, *Procedia Mater. Sci.* **1** (2012) 343–350.

[100] J.L. Bishop, E.B. Rampe, D.L. Bish, Z. Abidin, L.L. Baker, N. Matsue, Spectral and hydration properties of allophane and imogolite, *Clays Clay Miner.* **61** (1) (2013) 57–74.

[101] V.J. Ingram-Jones, R.C.T. Slade, T.W. Davies, J.C. Southern, S. Salvador, Dehydroxylation sequences of gibbsite and boehmite: study of differences between soak and flash calcination and of particle-size effects, *J. Mater. Chem.* **6** (1) (1996) 73–79.

[102] N.J.G. Deutou, T. Beda, M. Biesuz, L. Boubakar, U.C. Melo, E. Kamseu, V.M. Sglavo, Design and characterization of porous mullite based semi-vitrified ceramics, *Ceram. Int.* **44** (7) (2018) 7939–7948.

[103] V. Viswabaskaran, F.D. Gnanam, M. Balasubramanian, Mullitisation behaviour of calcined clay – alumina mixtures, *Ceram. Int.* **29** (2003) 561–571.

[104] Y. Kitagawa, Dehydration of allophane and its structural formula, *Am. Mineral.***59** (1974) 1094–1098.

[105] E.S. Larsen, The temperatures of magmas, *Am. Mineral.* **14** (1929) 81–94.

[106] M.J.A. Mijarsh, M.A.M. Johari, Z.A. Ahmad, Compressive strength of treated palm oil fuel ash based geopolymer mortar containing calcium hydroxide, aluminum hydroxide and silica fume as mineral additives, *Cem. Concr. Compos.* **60** (2015) 65–81.

[107] A.P. Rollet, R. Bouaziz, *L'analyse thermique: l'examen des processus chimiques, Tome 2*. Gauthier-Villars, 55, Quai des Grands-Augustins, Paris 6e, 1972.

[108] G. Kakali, T. Perraki, S. Tsivilis, E. Badogiannis, Thermal treatment of kaolin: the effect of mineralogy on the pozzolanic activity, *Appl. Clay Sci.* **20** (2001) 73–80.

[109] O.R. Njindam, D. Njoya, J.R. Mache, M. Mouafon, A. Messan, D. Njopwouo, Effect of glass powder on the technological properties and microstructure of clay mixture for porcelain stoneware tiles manufacture, *Constr. Build. Mater.* **170** (2018) 512–519.

[110] D.E.T. Mabah, H.K. Tchakouté, C.H. Rüscher, E. Kamseu, A. Elimbi, C. Leonelli, Design of low cost semi-crystalline calcium silicate from biomass for the improvement of the mechanical and microstructural properties of metakaolin-based geopolymer cements, *Mater. Chem. Phys.* **223** (1) (2019) 98–108.

[111] P. Duxson, G.C. Lukey, J.S.J. Van Deventer, Thermal evolution of metakaolin geopolymers: Part 1 – Physical evolution, *J. Non. Cryst. Solids* **352** (2006) 5541–5555.

[112] P. Duxson, G.C. Lukey, J.S.J. Van Deventer, The thermal evolution of metakaolin geopolymers: Part 2 – Phase stability and structural development, *J. Non. Cryst. Solids* **353** (2007) 2186–2200.

[113] C.Y. Heah,H. Kamarudin, A.M.M.A. Bakri, M. Bnhussain, M. Luqman, I.K. Nizar, C.M. Ruzaidi, Y.M. Liew, Study on solids-to-liquid and alkaline activator ratios on kaolin-based geopolymers, *Constr. Build. Mater.* **35** (2012) 912–922.

[114] H. Wang, H. Li, F. Yan, Synthesis and mechanical properties of metakaolinite-based geopolymer, *Colloids Surfaces A Physicochem. Eng. Asp.* **268** (2005) 1–6.

[115] G.E.D Benedetto, R. Laviano, L. Sabbatini, P.G. Zambonin, Infrared spectroscopy in the mineralogical characterization of ancient pottery, *J. Cult. Herit.* **3** (2002) 177–186.

[116] E. Obonyo, E. Kamseu, U.C. Melo, C. Leonelli, Advancing the use of secondary inputs in geopolymer binders for sustainable cementitious composites: a review, *Sustainability* **3** (2011) 410–423.

[117] J. Madejova, FTIR techniques in clay mineral studies, *Vib. Spectrosc.* **31** (2003) 1–10.

[118] T.E. Pougnong, P.D.B. Belibi, J. Baenla, A. Thamer, E. Tiffo, A. Elimbi, Effects of chemical composition of amorphous phase on the reactivity of phosphoric acid activation of volcanic ashes, *J. Non. Cryst. Solids* **575** (2022) 121213.

Annex

Laboratory equipments used

Electrical oven (Heraeus, type VT 5042 EK)

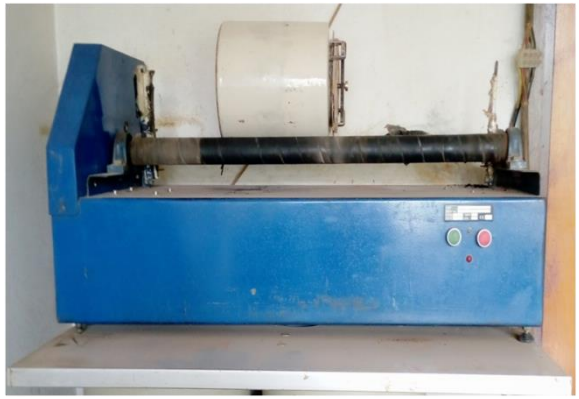

Ball mill apparatus

Electric furnace (Nabertherm, Mod. LH 60/14)

Hobart mixer (M & O model N50-G)

Electrical vibrating table
(M & O, type 202, No. 106)

Digital calliper

Electro-hydraulic press
(M & O, type 11.50, N0° 21)

Publications

Materials Chemistry and Physics 239 (2020) 122103

Contents lists available at ScienceDirect

Materials Chemistry and Physics

journal homepage: www.elsevier.com/locate/matchemphys

Physical and mechanical properties of unheated and heated kaolin based-geopolymers with partial replacement of aluminium hydroxide

Emmanuel Tiffo [a], Jean Batiste Bike Mbah [b], Placide Désiré Belibi Belibi [c], Jean Noel Yankwa Djobo [d], Antoine Elimbi [a,*]

[a] Laboratory of Applied Inorganic Chemistry, Faculty of Science, P.O. Box 812, Yaoundé, University of Yaoundé 1, Cameroon
[b] Laboratoire de Matériaux et de Chimie Industrielle, ENSAI B.P. 445, Ngaoundéré, Université de Ngaoundéré, Cameroon
[c] Applied Physical and Theoretical Chemistry Laboratory, Faculty of Science, P.O. Box 812, Yaoundé, University of Yaoundé 1, Cameroon
[d] Local Materials Promotion Authority, P.O. Box 2396, Nkolbikok, Yaoundé, Cameroon

HIGHLIGHTS

- Aluminium hydroxide and oxy-hydroxide were used to replace kaolin (30% by mass).
- The mixtures were used to produce kaolin based-geopolymers via alkaline activation.
- Compressive strength of geopolymers with up to 30% of replacement was low.
- Heated products with 10% of aluminum hydroxide gave compressive strength of 60 MPa.
- Certain proportions of replacement allowed thermal stability of heated products.

GRAPHICAL ABSTRACT

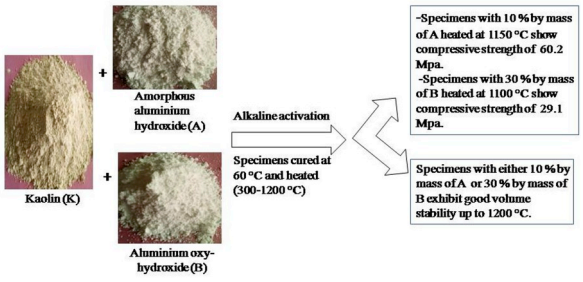

ARTICLE INFO

Keywords:
Kaolin
Geopolymers
Heating
Compressive strength
Thermal stability

ABSTRACT

Amorphous aluminium hydroxide and aluminium oxy-hydroxide were used as replacements in the synthesis of kaolin based-geopolymers. Physical and mechanical properties of geopolymers cured at 60 °C and exposed at elevated temperatures (300–1200 °C) were investigated. It was found that when cured at 60 °C, specimens with replacements exhibited low compressive strength as compared to those without replacement. Conversely, when heated as from 1100 °C, both compressive strength and volume stability of specimens with replacement were improved. Thus, specimens without replacement were morphologically damaged at 1150 °C whereas those with 10% by mass of amorphous aluminium hydroxide or with 30% by mass of aluminium oxy-hydroxide showed good volume stability at 1150 and 1200 °C respectively. Additionally, geopolymers with 30% by mass of aluminium oxy-hydroxide that were heated at 1100 °C showed compressive strength of 29.1 MPa whereas those with 10% by mass of amorphous aluminium hydroxide gave 60.2 MPa at 1150 °C. This was attributed to the improvement of compactness of specimens along with the formation of stable crystalline phases. Yet, heating geopolymers at 1200 °C led to partial dissolution of nepheline and carnegieite which generates closed pores hence decrease of compressive strength. Partial replacement of amorphous aluminium hydroxide or aluminium oxy-hydroxide in the synthesis of kaolin-based geopolymers allows both improvement of compressive strength and thermal stability of heated kaolin-based geopolymers.

* Corresponding author.
E-mail address: aelimbi2002@yahoo.fr (A. Elimbi).

https://doi.org/10.1016/j.matchemphys.2019.122103
Received 27 May 2019; Received in revised form 28 August 2019; Accepted 29 August 2019
Available online 29 August 2019

1. Introduction

Geopolymer is a term used to describe inorganic polymers obtained mostly by alkaline or phosphoric acid activation of aluminosilicates [1]. These materials have recently drawn more attention as novel and sustainable binders because of their good physical properties, durability and eco-friendliness [2,3]. Geopolymer properties are strongly related to the nature of aluminosilicate source, synthesis process, type and concentration of activating solution [4]. Moreover, these properties can be tailored by varying the Si/Al molar ratio [5–7]. Also, it was found that by varying the Si/Al molar ratio, geopolymer fire resistance characteristics can be improved [8]. Metakaolin (MK), the output product of thermal treatment of kaolin is the most commonly used model precursor for the synthesis of geopolymers thanks to its high reactivity [5,9–11] although its thermal activation is energy consuming. From technical point of view, the use of MK for geopolymer synthesis involves great water or activating solution demand associated with the sheet-like structure of its particles and corresponding high specific surface area [12]. Recently, Elimbi et al. [13] investigated the thermal behaviour of metakaolin-based geopolymers produced from MK by alkaline activation. It was found that the thermal behaviour of geopolymer is characterized by removal of bound water up to 750 °C followed by sintering and crystallization of new phases. Moreover, Lahoti et al. [5] reported that MK-based geopolymers with Si/Al molar ratio between 1.5 and 1.03 exhibit the lowest thermal shrinkage. Additionally, it was found that due to high level of cracks, damage and low residual strength retention, it is necessary to improve the macro-scale thermal stability (compressive strength) of MK-based geopolymers for structural fire resistance applications. Many studies based on thermal resistance of calcined-clays based-geopolymers have been reported [5,6,14,15]. However, there is lack of data in regard with heated products of kaolin-based geopolymers. It is worth pointing out that the use of kaolin for geopolymerisation is limited because of its low reactivity. The aim of this work is to get heated kaolin based-geopolymers with improved characteristics by partially replacing kaolin by amorphous aluminium hydroxide or aluminium oxy-hydroxide. Depending on the raw materials and the synthesized products, the characteristics were assessed in term of thermal analysis, water absorption and compressive strength. Microstructural characterization (XRD, FTIR spectroscopy and SEM) were carried out as well.

2. Materials and experimental procedures

2.1. Materials

The kaolin was provided by the NUBRU Holding Group which operates on the valorization of certain local raw materials in Cameroon. Before use, the as-received kaolin was washed according to Stokes' law [16]. The clay fraction obtained was denoted as K and both its chemical and mineralogical compositions are given in Table 1 and Fig. 1 respectively. It is mainly composed of kaolinite and gibbsite as major minerals associated with quartz, anatase and illite. Two types of aluminium sources were used as replacements: amorphous aluminium hydroxide ($Al(OH)_3$) labelled as A and semi-crystalline aluminium oxy-hydroxide (γ-AlO(OH)) labelled as B. Both were supplied by Sigma Aldrich in form of powder (sample A) and in form of granular (sample B) respectively. XRD patterns of A and B are also given in Fig. 1. For the use purpose, both kaolin (K) and aluminium oxy-hydroxide (B) were each crushed in a porcelain mortar and then sifted to 90 μm mesh-sifter. The alkaline activating solution was obtained by mixing sodium hydroxide (pellets of 99% by mass of NaOH) solution and commercial sodium silicate (% by mass: SiO_2 (28.7), Na_2O (8.9), H_2O (62.4)) in order to get the following molar ratios: $SiO_2/Na_2O = 1.45$ and $H_2O/Na_2O = 16$. This solution was sealed and stored for at least 24 h at ambient temperature (24 ± 3 °C) of the laboratory prior to be used in order to allow full silicate depolymerization.

2.2. Experimental procedures

Mixtures of powders were obtained by partially replacing kaolin by 0, 10, 20 and 30% by mass by each aluminium source (A or B) respectively. In each mixture, dried powders were firstly mixed in a Hobart mixer (M & O model N50-G) for 5 min. Then, the alkaline activating solution was gradually added for other 5 min. In each mixture, liquid to solid mass ratio (L/S) was done as given in Table 2. Fresh geopolymer pastes obtained were poured into cylindrical moulds (height: 46 mm; diameter: 23 mm), vibrated for 5 min in an electrical vibrating table (M & O, type 202, No. 106) in order to remove entrapped air bubbles and then cured at 60 °C in an oven (Heraeus, type VT 5042 EK) for 7 days. After demoulding, batches of geopolymer specimens denoted as GK, GK_A^{10}, GK_A^{20}, GK_A^{30}, GK_B^{10}, GK_B^{20} and GK_B^{30} (Table 2) were respectively heated at 300, 700, 900, 1100, 1150 and 1200 °C for 2 h in a programmable electric furnace (Nabertherm, Mod.LH60/14) at heating rate of 5 °C/Min.

The chemical analysis of K was determined by ICP-OES using a PerkinElmer Spectrometer (Optima™ 7000 DV ICP-OES). Powders of the raw materials (K, A and B) and the selected geopolymers (GK, GK_A^{10} and GK_B^{30}) were subjected to thermal analyses (TG and DTA) using a NETZSCH STA 429 (CD) device from 20 to 1200 °C in a self-generated atmosphere of air at heating rate of 5 °C/Min. X-ray diffraction (Bruker D4 device) was done using CuKα radiation in the range of 5–70° (2θ) and crystalline phases were identified by comparing the obtained patterns with the Powder Diffraction File (PDF) standards from the International Centre for Diffraction Data (ICDD). FTIR (Bruker Vertex 80v device) was performed in absorbance mode (interval of wave number: 4000-400 cm^{-1}) according to KBr pellet method. Water absorption test (WA) was carried out with respect to ASTM C373-88 standard [17] and three replicate specimens were experimented on each batch. Compressive strength was assessed by the means of a hydro-electric press (M & O, type 11.50, N° 21) which operates at an average rate of 3 mm/Min according to EN 196-1 standard [16] and four specimens of each batch were used for measurement. After compressive strength test, fragments of both geopolymers and heated products of GK, GK_A^{10} and GK_B^{30} were crushed, passed through a 90 μm mesh-sifter and the obtained powders were used to carry out both XRD and FTIR spectroscopic analyses. Also, fragments obtained from mechanical test were used for microstructural observations thanks to a FEI QUANTA FEG 450 ESEM microscope.

3. Results and discussion

3.1. Workability and visual aspect of specimens

Fig. 2 depicts the workability of geopolymer pastes expressed in terms of replacement content and liquid to solid mass ratio (L/S). L/S of

Table 1
Chemical composition (% by mass) of the kaolin (K).

Composition	(%)
SiO_2	38.00
Al_2O_3	40.10
CaO	0.05
Fe_2O_3	0.70
Na_2O	0.04
K_2O	0.24
MgO	0.13
TiO_2	1.10
SO_3	0.01
P_2O_5	0.07
Cr_2O_3	0.02
Mn_2O_3	<0.01
LOI	18.75
Total	99.21

LOI: Loss On Ignition.

0.86 was suitable for GK which was considered as the reference mixture. The same value of liquid to solid mass ratio was suitable for the mixtures GK_B^{10}, GK_B^{20} and GK_B^{30} with aluminium oxy-hydroxide as replacement. They displayed good workability and were consistent and homogeneous mixtures of particles during and after moulding. As for the mixtures with amorphous aluminium hydroxide as replacement, L/S of 1.17 was suitable for GK_A^{10} whereas L/S of 1.51 and 1.84 were respectively tested for GK_A^{20} and GK_A^{30} but this did not allow consolidated specimens. Actually, the difference between the two replacements pertaining to the mass ratio L/S could be ascribed either to the particle size distribution or to the ability of particles to absorb the activating solution. For instance, particle size distribution of amorphous aluminium hydroxide could be very small as compared to that of aluminium oxy-hydroxide, meanwhile contact angle of the former may be smaller than the latter, thereby may require great amount of activating solution to achieve good wettability. It is worth noting that the specimens of GK_A^{20} and GK_A^{30} were not well consolidated even after 7 days of curing at 60 °C. This suggested that excess of amorphous aluminium hydroxide may hinder the extent of geopolymerisation [18,19]. Hence, partial replacement of kaolin by 30% by mass of aluminium oxy-hydroxide or by 10% by mass of amorphous aluminium hydroxide gave suitable mix designs that led to consolidated geopolymers with good workability.

For further assessment in this study, microstructural and mineralogical characterizations were performed only for GK, GK_A^{10} and GK_B^{30} whose visual aspects of unheated and heated specimens are shown in Fig. 3. At 1100 °C, GK showed poor volume stability as compared to GK_A^{10} and GK_B^{30}. Moreover, GK specimens heated at 1150 °C exhibited cracks, swelled and volume shrinkage was negative (−14.59%). Conversely, GK_A^{10} and GK_B^{30} did not show cracks but rather good volume stability at 1150 and 1200 °C respectively. Thus, with a determined liquid to solid mass ratio, amorphous aluminium hydroxide and aluminium oxy-hydroxide allowed improvement of thermal stability of kaolin-based geopolymers.

Table 2
Mix proportions in geopolymer pastes (% by mass).

Formulations	Kaolin (K)	Replacements (A or B)	L/S mass ratio
GK	100	00	0.86
GK_A^{10}	90	10	1.17
GK_A^{20}	80	20	1.51
GK_A^{30}	70	30	1.84
GK_B^{10}	90	10	0.86
GK_B^{20}	80	20	0.86
GK_B^{30}	70	30	0.86

3.2. Thermal behaviour

Thermal analyses (TG and DTA) of both the raw materials (K, A and B) and the geopolymers (GK, GK_A^{10} and GK_B^{30}) are given in Figs. 4 and 5. The TG curve of kaolin (Fig. 4) exhibits three mass losses. The first one corresponds to the loss of free water and it is expressed by an endothermic peak with a maximum at 42 °C (Fig. 5) [20]. The second one refers to thermal decomposition of gibbsite and this is expressed by an endothermic peak at 274 °C [21–23]. The third mass loss (~10.5%) accounts for the dehydroxylation of kaolinite to form metakaolinite which is expressed by an endothermic peak with maximum at 500 °C [9,24]. Additionally, metakaolinite is exothermically transformed into mullite/spinel phase at 975 °C [21,24–26]. Both TG and DTA analyses allow to confirm that kaolinite and gibbsite were the major phases in K as indicated earlier (Fig. 1). Concerning the replacements (A and B), the TG curve of each displays two mass losses. For the amorphous aluminium hydroxide (A) (Fig. 4), the first mass loss is of about 35% and is very close to 34.6% by mass (theoretical value) [21]. The latter is related to hydration, zeolitic and structural water as consequence of its transformation into aluminium oxy-hydroxide and this is expressed by the large endothermic signal between 50 and 300 °C (Fig. 5) [13,26–28]. The aluminium oxy-hydroxide formed as an intermediate is testified by the endothermic dome displayed between 350 and 750 °C in the DTA curve [28]. For the aluminium oxy-hydroxide (B), the mass loss of about ~10% refers to hydration and bound water expressed by the presence of

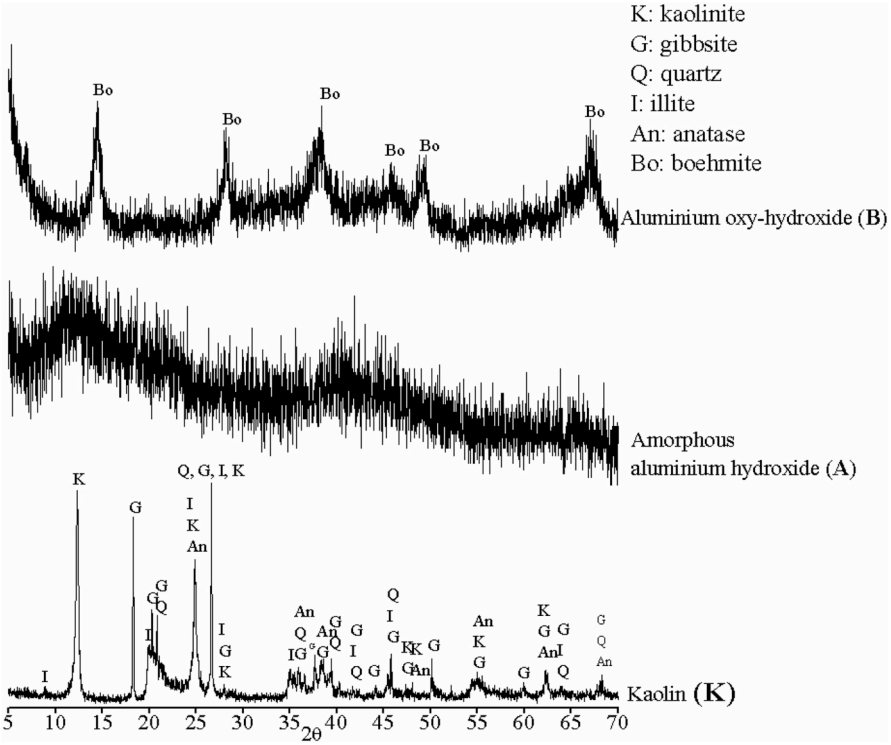

Fig. 1. XRD patterns of the raw materials.

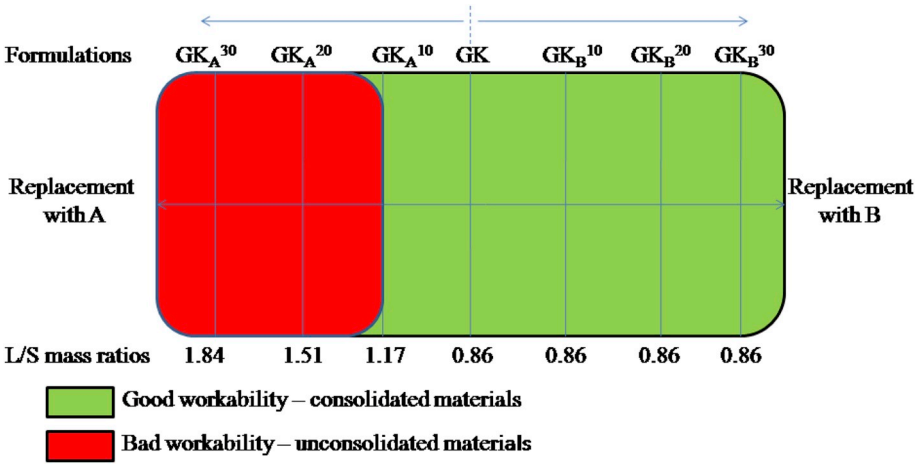

Fig. 2. Workability of the geopolymer pastes.

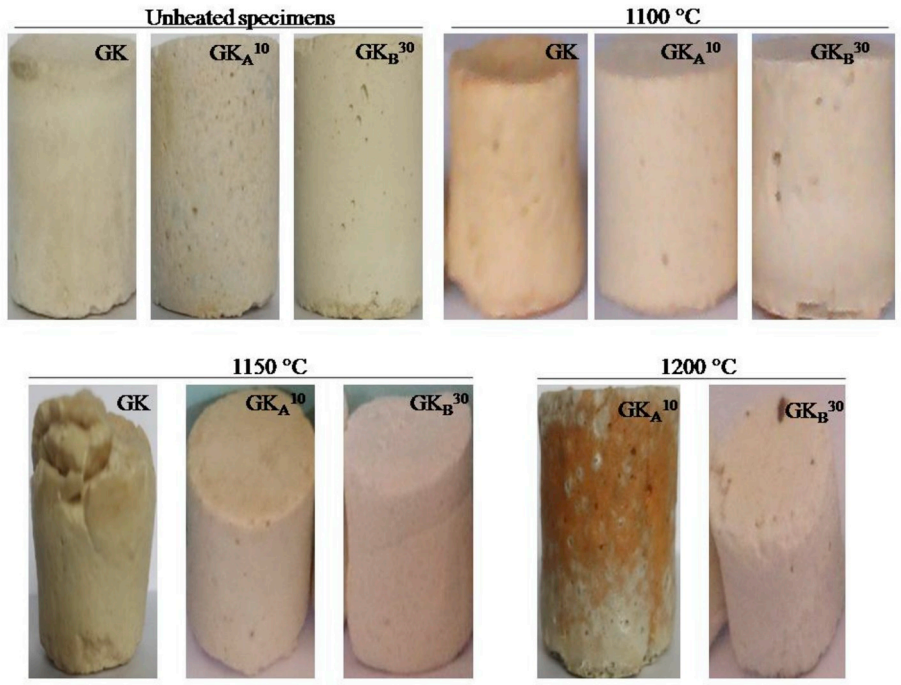

Fig. 3. Visual aspect of the geopolymers and of their heated products.

an endothermic peak around 60 °C on the DTA curve [20,26]. The final mass loss (~5%) for the amorphous aluminium hydroxide (A) accounts for the final dehydroxylation of aluminium oxy-hydroxide to give $\gamma-Al_2O_3$ that is expressed by an endothermic peak around 878 °C [22]. For typical aluminium oxy-hydroxide (B), the mass loss of about ~7% also corresponds to the same phenomenon but at a very moderate temperature (430 °C) [23,26]. The difference on dehydroxylation behaviour between A and B could be ascribed respectively to their particle size distributions, crystal shapes and various degrees of amorphicity [22] as highlighted by the workability of the geopolymer pastes (Fig. 2). The obtained $\gamma-Al_2O_3$ is transformed into α-Al_2O_3 (corundum) between 900 and 1200 °C and this is established by the broad exothermic peak on DTA with maximum at around 1050 °C [21,22]. TG curves of the geopolymers (GK, GK_A^{10} and GK_B^{30}) also present three mass losses (Fig. 4). The first one is attributed to free water absorbed or entrapped in large cavities of geopolymer framework and this is highlighted by an endothermic peak at 90 °C (Fig. 5) [13,29]. The second one is assigned to thermal decomposition of gibbsite, combined with partial dehydration and dehydroxylation of replacements (A or B) highlighted by an endothermic peak at 270 °C which is very close to the value observed with typical pure gibbsite [10,30]. The third mass loss is related to both the breakdown of residual kaolinite network and the complete transformation of aluminium oxy-hydroxide formed as an intermediate to give $\gamma-Al_2O_3$ [22,31]. The broad endothermic peaks observed between 350 and 700 °C account for dehydration of geopolymer gel and dehydroxylation of the replacements (A and B) respectively [22,26]. Referring to GK and GK_B^{30}, the above mentioned phenomena show a maximum around 473 °C. Conversely, for GK_A^{10}, the latter maximum is shifted at 564 °C. This is due to the thermal decomposition of the intermediate aluminium oxy-hydroxide of the amorphous aluminium hydroxide (A) [22,31]. Between 900 and 1200 °C, the DTA curves of the geopolymers exhibit a broad exothermic dome without mass change, related to structural reorganization along with crystallization of phases such as mullite and corundum which are respectively classical output products of thermal treatment of the raw materials (K, A and B), coupled to sintering/densification [26,32,33]. Regarding the samples GK_A^{10} and GK_B^{30},

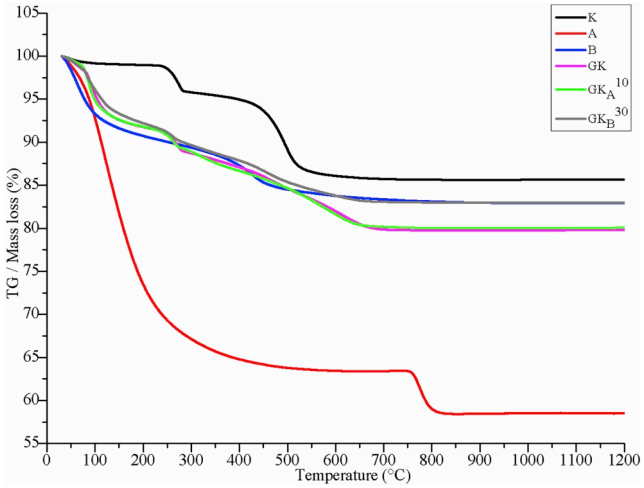

Fig. 4. TG curves of the raw materials and of the geopolymers.

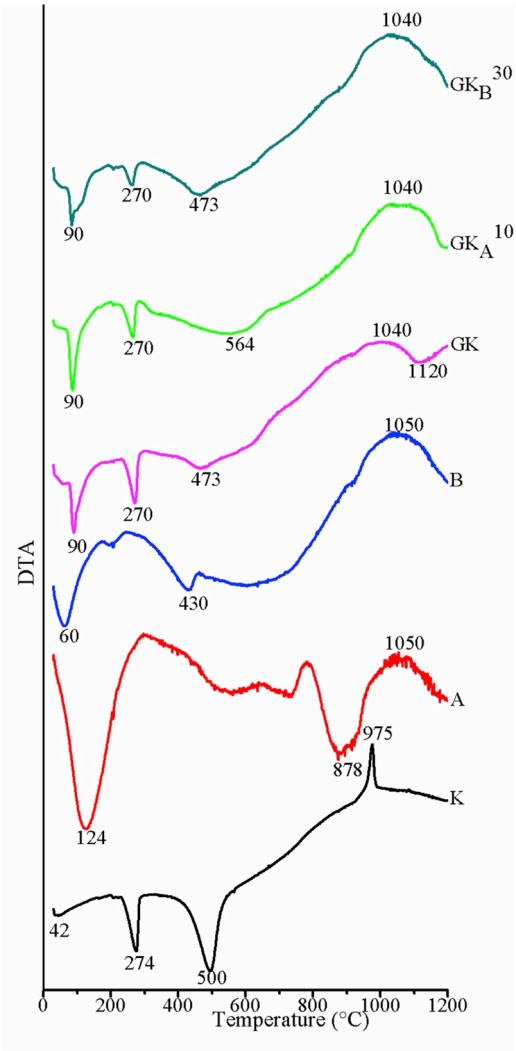

Fig. 5. DTA curves of the raw materials and of the geopolymers.

the intensity of their domes which are characteristic of maximum packing of particles is more pronounced [33]. This evidences the presence of thermal inert phases (mullite and corundum) in large quantity which contribute in improving their microstructures [21]. Conversely with GK, the intensity of its dome is weak, attesting low amount of thermal inert phases. Moreover, the dome of GK undergoes a deflection at 1120 °C which is ascribed to excessive sintering along with possible melting [5,13], which induces cracks, warping, swelling and leading to damaged structure in accordance with its visual aspect (Fig. 3). Conversely, GK_A^{10} and GK_B^{30} are thermally stable between 900 and 1200 °C as illustrated by their visual aspect and thermal behaviour (Figs. 3–5). Hence, using either amorphous aluminium hydroxide or aluminium oxy-hydroxide as replacements in the synthesis of kaolin-based geopolymers allows improvement of thermal stability of the heated products.

3.3. FTIR analysis

FTIR spectra of the geopolymers (GK, GK_A^{10} and GK_B^{30}) initially cured at 60 °C along with their heated (1100 °C) products are shown in Fig. 6. The peak at 1644 cm^{-1} is attributed to bending vibration of H–O–H which expresses surface absorbed or entrapped water in large cavities of geopolymer framework [34,35]. The band at 1464 cm^{-1} is ascribed to stretching vibration of C–O bond as consequence of efflorescence on geopolymers [9] whereas the one at 1388 cm^{-1} is attributed to asymmetric vibration of Al–O and Si–O bonds [13]. However, the intensity of the latter vibration band is reduced for GK_A^{10} and GK_B^{30} as consequence of presence of replacements, evidencing the decrease of the extent of cross-linking. The bands at 790 and 743 cm^{-1} are attributed to Si–O–Al vibrations [35]. The band at 911 cm^{-1} refers to Al–OH bending vibration, those observed within the range of 1025 and 998 cm^{-1} are related to Si–O–Si in-plane vibration whereas the one at 1113 cm^{-1} is assigned to apical Si–O stretching vibration of kaolinite network showing its low reactivity in strong alkaline medium [24,36,37]. The main band observed at 998 cm^{-1} (Fig. 6a) corresponds to symmetric and asymmetric stretching vibrations of Si–O-T (T: Si or Al) of geopolymer network [35,38], related to the formation of polysialate gel which is the fingerprint of geopolymer matrix [34,38]. The peak at 848 cm^{-1} is related to non-condensed Si–OH bending vibration in GK_A^{10} and GK_B^{30}, suggesting the occurrence of further condensation at elevated temperature and which could also contribute to the formation of geopolymer network [29]. The band at 790 cm^{-1} is assigned to AlO_4 vibration units of geopolymers [35]. The weak band around 663 cm^{-1} is attributed to symmetric stretching vibrations of Si–O–Al and Si–O–Si groups of geopolymers [35,39]. In the spectra of the heated (1100 °C) geopolymers (Fig. 6b), there is a shoulder at 1100 cm^{-1} attributed to stretching vibration of Si–O in tetrahedron along with vibration band at 690 cm^{-1} attributed to Si–O of quartz and peak at 512 cm^{-1} assigned to Si–O–Al bending vibration [5,24,40]. In fact, the latter appearance may account for new formed minerals such as nepheline/carnegieite, originating from the transformation of amorphous phase of geopolymer [5,41]. The major broad band at 980 cm^{-1} is related to Si–O-T (T: Si or Al) stretching vibrations. The bands observed within the range of 459 and 453 cm^{-1} are attributed to Si–O–Si and O–Si–O bending vibrations of quartz, showing that either it remains unreacted in strong alkaline medium or it has partially reacted during heating up to 1100 °C [13,35].

3.4. XRD analysis

XRD (Fig. 7) were done in order to get better understanding on crystalline phases of the geopolymers before and after heating (1100 °C). The geopolymers (GK and GK_A^{10}) contained kaolinite ($Al_2Si_2O_5(OH)_4$: PDF# 14–164), gibbsite ($Al(OH)_3$: PDF# 33–18), quartz (SiO_2: PDF# 46–1045), illite - 2M1 ($(K,H_3O)(Al,Mg,Fe)_2(Si,Al)_4O_{10}[(OH)_2, (H_2O)]$: PDF# 26–911) and anatase (TiO_2: PDF# 21–1272). In addition to the above mentioned crystalline phases, the sample GK_B^{30} contained boehmite (γ-AlO(OH): PDF# 21–1307) from the semi-crystalline aluminium oxy-hydroxide (Fig. 7a). This reveals the low reactivity of the above mentioned minerals in alkaline medium as shown by the intensities of their peaks. Conversely, all the heated geopolymers

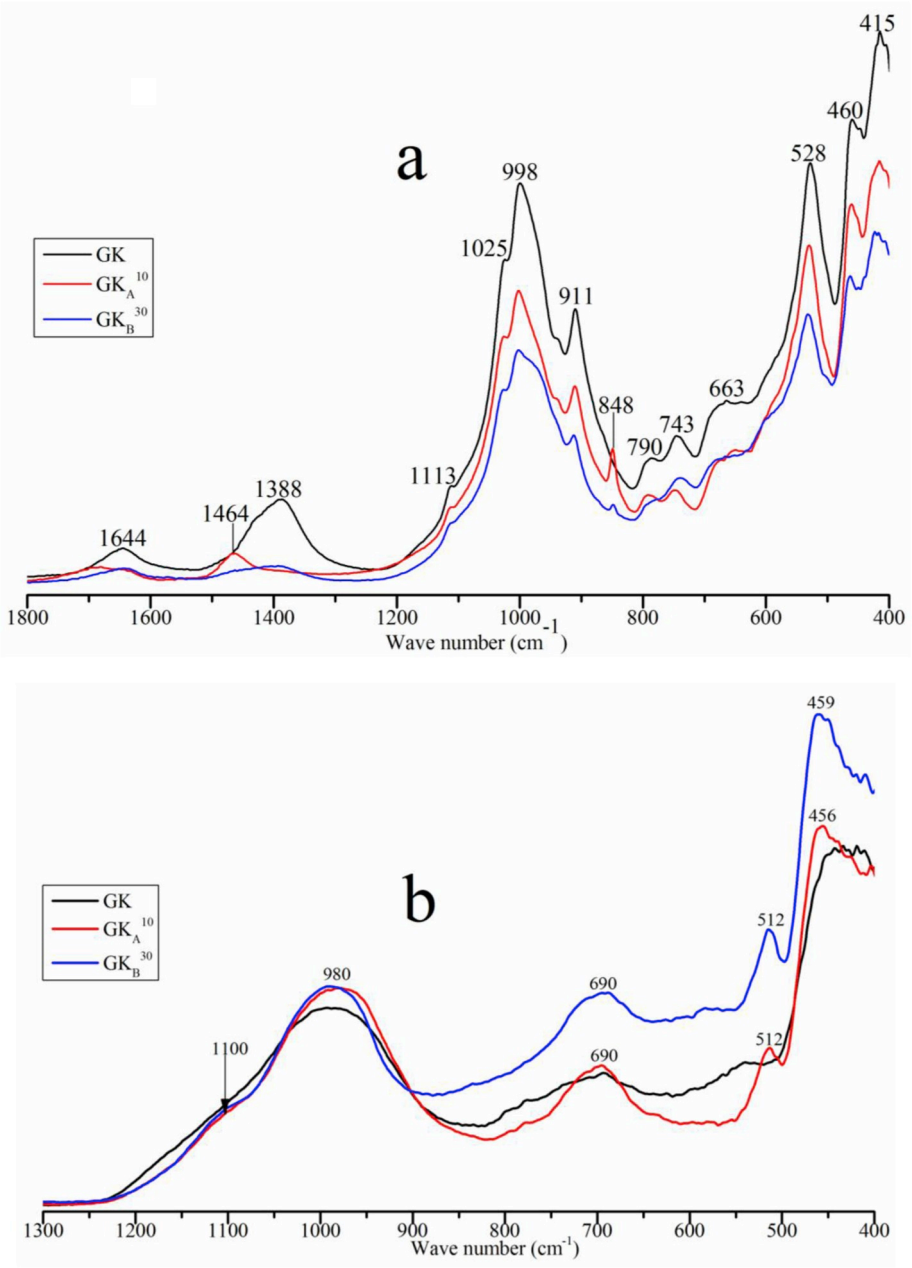

Fig. 6. FTIR spectra of the geopolymers (a) and of their heated (1100 °C) products (b).

(Fig. 7b) contain mullite ($Al_6Si_2O_{13}$: PDF# 15–776) and corundum (α-Al_2O_3: PDF# 10–173) associated with anatase, quartz and tridymite (SiO_2: PDF# 18–1170), nepheline ($NaAlSiO_4$: PDF# 9–458) and carnegieite ($NaAlSiO_4$: PDF# 11–220) as crystalline phases. The absence of kaolinite, illite, gibbsite and boehmite is attributed to their thermal transformations [20]. Moreover, the intensities of the peaks related to nepheline and carnegieite are greater in GK_A^{10} and GK_B^{30} than in GK. Since the formation of nepheline and carnegieite is generally attributed to the transformation of amorphous phase of geopolymer, it can be concluded that the presence of replacements (A and B) have improved the yield of their formations.

3.5. Microstructure

Fig. 8 shows the microstructure of the geopolymers (GK, GK_A^{10} and GK_B^{30}) and their heated products. Heated at 900 °C, GK is compact whereas GK_A^{10} and GK_B^{30} are sponge-like showing that replacements delay the densification. At 1100 °C, the compactness of GK has increased which may be due to the increase of melting of residual alkali from the activator [15]. Also, at 1100 °C, GK_A^{10} is compact in spite of the presence of some closed pores whereas the compactness of GK_B^{30} has increased but it still remains sponge-like. These differences may be ascribed to the high alumina content in GK_A^{10} and GK_B^{30}. Between 1150 and 1200 °C, the compactness of GK_A^{10} and GK_B^{30} has improved. Yet, GK_B^{30} displays some closed pores probably due to partial dissolution of nepheline and carnegieite.

3.6. Physical and mechanical properties

Fig. 9 presents the variation of water absorption (WA) versus temperature for the geopolymers and their heated products. For the geopolymers, WA increases with the increase of replacements which may show that the aluminium hydroxides do not or weakly take part in geopolymerisation [30]. Indeed, according to Fig. 8, kaolin contributes

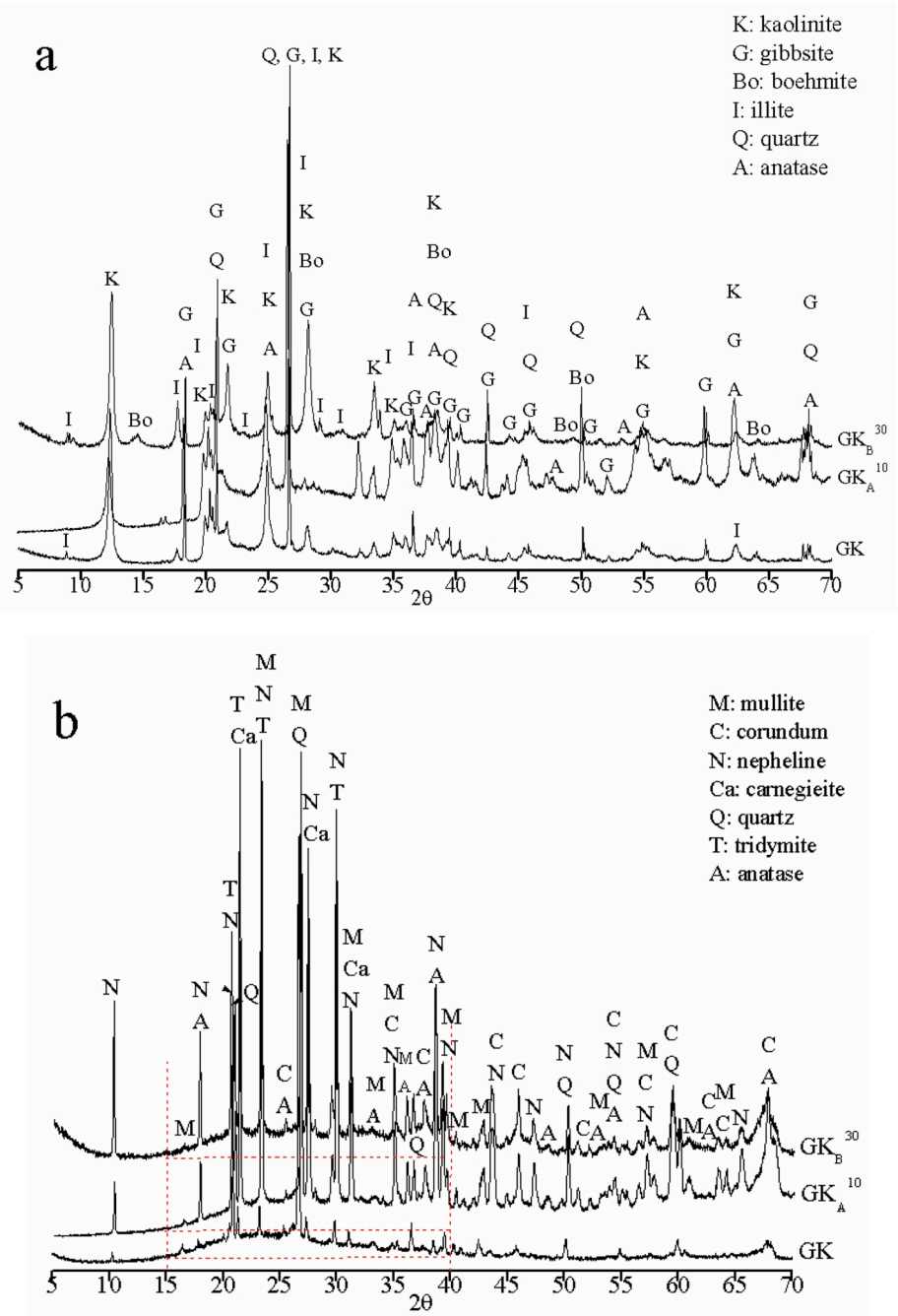

Fig. 7. XRD patterns of the geopolymers (a) and of their heated (1100 °C) products (b).

significantly to the formation of geopolymer gel (Sample GK) whereas the replacements behave as fillers (GK_A^{10} and GK_B^{30}) [18,19]. When comparing the geopolymers initially cured at 60 °C, WA has increased consistently at 300 °C most likely due to gradual transformation of geopolymer gel. Moreover, the loss of water of both gibbsite and replacements (Fig. 4) generates pores which contribute to raise WA [42]. Between 700 and 900 °C, WA of GK is reduced as result of the onset of densification thanks to the melting of non reacted alkaline activator. Concerning GK_A^{10} and GK_B^{30} heated respectively at 700 and 900 °C, WA still increases because of weak densification. In fact for these temperatures, replacements delay the densification process [27,33]. WA of GK heated at 1100 °C remains slightly constant showing that its maximum densification is achieved. As for GK_A^{30} and GK_B^{30}, WA is reduced at 1100 °C as compared to 900 °C. The difference between the behaviour of the former (GK) and the latter (GK_A^{30} and GK_B^{30}) is attributed to various mix proportions of the binder (kaolin) and the replacements (Table 2). Referring to GK_A^{10} and GK_B^{30}, WA is the lowest after heating at 1150 and 1200 °C respectively. In fact, the transformation of the binder has provoked the collapse of pores hence lessening of WA [43].

Compressive strength of the geopolymers and their heated products versus temperature is given in Fig. 10. For the geopolymers, there is decrease of compressive strength with the increase of replacements. Indeed, compressive strengths are 22.6, 14.1 and 9.7 MPa respectively for GK, GK_A^{10} and GK_B^{30} which shows that replacements contribute to reduce compressive strength. This decrease is also observed for the geopolymers heated at 300 °C, as result of gradual transformation of the geopolymer gel [40,41] which is in accordance with the increase of WA (Fig. 9). However, compressive strength of GK heated between 300 and 900 °C almost remains constant whereas that of specimens with replacement (GK_A^{10} and GK_B^{30}) increases weakly as result of weak

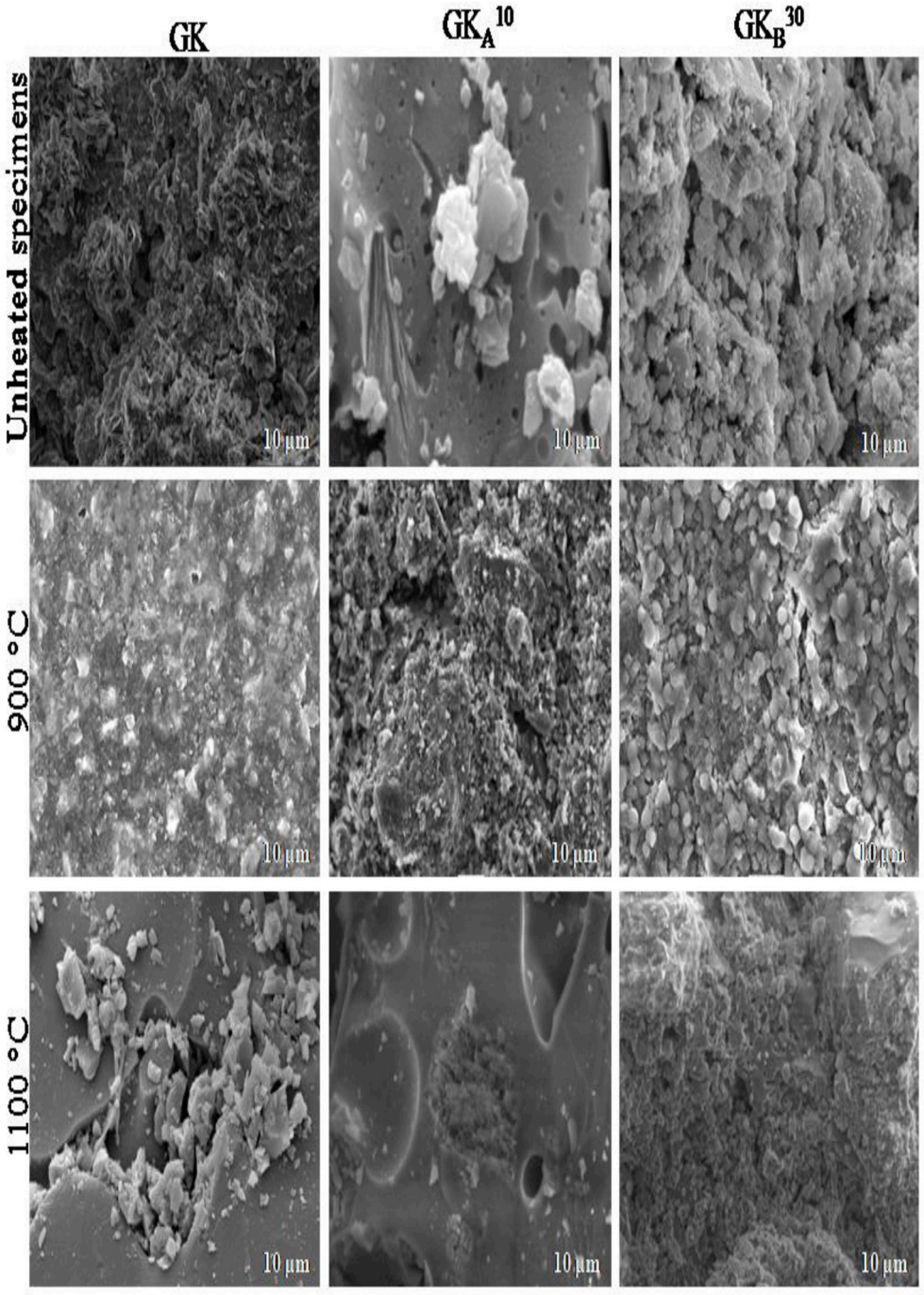

Fig. 8. SEM images of the geopolymers and of their heated products.

densification of the latter [6,7,33]. Conversely, after heating at 1100 °C, there is significant increase of compressive strength for GK_A^{10} and GK_B^{30} as compared to that of GK. This is mostly related to the formation of new crystalline phases (Fig. 7b). Indeed, as compared with GK heated at 1100 °C, the compressive strength of GK_B^{30} has increased of about 41.5% (Fig. 10b) whereas that of GK_A^{10} has increased of about 19.5% (Fig. 10a). Furthermore, the highest compressive strength is obtained at 1150 °C for GK_A^{10} (60.2 MPa) and is reduced at 1200 °C (40.0 MPa). This is due to the fact that at 1150 °C, its compactness has improved thanks to densification (Fig. 8) which contributes to gather and wrap up stable crystalline phases [20]. Additionally, GK_B^{30} heated at 1150 and 1200 °C respectively leads to constant compressive strength value (12.0 MPa) which is low as compared to the value at 1100 °C (29.1 MPa). The decrease of compressive strength at 1200 °C for GK_A^{10} and GK_B^{30} is probably due to partial dissolution of nepheline and carnegieite which allows the creation of closed pores (Fig. 8) [41]. Hence, replacement of amorphous aluminium hydroxide (10% by mass) or aluminium oxy-hydroxide (30% by mass) in alkaline activation of kaolin is an interesting process to get heated products with improved volume stability and compressive strength.

4. Conclusion

Amorphous aluminium hydroxide and aluminium oxy-hydroxide were used as replacements in the synthesis of kaolin based-geopolymers cured at 60 °C and exposed at elevated temperatures

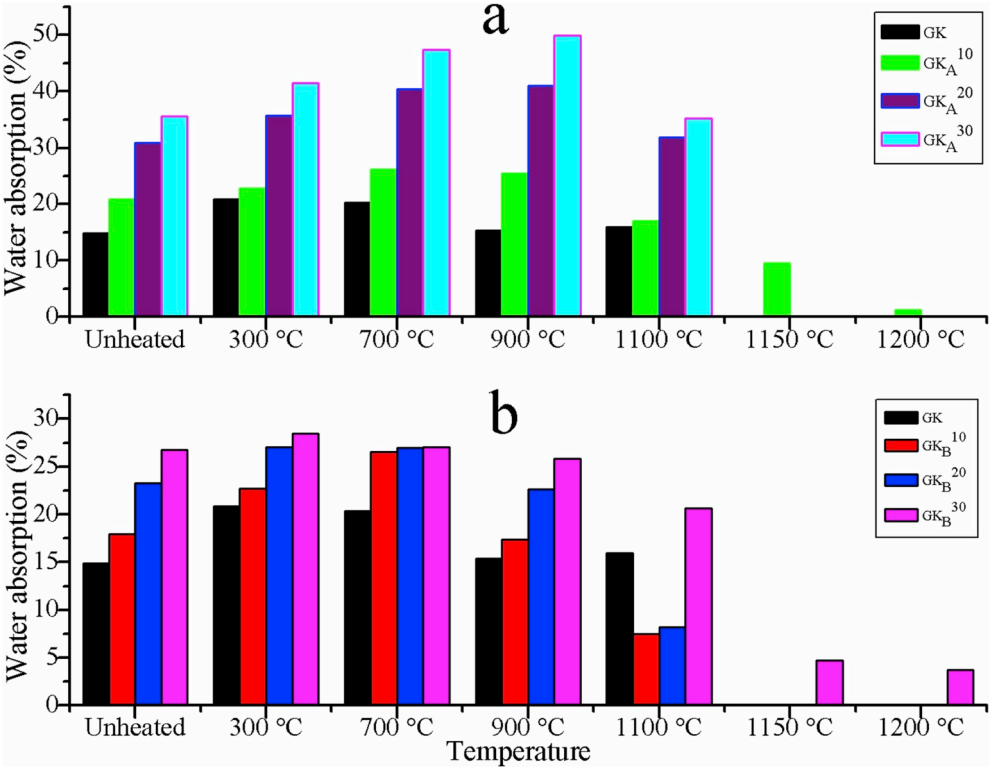

Fig. 9. Water absorption of the geopolymers and of their heated products.

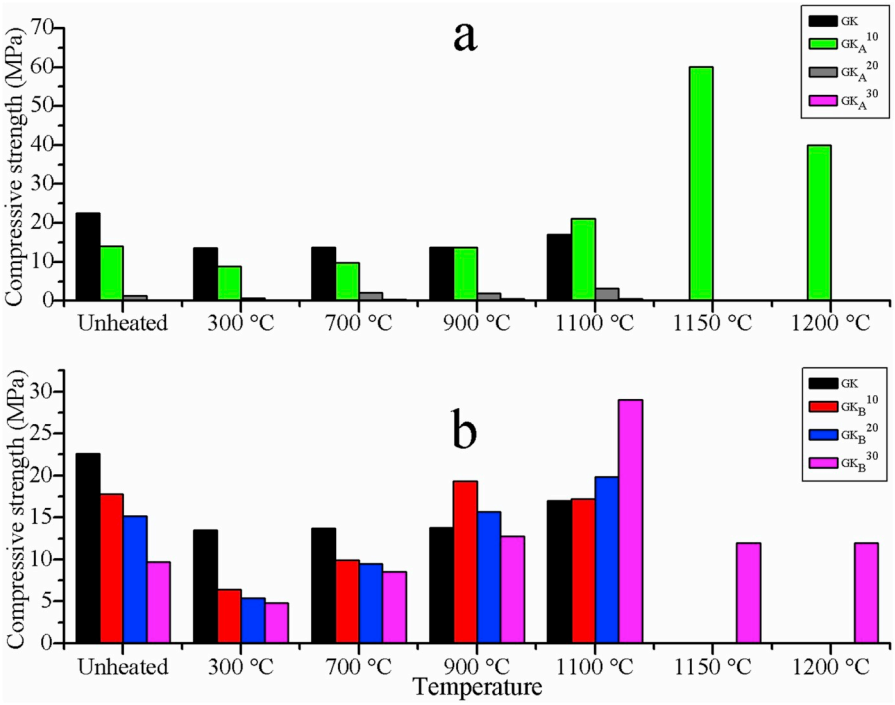

Fig. 10. Compressive strength of the geopolymers and of their heated products.

(300–1200 °C). Geopolymers with amorphous aluminium hydroxide of 10% by mass or with aluminium oxy-hydroxide of 30% by mass exhibit low compressive strength as compared to the reference geopolymer (GK). At 1100 °C, compressive strength of heated geopolymers with replacements is improved due to the formation of stable crystalline phases (mullite, corundum, nepheline and carnegieite) and to densification. Further heating of reference kaolin-based geopolymer (GK) at 1150 °C leads to damaged structure ascribed to both excessive sintering and swelling due to the transition of a part of quartz into tridymite. Conversely, specimens with 10% by mass of amorphous aluminium hydroxide or 30% by mass of aluminium oxy-hydroxide exhibit good volume stability up to 1200 °C. This is ascribed to the

thermal transformation of the replacements and to their contribution to form Al–Si minerals (nepheline and carnegieite). Unfortunately, at 1200 °C partial dissolution of nepheline and carnegieite provokes the formation of closed pores which lessens compressive strength. Used as replacements in certain percentages, amorphous aluminium hydroxide and aluminium oxy-hydroxide can successfully help to get heated kaolin-based geopolymers thermally stable and endowed with high compressive strength.

Acknowledgements

This research did not receive any specific grant from funding agencies in the public, commercial, or not-for-profit sectors. Additionally, the first author gratefully acknowledges Prof. Njoya Dayirou, Mr. Mouafon Mohamed and Mr. Pountouenchi Amadou respectively for SEM, Thermal and XRD analyses.

References

[1] H.K. Tchakouté, H.C. Rüscher, Mechanical and microstructural properties of metakaolin-based geopolymer cements from sodium water glass and phosphoric acid solution as hardeners: a comparative study, Appl. Clay Sci. 140 (2017) 81–87.
[2] M. Zhang, M. Zhao, G. Zhang, D. Mann, K. Lumsden, M. Tao, Durability of red mud-fly ash based geopolymer and leaching behavior of heavy metals in sulfuric acid solutions and deionized water, Constr. Build. Mater. 124 (2016) 373–382.
[3] D.L.Y. Kong, J.G. Sanjayan, Effect of elevated temperatures on geopolymer paste, mortar and concrete, Cement Concr. Res. 40 (2010) 334–339.
[4] A.D. Hounsi, G. Lecomte-nana, G. Djétéli, P. Blanchart, Kaolin-based geopolymers: effect of mechanical activation and curing process, Constr. Build. Mater. 42 (2013) 105–113.
[5] M. Lahoti, K.K. Wong, E. Yang, K.H. Tan, Effects of Si/Al molar ratio on strength endurance and volume stability of metakaolin geopolymers subject to elevated temperature, Ceram. Int. 44 (2018) 5726–5734.
[6] P. Duxson, G.C. Lukey, J.S.J. Van Deventer, Thermal evolution of metakaolin geopolymers: Part 1 – physical evolution, J. Non-Cryst. Solids 352 (2006) 5541–5555.
[7] P. Duxson, G.C. Lukey, J.S.J. Van Deventer, The thermal evolution of metakaolin geopolymers: Part 2–Phase stability and structural development, J. Non-Cryst. Solids 353 (2007) 2186–2200.
[8] J. Temuujin, A. Minjigmaa, W. Rickard, A. van Riessen, Thermal properties of spray-coated geopolymer-type compositions, J. Therm. Anal. Calorim. 107 (2012) 287–292.
[9] A. Elimbi, H.K. Tchakouté, D. Njopwouo, Effects of calcination temperature of kaolinite clays on the properties of geopolymer cements, Constr. Build. Mater. 25 (2011) 2805–2812.
[10] B.B. Kenne Diffo, A. Elimbi, M. Cyr, J. Dika Manga, K.H. Tchakouté, Effect of the rate of calcination of kaolin on the properties of metakaolin-based geopolymers, J. Asian Ceram. Soc. 3 (2015) 130–138.
[11] P. De Silva, K. Sagoe-Crenstil, V. Sirivivatnanon, Kinetics of geopolymerization: role of Al_2O_3 and SiO_2, Cement Concr. Res. 37 (2007) 512–518.
[12] A. Longhi, E.D. Rodríguez, S.A. Bernal, J.L. Provis, A. Paula, Valorisation of a kaolin mining waste for the production of geopolymers, J. Clean. Prod. 115 (2016) 265–272.
[13] A. Elimbi, H.K. Tchakouté, M. Kondoh, J. Dika Manga, Thermal behavior and characteristics of fired geopolymers produced from local Cameroonian metakaolin, Ceram. Int. 40 (2014) 4515–4520.
[14] L. Vidal, E. Joussein, M. Colas, J. Absi, S. Rossignol, Effect of the addition of ammonium molybdate on metakaolin-based geopolymer formation: shrinkage and crystallization, Powder Technol. 275 (2015) 211–219.
[15] D.L.Y. Kong, J.G. Sanjayan, K. Sagoe-crentsil, Comparative performance of geopolymers made with metakaolin and fly ash after exposure to elevated temperatures, Cement Concr. Res. 37 (2007) 1583–1589.
[16] R. Dupain, J.C. Lanchon, J.C. Saint Arroman, Sols, ciments et bétons, Casteilla, Paris, 2000, p. 226.
[17] ASTM C 373-88, Standard Test Method for Water Absorption, Bulk Density, Apparent Porosity, and Apparent Specific Gravity of Fired Whiteware Products, 2006.
[18] M. Monneron-gyurits, E. Joussein, M. Soubrand, P. Fondanèche, S. Rossignol, Valorization of mussel and oyster shells toward metakaolin-based alkaline activated material, Appl. Clay Sci. 162 (2018) 15–26.
[19] J.N. Yankwa Djobo, A. Elimbi, J. Dika Manga, I.B. Djon Li Ndjock, Partial replacement of volcanic ash by bauxite and calcined oyster shell in the synthesis of volcanic ash-based geopolymers, Constr. Build. Mater. 113 (2016) 673–681.
[20] E. Tiffo, A. Elimbi, J. Dika Manga, A.B. Tchamba, Red ceramics produced from mixtures of kaolinite clay and waste glass, Braz. J. Sci. Technol. 2 (2015) 1–13.
[21] H. De Souza Santos, T.W. Campos, P. De Souza Santos, P.K. Kiyohara, Thermal phase sequences in gibbsite/kaolinite clay: electron microscopy studies, Ceram. Int. 31 (2005) 1077–1084.
[22] V.J. Ingram-jones, T.C.R. Slade, W.T. Davies, C.J. Southern, S. Salvador, Dehydroxylation sequences of gibbsite and boehmite: study of differences between soak and flash calcination and of particle-size effects, J. Mater. Chem. 6 (1996) 73–79.
[23] P.T. Tanev, L.T. Vlaev, Effect of grain size on the synthesis of active alumina from gibbsite by flash calcination and rehydration, Catal. Lett. 19 (1993) 351–360.
[24] C. Bich, J. Ambroise, J. Péra, Influence of degree of dehydroxylation on the pozzolanic activity of metakaolin, Appl. Clay Sci. 44 (2009) 194–200.
[25] N.J.G. Deutou, T. Beda, M. Biesuz, L. Boubakar, U.C. Melo, E. Kamseu, M.V. Sglavo, Design and characterization of porous mullite based semi-vitrified ceramics, Ceram. Int. 44 (2018) 7939–7948.
[26] V. Viswabaskaran, F.D. Gnanam, M. Balasubramanian, Mullitisation behaviour of calcined clay – alumina mixtures, Ceram. Int. 29 (2003) 561–571.
[27] M.J.A. Mijarsh, M.A.M. Johari, Z. Arifin, Compressive strength of treated palm oil fuel ash based geopolymer mortar containing calcium hydroxide, aluminium hydroxide and silica fume as mineral additives, Cement Concr. Compos. 60 (2015) 65–81.
[28] A.P. Rollet, R. Bouaziz, L'analyse thermique : l'examen des processus chimiques, Tome 2, Gauthier-Villars, 55, Quai des Grands-Augustins, Paris 6e, 1972, p. 587.
[29] H.K. Tchakouté, C.H. Rüscher, S. Kong, E. Kamseu, C. Leonelli, Thermal behavior of metakaolin-based geopolymer cements using sodium waterglass from rice husk ash and waste glass as alternative activators, Waste Biomass Valor 8 (2017) 572–584.
[30] H.K. Tchakouté, C.H. Rüscher, J.N. Yankwa Djobo, B.B. Kenne Diffo, D. Njopwouo, Influence of gibbsite and quartz in kaolin on the properties of metakaolin-based geopolymer cements, Appl. Clay Sci. 107 (2015) 188–194.
[31] K.J.D. Mackenzie, J. Temuujin, K. Okada, Thermal decomposition of mechanically activated gibbsite, Thermochim. Acta 327 (1999) 103–108.
[32] G. Kakali, T. Perraki, S. Tsivilis, E. Badogiannis, Thermal treatment of kaolin: the effect of mineralogy on the pozzolanic activity, Appl. Clay Sci. 20 (2001) 73–80.
[33] E. Kamseu, A. Rizzuti, C. Leonelli, D. Perera, Enhanced thermal stability in K_2O-metakaolin-based geopolymer concretes by Al_2O_3 and SiO_2 fillers addition, J. Mater. Sci. 45 (2010) 1715–1724.
[34] J.N. Yankwa Djobo, L.N. Tchadjié, H.K. Tchakouté, B.B. Kenne Diffo, A. Elimbi, D. Njopwouo, Synthesis of geopolymer composites from a mixture of volcanic scoria and metakaolin, J. Asian Ceram. Soc. 2 (2014) 387–398.
[35] D. Panias, I.P. Giannopoulou, T. Perraki, Effect of synthesis parameters on the mechanical properties of fly ash-based geopolymers, Colloids Surfaces A Physicochem. Eng. Asp. 301 (2007) 246–254.
[36] G.E.D. Benedetto, R. Laviano, L. Sabbatini, P.G. Zambonin, Infrared spectroscopy in the mineralogical characterization of ancient pottery, J. Cult. Herit. 3 (2002) 177–186.
[37] H. Cheng, J. Yang, Q. Liu, J. Zhang, R.L. Frost, A spectroscopic comparison of selected Chinese kaolinite, coal bearing kaolinite and halloysite-A mid-infrared and near-infrared study, Spectrochim. Acta, Part A 77 (2010) 856–861.
[38] E. Obonyo, E. Kamseu, U.C. Melo, C. Leonelli, Advancing the use of secondary inputs in geopolymer binders for sustainable cementitious composites: a Review, Sustainability 3 (2011) 410–423.
[39] H.K. Tchakouté, A. Elimbi, E. Yanne, C.N. Djangang, Utilization of volcanic ashes for the production of geopolymers cured at ambient temperature, Cement Concr. Compos. 38 (2013) 75–81.
[40] P.N. Lemougna, K.J.D. Mackenzie, U.F.C. Melo, Synthesis and thermal properties of inorganic polymers (geopolymers) for structural and refractory applications from volcanic ash, Ceram. Int. 37 (2011) 3011–3018.
[41] C. Kuenzel, L.M. Grover, L. Vandeperre, A.R. Boccaccini, C.R. Cheeseman, Production of nepheline/quartz ceramics from geopolymer mortars, J. Eur. Ceram. Soc. 33 (2013) 251–258.
[42] J. Ye, W. Zhang, D. Shi, Effect of elevated temperature on the properties of geopolymer synthesized from calcined ore-dressing tailing of bauxite and ground-granulated blast furnace slag, Constr. Build. Mater. 69 (2014) 41–48.
[43] O.R. Njindam, D. Njoya, J.R. Mache, M. Mouafon, A. Messan, D. Njopwouo, Effect of glass powder on the technological properties and microstructure of clay mixture for porcelain stoneware tiles manufacture, Constr. Build. Mater. 170 (2018) 512–519.

Scientific African 14 (2021) e01015

Contents lists available at ScienceDirect

Scientific African

journal homepage: www.elsevier.com/locate/sciaf

Effect of various amounts of aluminium oxy-hydroxide coupled with thermal treatment on the performance of alkali-activated metakaolin and volcanic scoria

Emmanuel Tiffo[a], Placide Désiré Belibi Belibi[b], Jean Batiste Bike Mbah[c], Alomayri Thamer[d], Thierry Ebenizer Pougnong[a], Jean Baenla[a], Antoine Elimbi[a,*]

[a] Laboratory of Applied Inorganic Chemistry, Faculty of Science, University of Yaoundé I, P.O. Box 812, Yaoundé, Cameroon
[b] Applied Physical and Theoretical Chemistry Laboratory, Faculty of Science, University of Yaoundé I, P.O. Box 812, Yaoundé, Cameroon
[c] Laboratoire de Matériaux et de Chimie Industrielle, Ngaoundéré, Université de Ngaoundéré, ENSAI B.P. 445, Cameroun
[d] Department of Physics, Faculty of Applied Science, Umm Al-Qura University, P.O. Box 715, Makkah 21955, Saudi Arabia

ARTICLE INFO

Article history:
Received 4 May 2021
Revised 10 October 2021
Accepted 11 October 2021

Editor: DR B Gyampoh

Keywords:
Volcanic scoria
Metakaolin
Aluminium oxy-hydroxide
Alkali-activation
Thermal stability

ABSTRACT

This study aims to improve the stability of alkali-activated products, such as powdered volcanic scoria and metakaolin, by thermal treatment in addition to their partial replacement with aluminium oxy-hydroxide. To this effect, mixtures obtained from a partial replacement of aluminosilicate sources (volcanic scoria or metakaolin) with respectively 0, 10, 20 or 30 % of mass of aluminium oxy-hydroxide were alkali-activated and stored for 28 days at room temperature in the laboratory. The various specimens obtained were heated at 900–1200 °C and both the alkali-aluminosilicates and the heated products were analysed. It appeared that aluminium oxy-hydroxide improves the stability of heated products. Thus, without replacement, alkali-activated specimens of metakaolin showed cracks at 1100 °C while those of volcanic scoria melted at 1150 °C. Conversely, heated alkali-activated specimens of either volcanic scoria or metakaolin with the replacement showed stability up to 1200 °C and an improvement in the residual compressive strength as from 900 °C. Indeed, at 1150 °C, the metakaolin-based geopolymers or the alkali-activated volcanic scoria with 30 % of mass of the replacement showed residual compressive strength of 76.7 and 35.0 MPa, respectively, due to the sintering and to the formation of new crystalline phases (mullite, corundum, carnegieite and nepheline). Yet, residual compressive strength in the alkali-activated aluminosilicate specimens with replacement that were heated at 1200 °C dropped as a result of the partial dissolution of nepheline and carnegieite which may have generated closed pores within their microstructure. Hence, alkali-activation of volcanic scoria or metakaolin partially replaced with aluminium oxy-hydroxide is a remarkable process to get thermally stable products.

* Corresponding author.
E-mail address: aelimbi2002@yahoo.fr (A. Elimbi).

https://doi.org/10.1016/j.sciaf.2021.e01015

Introduction

Ordinary Portland Cement (OPC) is the main binder used in the production of mortars and concretes. However, its production is energy consuming and it generates about 5–8 % of world wide CO_2, which is responsible of global warming and acid rain [1]. Although OPC based-products possess excellent structural performances at ambient temperature, both their mechanical properties and volume stability are seriously degraded after exposure as from 300 to 400 °C [2]. In the last four decades, alternative energy-efficient materials, called geopolymers which are endowed with good volume stability up to 900 °C, attracted interest of researchers [1,2]. Indeed, geopolymerisation relies on a chemical reaction between a powder of aluminosilicate source and an alkaline or acid (mostly phosphoric acid) solution at ambient or slightly elevated temperature to form aluminosilicate inorganic polymers [3,4]. Geopolymers are of three dimensional silico-aluminate structure [5,6], consisting of SiO_4 and AlO_4 tetrahedra units linked by oxygen atoms [7]. The negative charge in the AlO_4 unit is balanced by compensating ions such as Na^+, K^+, Ca^{2+} [7,8]. Known for their sustainable binding abilities with good physical properties, durability and eco-friendliness, geopolymers can be potential fire-resistant due to their ceramic-like amorphous structure [9–11]. Nowadays, the concern of the stability of building material binders remains of research interest [11–15]. Indeed, the determination of the stability of building material binders is important among others for insurance of safe usage at certain temperature ranges [16,17]. For instance, when a binder ought to be used at high temperature, its expanding ability, phase stability and resistance to strength deterioration play significant roles [18]. From the past decades up to date, several studies based on thermal resistance of geopolymers obtained from a wide range of aluminosilicates have been reported. In that respect, Elimbi et al. [8] studied the thermal behavior of alkali-activated metakaolin based-geopolymer. They observed that its thermal behavior was characterized by the removal of bonded water at up to 750 °C followed by the crystallization of new phases with a significant decrease of compressive strength. Moreover, Lahoti et al. [17] studied the effects of Si / Al molar ratio on the strength endurance and the volume stability of metakaolin based-geopolymers subjected to high temperatures. They observed that thermal shrinkage induced the formation of cracks which reduce the residual strength of geopolymers obtained from Si / Al molar ratios less than or equal to 1.50. Inversely, they observed that densification in the matrix was the driving factor of residual strength for geopolymers with Si / Al molar ratio greater than 1.50. Elsewhere, Lemougna et al. [2] investigated the thermal properties of alkali-activated volcanic scoria and obtained specimens relatively stable to heat so that 60 % of initial compressive strength and low shrinkage were recorded at up to 900 °C. Hence, prior to be used for applications at temperatures greater than 900 °C, characteristics such as stability and residual compressive strength of alkali-activated aluminosilicate products need to be improved. In a previous study [19], both stability and enhancement of residual compressive strength of kaolin based-geopolymers with a partial replacement of aluminium hydroxide had been investigated. The present study makes use of aluminium oxy-hydroxide as a partial replacement coupled with thermal treatment to improve the performance of products resulting from alkali-activation of powdered volcanic scoria and metakaolin, respectively. Actually, aluminium oxy-hydroxide is solely used industrially to prepare transitional alumina having metastable structures or mixed with clay materials for elaboration of refractory products [20–21]. Also, it appears to be a suitable alumina source that can be used to improve heating properties of alkali-activated aluminosilicate products. Based on the initial raw materials (volcanic scoria, metakaolin and aluminium oxy-hydroxide), synthesized and heated products (900–1200 °C), mass and volume stabilities, mineralogical changes, water absorption and compressive strength were studied.

Materials and experimental procedures

The kaolin, provided by the NUBRU Holding Group that operates on the valorization of certain local raw materials in Cameroon, was washed according to Stokes' law [22] in order to enrich the resulting clay fraction in kaolinite mineral and the latter was denoted as K. The volcanic scoria, denoted as Z, was collected from the Cameroonian locality of Galim (5°40′05″latitude; 10°23′10″ longitude and 1143 m in altitude) [23]. Vesicular particles of Z were oven-dried at 105 °C for 24 h, ground using a ball mill afterwards sieving with a 90 μm mesh-sifter. The semi-crystalline aluminium oxy-hydroxide, supplied by Sigma Aldrich and denoted as B, was granular and was mainly composed of boehmite. Prior to be used, both K and B were separately crushed in porcelain mortars and sieved thanks to a 90 μm mesh-sifter. The powder of K was calcined in an electric furnace (Nabertherm, Mod. LH 60/14) for 4 h at 700 °C [24] at the rate of 1 °C / Min in order to get a suitable reactive metakaolin (MK) [25]. MK was mainly composed of quartz [PDF# 46–1045], anatase [PDF# 21–1272] and illite [PDF# 26–911]. Z was made of allophane [PDF# 02–0039], anorthoclase [PDF# 75–1635], anorthite ordered [PDF# 12–0301], forsterite ferroan [PDF# 87–0619], diopside [PDF# 87–0698], augite [PDF# 24–201], maghemite [PDF# 89–5894], haematite [PDF# 89–0596] and anatase. The activator was prepared by mixing sodium hydroxide (99 % by mass of NaOH) solution and commercial sodium silicate (% by mass: SiO_2 (28.7), Na_2O (8.9), H_2O (62.4)) to obtain, respectively molar ratios of SiO_2 / Na_2O =1.45 and H_2O / Na_2O =16. The resulting solution was then sealed and stored at least for 24 h at room temperature (24 ± 3 °C) in the laboratory so as to allow full silicate depolymerization. The designed mixtures were obtained by a partial replacement of the aluminosilicates (MK or Z) with 0, 10, 20 and 30 % of mass of aluminium oxy-hydroxide (B) respectively. Actually, the dried powders were first mixed in a Hobart mixer (M & O model N50-G) for 5 Min followed by a gradual addition of alkaline activator for the others 5 Min. For a good workability, the liquid to solid mass ratios were, respectively 1.13 (pastes from MK) and 0.84 (pastes from Z). The fresh pastes were poured into cylindrical moulds (height: 46 mm; diameter: 23 mm) and were vibrated for 5 Min on an electrical vibrating table (M & O, type 202, No. 106) in order to remove entrapped air bubbles. During the hardening of the pastes, the cylinders were firstly covered with thin films of

polyethylene in order to avoid water evaporation, and then kept for 24 h at room atmosphere in the laboratory (24 ± 3 °C) before the demoulding. The resulting specimens were denoted as GMK, GMK_B^{10}, GMK_B^{20}, GMK_B^{30} (specimens from MK) and GZ, GZ_B^{10}, GZ_B^{20} and GZ_B^{30} (specimens from Z), respectively. Prior to be heated (900, 1100, 1150 and 1200 °C, respectively) for 2 h in a programmable electric furnace (Nabertherm, Mod.LH60 / 14), the cylinder specimens were oven-dried at 105 °C for 24 h. The chemical analyses of MK and Z were done by ICP-OES using a Perkin Elmer Spectrometer (Optima™ 7000 DV ICP-OES). The mass loss was determined thanks to thermogravimetric (TG) analysis curves whereas the endothermic and exothermic phenomena were revealed by the Differential Thermal Analysis (DTA) [12], both recorded simultaneously with a NETZSCH STA 429 (CD) device. To this end, the powders of alkali-activated aluminosilicate pastes aged 28 days were heated in a self-generated atmosphere of air, from ambient temperature to 1200 °C. Water absorption was determined according to the ASTM C 373–88 standard [26] and three replicated specimens were experimented on each batch. The compressive strength was assessed using a hydro-electric press (M & O, type 11.50, N° 21) which operated at an average rate of 3 mm / Min according to the EN 196–1 standard [22] and four replicate specimens of each batch were used for measurement. After the compressive strength test, fragments of specimens (GMK and GMK_B^{30}; GZ and GZ_B^{30}) with their heated products were crushed, sieved with a 90 μm mesh-sifter and the resulting powders were used in carrying out XRD analysis. Actually, the X-ray diffraction analysis (Advance Bruker D8 device) was done with monochrometer CuKα radiation (λ= 1.54 Å), operated at 45 kV and 40 mA with a step size of 0.026 ° and a scanning rate of 0.1 °/ s in the 2θ range of 5–70 ° Additionally, crystalline phases were identified by comparing the obtained patterns with the Powder Diffraction File (PDF) standards from the International Centre for Diffraction Data (ICDD) [19].

Results and discussion

Thermal treatment of alkali-activated products and mass stability

Fig. 1 shows the thermal analyses (TG and DTA) of the powders of the metakaolin-based geopolymers (GMK and GMK_B^{30}) and the alkali-activated volcanic scoria (GZ and GZ_B^{30}) specimens which were cured at room temperature for duration of 28 days. The major mass loss is observed between room temperature and 250 °C (Fig. 1a) as depicted by the first broad endothermic peak (Fig. 1b). Indeed, the powders of GZ and GZ_B^{30} show 8.5 and 9.8 % of mass losses, respectively whereas those of GMK and GMK_B^{30} show 13.7 and 14.6 % of mass losses, respectively. These mass losses are attributed to the removal of physically absorb water, interstitial and chemically bound water from both the polysialate network and aluminium oxy-hydroxide [18,27,28]. Moreover, the amount of water released is greater in the metakaolin-based geopolymers than in the ones of alkali-activated volcanic scoria, indicating a higher condensed structure as compared to the latter synthesized products [27]. This could be due to the fineness of metakaolin particles which required a greater amount of alkaline activator to achieve better results as compared to the one of volcanic scoria [19,23]. Others mass losses (3.6 and 5.0 % for GZ and GZ_B^{30}, respectively; 2.4 and 3.6 % for GMK and GMK_B^{30}, respectively), considered as minor, occurred between 250 and 700 °C and were mostly attributed to hydroxyl water of polysialate gel, allophane and aluminium oxy-hydroxide [8,29,30]. Between 800 and 1200 °C, the TG curves did not show mass loss whereas the DTA displayed broad exothermic bands (GZ_B^{30}, GMK and GMK_B^{30}) and an endothermic peak (GZ). These thermal phenomena corresponded to the crystallization of new phases (GZ_B^{30}, GMK and GMK_B^{30}) and melting (GZ) [19,28]. Hence, a partial replacement with aluminium oxy-hydroxide is beneficial to prevent early melting of the alkali-activated volcanic scoria specimens. In the case of the metakaolin-based geopolymers, the appearance of new crystalline phases was observed between 900 and 1100 °C (GMK), whereas for GMK_B^{30}, there was a shift towards higher temperatures (1100–1200 °C). The latter observations showed that a partial replacement with aluminium oxy-hydroxide increases the stability of both metakaolin-based geopolymer and alkali-activated volcanic scoria up to 1200 °C.

Volume stability

The aspect of both the metakaolin-based geopolymers (GMK and GMK_B^{30}) and the alkali-activated volcanic scoria (GZ and GZ_B^{30}) along with their heated products is shown in Fig. 2. Globally, all the unheated and heated (900 °C) specimens show good volume stability with no apparent cracks. Conversely, at 1100 °C, there are cracks for GMK as a result of thermal expansion of the quartz (quartz α - quartz β - tridymite) [18] and the low stability, whereas GMK_B^{30} heated at 1200 °C shows a good volume stability and the absence of cracks. This could be due to the replacement (aluminium oxy-hydroxide) which hinders the formation of cracks probably as a result of its refractoriness [19]. Concerning the alkali-activated volcanic scoria GZ that was heated at 1100 °C, it darkens, swells and melts at 1150 °C. Inversely, GZ_B^{30} heated at least at 1150 °C shows good volume stability and there are neither apparent swellings nor cracks. Hence, due to its refractoriness, a partial replacement of either metakaolin or volcanic scoria with aluminium oxy-hydroxide leads to alkali-activated products with good volume stability up to 1200 °C.

Mineralogical changes

The XRD patterns of both the metakaolin-based geopolymers (GMK and GMK_B^{30}) and the alkali-activated volcanic scoria (GZ and GZ_B^{30}) along with their heated products are shown in Fig. 3. The unheated GMK contains illite – 2M1

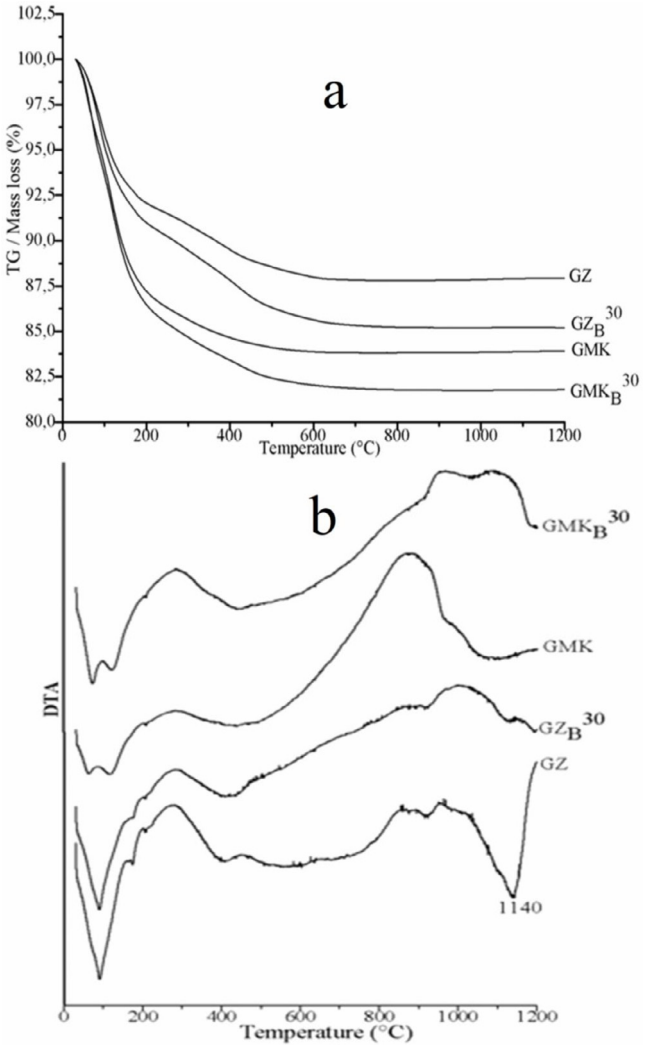

Fig. 1. TG (a) and DTA (b) curves of the alkali-activated products.

[$(K,H_3O)(Al,Mg,Fe)_2(Si,Al)_4O_{10}$ $(OH)_2$,(H_2O)]: PDF# 26–911], anatase [TiO_2: PDF# 21–1272] and quartz [SiO_2: PDF# 46–1045]. In addition, the unheated GMK_B^{30} (Fig. 3a) also contains boehmite [γ-AlO(OH): PDF# 21–1307] originating from aluminium oxy-hydroxide. As for the unheated alkali-activated volcanic scoria GZ (Fig. 3b), the crystalline phases are augite [$(Ca,Na)(Mg,Fe,Al)(Si,Al)_2O_6$: PDF# 24–201], diopside [$(Ca_{0,89}Mg_{1,11}Si_2O_6)$: PDF# 87–0698], hematite [Fe_2O_3: PDF# 89–0596], maghemite [γ-Fe_2O_3: PDF# 89–5894], forsterite ferroan [$Mg_{1,42}$ $Fe_{0,58}(Si_{0,99}Al_{0,01})O_4$: PDF# 87–0619)], anorthite ordered [$Ca_{0,66}Na_{0,34}Al_{1,66}Si_{2,34}O_8$: PDF# 12–0301, anorthoclase [$Na_{0,85}K_{0,15}(AlSi_3O_8)$: PDF# 75–1635], allophane [$SiO_2.Al_2O_3.H_2O$: PDF# 02–0039] and anatase. GZ_B^{30} contains as well boehmite originating from aluminium oxy-hydroxide. The presence of crystalline phases such as augite, diopside, hematite, maghemite, forsterite ferroan, anorthite ordered, anorthoclase, allophane, anatase and boehmite in the specimens of alkali-activated volcanic scoria is an indication of their low reactivity in alkaline medium [31,32]. After thermal exposure, the heated metakaolin-based geopolymers contain mullite [$Al(Al_{0.83}Si_{1.08}O_{4.85})$: PDF# 89–2814], corundum [α-Al_2O_3: PDF# 10–173], quartz, tridymite [SiO_2: PDF# 18–1170], rutile [TiO_2: PDF# 21–1276], nepheline [$(Na,K)AlSiO_4$: PDF# 89–8763] and carnegieite [$NaAlSiO_4$: PDF# 44–1496]. Regarding the heated alkali-activated volcanic scoria specimens, the crystalline phases are, respectively mullite, corundum, nepheline, carnegieite, hematite and rutile. It is worthy to mention that on the XRD patterns of the unheated and heated specimens of GMK (Fig. 3a), the order of magnitude of the diffused halo peak, characteristic of an amorphous phase ($17° < 2\theta < 38°$) is well highlighted [8,32], contrary to that of the unheated and heated GMK_B^{30} in which the halo is slightly reduced as a result of the presence of replacement (aluminium oxy-hydroxide). Furthermore, in the metakaolin-based geopolymers, as compared to the other temperatures, the intensities of the main peaks of nepheline and carnegieite are highest at 1100 °C. Conversely, at 1200 °C, there is probably a partial dissolution of the latter neoformed crystalline phases, which is highlighted

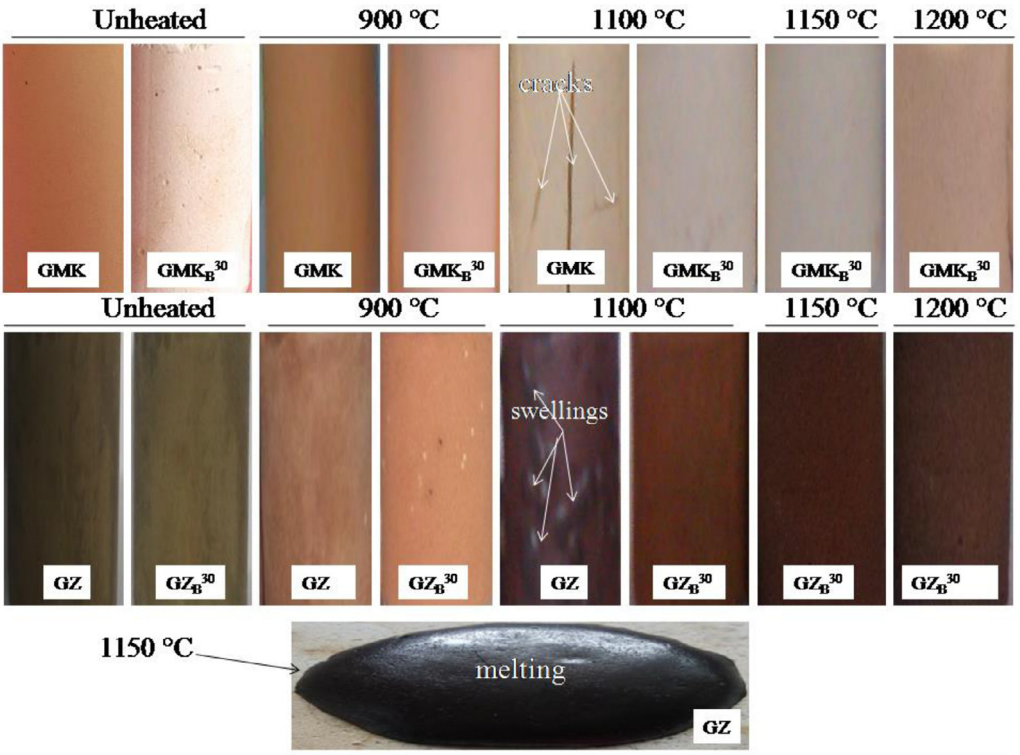

Fig. 2. Visual aspect of the alkali-activated aluminosilicates and their heated products.

by the decrease of the intensities of their main peaks (Fig. 3a). As for the heated alkali-activated volcanic scoria specimens (Fig. 3b), there is a gradual transformation of both the amorphous phase ($17° \leq 2\theta \leq 38°$) and boehmite, probably into Al-Si minerals (nepheline, carnegieite, mullite and corundum) which have high melting temperatures.

Water absorption

The variation of water absorption (WA) versus temperature of the alkali-activated aluminosilicates is presented in Fig. 4. WA in the unheated alkali-activated aluminosilicates increases with increasing amount of the replacement, which may indicate that aluminium oxy-hydroxide is either non-active or behaves as filler [19,33]. As compared to the unheated samples, WA in the metakaolin-based geopolymers heated at 900 °C has greatly decreased contrary to that in the alkali-activated volcanic scoria. This may arise from the value of L / S mass ratio. In fact, the L / S mass ratio is greater in the metakaolin-based geopolymers (1.13) than in the alkali-activated volcanic scoria (0.84). This great content of the activator in the metakaolin-based geopolymers enhances the level of sintering [34], hence more densification. In addition, WA is slightly low in the unheated alkali-activated volcanic scoria specimens as compared to that in the ones heated at 900 °C, which may be amongst others attributed to the elimination of various types of water within the latter products. As for the metakaolin-based geopolymers, at 900 °C, WA has lessened due to the sintering which is enhanced by the formation of a vitreous phase thanks to the great content of the activator. At 1100 °C, WA in the GMK and GZ specimens is lowest (< 2 %) as a result of the sintering which allows the close-down of pores. Compared with the values at 1100 °C, WA in GZ_B^{30} at 1150 °C remains slightly constant whereas that in GMK_B^{30} decreases moderately, which could be most likely attributed to the improvement of densification and to the formation of neocrystalline phases. Due to their good stability (Fig. 2), the GMK_B^{30} and GZ_B^{30} specimens were heated at 1200 °C. It appeared that WA decreases as a result of partial dissolution of nepheline and carnegieite (Fig. 3), which generate an extra vitreous phase that fills pores [35].

Compressive strength

Fig. 5 shows the compressive strength variation versus temperature in the alkali-activated aluminosilicates along with their heated products. The compressive strength in the unheated alkali-activated specimens decreases with increasing amount of replacement. This could be attributed to the fact that, gradual increase of aluminium oxy-hydroxide weakens

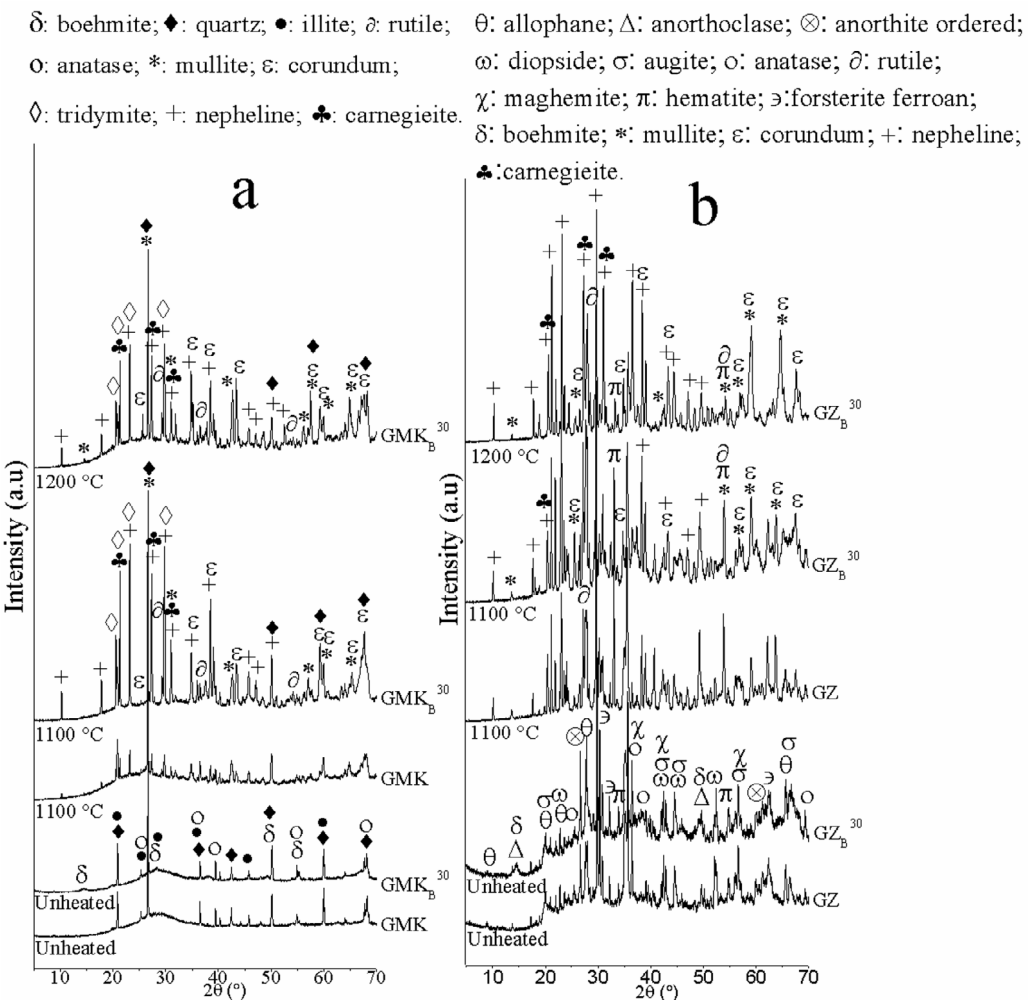

Fig. 3. XRD patterns of the metakaolin-based geopolymers (a) and the alkali-activated volcanic scoria (b) along with their heated products.

the mechanical strength of specimens because at this stage, the replacement is still behaving as filler. This is further highlighted by the presence of boehmite in their mineralogical composition (Fig. 3). However, the compressive strength values in the metakaolin-based geopolymers are greater than those in the alkali-activated volcanic scoria. This is due to greater reactivity of metakaolin in alkaline medium [23,36] as compared with volcanic scoria. At 900 °C, there is an improvement of the residual compressive strength for all the alkali-activated aluminosilicates. This is ascribed to the formation of new crystalline phases (Fig. 3) along with densification via polysialate matrix [2,19,37]. However, the specimens with the replacement exhibit lower residual compressive strength values than those without aluminium oxy-hydroxide. This is due to the fact that, the replacement delayed the densification process because of its refractoriness [19,28]. The improvement of the residual compressive strength in GMK can be attributed the mineralogical composition of the raw kaolin (K) used to obtain metakaolin. Indeed, a large content of gibbsite in the kaolin (K) [19] leads to the formation of α-Al_2O_3 at high temperatures (900–1100 °C) [38,39], which provides the stability of GMK. Additionally, the low value of water absorption (WA < 1 %) and the absence of cracks (Fig. 2) at 900 °C account for the improvement of the residual compressive strength observed in GMK. At 1100 °C, the residual compressive strength values in the alkali-activated volcanic scoria specimens remain improved, contrary to that in the metakaolin-based geopolymers that globally deplete. Thus, for the specimens of GMK, the low value of residual compressive strength may be due to the formation of cracks (Fig. 2) that probably originate from the quartz transition [18]. As for the other specimens (GMK^{10}, GMK^{20} and GMK^{30}), the slight increase of residual compressive strength is likely due to the presence of the replacement which hinders the formation of cracks because of its refractoriness and its aptitude to form Al-Si minerals [19]. At 1150 °C, GMK$_B^{30}$ and GZ$_B^{30}$ specimens exhibit highest residual compressive strengths (76.7 and 35.0 MPa, respectively) as a result of both densification and the highest content of the new formed crystalline phases [35,37]. Because of their good stability, the specimens of GMK$_B^{30}$ and GZ$_B^{30}$ were further heated at 1200 °C, unfortunately, they exhibited important compressive strength losses.

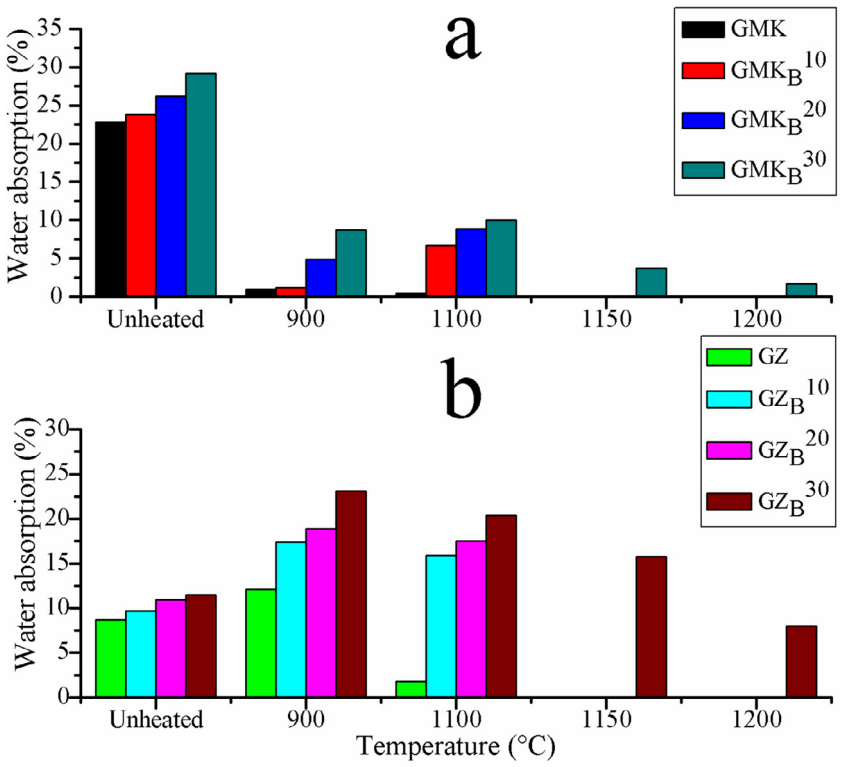

Fig. 4. Water absorption in the metakaolin-based geopolymers (a) and the alkali-activated volcanic scoria (b) specimens along with their heated products.

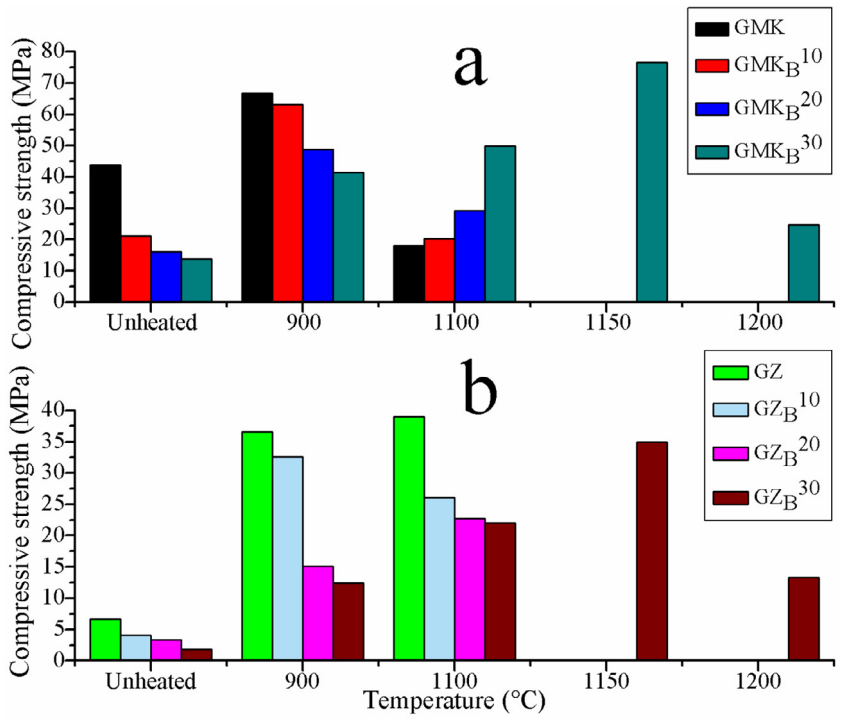

Fig. 5. Compressive strength in the metakaolin-based geopolymers (a) and the alkali-activated volcanic scoria (b) along with their heated products.

Conclusion

During the alkali-activation of both volcanic scoria and metakaolin, aluminium oxy-hydroxide was used as a partial replacement. The replacement improved the stability of the heated alkali-activated aluminosilicates (900 - 1200 °C). Thus, without the replacement, the metakaolin-based geopolymers showed visible cracks at 1100 °C while the alkali-activated volcanic scoria melted at 1150 °C. Conversely, heating the specimens of alkali-activated volcanic scoria or metakaolin-based geopolymers with the replacement led to better volume stability up to 1200 °C. This could be attributed to the refractoriness of the replacement along with its ability to form thermally stable minerals (corundum, mullite, nepheline and carnegieite). Also, at 1150 °C, the specimens with 30 % of mass of the replacement let to highest residual compressive strength (76.7 MPa for metakaolin-based geopolymers; 35.0 MPa for alkali-activated volcanic scoria) due to both increasing content of thermally stable minerals and improvement of densification. Unfortunately, the residual compressive strength in the alkali-activated aluminosilicates with the replacement that were heated at 1200 °C lessened as a result of partial dissolution of nepheline and carnegieite which may have generated closed pores within their microstructure. Hence, a partial replacement of volcanic scoria or metakaolin with up to 30 % of mass of aluminium oxy-hydroxide is a suitable process to get thermally stable alkali-activated products.

Declaration of Competing Interest

The authors declare that they have no known competing financial interests or personal relationships that could appeared to influence the work reported in this paper.

Acknowledgements

This research did not receive any specific grant from funding agencies in the public, commercial, or non-profit sectors. Additionally, the first author gratefully acknowledges Drs Mouafon Mohamed and Pountouenchi Amadou, respectively for Thermal and XRD analyses.

References

[1] A.M. Rashad, Alkali-activated metakaolin: a short guide for civil engineer - an overview, Constr. Build. Mater. 41 (2013) 751–765.
[2] P.N. Lemougna, K.J.D. Mackenzie, U.F.C. Melo, Synthesis and thermal properties of inorganic polymers (geopolymers) for structural and refractory applications from volcanic ash, Ceram. Int. 37 (2011) 3011–3018.
[3] A.M.N. Moudio, H.K. Tchakouté, D.L.V. Ngnintedem, F. Andreola, E. Kamseu, C.P. Nanseu-Njiki, C. Leonelli, C.H. Rüscher, Influence of the synthetic calcium aluminate hydrate and the mixture of calcium aluminate and silicates hydrates on the compressive strengths and the microstructure of metakaolin-based geopolymer cements, Mater. Chem. Phys. 264 (2021) 124459.
[4] C.N. Bewa, H.K. Tchakouté, C. Banenzoué, L. Cakanou, T.T. Mbakop, E. Kamseu, C.H. Rüscher, Acid-based geopolymers using waste fired brick and different metakaolins as raw materials, Appl. Clay Sci 198 (2020) 105813.
[5] J. Davidovits, Geopolymers inorganic polymeric new materials, J. Therm. Anal. 37 (1991) 1633–1656.
[6] J. Davidovits, Properties of geopolymer cements, in: Proceedings of the First International Conference on Alkaline Cements and Concretes, SRJBM, 1, Kiev, Ukraine, 1994, pp. 131–149. pp..
[7] J.N. Yankwa Djobo, A. Elimbi, H.K. Tchakouté, S. Kumar, Mechanical properties and durability of volcanic ash based geopolymer mortars, Constr. Build. Mater. 124 (2016) 606–614.
[8] A. Elimbi, H.K. Tchakouté, M. Kondoh, J.Dika Manga, Thermal behavior and characteristics of fired geopolymers produced from local Cameroonian metakaolin, Ceram. Int. 40 (2014) 4515–4520.
[9] X. Jiao, Y. Zhang, T. Chen, Thermal stability of a silica-rich vanadium tailing based geopolymer, Constr. Build. Mater. 38 (2013) 43–47.
[10] M. Zhang, M. Zhao, G. Zhang, D. Mann, K. Lumsden, M. Tao, Durability of red mud-fly ash based geopolymer and leaching behavior of heavy metals in sulfuric acid solutions and deionized water, Constr. Build. Mater 124 (2016) 373–382.
[11] D.L.Y. Kong, J.G. Sanjayan, K. Sagoe-Crentsil, Comparative performance of geopolymers made with metakaolin and fly ash after exposure to elevated temperatures, Cem. Con. Res. 37 (2007) 1583–1589.
[12] C.R. Kaze, A. Nana, G.L. Lecomte-Nana, J.G.N. Deutou, E. Kamseu, U.C. Melo, F. Andreola, C. Leonelli, Thermal behaviour and microstructural evolution of metakaolin and meta-halloysite-based geopolymer binders: a comparative study, J. Therm. Anal. Calorim. (2021), doi:10.1007/s10973-021-10555-2.
[13] D.L.Y. Kong, J.G. Sanjayan, Effect of elevated temperatures on geopolymer paste, mortar and concrete, Cem. Con. Res. 40 (2010) 334–339.
[14] C. Kuenzel, L.M. Grover, L. Vandeperre, A.R. Boccaccini, C.R. Cheeseman, Production of nepheline /quartz ceramics from geopolymer mortars, J. Eur. Ceram. Soc 33 (2013) 251–258.
[15] P.N. Lemougna, A. Adediran, J. Yliniemi, A. Ismailov, E. Levanen, P. Tanskanen, P. Kinnunen, J. Roning, M. Illikainen, Thermal stability of one-part metakaolin geopolymer composites containing high volume of spodumene tailings and glass wool, Cem. Con. Comp. 114 (2020) 103792.
[16] H. Cheng-Yong, L. Yun-Ming, M.M.A.B. Abdullah, K. Hussen, Thermal resistance variations of Fly Ash geopolymers: foaming responses, Sci. Rep. 7 (2017) 45355.
[17] M. Lahoti, K.K. Wong, E. Yang, K.H. Tan, Effects of Si /Al molar ratio on strength endurance and volume stability of metakaolin geopolymers subject to elevated temperature, Ceram. Int. 44 (2018) 5726–5734.
[18] J. Ye, W. Zhang, D. Shi, Effect of elevated temperature on the properties of geopolymer synthesized from calcined ore-dressing tailing of bauxite and ground-granulated blast furnace slag, Constr. Build. Mater. 69 (2014) 41–48.
[19] E. Tiffo, J.B. Bike Mbah, P.D. Belibi Belibi, J.N. Yankwa Djobo, A. Elimbi, Physical and mechanical properties of unheated and heated kaolin based–geopolymers with partial replacement of aluminium hydroxide, Mater. Chem. Phys. 239 (2020) 122103.
[20] C.N. Djangang, A.B. Tchamba, E. Kamseu, U.C. Melo, A. Elimbi, A.M. Ferrari, C. Leonelli, Reaction sintering and microstructural evolution in metakaolin-metastable alumina composites, J. Therm. Anal. Calorim. 117 (2014) 1035–1045.
[21] C.N. Djangang, E. Kamseu, M.K. Ndikontar, G.L. Lecomte Nana, J. Soro, U.C. Melo, A. Elimbi, P. Blanchart, D. Njopwouo, Sintering behaviour of porous ceramic kaolin-corundum composites: Phase evolution and densification, Mater. Sci. Eng. A 528 (2011) 8311–8318.
[22] R. Dupain, J.C. Lanchon, J.C. Saint Arroman, Sols, Ciments Et Bétons, Casteilla, Paris, 2000 p. 226.
[23] H.K Tchakouté, Elaboration et caractérisation de ciments géopolymères à base de scories volcaniques, Thèse de Doctorat / PhD, Faculté des Sciences, Universtité de Yaoundé I, Cameroun (2013) 1–189.

[24] A. Elimbi, H.K. Tchakouté, D. Njopwouo, Effects of calcination temperature of kaolinite clays on the properties of geopolymer cements, Constr. Build. Mater. 25 (2011) 2805–2812.
[25] B.B. Kenne Diffo, A. Elimbi, M. Cyr, J. Dika Manga, K.H. Tchakouté, Effect of the rate of calcination of kaolin on the properties of metakaolin-based geopolymers, J. Asian Ceram. Soc. 3 (2015) 130–138.
[26] ASTM C 373-88 (2006), Standard test method for water absorption, bulk density, apparent porosity, and apparent specific gravity of fired whiteware products.
[27] H.K. Tchakouté, C.H. Rüscher, S. Kong, E. Kamseu, C. Leonelli, Thermal behavior of metakaolin-based geopolymer cements using sodium waterglass from rice husk ash and waste glass as alternative activators, Waste Biomass Valor. 8 (2017) 572–584.
[28] E. Kamseu, A. Rizzuti, C. Leonelli, D. Perera, Enhanced thermal stability in K_2O metakaolin-based geopolymer concretes by Al_2O_3 and SiO_2 fillers addition, J. Mater. Sci. 45 (2010) 1715–1724.
[29] K.J.D. Mackenzie, J. Temuujin, K. Okada, Thermal decomposition of mechanically activated gibbsite, Thermochim. Acta 327 (1999) 103–108.
[30] A.-P. Rollet, R. Bouaziz, L'analyse thermique : l'examen des processus chimiques, tome 2, Gauthier-Villars, 55, Quai des Grands-Augustins, Paris 6e, 1972, 361–587 pages.
[31] I.B. Djon Li Ndjock, A. Elimbi, M. Cyr, Rational utilization of volcanic ashes based on factors affecting their alkaline activation, J. Non. Cryst. Solids 463 (2017) 31–39.
[32] J. Baenla, J.B. Bike Mbah, I.B. Djon Li Ndjock, A. Elimbi, Partial replacement of low reactive volcanic ash by cassava peel ash in the synthesis of volcanic ash based geopolymer, Constr. Build. Mater. 227 (2019) 116689.
[33] H.K. Tchakouté, C.H. Rüscher, J.N. Yankwa Djobo, B.B. Kenne Diffo, D. Njopwouo, Influence of gibbsite and quartz in kaolin on the properties of metakaolin-based geopolymer cements, Appl. Clay Sci. 107 (2015) 188–194.
[34] E. Tiffo, A. Elimbi, J. Dika Manga, A.B. Tchamba, Red ceramics produced from mixtures of kaolinite clay and waste glass, Braz. J. Sci. Technol. 2 (2015) 1–13.
[35] O.R. Njindam, D. Njoya, J.R. Mache, M. Mouafon, A. Messan, D. Njopwouo, Effect of glass powder on the technological properties and microstructure of clay mixture for porcelain stoneware tiles manufacture, Constr. Build. Mater. 170 (2018) 512–519.
[36] J.N. Yankwa Djobo, L.N. Tchadjié, H.K. Tchakouté, B.B. Kenne Diffo, A. Elimbi, D. Njopwouo, Synthesis of geopolymer composites from a mixture of volcanic scoria and metakaolin, J. Asian Ceram. Soc. 2 (2014) 387–398.
[37] Y. Ding, J.G. Dai, C.J. Shi, Mechanical properties of alkali-activated concrete: A state-of-the-art review, Constr. Build. Mater. 127 (2016) 68–79.
[38] H. De Souza Santos, T.W. Campos, P. De Souza Santos, P.K. Kiyohara, Thermal phase sequences in gibbsite /kaolinite clay: electron microscopy studies, Ceram. Int. 31 (2005) 1077–1084.
[39] J.T. Kloprogge, H.D. Ruan, R.L. Frost, Thermal decomposition of bauxite minerals: infrared emission spectroscopy of gibbsite, boehmite and diaspore, J. Mater. Sci. 37 (2002) 1121–1129.